Cover Page

Universiteit Leiden
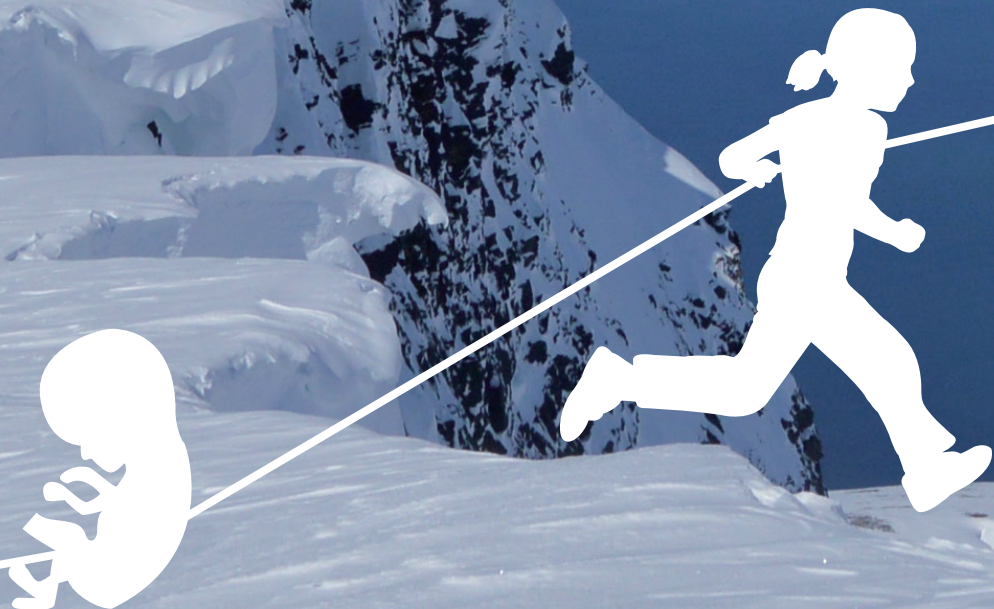
Leiden University
Repository

Author: Calkoen, Emmeline E.
Title: Atrioventricular septal defect : advanced imaging from early development to long-term follow-up
Issue Date: 2016-03-24

Atrioventricular septal defect

Advanced imaging from early development to long-term follow-up

Emmeline E. Calkoen

Atrioventricular septal defect:
Advanced imaging from early development to long-term follow-up

Emmeline Ernestine Calkoen

Atrioventricular septal defect:
Advanced imaging from early development to long-term follow-up

ter verkrijging van de graad van Doctor aan de Universiteit Leiden, op gezag van Rector Magnificus prof.mr. C.J.J.M. Stolker, volgens besluit van het College voor Promoties te verdedigen op donderdag 24 maart 2016 klokke 16.15 uur

door
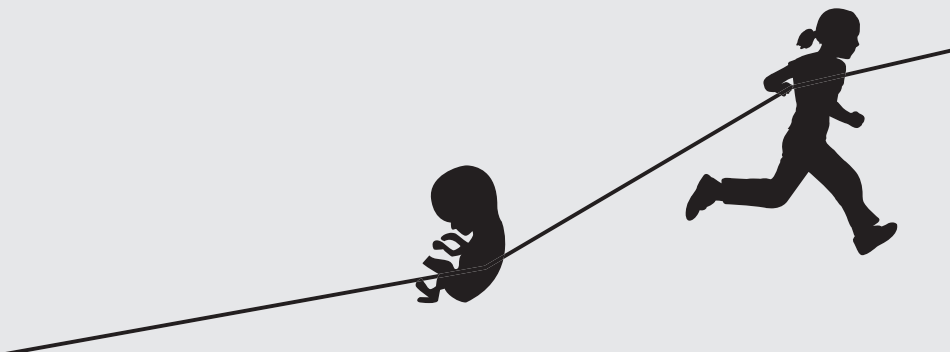
Emmeline E. Calkoen geboren te Rotterdam in 1985

Aan mijn ouders en mijn grootvader Prof. dr. J. Nauta (1922-2013)

CONTENTS

Part 1

Introduction

Chapter 1.1

General introduction and
outline of the thesis
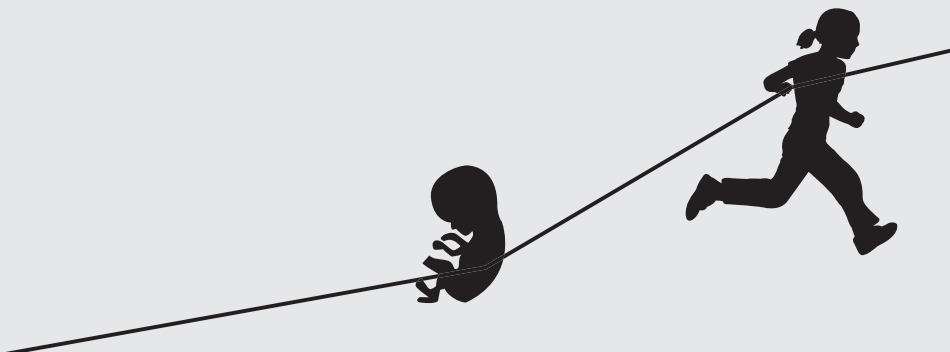
BACKGROUND

Atrioventricular septal defect (AVSD) covers a spectrum of heart anomalies with a common atrioventricular junction. AVSD comprises 7% of all congenital heart diseases (CHD) and is often associated with Down syndrome [1;2]. The nomenclature used to subdivide AVSD based on the variability in the defect in the septal tissue around the atrioventricular valves is not consistently used in literature, potentially hampering comparison of results reported between different centers. Currently, the diagnosis of AVSD is usually made prenatelly and can in specialized centers be made during early pregnancy [3]. Surgical correction of an AVSD is usually performed in early life to prevent longstanding pulmonary overflow [4]. Survival after correction is excellent in the current era. However re-operation frequency is relatively high due to regurgitation of the left atrioventricular valve (LAVV) [5]. The optimal timing for reoperation is still unclear [6].

Knowledge regarding development of CHD has markedly increased in the last decades [7]. Multiple genetic [8;9] and epigenetic [10] factors have been associated with AVSD development, but the exact pathogenesis is not completely unraveled. Evaluation of the cardiac morphology in the developing human fetus is restricted due to the limited availability of human embryonic and fetal material. Literature describes differences in morphology of AVSD between patients with Down syndrome and non-syndromic patients [11;12] and cardiac anomalies have been suggested in patients with Down syndrome without overt septal defects [13]. Blood flow through the heart has been marked as an essential factor for proper cardiogenesis [14]. Recently, high frequency ultrasound became available to analyze blood flow during the early stages of heart development in mouse embryos [15]. This allows the evaluation of the influence of blood flow during heart development.

Also after birth, in children and adults with (congenital and acquired) heart disease, intra-cardiac blood flow plays an important role in cardiac remodeling [16] and can be evaluated with echocardiography and MRI. Data on cardiac function long-term after AVSD correction is scarce. As the LAVV after AVSD correction has an aberrant morphology, intra-cardiac blood flow might be affected in these patients, possibly resulting in less efficient flow. Furthermore, quantification of LAVV regurgitation showed to be challenging with echocardiography in patients after AVSD correction [17]. 4-dimensional velocity-encoded cardiac magnetic resonance imaging (4DFlow MRI) allows direct quantification of intra-cardiac blood flow [18]. Moreover, newly available applications to visualize blood flow, such as streamlines [19] and particle tracing [20] and analysis of vortex formation [21;22] potentially provide further insight into intra-cardiac blood flow pathways in healthy hearts and those with CHD.

AIM

The first aim of this thesis was to review current knowledge, as well as current unclarities regarding the development, morphology, diagnosis and treatment of AVSD (**Part 1**). The second aim was to study the pathology of AVSD in human and rodents, using microscopic analysis, gene expression patterns, electrophysiological studies including optical mapping as well as high frequency ultrasound measurements in developing hearts (**Part 2**). Finally, cardiac function long-term after AVSD correction was analysed with special emphasis on intra-cardiac flow patterns with the use of 4DFlow MRI in corrected AVSD patients and healthy controls. (**Part 3**).

OUTLINE OF THE THESIS

In **Part 1, Chapter 1.2** the available literature regarding developmental aspects, involved genetic and epigenetic factors, nomenclature, anatomy, diagnosis, surgical techniques and outcome of AVSD is summarized. In this bench to bedside review special consideration is given to differences between non-syndromic AVSD and AVSD in patients with Down syndrome.

Subsequently, in **Part 2** of this thesis the developmental aspects of AVSD are further investigated. In **Chapter 2.1** the membranous septum and atrioventricular valves, that are aberrantly evolved in AVSD hearts, are studied in depth in patients with Down syndrome without an AVSD, as literature suggests that abnormalities are also present in this patient group. In **Chapter 2.2** the possibilities and limitations of fetal echocardiography to detect CHD in the first trimester in human are examined and correlated with morphology in fetal human specimens. Fetal echocardiography in mice allows analyses of intra-cardiac flow during heart development. In **Chapter 2.3** reference values of high frequency fetal echocardiography in subsequent developmental stages of wild type mouse embryos are provided and discussed. This technique is combined with optical mapping, immunohistochemical analysis and qPCR in **Chapter 2.4**, to analyze heart development in a mouse model with a mutation in the Vascular Endothelial Growth Factor gene, which in human is associated with AVSD and Tetralogy of Fallot. In this chapter special attention is given to the inflow tract of the heart, including the sinoatrial node.

In **Part 3** of this thesis, long-term follow-up data of corrected AVSD patients is provided. In **Chapter 3.1** an overview of the clinical use of 4DFlow MRI is given and novel blood flow visualization applications are discussed. In **Chapter 3.2** streamline visualization is used to optimize left ventricular inflow quantification and differences in inflow direction between healthy controls and corrected AVSD patients are analysed. The difference in intra-ventricular blood flow between patients and controls is further investigated with the use of particle tracing in **Chapter 3.3**. In **Chapter 3.4** a novel MRI method to assess velocity propagation, a parameter used to analyze diastolic function, is described. In **Chapter 3.5**, a previously published method to analyse three-dimensional quantitative vortex core formation in the left ventricle [22] is ap-

plied in corrected AVSD patients to study the impact of the abnormal LAVV and the lateral inflow direction on vortex formation. In **Chapter 3.6** 4DFlow MRI with retrospective valve tracking and streamline evaluation is used to characterize and directly quantify regurgitation of the LAVV in corrected AVSD patients. In **Chapter 3.7** the blood flow in the left atrium in patients with LAVV regurgitation after AVSD correction is described with the use of streamlines, vortex extraction, particle tracing and quantification of pulmonary vein flow.

Part 4 summarizes the key findings of this thesis and discusses future perspectives.

REFERENCES

1. Hoffman JI, Kaplan S, Liberthson RR. Prevalence of congenital heart disease. Am Heart J 2004 Mar;147:425-39.

2. Christensen N, Andersen H, Garne E, et al. Atrioventricular septal defects among infants in Europe: a population-based study of prevalence, associated anomalies, and survival. Cardiol Young 2012;27:1-8.

3. van Velzen C, Clur S, Rijlaarsdam M, et al. Prenatal detection of congenital heart disease-results of a national screening programme. BJOG 2015 Jan 27.

4. Fleishman CE, Marx GR. Atrioventricular Canal Defects. In: Crawford MH, DiMarco JP, Paulus WJ, editors. Cardiology. 3 ed. Philadelphia, USA: Elsevier; 2010. p. 1561-71.

5. Hoohenkerk GJ, Bruggemans EF, Rijlaarsdam M, et al. More than 30 years' experience with surgical correction of atrioventricular septal defects. Ann Thorac Surg 2010;90:1554-61.

6. Bonow RO. Chronic mitral regurgitation and aortic regurgitation: have indications for surgery changed? J Am Coll Cardiol 2013;61:693-701.

7. Gelb BD. Recent advances in understanding the genetics of congenital heart defects. Curr Opin Pediatr 2013;25:561-6.

8. Ackerman C, Locke AE, Feingold E, et al. An Excess of Deleterious Variants in VEGF-A Pathway Genes in Down-Syndrome-Associated Atrioventricular Septal Defects. Am J Hum Genet 2012;91:646-59.

9. Li H, Cherry S, Klinedinst D, et al. Genetic modifiers predisposing to congenital heart disease in the sensitized Down syndrome population. Circ Cardiovasc Genet 2012;5:301-8.

10. Agopian AJ, Moulik M, Gupta-Malhotra M, et al. Descriptive Epidemiology of Non-syndromic Complete Atrioventricular Canal Defects. Paediatr Perinat Epidemiol 2012;26:515-24.

11. Al-Hay AA, MacNeill SJ, Yacoub M, et al. Complete atrioventricular septal defect, Down syndrome, and surgical outcome: risk factors. Ann Thorac Surg 2003;75:412-21.

12. Loffredo CA, Hirata J, Wilson PD, et al. Atrioventricular septal defects: possible etiologic differences between complete and partial defects. Teratology 2001;63:87-93.

13. Geggel RL, O'Brien JE, Feingold M. Development of valve dysfunction in adolescents and young adults with Down syndrome and no known congenital heart disease. J Pediatr 1993;122:821-3.

14. Hove JR, Koster RW, Forouhar AS, et al. Intracardiac fluid forces are an essential epigenetic factor for embryonic cardiogenesis. Nature 2003 Jan 9;421:172-7.

15. Zhou YQ, Foster FS, Parkes R, et al. Developmental changes in left and right ventricular diastolic filling patterns in mice. Am J Physiol Heart Circ Physiol 2003;285:H1563-H1575.

16. Pasipoularides A. Diastolic filling vortex forces and cardiac adaptations: probing the epigenetic nexus. Hellenic J Cardiol 2012 Nov;53:458-69.

17. Prakash A, Lacro RV, Sleeper LA, et al. Challenges in Echocardiographic Assessment of Mitral Regurgitation in Children After Repair of Atrioventricular Septal Defect. Pediatr Cardiol 2012;33:205-14.

18. Westenberg JJ, Roes SD, Ajmone MN, et al. Mitral valve and tricuspid valve blood flow: accurate quantification with 3D velocity-encoded MR imaging with retrospective valve tracking. Radiology 2008;249:792-800.

19. Napel S, Lee DH, Frayne R, et al. Visualizing three-dimensional flow with simulated streamlines and three-dimensional phase-contrast MR imaging. J Magn Reson Imaging 1992:143-53.

20. Eriksson J, Carlhall CJ, Dyverfeldt P, et al. Semi-automatic quantification of 4D left ventricular blood flow. J Cardiovasc Magn Reson 2010;12:9.

21. Kheradvar A, Pedrizzetti G. Vortex formation in the heart. Vortex formatin in the cardiovascular system. London: Springer; 2012. p. 45-53.

22. Elbaz MS, Calkoen EE, Westenberg JJ, et al. Vortex flow during early and late left ventricular filling in normal subjects: quantitative characterization using retrospectively-gated 4D flow cardiovascular magnetic resonance and three-dimensional vortex core analysis. J Cardiovasc Magn Reson 2014;16:78.

ABBREVIATIONS

2D	Two dimensional
3D	Three dimensional
4D	Four dimensional
A-peak	Late diastolic filling peak
AVSD	Atrioventricular septal defect
CHD	Congenital heart disease
CMR	Cardiovascular magnetic resonance
CX	Connexin
DS	Down syndrome
EF%	Ejection fraction
E-peak	Early diastolic filling peak
LA	Left atrium
LAVV	Left atrioventricular valve
LV	Left ventricle
MRI	Magnetic resonance imaging
SAN	Sinoatrial node
VEGF	Vascular endothelial growth factor

Chapter 1.2

Atrioventricular septal defect:
from embryonic development
to long-term follow-up

Emmeline E. Calkoen, Mark G. Hazekamp, Nico A. Blom, Bernadette B.L.J. Elders,
Adriana C. Gittenberger-de Groot, Monique C. Haak, Margot M. Bartelings,
Arno A.W. Roest* and Monique R.M. Jongbloed*
* Equal contributions

ABSTRACT

Atrioventricular septal defect (AVSD) covers a spectrum of heart anomalies with a common atrioventricular connection and has an incidence of 4–5.3 per 10.000 live births. About half of the AVSDs occur in patients with Down syndrome. This review provides a bench to bedside overview of AVSD. Developmental aspects, nomenclature, anatomy, and classification of AVSD are discussed. Furthermore an overview of genetic and maternal risk factors for AVSD is provided, and available literature on (fetal) diagnosis, surgical techniques and follow-up is presented. Special attention is given to differences in developmental, anatomical and prognostic factors of AVSD between non-syndromic and Down syndrome patients.

INTRODUCTION

The term atrioventricular septal defect (AVSD) covers a spectrum of heart anomalies with a common atrioventricular (AV) junction [1]. With an incidence of 4–5.3 per 10.000 live births, AVSD comprises 7% of all congenital heart diseases (CHD) and is often associated with Down syndrome [2–5]. Despite intensive investigation, the morphogenesis of AVSD is still not fully understood. Furthermore controversy remains in nomenclature and long-term follow-up data are scarce. Recent developments in knowledge on heart development provide new insights in (epi)genetic factors in AVSD development.

   The aim of the current review is to give a complete bench to bedside overview, from embryonic development to clinical aspects of AVSD. Special attention is given to the difference between non-syndromic and syndromic, in particular Down syndrome, patients.

NOMENCLATURE AND TYPES OF AVSD

An overview of nomenclature is presented in Figure 1. Controversies exist on nomenclature and subdivision of the varying morphology of AVSDs, and several different descriptions are currently used. The terms 'atrioventricular canal defect' and 'endocardial cushion defect' are used as synonyms for AVSD.

In this review we will use the classification as agreed upon by the International Paediatric and Congenital Cardiac Code (www.IPCCC.net) [6, 7]. *Complete AVSD* according to the IPCCC includes an ostium primum defect of the atrial septum and a non-restrictive defect in the inlet portion of the ventricular septum, with one AV annulus and a common AV valve. The common AV valve classically is composed of two (a superior and an inferior) leaflets bridging across the ventricular septum, as well as a left lateral (mural) leaflet, a right antero-superior and a right inferior leaflet (Figure 1). In complete AVSD shunting takes place at both the atrial and ventricular level. In an AVSD with an *isolated atrial component* (also known as *ASD primum, ostium primum defect* or *partial AVSD*) the bridging leaflets are attached to the ventricular septum. Although there is one annulus, the attachment of the bridging leaflets to the ventricular septum results in two orifices and shunting can take place only above this level, at the atrial level (Figure 1). Less common is an AVSD with an *isolated ventricular component* (also known as *partial AVSD*), where the partially fused bridging leaflets are attached to the atrial septum and shunting is just at the ventricular level. This type of AVSD is in the clinical setting mostly referred to an inlet VSD (Figure 1). Fourthly, the IPCCC defines an *intermediate* (or *transitional*) AVSD with an ostium primum defect and a (often restrictive) VSD just below the AV valves, but with two remaining separate AV orifices due to fusion of the bridging leaflets (Figure 1). Of note, some authors distinguish between a transitional AVSD, being an AVSD with two annuli and an inlet VSD and an intermediate AVSD,

being an AVSD with 1 annuli and 2 orifices [8]. This difference is not acknowledged by the IPCCC that equally classifies the 2 forms. We support the latter, as we do not consider AVSD to have 2 annuli, but rather a common annulus and a common AV valve that can have 2 orifices in case of attachment of the valve to either the ventricular (most common) or atrial septum. Fifth, the IPCCC describes an AVSD with *ventricular imbalance*, with an unequal position of the common AV valve above the (unbalanced) ventricles with a variable degree of ventricular hypoplasia. The imbalance may occur in the setting of either a complete, partial or intermediate/transitional AVSD.

Another defect at the level of the AV septum is the so-called Gerbode defect. This malformation is on the spectrum between an AVSD and a membranous VSD being a defect in the membranous part of the AV septum allowing shunting between the left ventricle (LV) and right atrium (RA). According to Gerbode [8] shunting can take place either directly (supra-annular) through the membranous septum or indirect (infra-annular) via a perimembranous VSD and a defect in the tricuspid valve. In the IPCCC the Gerbode defect is classified as a subtype of VSD [9], however as the defect is present in the AV septum one could also argue that the anomaly could be designated a form of AVSD.

The Rastelli classification, originally described in 1966 [10], subdivides complete AVSD based on the anatomy of the superior (anterior) common/bridging leaflet. A completely split leaflet (i.e., the superior bridging leaflet is divided), with the superior bridging leaflet almost completely adherent to the left ventricle and firmly attached on the ventricular septum by multiple chordal insertions is designated as Rastelli type A. Type A is the most frequently found [11]. A divided (split) superior leaflet, with the superior bridging leaflet attached over the ventricular septum by an anomalous papillary muscle of the right ventricle is designated Rastelli type B. Rastelli type C indicates a large, non-divided, superior leaflet without chordal attachment to the interventricular septum, also known as the 'free floating'. Type C is often seen in association with other cardiac defects [12]. From classes A to C ventricular shunting increases. The Rastelli classification was originally designed to predict the outcome of surgery. However, due to the lack of correspondence between the classification and surgical outcome and enormous variability in leaflets [13,14], the use of the Rastelli classification is currently largely omitted in literature.

A mitral cleft in an otherwise normal mitral valve (*isolated mitral cleft*) should not be considered the same as the 'cleft' in the left part of the common AV valve in AVSD. An isolated cleft is a cleft in the aortic (anterior) mitral leaflet, whereas a 'cleft' in the setting of AVSD is a gap between the superior and inferior bridging leaflets, clearly distinguishing the anatomy of the left AV valve in AVSD from a normal mitral valve anatomy [15–17]. Although anatomically features are different from the cleft in AVSD, an *isolated mitral cleft* is frequently seen in families with AVSD and, like AVSD, is associated with Down syndrome [18], therefore a developmental relationship between an isolated mitral cleft and a cleft seen in AVSD has been suggested [18].

Distribution numbers of AVSD-types vary in the literature, which may be due to an inconsistent use of nomenclature. The majority (56%–75%) of AVSDs are complete AVSDs [2,4,19]. Subtype

distribution of AVSD differs between patients with and without chromosomal abnormalities, with complete AVSD more frequently seen in syndromic patients [4,5,20] (Table 1). Unbalanced AVSD occurs in 6%–10% of complete AVSDs [5,21,22] and is more frequently seen in non-syndromic patients (Table 1).

The spectrum of AVSD can thus range from partial AVSD to intermediate AVSD and complete AVSD. Abnormalities are also found in the membranous septum of relatives of patients with AVSD [23] and in patients with Down syndrome without AVSD [24,25], indicating that the AV septum may be abnormal without overt deficiency. Some authors have even suggested the oc-currence of AVSD without shunting, i.e., an AVSD-valve morphology (common valve with linear insertion), where the common valve is attached to both the atrial and the ventricular septum [26]. The observed variability in anatomy may relate to the complex development of the AV septum and AV valves during embryology.

Figure 1. Schematic presentation of nomenclature of different types of AVSD.
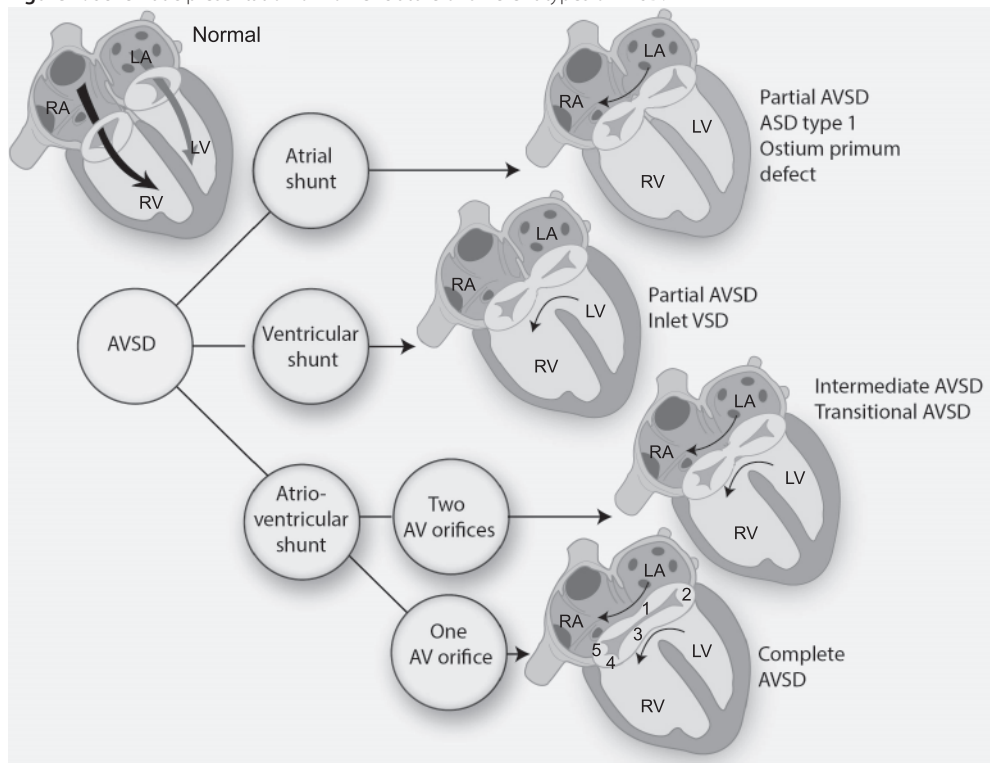
The defect can occur at atrial, ventricular or atrioventricular level. Black arrows indicate the defects, but do not neces-sarily represent blood flow direction. RA = right atrium, LA = left atrium, RV = right ventricle, LV = left ventricle. In the complete AVSD the five leaflets are shown: superior bridging leaflet (1), left lateral (mural) leaflet (2), inferior bridging leaflet (3), right inferior leaflet (4) and right antero-superior leaflet (5).

Table 1. Studies that report differences between non-syndromic (NS) patients with AVSD and patients with AVSD and Down syndrome (DS) in incidence of type of AVSD, associated (cardiac and non-cardiac) defects and outcome. Ao = aorta, papill. = papillary, IVC = inferior vena cava, LAVR = left atrioventricular valve repair. * Indicates a study only in patients with complete AVSD.

	NS	DS	Reference
Type of AVSD			
Partial	30 %	24 %	[20]
	60 %	20 %	[4]
	70 %	12 %	[117]
	51 %	13 %	[19]
Complete	26 %	70 %	[20]
	40 %	80 %	[4]
	30 %	88 %	[117]
	29 %	73 %	[19]
Unbalanced	31 %	35 %	[21]*
	29 %	5 %	[115]*
	25 %	3 %	[71]*
	11 %	6 %	[69]
Associated cardiac			
AV Valve dysplasia	24 %	3 %	[53]*
	10 %	13 %	[54]*
Heterotaxy	32 %	0 %	[20]
Tetralogy of Fallot	3 %	9 %	[71]
	4 %	13 %	[69]
Coarctation Ao	17 %	1 %	[71]
	6 %	0 %	[115]
	17 %	5 %	[69]
Sub Ao stenosis	3 %	0 %	[71]
	3 %	1 %	[112]
	8 %	4 %	[69]
Single papill. muscle	9 %	2 %	[71]
Double orifice MV	4 %	2 %	[71]
Additional VSD	4 %	1 %	[71]
	6 %	7 %	[115]
	4 %	2 %	[112]
	7 %	1 %	[69]
PDA	33 %	70 %	[115]
	17 %	33 %	[112]
	5 %	5 %	[69]
Common atrium	7 %	1 %	[112]
Extra cardiac			
Laterality	23 %	0 %	[20]
Musculoskeletal	13 %	25 %	[20]

Table 1. (Continued)

	NS	DS	Reference
Eye and ear	0 %	10 %	[20]
Central Nerve	0 %	9 %	[20]
Renal and urinary	11 %	5 %	[20]
Digestive	7 %	5 %	[20]
Respiratory	6 %	0 %	[20]
Facial cleft	5 %	0 %	[20]
Outcome			
In hospital mortality	4 %	2.6 %	[111]
	14 %	10 %	[115]
	12 %	16 %	[53]
	5 %	13 %	[116]
	46 %	17 %	[117] *
	13 %	5 %	[71]
	6 %	5 %	[112]
Non-cardiac compl.	15 %	49 %	[54]*
Long term survival	75 %	84 %	[112]
	75 %	87 %	[20]
	95 %	80 %	[116]
	85 %	78 %	[136]
	90 %	94 %	[137]*
	86 %	94 %	[71]
Re-operation	19 %	5 %	[71]
	11 %	8 %	[115]
	32 %	11 %	[53]
	29 %	25 %	[112]
Re-operation due to LAVR	27 %	18 %	[112]
	13 %	9 %	[136]
	15 %	4 %	[137]*

EMBRYONIC AND FETAL DEVELOPMENT: (ABNORMAL) ATRIOVENTRICULAR SEPTATION

Normal development

Cardiac septation takes place in the first 9 weeks of pregnancy. The primary heart tube forms from a myocardial progenitor population from the splanchnic mesoderm. Additionally, a second pool from the splanchnic mesoderm, the so-called second heart field population, situated dorsal to the primary heart tube, will contribute cells to the arterial and venous side of the heart.

The heart tube initially consists of an inner endocardial layer and outer myocardial layer, separated by cardiac jelly. Cells from the endothelium migrate into this jelly mesenchyme, a process known as endothelial to mesenchymal transformation (EMT) [27]. As a result four endocardial cushions are formed at the AV junction: inferior, superior and two lateral cushions (purple in Figure 2A), that will contribute to the AV valves during later development. Besides endocardial cushion formation, AV septation requires growth of the muscular atrial septum primum toward the AV canal with on its lower rim a cushion-like structure, known as the mesenchymal cap (green in Figure 2A). Initially, the septum primum will not connect to the AV canal, leaving an opening, the ostium primum. Subsequently, the mesenchymal cap fuses with the superior and inferior AV endocardial cushions. To complete AV septation, the mentioned structures fuse with the so-called dorsal mesenchymal protrusion (DMP) or vestibular spine (yellow in Figure 2A), a mesenchymal (second heart field) protrusion at the base of the atrial septum [28,29] (Figure 2). During development the DMP will partly myocardialize, and a remnant of the DMP will form the tendon of Todaro, which is the continuation of the Eustachian valve of the inferior vena cava and the Thebesian valve of the coronary sinus [30].

Figure 2. Anatomical structures involved in normal and abnormal atrioventricular septation during development.
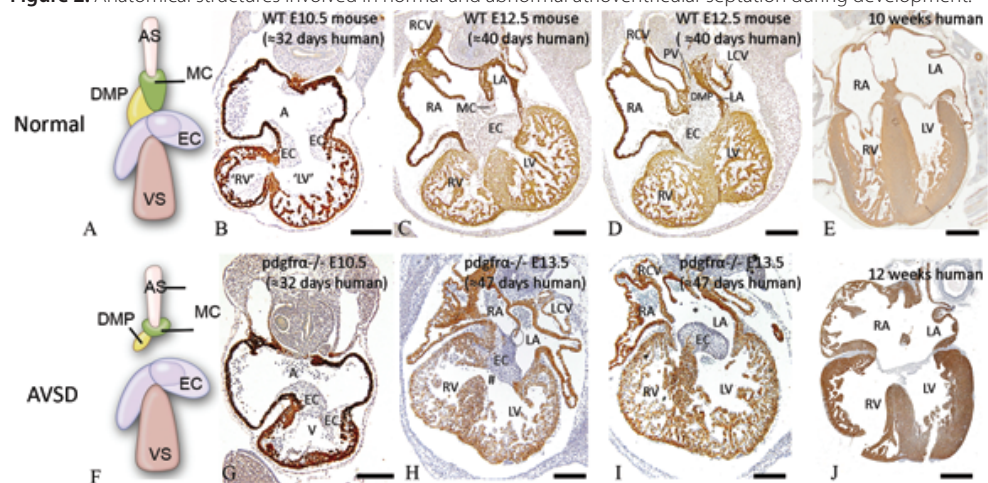
Panel A shows the three main structures involved in AV-septation: endocardial cushions (EC, light purple), mesenchymal cap (MC, green) and dorsal mesenchymal protrusion (DMP, yellow). Modified after Webb et al. [28]. Panel B shows an early stage (E10.5) embryonic heart, with a common AV canal, guarded by two endocardial cushions. In panels C and D (caudal section) the three structures are shown in a wild type 12.5 day old mouse embryo, where only a small ostium primum can be seen at this developmental stage. Panel E shows the situation after AV septation has been completed in human. The ostium primum had been closed. In the Pdgfr-α knock-out embryo the MC and DMP are less well formed as schematically shown in F. Panel G shows an early (E10.5) embryo and subsequent sections show a 13.5 day old Pdgfr-α−/− embryo (E-F) with a dotted circle showing the reduced volume of the MC, the * showing the atrial defect and the # the ventricular defect. In Panel J, a complete AVSD is shown. Developmental stages are given as days/weeks after conception. Right atrium (RA), LA = left atrium, RV = right ventricle, LV = left ventricle, RCV = right cardinal vein, LCV= left cardinal vein, PV = pulmonary vein, VS = ventricular septum, AS= atrial septum. Black bars in panels B–D and G–I indicate 200 um and in panels E and J 1 mm. Panel J is published with permission from Calkoen et al. [25].

1.2

The endocardial cushions, mesenchymal cap and DMP thus all contribute to the membranous septum. The membranous septum will eventually contain an *atrioventricular* part, situated between the left ventricle and right atrium and an *interventricular* part, situated between the left and right ventricles. Initially however, only the AV part is present, but with detachment of the tricuspid valve the interventricular membranous septum develops [31]. The superior and inferior endocardial cushions also contribute to the septal leaflet of the tricuspid valve, and the anterior (aortic) leaflet of the mitral valve [32]. The right lateral cushions will form the lateral (anterior and posterior) leaflets of the tricuspid valve and the left lateral cushion forms the lateral (posterior) leaflet of the mitral valve [32]. Next to cells derived from the endocardium, also epicardial derived cells contribute to the formation of the annulus fibrosis and the parietal leaflets of the mitral and tricuspid valves [33,34].

Abnormal development

Early studies on AVSD development with transgenic mouse models focused mainly on malformation of the endocardial cushions. Attention has shifted in the past decades to the DMP as well as the mesenchymal cap. Also abnormal looping may play a role. Several examples are listed below. The trisomy 16 (Ts16) mouse which is suggested to be a model for Down syndrome, develops, among other cardiac malformations, a complete AVSD. The pathogenesis of complete AVSD in the Ts16 mouse model is attributed to insufficient looping, fused but smaller endocardial cushions [35], as well as aberrant mesenchymal cap and DMP development [36]. Heterozygous mutations in the genes *GATA4* [37] and *NR2F2* [38] in mouse can result in partial (ASD1) or complete AVSDs, suggested to be caused by deficient endocardial cushion formation. Wnt [39], (SHF specific) Shh [40] and Pdgfr-a [41] knock-out mice all have a diminished DMP development leading to a partial or complete AVSD. In general, in mutant mouse studies little attention is addressed to difference in origin of partial, intermediate or complete AVSD. Also, the significance of knowledge of the "culprit" anatomical deficiency (i.e., due to a defect in either endocardial cushion, mesenchymal cap, DMP, or a combination) in terms of outcome/prognosis of the resulting AVSD, is currently unclear. In human embryos with AVSD no abnormal development of the endocardial cushions is described to date [42], whereas a diminished DMP development was observed in fetuses with Down syndrome and an AVSD [43]. In addition, abnormalities in fetal blood flow may affect septation and valve formation [44–46].

Abnormal AV septation may also affect formation of the AV conduction system. During normal development both an anterior and posterior node are present and a fusion of both nodes in order to form the definitive AV node was suggested [47]. A study in human embryos with Down syndrome showed that the posterior and anterior AV-node fail to fuse in AVSD and that the (posterior) AV node remains at a more posterior position in AVSD hearts comparable to normal hearts at earlier developmental stages [48].

ANATOMY OF THE AV VALVES AND CONDUCTION SYSTEM IN AVSD

It is important to realize that the leaflets, chordae and papillary muscles of the AV valves of all AVSD types, even after surgical correction, are different compared to the normal tricuspid and mitral valves [49]. Basically, in all types of AVSD, there is a common valve, in which the leaflets are to a variable extent fused with each other and/or with the atrial or ventricular septum. The posterior (lateral) leaflet of the normal mitral valve covers about 2/3 of the circumference of the valve, whereas the left posterior (lateral) leaflet in a corrected AVSD heart only covers 1/5. The right half of the inferior leaflet in AVSD is comparable with the normal posterior tricuspid leaflet. The size of the right anterior leaflets depends on the superior bridging leaflet. The different valve leaflet division causes a different position of the papillary muscles as compared to normal hearts, which can cause regurgitation or stenosis [50] and influences the direction of the inflow of blood into the LV [51].

Another feature that may contribute to valvular dysfunction later in life is dysplasia of the common AV valve, especially of the lateral leaflet [52]. Al-Hay et al. [53] reported marked differences in valve dysplasia in patients with Down syndrome (3%) versus non-syndromic patients (24%), although this was not confirmed by a recent study (nonsyndromic 10% and Down syndrome 13%) [54].

Right bundle branch block, first degree AV block and more rarely 2nd and 3rd degree AV block are all described in patients with AVSD even before surgical correction [55,56]. Several studies in human hearts have described the morphology and position of the cardiac conduction system in AVSD [50,57]. The AV node is positioned more posteriorly and inferiorly compared to the normal position in the triangle of Koch (Fig. 3). This aberrant position, especially when it is combined with a significant defect of the ventricular septum, necessitates the presence of a long non-branching (His) bundle, in order to reach the top of the ventricular septum [57]. Knowledge on the anatomy of the conduction system in AVSD contributes to reduction of surgically induced AVblock [50].

SYNDROMES, GENES AND MATERNAL RISK FACTORS INVOLVED IN HUMAN AVSD

Several syndromes are associated with AVSD. In a recently studied large cohort, 49% of patients with an AVSD had Down syndrome [5]. In live born children with Down syndrome the incidence of AVSD is as high as 25% [58]. In patients with heterotaxia syndrome AVSD is often found; in right isomerism (or asplenia syndrome), the prevalence of complete AVSD is 90% [59]. In left isomerism (or polysplenia syndrome), the prevalence of partial AVSD is 60%–70% [60], indicating that the morphogenesis of at least some cases of AVSD may be related to the loss of normal right/left asymmetry in the body. Genes involved in regulation of normal body asymmetry including *PITX2, NODAL, ZIC3, CFC1*, and *NKX2.5* are also associated with AVSD. Other regularly encountered

Figure 3. The cardiac conduction system.
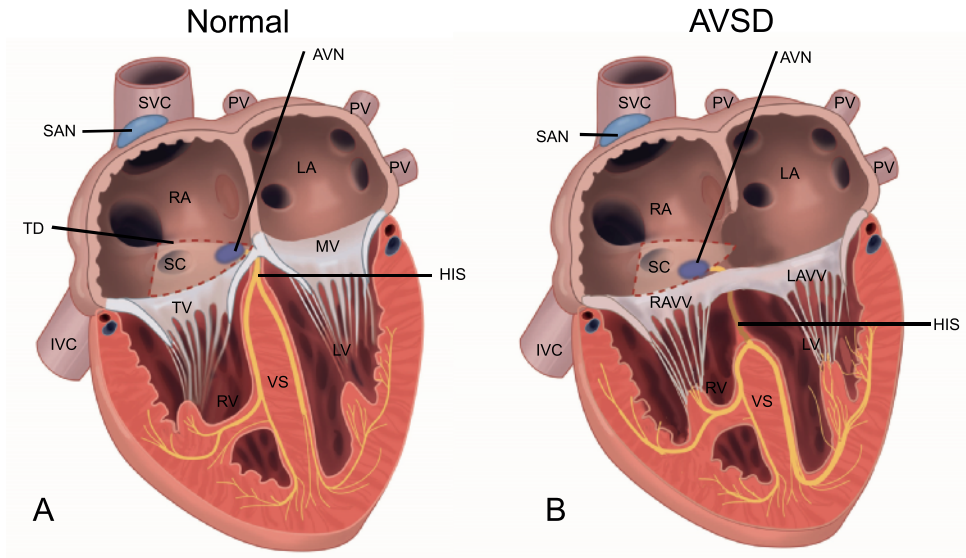
Panel A shows the normal heart. The atrioventricular node (AVN) is positioned in the triangle of Koch (red dotted line), formed by the septal tricuspid valve leaflet, the ostium of the coronary sinus and the Tendon of Todaro (TD) (remnant of the embryological dorsal mesenchymal protrusion). In AVSD hearts (panel B), the AVN is positioned more posteriorly and inferiorly (to the base of the triangle of Koch) as compared to the normal heart and the His bundle needs a longer course in order to reach its position on top of the ventricular septum. RA = right atrium, LA = left atrium, RV = right ventricle, LV = left ventricle, SCV = superior vena cava, IVC = inferior vena cava, SAN = sinoatrial node, SC = sinus coronarius, PV = pulmonary vein, TV = tricuspid valve, MV = mitral valve, RAVV= right atrioventricular valve, LAVV= left atrioventricular valve, VS = ventricular septum.

associated syndromes are CHARGE (coloboma, heart defects, atresia of choanae, retardation of growth, genital defect, ear anomalies) syndrome, Noonan syndrome, VATER (vertebral anomalies, anal atresia, trachealoesophageal fistula, renal anomalies) association, Holt–Oram syndrome and Smith–Lemli–Opitz syndrome [5,20,61–63].

The high incidence of Down syndrome in AVSD patients makes genes located on chromosome 21 suspect for involvement in the morphogenesis of AVSD. However not all patients with trisomy 21 develop an AVSD, suggesting a multigenic influence. The most frequently described associated gene in both patients with and without Down syndrome is CRELD1 on chromosome 3. The penetrance of AVSD in Down syndrome is incomplete; therefore CRELD1 is seen as a risk factor [64,65]. Interestingly CRELD+/− mice do not have septal defects. When they are however crossed onto the 'Down syndrome mice' Ts65Dn, they do develop septal defects [66]. Table 2 gives a summary of other reported humane genes associated with AVSD. Several syndromes associated with AVSD have mutations in genes related to Sonic Hedgehoc (SHH) [63]. SHH acts on the outflow tract formation via contribution of endocardial cushion cells as well as on AV septation via DMP contribution [40]. These studies all suggest that a single gene can contribute

to the arterial pole of the heart causing outflow tract defects and the venous pole of the heart (DMP), causing AVSD [67], which could also explain frequent co-occurrence of AVSD with for example tetralogy of Fallot. This may also relate to recent findings that genes involved in the VEGF-A pathway are not only associated with outflow tract defects, but also AVSD [64].

Table 2. Genes involved in human development of AVSD.

Affected humane gene	Chromosome	Ref	Proposed impact
GATA4	8	[138]	Looping Epicardial contribution Cardiomyocyte differentitation (affects Tbx5)
GATA5	20	[65]	Myocardial and endocardial differentiation. Interaction with GATA4 and VEGF
GATA6	18	[139]	Looping Epicardial contribution Cardiomyocyte differentitation
Nkx2.5	5	[140,141]	Looping SHF contribution
Zic3	X	[142]	Left right asymmetry
TBX5	12	[143]	Cardiomyocyte differentitation SHF Interacts with Nkx2.5 and Gata4
NODAL	10	[144]	Looping Left right asymmetry
CFC1/CRYPTIC	2	[144]	Looping Left right asymmetry (nodal related)
LEFTY2	1	[144]	Left right asymmetry (nodal related)
ACVR2B	3	[145]	Left right asymmetry (nodal related)
BMP4	14	[140]	Endocardial cushions SHF contribution
ACVR1/ALK2	2	[146]	SHF contribution (via BMP signaling)
VEGF	6	[147]	Endocardial cushions
COL6A1-2	21	[24,64]	Endocardial cushions (Vegf path)
FBLN2	3	[64]	Endocardial cushions (Vegf path)[148]
FRZB	2	[64]	Endocardial cushions (Vegf path) [149]
DSCAM	21	[150]	Cell-cell adhesion of cushion fibroblasts[150]
CRELD1	3	[65]	Left right asymmetry (Vegf path)
GJA1/Cx43	6	[151]	Looping Left right asymmetry
NR2F2/Coup-TFII	15	[38]	Endocardial cushion (EMT)

Besides genetic risk factors there are several maternal risk factors reported. In infants without Down syndrome a strong association between complete AVSD and maternal diabetes was found (odds ratio 21) [4]. Moreover, a recent study found an association between complete AVSD and pregestational diabetes, gestational diabetes and obesity (BMI N 30 kg/m^2) [68]. In another study, correlation between heavy smoking and AVSD was seen [62], however this study did not correct for diabetes. These findings indicate that epigenetic and genetic factors are likely to contribute to the genesis of AVSD.

ASSOCIATED ANOMALIES

Non-syndromic AVSD patients often have associated cardiac anomalies [7,69]. In patients with chromosomal anomalies associated cardiac defects are rare (8%) [5,70], with the exception of tetralogy of Fallot cooccurring more often with AVSD in patients with Down syndrome than in non-syndromic patients [71] (Table 1). In patients with an AVSD the aorta is in a more anterior position, possibly due to improper wedging of the outflow tract during development. Moreover the ventricular septum is shorter in AVSD patients [72]. This together leads to a longer outlet than inlet part. The anterior position of the aorta can be seen on a chest x-ray or ventricular angiography and is described as a "gooseneck". There is a correlation between different arrangements of the out- flow tract and Rastelli subtypes [73]. The combination of the more anterior placed aorta and a narrow sub-aortic outflow tract [74] might lead to the most frequent associated cardiac anomalies: subaortic stenosis and coarctation of the aorta [5].

Taking syndromic and non-syndromic patients together, in 5% of patients with a complete AVSD a double outlet right ventricle (DORV) is seen [75]. Double orifices of the left AV valve and a single papillary muscle (i.e., parachute valve) are observed in AVSD patients in respectively 14% and 1% [76]. AVSD is commonly observed in heterotaxy syndrome, and can also occur concomitant with Ebstein's anomaly, anomalous pulmonary venous return and transposition of the great arteries. 75% of patients with an AVSD have anomalies in other organs than the heart. Reported congenital anomalies occur in both non-syndromic and syndromic patients (Table 1) [5,20,22,64,70].

DIAGNOSIS

### Prenatal diagnosis

In utero prevalence of AVSD has been reported as high as 18% of CHD affected individuals. The discrepancy with the prevalence in live births is possibly due to a high number of fetal demises and elective termination, most frequently in cases with aneuploidy [77]. AVSD can be detected with fetal echocardiography as early as 12 weeks of gestation specialized centers [78]

(Figure 4A–C). The detection rate in routine screening, using the four-chamber view, is, however reported to be as low as 27% [79]. Recent data show, however, that detection rate as high as 67% for balanced AVSD and 93% for unbalanced AVSDs can be achieved in national organized screening programs, using distinct protocols and adequate training of the ultrasonographers [80]. To improve detection rate, additional tools as the atrial to ventricular ratio [81] and level of linear insertion [82] have been suggested. Recent reports from the United States and Europe report elective termination of pregnancy of respectively 32% [83] and 31% [5] of cases, however in these studies the incidence of Down syndrome and associated CHD in the terminated fetuses were not specifically reported. Heterotaxia, unbalanced ventricles and a syndrome other than Down syndrome were detected as negative prognostic factors for late survival when an AVSD was detected at 20 weeks' gestation [83]. When pregnancy is not terminated, fetuses with Down syndrome have a better survival compared with nonsyndromic fetuses [84]. As the incidence of associated cardiac anomalies, extra-cardiac abnormalities and aneuploidy (40%–50% Down syndrome) is high in AVSD patients, third level ultrasound and invasive testing should be offered, including array comparative genomic hybridization to detect the presence of copy number

Figure 4. Diagnosis of AVSD.
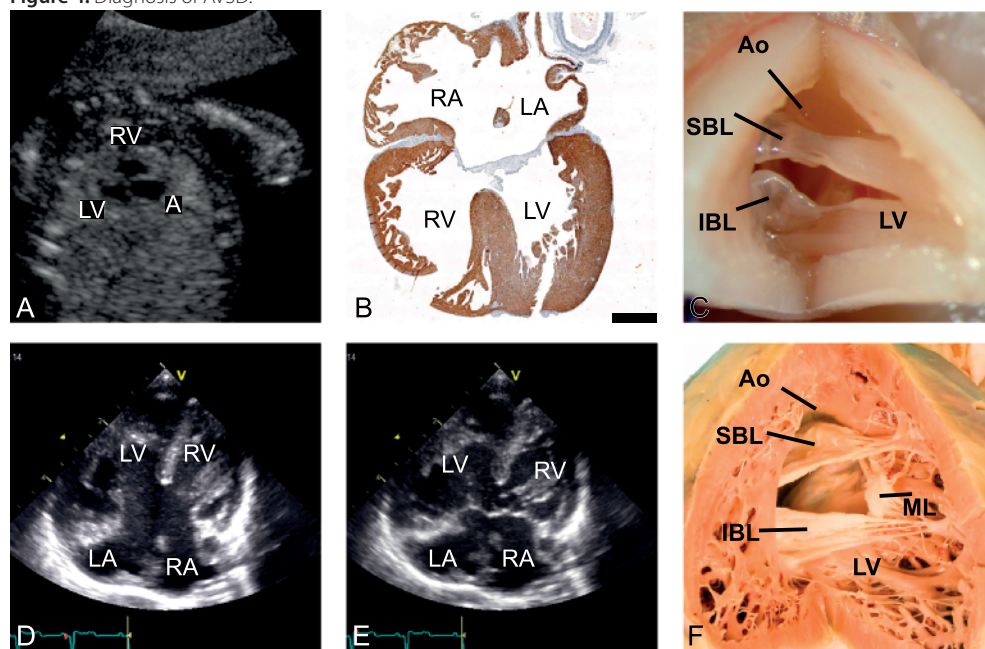
(A) Prenatal ultrasound with an oblique plane through the thorax at 12 weeks pregnancy. (B) Section of a complete AVSD heart of fertilization age 14 weeks stained with troponin I with black scale bar indicating 1 mm. (C) The common valve seen from the left ventricle in a specimen of a 13 week old AVSD heart. D and E) Echocardiography of a 5-week-old patient with a complete AVSD during diastole (D) and systole (E). (F) A specimen of an uncorrected partial AVSD (ASD1). RV = right ventricle, LV = left ventricle, A = atrium, RA = right atrium, LA = left atrium, Ao = Aorta, SBL = superior bridging leaflet, IBL = inferior bridging leaflet, ML = mural leaflet. Modified after Jansen et al. [78].

variations [85]. No studies are performed that investigate the advantage of prenatal diagnosis of AVSD above postnatal diagnosis on postnatal morbidity and mortality, but the association with other defects makes prenatal detection important to provide parents all necessary information to aid the decision to continue the pregnancy.

Postnatal diagnosis.

Clinical presentation depends on the type of AVSD with the associated level and degree of shunting. Mild central cyanosis can be present in the newborn due to bidirectional shunting because of the high pulmonary resistance at birth. Due to the left to right shunt at atrial and ventricular level in complete AVSD and, if present, the AVV regurgitation, the child will develop congestive heart failure and if uncorrected, eventually Eisenmenger's syndrome [86]. Cases with a partial AVSD (ASD1) can remain asymptomatic for years. With physical examination the AVV regurgitation can be heard as a holosystolic murmur and the increased diastolic flow as a mid-diastolic rumble. On electrocardiography the posterior and inferior displacement of the conduction system results in a left and superior QRS axis. First degree AV block can be present due to enlargement of the right atrium, or displacement of the AV-node Also higher degree AV block including complete heart block can be observed. On chest x-ray ventricular enlarge- ment and the "goose neck" appearance reflecting the more anterior position of the aorta can be detected. Echocardiography is the main diagnostic modality of AVSD (Fig. 4D–E) and can assess the presence and size of atrial and ventricular shunting, AVV morphology and orientation, size of left and right ventricle, number and location of papillary muscles, left and right outflow tract obstruction, additional septal defects and associated anomalies [87].

Three-dimensional echocardiography can have additive value in surgical planning, because AVV and LVOT morphology can be assessed with more detail, as is reviewed by Kutty and Smallhorn [88]. Although intra-operative transoesophageal echocardiography is influenced by differences in hemodynamics during surgery and does not always correspond with post- operative echocardiography [89], it can decrease the incidence of re-operation due to left AVV regurgitation [90]. Small studies reported the use of MRI in pre-operative assessment of AVSD, to visualize morphology and quantify ventricular size pre-operatively [91]. Angiography is not suggested in clinical decisions making prior to AVSD correction [87].

TREATMENT

Before surgical repair digoxin, diuretics and angiotensin-converting enzyme inhibitors may be used to treat congestive heart failure and food supplements may be necessary to achieve weight gain [87,92].

Surgical repair of a complete AVSD was first described by Lillehei et al. [93] in 1955. Three techniques have been described (Figure 5) [87]: 1) the single-patch technique where one piece

of prosthetic material is used to close the atrial or ventricular shunt (Figure 5A), 2) the twopatch technique where one patch is used to close the VSD and one other patch used to close the ASD (Figure 5B), and 3) the modified single-patch technique in which the common valve is sutured to the ventricular septum and the ASD is closed with a patch (Figure 5C). Partial AVSDs are closed with the single-patch technique. Complete AVSDs are mostly closed with the double-patch technique. An intermediate AVSD can be closed by the double-patch technique or modified singlepatch. Recent studies report the modified single-patch technique for closure of a complete AVSD, with the benefit of a shorter cardiac pulmonary bypass and aortic cross-clamp time and low mortality and low incidence of left AVV (LAVV) regurgitation [94]. Choice of techniques varies from patient to patient and depends on the extent of the atrial and ventricular defects. In all three techniques besides insertion of a patch 1) the "cleft" of the left AVV is suture-closed, to prevent AVV regurgitation [95–97]; 2) the anterior and posterior right leaflets of the RAVV are approximated; and 3) the two left lateral commissures of the LAVV are approximated (Figure 5 lower planes). As AVSD can cooccur with tetralogy of Fallot and DORV, combined repair is often performed with desirable results [75]. Patients with an unbalanced AVSD, where a biventricular repair is not possible, are a high risk group [97]. Decisions to perform a univentricular repair can be made based on the so-called *AV valve index*, (i.e., the LAVV area/total AV valve area), with an index between 0.4 and 0.6 considered as a balanced AVSD [98].

Because morbidity of AVSD repair in small infants is low in the current era [99–101] and pulmonary vascular obstructive disease needs to be prevented [102], repair of complete AVSD currently is advised to be performed around 3 months of age [87]. However timing of surgery is influenced by many factors, as co-occurrence of other heart defects. Correction in children below 5 kg was suggested a risk factor for late LAVV regurgitation [99], however, correction at an age above 6 months has also been considered a risk factor for reoperation [103]. In studies including patients corrected after the year 2000, the mean age at correction of complete AVSD ranged between 3.6 months [19] and 7.2 months [7]. Patients with intermediate AVSD usually undergo surgery around 1 year of age [104]. Patients with partial AVSD (ASD1) without severe LAVV regurgitation, can be asymptomatic and controversy exists when repair is indicated and what the optimal age for repair of partial AVSD is. The median age of surgical correction reported in recent studies varied from 1.8 [104] to 7.9 years [105]. In a study by Minich et al. [104] surgical correction of partial AVSD before 4 years of age is associated with significant catch-up growth and less LAVV regurgitation [104], whereas Bowman et al. [105] report that older age at surgical correction results in less morbidity and mortality. The guidelines of the European Society of Cardiology (ESC) for Grown-up Congenital Heart Disease (GUCH) [106] recommend surgical correction of partial AVSD in case of significant overload of the RV (Class I, level of evidence C).

1.2

Figure 5. Different surgical techniques for correction of an AVSD.
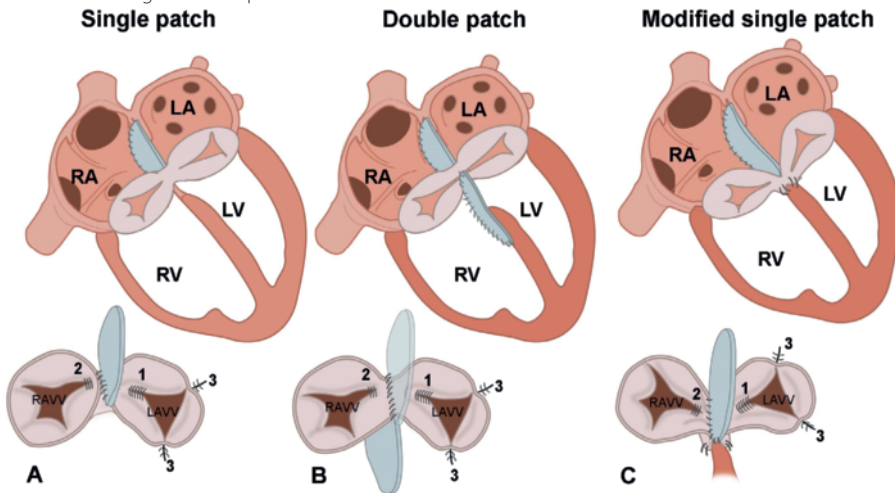
Single patch correction (A), double patch correction (B) and modified single patch (C) where the valve is attached to the ventricular septum are shown. In all techniques closure of the so-called cleft in the left atrioventricular valve (LAVV) is performed (1) and often approximation of the septal parts of the right atrioventricular valve (RAVV) (2) and approximation of the 2 left lateral commissures of the LAVV (3) are performed. RA = right atrium, LA = left atrium, RV = right ventricle, LV = left ventricle.

Figure 6. 4D-Flow MRI with streamline visualization.
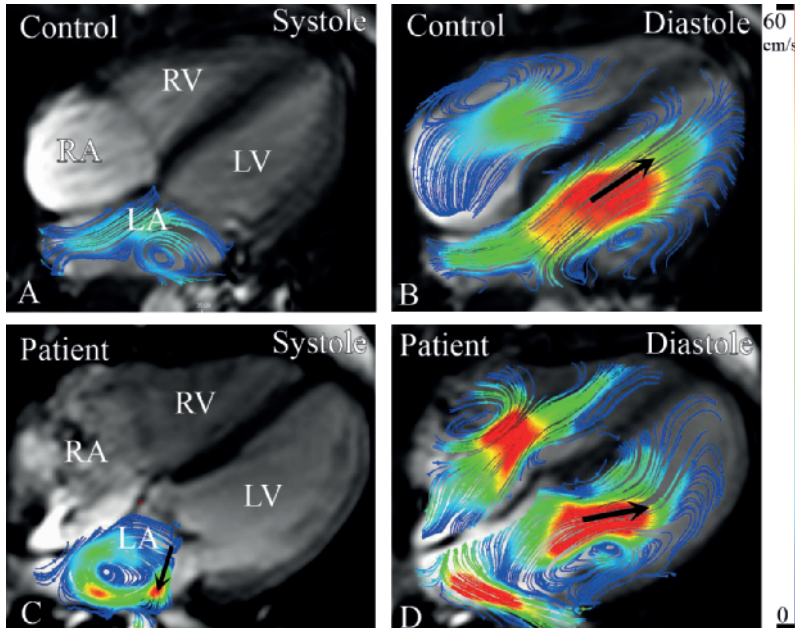
Disturbed inflow and regurgitation after AVSD correction. Compared to a control heart (A and B) in patients with a corrected AVSD eccentric regurgitation (arrow in C) can be seen and more laterally directed inflow (arrow in D). Streamlines with color coding representing velocity magnitude. RV = right ventricle, LV = left ventricle, RA = right atrium, LA = left atrium.

FOLLOW-UP

Early postoperative outcome

Early hospital mortality (thirty-day mortality) of biventricular AVSD correction has decreased in the last decades [107] and in current era (2000–2014) ranges between 0% [54,101,108,109] and 10.7% [110]. According to some studies early mortality is associated with a younger age at operation [56,95], whereas others report AVSD correction to be save at younger age [99–101]. Weight below 3.5 kg showed to be a risk factor for mortality [111]. Controversy in literature exists as to whether the presence of Down syndrome influences early postoperative outcome of AVSD correction (Table 1). On the one hand patients with Down syndrome have a higher incidence of pulmonary hypertension, pulmonary vascular obstructive disease and respiratory disease, which can complicate anesthesia. On the other hand extensive abnormalities of the AV valves, complex co-occurring cardiac anomalies (as in heterotaxia [20]), left ventricular outflow tract obstruction and right ventricular dominance are more frequently seen in patients with a normal karyotype [53,112,113]. While an early study suggested that patients with Down syndrome are of higher risk and should be treated differently [114], more recent studies do not show difference in early hospital mortality between Down syndrome and non-Down syndrome patients [53, 71,112,115–117] or even a lower in-hospital mortality and complication incidence in patients with Down syndrome [111] (Table 1).

Late follow-up

The overall 10 year survival after surgical AVSD correction also decreased in the last decades [107] ranging between and 70% [118] and 100% [108], largely dependent on era of surgery and complexity of the cardiac anatomy [20,118]. Surgery related postoperative arrhythmias, including complete heart block leading to pacemaker implantation (incidence ranging between 0.5% [19] an 7.5% [109]), are more frequently seen after repair of complete AVSD.

After correction of the AVSD, the need for reoperation ranges from 1.8% [119] to 28.9% [120] of all patients. In most cases reoperation is performed for the indication of LAVV regurgitation [53,121–123]. Other indications for reoperation are sub-aortic stenosis [122–124], a residual atrial septal- or ventricular septal defect [122,123], left ventricular out- flow tract obstruction [123] and right AVV regurgitation [122]. According to several studies patients with Down syndrome have a lower risk of reoperations compared to patients without Down syndrome (Table 1). This may be due to less LAVV abnormalities and less dysplastic mural leaflets [52,53] as compared to non-Down patients. LAVV regurgitation is equally found in patients with corrected partial and complete AVSD [95]. The guidelines of the ESC for adults (GUCH) [106] suggest surgical correction of moderate to severe LAVV regurgitation in symptomatic patients or asymptomatic patients with enlarged left ventricle and/or reduced EF% (Class I recommendation). Furthermore, surgical correction should be considered in asymptomatic patients with moderate to severe LAVV regurgitation who have signs of volume overload of the LV and a substrate of regurgitation

that is very likely to be amenable for surgical repair (Class 2a recommendation) [106]. However guidelines are based on level B and C evidence, as data from large randomized cohorts are lacking. Decision making for surgical correction is especially challenging due to the difficulty to quantify LAVV regurgitation reliably with echocardiography, which is due to presence of dynamic, eccentric regurgitation jets (Figure 6C). 4DFlow MRI enables characterization and more reliable quantification of these jets [125].

Rhodes et al. [126] report that after increase of LAVV regurgitation in the first 3 years after re-operation, regurgitation stays stable. The longterm effect of chronic regurgitation on exercise capacity, cardiac function and arrhythmias requires further investigation. Surgical correction of LAVV regurgitation can be performed by LAVV repair or LAVV replacement [127]. Survival is higher after valve repair than after replacement [121,128,129]. Furthermore, valve replacement has the disadvantage of the need for anti-coagulants, increased risk of infection and during pregnancy a higher risk of cardiac and neonatal complications [130]. In a study by Hoohenkerk et al. [121] a second re-operation (mostly replacement) in patients who underwent a LAVV repair was performed in 33%. The incidence of heart block after LAVV repair is reported as high as 37.5% [131]. Because of the occurrence of LAVV regurgitation, residual shunts, subaortic stenosis and arrhythmias the guidelines of the ESC for GUCH [106] suggest lifelong follow-up at least every 2–3 years in a GUCH center, although this does not seems to be general practice currently as low follow-up rates at out-patient clinics have been reported [132].

The majority of studies on AVSD follow-up focus on survival and reoperation, and little is known about systolic and diastolic function after AVSD correction. Takahashi et al. [133] extensively studied the LAVV, AV annuli and papillary muscles after AVSD correction using 3D echocardiography. They observed a larger annular area, more prolapse of the mural leaflet and a lateral displacement and angulation of the anterolateral papillary muscle in corrected AVSD patients with moderate regurgitation as compared to healthy control hearts. The abnormal valvular structure is a possible explanation of the lateral inflow direction in corrected AVSD patients (Fig. 6D) [51]. Whether the disturbed inflow direction leads to less efficient cardiac pumping remains to be investigated.

Pregnancy

According to the ESC GUCH guidelines closure of a significant partial AVSD before pregnancy should be considered. In patients with severe pulmonary hypertension pregnancy is contra-indicated [106]. Patients with a corrected AVSD with AVV regurgitation who have no indication for surgery tolerate pregnancy well [106]. However in 17% of pregnancies of women with a corrected AVSD increase of the LAVV regurgitation is observed, in 23% deterioration of the NYHA class is observed and in 19% arrhythmias were recorded [134]. These cardiac complications were more frequently seen in patients after surgical correction of complete AVSD compared with patients after partial AVSD correction. Recurrence of AVSD in the offspring of mothers with an AVSD is reported to be 10%–12.5% [134,135].

CONCLUSION AND FUTURE STUDIES

AVSD is a spectrum of cardiac anomalies with a common AV junction with a variety in septal defect(s) and valve abnormalities, which can be divided in partial (atrial or ventricular shunt), intermediate and complete AVSD. More consistent use of nomenclature will improve communication between anatomists, (pediatric) cardiologists and surgeons and enable better comparison of studies. Recent studies concerning AVSD development focus on the role of abnormal DMP, endocardial cushions and mesenchymal cap with the atrial and ventricular septum. Whether the range of defects found is a result of a sliding scale in maldevelopment of the different structures involved in AV septation and/or of differences in which gene is disturbed, remains to be investigated.

Recent genetic studies suggest CRELD and genes in the VEGF-A and SHH pathway to be important culprit genes for AVSD development. Early detection rate of AVSD is increasing due to improvement of early fetal echocardiography. Although correction of AVSD in early life has a good prognosis, re-operation due to regurgitation of the LAVV is often required. Because indications for surgical re-operation are debatable, improvement of quantification techniques is necessary to measure complex regurgitation in corrected AVSD patients. Quantification of LAVV regurgitation is challenging with echocardiography, while velocity encoded MRI might allow for reliable quantification and can contribute to surgical decision making for correction of the LAVV regurgitation. The corrected LAVV differs from the normal mitral valve in many aspects, and this might not only result in regurgitation of the LAVV, but also in abnormal inflow. Future studies focusing on the impact of valve abnormalities on intra-cardiac flow patterns and efficiency will add to knowledge of pathophysiological mechanisms and may contribute to identification of prognostic factors for valve and chamber dysfunction. The disturbance of the cardiac conduction anatomy in AVSD patients is known, but future studies are required to report types of arrhythmia and conduction disorders and risk factors. Furthermore little is known about diastolic and systolic function as well as exercise capacity, long after AVSD correction. As pregnancy in corrected AVSD patients is related to cardiac complications and recurrence of congenital heart disease in offspring, careful follow-up during pregnancy is warranted.

Anatomy and associated cardiac defect are different between patients with Down syndrome and non-syndromic patients. Although, the current available literature is not consistent enough to consider Down syndrome a risk or protective factor for outcome, most recent studies suggest a better outcome in Down syndrome patients than nonsyndromic patients. Long-term follow-up will have to establish the impact of AVSD correction on cardiac function and the possible differences in outcome of AVSD repair in non-syndromic patients and patients with Down syndrome.

REFERENCES

1. B. Craig, Atrioventricular septal defect: from fetus to adult, Heart 2006;92:1879–1885.

2. J.I. Hoffman, S. Kaplan, R.R. Liberthson, Prevalence of congenital heart disease, Am. Heart J. 2004;147:425–439.

3. M.D. Reller, M.J. Strickland, T. Riehle-Colarusso, et al., Prevalence of congenital heart defects in metropolitan Atlanta, 1998–2005, J. Pediatr. 2008;153:807–813.

4. C.A. Loffredo, J. Hirata, P.D. Wilson, et al., Atrioventricular septal defects: possible etiologic differences between complete and partial defects, Teratology 2001;63:87–93.

5. N. Christensen, H. Andersen, E. Garne, et al., Atrioventricular septal defects among infants in Europe: a population-based study of prevalence, associated anomalies, and survival, Cardiol. Young 2012:1–8.

6. J.P. Jacobs, R.P. Burke, J.A. Quintessenza, et al., Congenital Heart Surgery Nomenclature and Database Project: atrioventricular canal defect, Ann. Thorac. Surg. 2000;69:S36–S43.

7. J.P. Jacobs, M.L. Jacobs, C. Mavroudis, et al., Atrioventricular septal defects: lessons learned about patterns of practice and outcomes from the congenital heart surgery database of the society of thoracic surgeons, World J. Pediatr. Congenit. Heart Surg. 2010;1:68–77.

8. F. Cetta, L.L. Minich, W.D. Edwards, et al., Atrioventricular septal defect, in: H.D. Allen, D.J. Driscoll, R. Shaddy, T.F. Feltes (Eds.), Moss and Adams' heart disease in infants, children and adolescents, Lippincott William and Wilkins, Philadelphia 2008, p. 648.

9. J.P. Jacobs, R.P. Burke, J.A. Quintessenza, et al., Congenital Heart Surgery Nomenclature and Database Project: ventricular septal defect, Ann. Thorac. Surg. 2000;69:S25–S35.

10. G. Rastelli, J.W. Kirklin, J.L. Titus, Anatomic observations on complete form of persistent common atrioventricular canal with special reference to atrioventricular valves, Mayo Clin. Proc. 1966;41:296–308.

11. R. Praagh van, J. Papagiannis, Y.I. Bar-El, et al., The heart in Down syndrome pathologic anatomy, in: B. Marino, S.M. Pueschel (Eds.), Heart disease in persons with Down syndrome, Paul H. Brookes, Baltimore 1996, pp. 69–110.

12. S. Bharati, J.W. Kirklin, H.A. McAllister Jr., et al., The surgical anatomy of common atrioventricular orifice associated with tetralogy of Fallot, double outlet right ventricle and complete regular transposition, Circulation 1980;61:1142–1149.

13. T.J. Berger, J.W. Kirklin, E.H. Blackstone, et al., Primary repair of complete atrioventricular canal in patients less than 2 years old, Am. J. Cardiol. 1978;41:906–913.

14. R.S. Fortuna, D.A. Ashburn, O.N. Carias De, et al., Atrioventricular septal defects: effect of bridging leaflet division on early valve function, Ann. Thorac. Surg. 2004;77:895–902.

15. J.F. Smallhorn, M. de Leval, J. Stark, et al., Isolated anterior mitral cleft. Two dimensional echocardiographic assessment and differentiation from "clefts" associated with atrioventricular septal defect, Br. Heart J. 1982;48:109–116.

16. G. Sigfusson, J.A. Ettedgui, N.H. Silverman, et al., Is a cleft in the anterior leaflet of an otherwise normal mitral valve an atrioventricular canal malformation? J. Am. Coll. Cardiol. 1995;26:508–515.

17. Anderson RH, Zuberbuhler JR, Penkoske PA et al. Of clefts, commissures and things. 90 ed. 1985. p. 605–10.

18. E. Boccuzzi, E. Casinelli, P. Versacci, et al., Isolated cleft of the mitral valve: its pathogenic relationship with endocardial cushion defects, Tex. Heart Inst. J. 2010;37:503.

19. A.K. Kaza, S.D. Colan, J. Jaggers, et al., Surgical interventions for atrioventricular septal defect subtypes: the pediatric heart network experience, Ann. Thorac. Surg. 2011;92:1468–1475.

20. A. Miller, C. Siffel, C. Lu, et al., Long-term survival of infants with atrioventricular septal defects, J. Pediatr. 2010;156:994–1000.

21. M.S. Cohen, M.L. Jacobs, P.M. Weinberg, et al., Morphometric analysis of unbalanced common atrio-

ventricular canal using two-dimensional echocardiography, J. Am. Coll. Cardiol. 1996;28:1017–1023.

22.   G. Yildirim, K. Gungorduk, F. Yazicioglu, et al., Prenatal diagnosis of complete atrioventricular septal defect: perinatal and neonatal outcomes, Obstet. Gynecol. Int. 2009:958496.

23.   S.S. Patel, L.T. Mahoney, T.L. Burns, Is a shorter atrioventricular septal length an intermediate phenotype in the spectrum of nonsyndromic atrioventricular septal defects? J. Am. Soc. Echocardiogr. 2012;25: 782–789.

24.   A.C. Gittenberger-de Groot, U. Bartram, P.W. Oosthoek, et al., Collagen type VI expression during cardiac development and in human fetuses with trisomy 21, Anat. Rec. A: Discov. Mol. Cell. Evol. Biol. 2003;275:1109–1116.

25.   E. Calkoen, B. Adriaanse, M. Haak, et al., How normal is a 'normal' heart in fetuses and infants with Down syndrome? Fetal Diagn. Ther. 2015

26.   G.C. Rosenquist, L.J. Sweeney, J. Amsel, et al., Enlargement of the membranous ventricular septum: an internal stigma of Down's syndrome, J. Pediatr. 1974;85:490–493.

27.   A.D. Person, S.E. Klewer, R.B. Runyan, Cell biology of cardiac cushion development, Int. Rev. Cytol. 2005;243:287–335.

28.   S. Webb, N.A. Brown, R.H. Anderson, Formation of the atrioventricular septal structures in the normal mouse, Circ. Res. 1998;82:645–656.

29.   L.E. Briggs, J. Kakarla, A. Wessels, The pathogenesis of atrial and atrioventricular septal defects with special emphasis on the role of the dorsal mesenchymal protrusion, Differentiation 2012;84:117–130.

30.   J.S. Kim, S. Viragh, A.F. Moorman, et al., Development of the myocardium of the atrioventricular canal and the vestibular spine in the human heart, Circ. Res. 2001;88:395–402.

31.   S.P. Allwork, R.H. Anderson, Developmental anatomy of the membranous part of the ventricular septum in the human heart, Br. Heart J. 1979;41:275–280.

32.   F.J. de Lange, A.F. Moorman, R.H. Anderson, et al., Lineage and morphogenetic analysis of the cardiac valves, Circ. Res. 2004;95:645–654.

33.   M.M. Lockhart, A.L. Phelps, M.J. van den Hoff, et al., The epicardium and the development of the atrioventricular junction in the murine heart, J. Dev. Biol. 2014;2:1–17.

34.   A. Wessels, M.J. van den Hoff, R.F. Adamo, et al., Epicardially derived fibroblasts preferentially contribute to the parietal leaflets of the atrioventricular valves in the murine heart, Dev. Biol. 2012;366:111–124.

35.   S. Webb, R.H. Anderson, N.A. Brown, Endocardial cushion development and heart loop architecture in the trisomy 16 mouse, Dev. Dyn. 1996;206:301–309.

36.   S. Webb, R.H. Anderson, W.H. Lamers, et al., Mechanisms of deficient cardiac septation in the mouse with trisomy 16, Circ. Res. 1999;84:897–905.

37.   S.K. Rajagopal, Q. Ma, D. Obler, et al., Spectrum of heart disease associated with murine and human GATA4 mutation, J. Mol. Cell. Cardiol. 2007;43:677–685.

38.   T.S. Al, A.K. Manickaraj, C.L. Mercer, et al., Rare variants in NR2F2 cause congenital heart defects in humans, Am. J. Hum. Genet. 2014;94:574–585.

39.   Y. Tian, L. Yuan, A.M. Goss, et al., Characterization and in vivo pharmacological rescue of a Wnt2-Gata6 pathway required for cardiac inflow tract development, Dev. Cell 2010;18:275–287.

40.   M.M. Goddeeris, S. Rho, A. Petiet, et al., Intracardiac septation requires hedgehogdependent cellular contributions from outside the heart, Development 2008;135 : 1887–1895.

41.   N.A. Bax, S.B. Bleyl, R. Gallini, et al., Cardiac malformations in Pdgfralpha mutant embryos are associated with increased expression of WT1 and Nkx2.5 in the second heart field, Dev. Dyn. 2010;239:2307–2317.

42.   A.C. Wenink, J.C. Zevallos, Developmental aspects of atrioventricular septal defects, Int. J. Cardiol. 18 (1988) 65–78.

43.   N.A. Blom, J. Ottenkamp, A.G. Wenink, et al., Deficiency of the vestibular spine in atrioventricular septal defects in human fetuses with down syndrome, Am. J. Cardiol. 2003;91: 180–184.

44.   W.J. Larsen, Development of the heart, in: L.S. Sherman, S.S. Potter, W.J. Scott (Eds.), Human

embryology, Churchill Livingstone, New York 1999, pp. 157–180.

45. J.R. Hove, R.W. Koster, A.S. Forouhar, et al., Intracardiac fluid forces are an essential epigenetic factor for embryonic cardiogenesis, Nature 2003;421:172–177.

46. J. Vermot, A.S. Forouhar, M. Liebling, et al., Reversing blood flows act through klf2a to ensure normal valvulogenesis in the developing heart, PLoS Biol. 2009;7:e1000246.

47. N.A. Blom, A.C. Gittenberger-de Groot, M.C. Deruiter, et al., Development of the cardiac conduction tissue in human embryos using HNK-1 antigen expression: possible relevance for understanding of abnormal atrial automaticity, Circulation 1999;99:800–806.

48. N.A. Blom, J. Ottenkamp, M.C. Deruiter, et al., Development of the cardiac conduction system in atrioventricular septal defect in human trisomy 21, Pediatr. Res. 2005;58:516–520.

49. P.A. Penkoske, W.H. Neches, R.H. Anderson, et al., Further observations on the morphology of atrioventricular septal defects, J. Thorac. Cardiovasc. Surg. 1985;90:611–622.

50. I. Adachi, H. Uemura, K.P. McCarthy, et al., Surgical anatomy of atrioventricular septal defect, Asian Cardiovasc. Thorac. Ann. 2008;16:497–502.

51. E.E. Calkoen, A.A. Roest, L.J. Kroft, et al., Characterization and improved quantification of left ventricular inflow using streamline visualization with 4DFlow MRI in healthy controls and patients after atrioventricular septal defect correction, J. Magn. Reson. Imaging 2014;41:1512–1520.

52. G.J. Hoohenkerk, A.C. Wenink, P.H. Schoof, et al., Results of surgical repair of atrioventricular septal defect with double-orifice left atrioventricular valve, J. Thorac. Cardiovasc. Surg. 2009;138: 1167–1171.

53. A.A. Al-Hay, S.J. MacNeill, M. Yacoub, et al., Complete atrioventricular septal defect, Down syndrome, and surgical outcome: risk factors, Ann. Thorac. Surg. 2003;75:412–421.

54. A.R. Desai, R.G. Branco, G.A. Comitis, et al., Early postoperative outcomes following surgical repair of complete atrioventricular septal defects: is down syndrome a risk factor? Pediatr. Crit. Care Med. 2014;15:35–41.

55. Y. Okada, K. Tatsuno, T. Kikuchi, et al., Complete atrioventricular septal defect associated with tetralogy of Fallot: surgical indications and results, Jpn. Circ. J. 1999;63:889–892.

56. T. Gunther, D. Mazzitelli, C.J. Haehnel, et al., Long-term results after repair of complete atrioventricular septal defects: analysis of risk factors, Ann. Thorac. Surg. 1998;65:754–759.

57. G. Thiene, A.C.G. Wenink, C. Frescura, et al., Surgical anatomy and pathology of the conduction tissues in atrioventricular defects, J. Thorac. Cardiovasc. Surg. 1981;82:928–937.

58. D. Paladini, A. Tartaglione, A. Agangi, et al., The association between congenital heart disease and Down syndrome in prenatal life, Ultrasound Obstet. Gynecol. 2000;15:104–108.

59. C.K. Phoon, C.A. Neill, Asplenia syndrome: insight into embryology through an analysis of cardiac and extracardiac anomalies, Am. J. Cardiol. 1994;73:581–587.

60. W.M. Peoples, J.H. Moller, J.E. Edwards, Polysplenia: a review of 146 cases, Pediatr. Cardiol. 1983;4:129–137.

61. C.A. Irving, M.P. Chaudhari, Cardiovascular abnormalities in Down's syndrome: spectrum, management and survival over 22 years, Arch. Dis. Child. 2012;97:326–330.

62. S.S. Patel, T.L. Burns, L.D. Botto, et al., Analysis of selected maternal exposures and non-syndromic atrioventricular septal defects in the National Birth Defects Prevention Study, 1997–2005, Am. J. Med. Genet. 2012;158A:2447–2455.

63. A.C. Gittenberger-de Groot, E.E. Calkoen, R.E. Poelmann, et al., Morphogenesis and molecular considerations on congenital cardiac septal defects, Ann. Med. 2014;46:640–652.

64. C. Ackerman, A.E. Locke, E. Feingold, et al., An excess of deleterious variants in VEGF-A pathway genes in Down-syndrome-associated atrioventricular septal defects, Am. J. Hum. Genet. 2012;91:646–659.

65. S.W. Robinson, C.D. Morris, E. Goldmuntz, et al., Missense mutations in CRELD1 are associated with cardiac atrioventricular septal defects, Am. J. Hum. Genet. 2003;72:1047–1052.

66.   H. Li, S. Cherry, D. Klinedinst, et al., Genetic modifiers predisposing to congenital heart disease in the sensitized Down syndrome population, Circ. Cardiovasc. Genet. 2012;5:301–308.

67.   H.H. Nguyen, P.Y. Jay, A single misstep in cardiac development explains the cooccurrence of tetralogy of Fallot and complete atrioventricular septal defect in Down syndrome, J. Pediatr. 2014;165:194–196.

68.   A.J. Agopian, M. Moulik, M. Gupta-Malhotra, et al., Descriptive epidemiology of non-syndromic complete atrioventricular canal defects, Paediatr. Perinat. Epidemiol. 2012;26: 515–524.

69.   B. Marino, U. Vairo, A. Corno, et al., Atrioventricular canal in Down syndrome. Prevalence of associated cardiac malformations compared with patients without Down syndrome, Am. J. Dis. Child. 1990;144:1120–1122.

70.   R.J. Hartman, T. Riehle-Colarusso, A. Lin, et al., Descriptive study of nonsyndromic atrioventricular septal defects in the National Birth Defects Prevention Study, 1997–2005, Am. J. Med. Genet. 2011;155A:555–564.

71.   R. Formigari, R.M. Di Donato, G. Gargiulo, et al., Better surgical prognosis for patients with complete atrioventricular septal defect and Down's syndrome, Ann. Thorac. Surg. 2004;78:666–672.

72.   T. Ebels, R.H. Anderson, W.A. Devine, et al., Anomalies of the left atrioventricular valve and related ventricular septal morphology in atrioventricular septal defects, J. Thorac. Cardiovasc. Surg. 1990;99:299–307.

73.   K. Suzuki, S.Y. Ho, R.H. Anderson, et al., Morphometric analysis of atrioventricular septal defect with common valve orifice, J. Am. Coll. Cardiol. 1998;31:217–223.

74.   Y. Shiokawa, A.E. Becker, The left ventricular outflow tract in atrioventricular septal defect revisited: surgical considerations regarding preservation of aortic valve integrity in the perspective of anatomic observations, J. Thorac. Cardiovasc. Surg. 1997;114:586–593.

75.   J. Ong, C.P. Brizard, Y. d'Udekem, et al., Repair of atrioventricular septal defect associated with tetralogy of Fallot or double-outlet right ventricle: 30 years of experience, Ann. Thorac. Surg. 2012;94:172–178.

76.   H.A. Draulans-Noe, A.C. Wenink, J. Quaegebeur, Single papillary muscle ("parachute valve") and double-orifice left ventricle in atrioventricular septal defect convergence of chordal attachment: surgical anatomy and results of surgery, Pediatr. Cardiol. 1990;11:29–35.

77.   L.D. Allan, G.K. Sharland, A. Milburn, et al., Prospective diagnosis of 1,006 consecutive cases of congenital heart disease in the fetus, J. Am. Coll. Cardiol. 1994;23:1452–1458.

78.   F.A. Jansen, E.E. Calkoen, M.R. Jongbloed, et al., Imaging the first trimester heart: ultrasound correlation with morphology, Cardiol. Young 2014;24:suppl2:3-12.

79.   H. ter Heide, J.D. Thomson, G.A. Wharton, et al., Poor sensitivity of routine fetal anomaly ultrasound screening for antenatal detection of atrioventricular septal defect, Heart 2004:90:916–917.

80.   C. van Velzen, S. Clur, M. Rijlaarsdam, et al., Prenatal detection of congenital heart disease-results of a national screening programme, BJOG;2015:in press

81.   A. Machlitt, K.S. Heling, R. Chaoui, Increased cardiac atrial-to-ventricular length ratio in the fetal four-chamber view: a new marker for atrioventricular septal defects, Ultrasound Obstet. Gynecol. 2004;24:618–622.

82.   B.M. Adriaanse, M.M. Bartelings, J.M. van Vugt, et al., The differential and linear insertion of the atrioventricular valves: a useful tool? Ultrasound Obstet. Gynecol. 2014;44:568–574.

83.   A.Z. Beaton, J.I. Pike, C. Stallings, et al., Predictors of repair and outcome in prenatally diagnosed atrioventricular septal defects, J. Am. Soc. Echocardiogr. 2013;26:208–216.

84.   C. Berg, C. Kaiser, F. Bender, et al., Atrioventricular septal defect in the fetus—associated conditions and outcome in 246 cases, Ultraschall Med. 2009;30:25–32.

85.   F.A. Jansen, Y.J. Blumenfeld, A. Fisher, et al., Array comparative genomic hybridization and fetal congenital heart defects: a systematic review and meta-analysis, Ultrasound Obstet. Gynecol. 2015;45:27–35.

86.   N.H. Silverman, J.R. Zuberbuhler, R.H. Anderson, Atrioventricular septal defects: cross-sectional echocardiographic and morphologic comparisons, Int. J. Cardiol. 1986;13:309–331.

87.   C.E. Fleishman, G.R. Marx, Atrioventricular canal defects, in: M.H. Crawford, J.P. DiMarco, W.J. Paulus (Eds.), Cardiology, 3 ed.Elsevier, Philadelphia, USA 2010, pp. 1561–1571.

88.   S. Kutty, J.F. Smallhorn, Evaluation of atrioventricular septal defects by threedimensional echocardiography: benefits of navigating the third dimension, J. Am. Soc. Echocardiogr. 2012;25:932–944.

89.   H.R. Lee, L.M. Montenegro, S.C. Nicolson, et al., Usefulness of intraoperative transesophageal echocardiography in predicting the degree of mitral regurgitation secondary to atrioventricular defect in children, Am. J. Cardiol. 1999;83:750–753.

90.   H.K. Kim, W.H. Kim, S.W. Hwang, et al., Predictive value of intraoperative transesophageal echocardiography in complete atrioventricular septal defect, Ann. Thorac. Surg. 2005;80:56–59.

91.   M.D. Jacobstein, B.D. Fletcher, S. Goldstein, et al., Evaluation of atrioventricular septal defect by magnetic resonance imaging, Am. J. Cardiol. 1985;55:1158–1161.

92.   R. Kirk, A.I. Dipchand, D.N. Rosenthal, et al., The International Society of Heart and Lung Transplantation guidelines for the management of pediatric heart failure: executive summary, J. Heart Lung Transplant. 2014;33:888–909.

93.   C.W. Lillehei, M. Cohen, Warden, et al., The direct-vision intracardiac correction of congenital anomalies by controlled cross circulation; results in thirty-two patients with ventricular septal defects, tetralogy of Fallot, and atrioventricularis communis defects, Surgery 1955;38:11–29.

94.   G. Pan, L. Song, X. Zhou, et al., Complete atrioventricular septal defect: comparison of modified single-patch technique with two-patch technique in infants, J. Card. Surg. 2014;29:251–255.

95.   G.J. Hoohenkerk, E.F. Bruggemans, M. Rijlaarsdam, et al., More than 30 years' experience with surgical correction of atrioventricular septal defects, Ann. Thorac. Surg. 2010;90:1554–1561.

96.   E.K. El-Najdawi, D.J. Driscoll, F.J. Puga, et al., Operation for partial atrioventricular septal defect: a forty-year review, J. Thorac. Cardiovasc. Surg. 2000;119:880–889.

97.   J. Wetter, N. Sinzobahamvya, C. Blaschczok, et al., Closure of the zone of apposition at correction of complete atrioventricular septal defect improves outcome, Eur. J. Cardiothorac. Surg. 2000;17:146–153.

98.   A. Jegatheeswaran, C. Pizarro, C.A. Caldarone, et al., Echocardiographic definition and surgical decision-making in unbalanced atrioventricular septal defect: a Congenital Heart Surgeons' Society multiinstitutional study, Circulation 2010;122:S209–S215.

99.   E. Prifti, M. Bonacchi, M. Bernabei, et al., Repair of complete atrioventricular septal defects in patients weighing less than 5 kg, Ann. Thorac. Surg. 2004;77:1717–1726.

100.   R.R. Singh, P.S. Warren, T.B. Reece, et al., Early repair of complete atrioventricular septal defect is safe and effective, Ann. Thorac. Surg. 2006;82:1598–1601.

101.   B.E. Kogon, H. Butler, M. McConnell, et al., What is the optimal time to repair atrioventricular septal defect and common atrioventricular valvar orifice? Cardiol. Young 2007;17:356–359.

102.   M. Kobayashi, Y. Takahashi, M. Ando, Ideal timing of surgical repair of isolated complete atrioventricular septal defect, Interact. Cardiovasc. Thorac. Surg. 2007;6:24–26. 794.

103.   O. Xie, C.P. Brizard, Y. d'Udekem, et al., Outcomes of repair of complete atrioventricular septal defect in the current era, Eur. J. Cardiothorac. Surg. 2014;45:610–617.

104.   L.L. Minich, A.M. Atz, S.D. Colan, et al., Partial and transitional atrioventricular septal defect outcomes, Ann. Thorac. Surg. 2010;89:530–536.

105.   J.L. Bowman, J.A. Dearani, H.M. Burkhart, et al., Should repair of partial atrioventricular septal defect be delayed until later in childhood? Am. J. Cardiol. 2014;114:463–467.

106.   H. Baumgartner, P. Bonhoeffer, N.M. De Groot, et al., ESC guidelines for the management of grown-up congenital heart disease, Eur. Heart J. 2010;31:2915–2957.

107.   G. Erikssen, K. Liestol, E. Seem, et al., Achievements in congenital heart defect surgery: a prospec-

1.2

tive, 40-year study of 7038 patients, Circulation 2015;131:337–346.

108. F. Bakhtiary, J. Takacs, M.Y. Cho, et al., Long-term results after repair of complete atrioventricular septal defect with two-patch technique, Ann. Thorac. Surg. 2010;89:1239–1243.

109. H.A. Vohra, A.X. Chia, H.M. Yuen, et al., Primary bi-ventricular repair of atrioventricular septal defects: an analysis of reoperations, Ann. Thorac. Surg. 2010;90:830–837.

110. B. Harmandar, N.A. Aydemir, A.R. Karaci, et al., Results for surgical correction of complete atrio-ventricular septal defect: associations with age, surgical era, and technique, J. Card. Surg. 27 (2012) 745–753.

111. J.D. St Louis, U. Jodhka, J.P. Jacobs, et al., Contem-porary outcomes of complete atrioventricular sep-tal defect repair: analysis of the Society of Thoracic Surgeons Congenital Heart Surgery Database, J. Thorac. Cardiovasc. Surg. 148 (2014) 2526–2531.

112. R. Lange, T. Guenther, R. Busch, et al., The presence of Down syndrome is not a risk factor in complete atrioventricular septal defect repair, J. Thorac. Cardiovasc. Surg. 2007;134:304–310.

113. B.L. De, C. Di, L. Ballerini, et al., Prevalence of left-sided obstructive lesions in patients with atrioventricular canal without Down's syndrome, J. Thorac. Cardiovasc. Surg. 1986;91:467–469.

114. C. Bull, M.L. Rigby, E.A. Shinebourne, Should man-agement of complete atrioventricular canal defect be influenced by coexistent Down syndrome? Lancet 1985;1;1147–1149.

115. K.A. Dunlop, H.C. Mulholland, F.A. Casey, et al., A ten year review of atrioventricular septal defects, Cardiol. Young 2004;14:15–23.

116. M.D. Reller, C.D. Morris, Is Down syndrome a risk factor for poor outcome after repair of congenital heart defects? J. Pediatr. 1998;132:738–741.

117. T.W. Vet, J. Ottenkamp, Correction of atrioven-tricular septal defect. Results influenced by Down syndrome? Am. J. Dis. Child. 1989;143:1361–1365.

118. F. Lacour-Gayet, N. Bonnet, D. Piot, et al., Surgical management of atrio ventricular septal defects with normal caryotype, Eur. J. Cardiothorac. Surg. 1997;11:466–472.

119. C.L. Backer, R.D. Stewart, F. Bailliard, et al., Complete atrioventricular canal: comparison of modified single-patch technique with two-patch technique, Ann. Thorac. Surg. 2007;84:2038–2046.

120. J.L. Monro, C. Alexiou, A.P. Salmon, et al., Reopera-tions and survival after primary repair of congeni-tal heart defects in children, J. Thorac. Cardiovasc. Surg. 2003;126:511–520.

121. G.J. Hoohenkerk, E.F. Bruggemans, D.R. Koolber-gen, et al., Long-term results of reoperation for left atrioventricular valve regurgitation after correc-tion of atrioventricular septal defects, Ann. Thorac. Surg. 2012;93:849–855.

122. J.M. Stulak, H.M. Burkhart, J.A. Dearani, et al., Reoperations after repair of partial atrioventricular septal defect: a 45-year single-center experience, Ann. Thorac. Surg. 2010;89:1352–1359.

123. O. Birim, G.M. van, P.L. de Jong, et al., Outcome after reoperation for atrioventricular septal defect repair, Interact. Cardiovasc. Thorac. Surg. 2009;9:83–87.

124. B. Alsoufi, Z. Al-Halees, F. Khouqeer, et al., Results of left atrioventricular valve reoperations following previous repair of atrioventricular septal defects, J. Card. Surg. 2010;25:74–78.

125. E.E. Calkoen, J.J. Westenberg, L.J. Kroft, et al., Characterization and quantification of dynamic eccentric regurgitation of the left atrioventricular valve after atrioventricular septal defect correction with 4D Flow cardiovascular magnetic resonance and retrospective valve tracking, J. Cardiovasc. Magn. Reson. 2015;19:17.

126. J. Rhodes, K.G. Warner, D.R. Fulton, et al., Fate of mitral regurgitation following repair of atrioventricular septal defect, Am. J. Cardiol. 1997;80:1194–1197.

127. J.W. Brown, A.C. Fiore, M. Ruzmetov, et al., Evolution of mitral valve replacement in children: a 40-year experience, Ann. Thorac. Surg. 2011;93:626–633.

128. S.S. Patel, T.L. Burns, L. Kochilas, Early outcomes and prognostic factors for left atrioventricular valve reoperation after primary atrioventricular septal defect repair, Pediatr. Cardiol. 2012;33:129–140.

129. M. Pontailler, D. Kalfa, E. Garcia, et al., Reoperations for left atrioventricular valve dysfunction after

repair of atrioventricular septal defect, Eur. J. Cardiothorac. Surg. 2014;45:557–562.

130. W. Drenthen, E. Boersma, A. Balci, et al., Predictors of pregnancy complications in women with congenital heart disease, Eur. Heart J. 31 (2010) 2124–2132.

131. A.M. Moran, S. Daebritz, J.F. Keane, et al., Surgical management of mitral regurgitation after repair of endocardial cushion defects: early and midterm results, Circulation 2000;102:III160–III165.

132. E. Buratto, B. McCrossan, J.C. Galati, et al., Repair of partial atrioventricular septal defect: a 37-year experience, Eur. J. Cardiothorac. Surg. 2014;47:796–798.

133. K. Takahashi, A.S. Mackie, R. Thompson, et al., Quantitative real-time threedimensional echocardiography provides new insight into the mechanisms of mitral valve regurgitation post-repair of atrioventricular septal defect, J. Am. Soc. Echocardiogr. 2012;25:1231–1244.

134. W. Drenthen, P.G. Pieper, K. van der Tuuk, et al., Cardiac complications relating to pregnancy and recurrence of disease in the offspring of women with atrioventricular septal defects, Eur. Heart J. 2005;26:2581–2587.

135. J. Burn, P. Brennan, J. Little, et al., Recurrence risks in offspring of adults with major heart defects: results from first cohort of British collaborative study, Lancet 351 (1998) 311–316.

136. F.A. Crawford Jr., M.R. Stroud, Surgical repair of complete atrioventricular septal defect, Ann. Thorac. Surg. 2001;72:1621–1628.

137. M. Masuda, H. Kado, Y. Tanoue, et al., Does Down syndrome affect the long-term results of complete atrioventricular septal defect when the defect is repaired during the first year of life? Eur. J. Cardiothorac. Surg. 2005;27:405–409.

138. V. Garg, I.S. Kathiriya, R. Barnes, et al., GATA4 mutations cause human congenital heart defects and reveal an interaction with TBX5, Nature 2003;424:443–447.

139. M. Maitra, S.N. Koenig, D. Srivastava, et al., Identification of GATA6 sequence variants in patients with congenital heart defects, Pediatr. Res. 2010;68:281–285.

140. M.G. Posch, A. Perrot, K. Schmitt, et al., Mutations in GATA4, NKX2.5, CRELD1, and BMP4 are infrequently found in patients with congenital cardiac septal defects, Am. J. Med. Genet. 2008;146A:251–253.

141. S.M. Reamon-Buettner, H. Hecker, K. Spanel-Borowski, et al., Novel NKX2–5 mutations in diseased heart tissues of patients with cardiac malformations, Am. J. Pathol. 2004;164:2117–2125.

142. L. Ma, E.S. Selamet Tierney, T. Lee, et al., Mutations in ZIC3 and ACVR2B are a common cause of heterotaxy and associated cardiovascular anomalies, Cardiol. Young 2012;22:194–201.

143. S.M. Reamon-Buettner, J. Borlak, TBX5 mutations in non-Holt–Oram syndrome (HOS) malformed hearts, Hum. Mutat. 2004;24:104.

144. A.C. Fahed, B.D. Gelb, J.G. Seidman, et al., Genetics of congenital heart disease: the glass half empty, Circ. Res. 2013;112:707–720.

145. R. Kosaki, M. Gebbia, K. Kosaki, et al., Left-right axis malformations associated with mutations in ACVR2B, the gene for human activin receptor type IIB, Am. J. Med. Genet. 1999;82:70–76.

146. I.C. Joziasse, K.A. Smith, S. Chocron, et al., ALK2 mutation in a patient with Down's syndrome and a congenital heart defect, Eur. J. Hum. Genet. 2011;19:389–393.

147. H.P. Smedts, A. Isaacs, C.D. de, et al., VEGF polymorphisms are associated with endocardial cushion defects: a family-based case-control study, Pediatr. Res. 2010;67:23–28.

148. F.X. Sicot, T. Tsuda, D. Markova, et al., Fibulin-2 is dispensable for mouse development and elastic fiber formation, Mol. Cell. Biol. 2008;28:1061–1067.

149. A.D. Person, R.J. Garriock, P.A. Krieg, et al., Frzb modulates Wnt-9a-mediated betacatenin signaling during avian atrioventricular cardiac cushion development, Dev. Biol. 2005;278:35–48.

150. G.M. Barlow, X.N. Chen, Z.Y. Shi, et al., Down syndrome congenital heart disease: a narrowed region and a candidate gene, Genet. Med. 2001;3:91–101.

151. C. Dasgupta, A.M. Martinez, C.W. Zuppan, et al., Identification of connexin43 (alpha1) gap junction gene mutations in patients with hypoplastic left heart syndrome by denaturing gradient gel electrophoresis (DGGE), Mutat. Res. 2001;479:173–186.

Part 2

Development of an
atrioventricular septal defect

Chapter 2.1

How normal is a "normal" heart in fetuses and infants with Down syndrome?

Emmeline E. Calkoen*, Bauke M.E. Adriaanse*, Monique C. Haak, Margot M. Bartelings, Adam Kolesnik, Chezary Niszczota, John M.G. van Vugt, Arno A.W. Roest, Nico A. Blom, Ardiana C. Gittenberger-de Groot and Monique R.M. Jongbloed
* Equal contributions

ABSTRACT

Background

Congenital heart disease is present in 44–56% of fetuses with Down syndrome (DS). There are, however, signs that hearts in DS without apparent structural heart defects also differ from those in the normal population. We aimed to compare the atrioventricular (AV) septum and valves in 3 groups: DS without AV septal defect (DS noAVSD), DS with AVSD (DS AVSD) and control hearts.

Methods

The ventricular septum, membranous septum and AV valves were examined and measured in histological sections of 15 DS no-AVSD, 8 DS AVSD and 34 control hearts. In addition, the ventricular septum length was measured on ultrasound images of fetal (6 DS AVSD, 9 controls) and infant (10 DS no-AVSD, 10 DS AVSD, 10 controls) hearts.

Results

The membranous septum was 3 times larger in DS no-AVSD fetuses compared to control fetuses, and valve dysplasia was frequently (64%) observed. The ventricular septum was shorter in patients with DS both with and without AVSD, as compared to the control group.

Conclusion

DS no-AVSD hearts are not normal as they have a larger membranous septum, shorter ventricular septum and dysplasia of the AV valves as compared to control hearts.

2.1

INTRODUCTION

Congenital heart disease (CHD) occurs in 44–56% of fetuses with Down syndrome (DS), most commonly in the form of atrioventricular septal defects (AVSDs) [1, 2]. In AVSDs, the membranous septum is partly or completely absent. During normal development, several structures contribute to the formation of the membranous septum, which consists of an atrioventricular (AV) and an interventricular part. These structures include the endocardial cushions present in the AV canal (also contributing to the putative AV valves), the so-called dorsal mesenchymal protrusion (DMP) [3] (also known as vestibular spine, a mesenchymal protrusion at the base of the atrial septum), and an extension of cushion tissue covering the lower rim of the interatrial septum, known as the mesenchymal cap. The AV part of the membranous septum is positioned between the left ventricle and right atrium, and the interventricular part is positioned between the left and right ventricles [4]. AVSDs cover a spectrum of heart anomalies with a common AV junction. In the case of a complete AVSD, a common AV valve, with 2 bridging leaflets, is present between the atria and ventricles with shunting occurring at both the atrial and ventricular level. When the bridging leaflets are attached to the atrial or ventricular septum (partial AVSD), shunting can solely take place at the ventricular or atrial level, respectively.

In addition to AVSD, patients with DS may present with other septal anomalies, such as aneurysms of the membranous ventricular septum [5] and inlet ventricular septal defects [6]. Although half of the patients with DS do not present with CHD, there are signs that the hearts of these fetuses, in particular the AV valves, are not normal. Tricuspid regurgitation during prenatal echocardiography is associated with DS [7, 8], and adults with DS without overt CHD show a high frequency of mitral valve prolapse [9, 10] .

The above data suggest that fetuses with DS without overt congenital heart defects are still at risk of developing cardiac abnormalities. Furthermore, the etiology of maldevelopment of the (AV) membranous septum in patients with DS seems largely unexplained to date. The question arises whether hearts designated as normal in DS may in fact be abnormal, and if so, what causes this abnormality? Interestingly, recent studies on cerebellar and neural cells in DS have shown a response deficit to the mitogenic effects of sonic hedgehog (SHH), a gene involved in establishing cell fates at multiple points during development and known to contribute to cardiac septation [11, 12] . SHH is therefore one of the candidate genes for heart abnormalities in DS patients. The aim of the current study was to evaluate the hearts of fetuses with DS without overt CHD, focusing on: (1) morphology and size of the membranous septum (AV and interventricular part), (2) morphology and the size of the ventricular septum and (3) morphology of the AV valves.

METHODS

Light microscopy of serial sections

This study was performed in accordance with the local ethics committee and the Dutch and Polish regulations for proper use of human tissue for medical research purposes. Serial sections of postmortem fetal hearts were selected from the Leiden Collection (Department of Anatomy and Embryology, LUMC, the Netherlands) and the heart collection of The Medical University of Warsaw in order to examine the fibrous tissue, the interventricular septum and the valvular structures. The age of the specimens ranged from 10 + 0 weeks' gestational age (GA) to 3 days postpartum.

For the current study, 3 groups of hearts with known karyotype were selected. Group 1 included 15 human hearts with DS without septal defect (GA 12–22 weeks, further referred to as DS noAVSD); group 2 contained 8 human hearts with DS and AVSD (GA age 11–18 weeks, further referred to as DS AVSD); group 3 contained 34 structural normal human hearts with normal karyotype (GA 10 weeks to 3 days postnatally, further referred to as control hearts).

All fetuses were obtained either following pregnancy termination or miscarriage after fetal or neonatal death. The hearts were sectioned in transverse, frontal, or sagittal planes. The histological and immunohistochemical tissue markers used in these serial sections were HE (to analyze general anatomy), resorcin-fuchsin-iron (staining fibrous tissue), hematoxylin-picric acid-thiazin red (modified Van Gieson's stain, staining fibrous tissue and myocardium) and troponin I (staining myocardial tissue, 1/250 SC-15368, Santa Cruz Biotechnology Inc., Dallas, Tex., USA). To assess a possible role of the SHH pathway in septation and valve development, selected hearts were also stained with antibodies for SHH (1/100 SC- 1194, Santa Cruz Biotechnology) and its downstream effector Gli1 (1:50 AB-49314; Abcam, Cambridge, Mass., USA). Primary antibodies were dissolved in PBS-Tween-20 with 1% bovine serum albumin (Sigma Aldrich, St. Louis, Mo., USA). Between subsequent incubation steps, all slides were rinsed in PBS (2×) and PBSTween-20 (1×). The slides were incubated with the secondary antibodies for 60 min: for troponin I and Gli1 with 1/200 goat antirabbit biotin (BA-1000, Vector Laboratories, Burlingame, Calif., USA) and 1/66 goat serum (S1000, Vector Laboratories) in PBSTween-20, and for SHH with 1/200 horse anti-goat biotin (BA-9500 Vector Laboratories) and 1/66 horse serum (S-2000, Vector Laboratories) in PBS-Tween-20. To amplify the signal, all slides were incubated with ABC reagent (PK6100, Vector Laboratories) for 40 min. For visualization, the slides were incubated for 10 min with 400 µg/ml 3-3 ′ diaminobenzidine tetrahydrochloride (D5637, SigmaAldrich) dissolved in Tris-maleate buffer pH 7.6 to which 20 µl of H_2O_2 was added. Counterstaining was performed with 0.1% hematoxylin (Merck, Darmstadt, Germany) for 3 s, followed by rinsing with tap water for 10 min. Finally, all slides were dehydrated and mounted with Entellan (Merck). As staining quality depended on the fixation method of the hearts, we used the smooth muscle cells in the esophagus as positive control for SHH and Gli1 in each heart.

Membranous septum measurements in sections of fetal hearts

The membranous septum was defined as a nonmuscular structure comprising an interventricular part between the left and right ventricle and an AV part between the left ventricle and right atrium, as previously described by Allwork and Anderson [4] (figure. 1 a, b). In hearts with sufficient four-chamber views (defined as visibility of 2 atria, 2 ventricles and the AV valves) in transverse sections of similar GA (DS no-AVSD, n = 6; DS AVSD, n = 6; control, n = 10), the presence of the AV part of the membranous septum and the ventricular part of the membranous septum was analyzed. The volume of the membranous septum was estimated based on the Cavelieri's principle [13] . Regularly spaced (49 mm 2) points were randomly placed on resorcin-fuchsin-iron- or troponin-stained hearts. The distance between the subsequent sections was between 0.056 and 0.2 mm. Volume measurements were performed using an Olympus microscope with a ×40 magnification objective for hearts of embryos 13 weeks.

Echocardiographic assessment of the ventricular septum in fetal hearts

The ventricular septum length was assessed in DS AVSD and control fetuses to compare the findings in the fetal specimens with living fetuses. We examined 2-D ultrasound images, obtained from STIC (spatiotemporal image correlation) volumes, of all cases with DS from a prospectively recorded database of fetuses, which were referred to our center for fetal echocardiography. STIC is a modality to record the heart in 3 directions during one complete heart cycle, which allows the heart to be visualized in any desired plane [14, 15] . This database also contains a series of normal controls. Fetal ultrasound images of 6 DS AVSD fetuses (GA 20 + 0 to 30 + 0 weeks) and 9 randomly selected controls of comparable GA (GA 19 + 4 to 32 + 2 weeks) were available. The ventricular septum was measured on the available four-chamber view from the septal attachment of the tricuspid valve to the endocardium of the apex.

Transthoracic echocardiographic assessment of the ventricular septum in hearts of infants

To gain more insight into the postnatal situation, measurements were also obtained from hearts of live-born infants. Ten DS no-AVSD infants (1 day to 15 years), 9 DS AVSD infants (39 days to 2 years) and 10 control infants (1 day to 15 years) were measured. We selected all cases with DS from a prospectively recorded database of ultrasound images of infants who were referred to our center for echocardiography. No ultrasound recordings were available of older patients with AVSD, as most of these patients undergo surgery at an early age. The ventricular septum was measured from the septal attachment of the tricuspid valve to the endocardium of the apex on the available four-chamber view in the case of sufficient quality (figure 2).

Morphology of the AV valves in sections of fetal hearts

The insertion of the AV valves was studied in specimens in the 3 groups (DS no-AVSD, n = 15; DS AVSD, n = 8; control, n = 34). Furthermore, each heart was assessed for dysplastic features of the

AV valves (plump, irregular contours). The tricuspid valve of a normal heart has a more apical insertion as compared to the mitral valve, also known as 'differential insertion of the atrioventricular valves' [16] . A linear insertion (attachment of the AV valves to the septum forming a straight line) is a feature of AVSD when imaging is performed at a specific level [16]. Linear insertion has also been suggested as a landmark for DS without AVSD, although data are limited [17].

Statistical analysis

Statistical analysis of the differences in length and volume measurements of the membranous septum between (1) DS no-AVSD hearts, (2) DS AVSD hearts and (3) control hearts was performed with SPSS software (SPSS Inc., Chicago, Ill., USA). A linear regression analysis was performed, and data were corrected for GA. Outcome data as well as GA were log transformed to reach normality, and the antilog was used for the result.

RESULTS

Membranous septum: morphology

Between 8 and 16 weeks' GA, neither DS no-AVSD hearts nor the hearts of controls showed an interventricular component of the membranous septum. At 16– 28 weeks' GA, 66% of the fetuses in the control group showed both an interventricular and an AV component of the membranous septum. The remaining 43% only had an AV septum (figure 1 a–c).

In the DS no-AVSD hearts (figure 1 d), more variations in the membranous septum were observed: only 20% presented with both an interventricular and an AV septum, 20% with only an interventricular septum, 40% with only an AV septum and 20% with merely a fibrous continuity between the left and right AV valves. In the DS fetuses with a (complete) AVSD, fibrous tissue was observed at the top of the ventricular septum in 3 cases. In one of these cases, the central part of this fibrous tissue was attached to the ventricular septum as well as to the atrial septum in the four-chamber view immediately beneath the aortic outflow tract (figure 1 e). The shunt was only visible at another level (figure 1 f, g).

In summary, in DS no-AVSD fewer fetuses had both components of the membranous septum as compared to controls, and in DS AVSD a part of the AV septum is present.

Membranous septum: volume

Linear regression analysis showed a 2.6 times (p = 0.0001, 95% CI 1.70–3.98) larger volume of the membranous septum in DS no-AVSD as compared to controls. The mean membranous septum volume estimation was 0.19 cm 3 in DS no-AVSD hearts (GA 16 ± 4 weeks) and 0.08 cm 3 in control hearts (GA 14 ± 6 weeks).

Figure 1. The atrioventricular and ventricular components of the membranous septum.
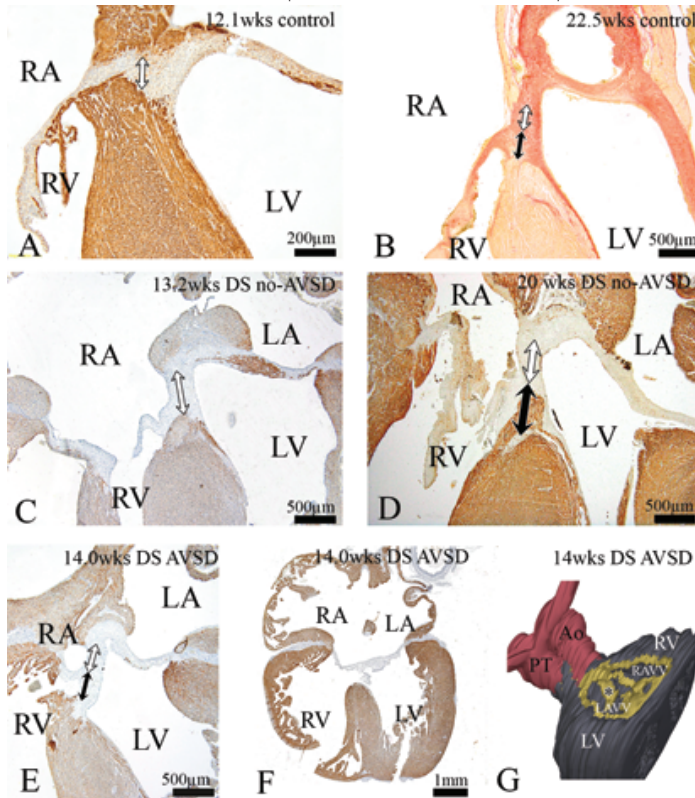
A: Transverse section immediately beneath the aortic outflow tract of a first-trimester control heart with solely an AV (white arrow) component of the membranous septum. B: Transverse section immediately beneath the aortic outflow tract of a second-trimester control heart with an AV (white arrow) and an interventricular (black arrow) membranous septum. C , D: Transverse section immediately beneath the aortic outflow tract in 2 hearts of fetuses with DS no-AVSD showing a longer and plump membranous septum with white arrows indicating the AV component of the membranous septum and the black arrow the interventricular component. E: Transverse section immediately beneath the aortic outflow tract of a heart from a patient with DS AVSD showing a membranous septum [with an AV (white arrow) and an interventricular (black arrow) part] where the central fibrous body attaches to the ventricular septum as well as the atrial septum. F: Same heart as in e in the fourchamber view, more towards the diaphragm. At this level, the complete AVSD can be observed. G: 3-D reconstruction of the same DS AVSD heart with part of the membranous septum (asterisk). Red indicates the great arteries, yellow fibrous tissue and grey ventricular myocardium. Colors refer to the online version only. The section in B is stained with resorcin-fuchsin-iron, all other sections are stained with troponin I. RA = Right atrium; RV = right ventricle; LA = left atrium; LV = left ventricle; LAVV = left AV valve; RAVV = right AV valve.

Ventricular septum length

Using ultrasound imaging, the ventricular septum length was measured in fetuses and in infants. In fetuses, the ventricular septum length in DS AVSD was 0.7 times the length of controls (p = 0.001, 95% CI 0.6–0.9). Infants with DS with and without AVSD both showed a smaller ventricular septum length compared to controls (DS noAVSD 0.78 times the size of the control, 95% CI 0.65– 0.93, p < 0.0001; DS AVSD 0.67 times the size of the control, 95% CI 0.56–0.79, p = 0.006;

figure 2). There was no statistically significant difference in septum length between infants with DS with and without AVSD (p = 0.07).

Morphology and insertion of the AV valves

Control hearts (n = 34) showed a differential insertion of the AV valves just below the aortic outflow tract. Fetal DS AVSD hearts (n = 15) showed a linear insertion in the four-chamber view just below the aortic outflow tract, as described previously [16] . The AV valves of hearts with DS without septal defect showed either a differential (n = 12) or a linear insertion (n = 3, with GA 12.3, 14.4 and 22 weeks) in the four-chamber view sections just below the aortic outflow tract. Furthermore, the AV valves of these hearts showed dysplastic features in 4 of the 5 hearts between 8 and 16 weeks' GA and in 3 of 6 hearts between 16 and 28 weeks' GA (figure 3). The tricuspid valve appeared more affected than the mitral valve. Dysplastic features of valves were not observed in control fetuses.

Expression of SHH/Gli1

In first-trimester hearts, clear SHH expression was detected in the tendon of Todaro (the remnant of the DMP [18]) in control hearts (figure 4 c). This was also observed in DS no-AVSD and DS AVSD hearts (figure 4 d). In first-trimester hearts, Gli1 expression was not observed in the AV valves and septum of control hearts (n = 5). In contrast, in DS no-AVSD fetuses, clear expression of Gli1 was present in the dysplastic plump AV valves and membranous septum in 2 out of 4 cases (figure 4 f). In DS AVSD fetuses, no Gli1 expression was observed. In the second-trimester hearts, no clear SHH and Gli1 staining could be detected in any group.

Figure 2. Method of ventricular septal length measurement (white arrow) with transthoracic echocardiography.
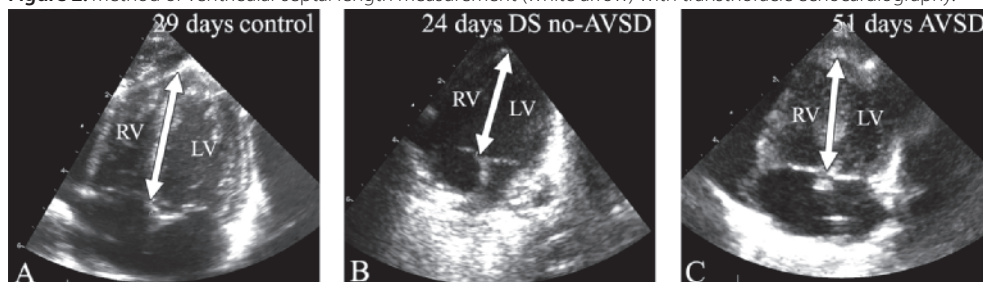
Measurements were performed in four-chamber views, from the endocardial border to the septal attachment of the tricuspid valve. A: Control postnatal heart of a 29-day-old infant. B: Heart of a 24-day-old infant with DS no-AVSD. C: Heart of a 51-day-old infant with DS AVSD. RV = Right ventricle; LV = left ventricle.

Figure 3. Plump atrioventricular valves in hearts of patients with DS no-AVSD.
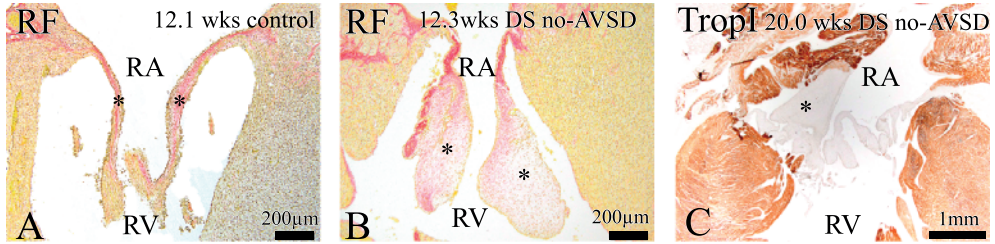
A: Transverse section of a control heart, 12 + 1 weeks, with resorcin-fuchsin-iron (RF) staining showing slim, well-developed tricuspid valve leaflets (asterisks). B , C: Transverse sections of DS no-AVSD hearts (B 12 + 3 weeks, stained with RF; C 20 + 0 weeks stained against troponin I) with plump (asterisks) AV valve leaflets compared to the control heart. RA = Right atrium; RV = right ventricle.

Figure 4. Expression of SHH and Gli1.
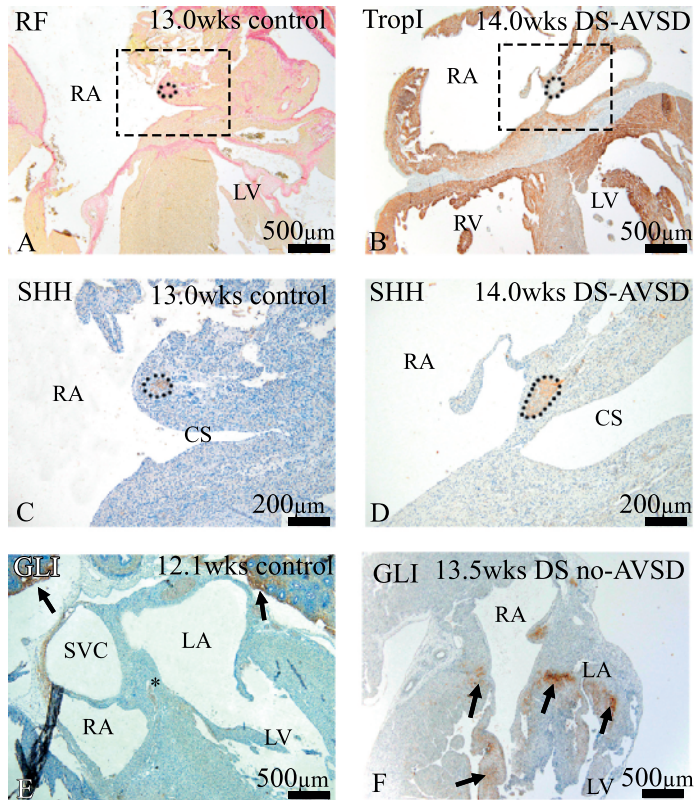
A: Transverse section of a control heart with resorcin-fuchsin-iron (RF) staining, showing the tendon of Todaro (rectangle). B: Transverse section of a DS AVSD heart with troponin I staining, showing the tendon of Todaro (rectangle). C: A consecutive slide of the section in A, with SHH expression in the tendon of Todaro. D: A consecutive slide of the section in b with SHH expression in the tendon of Todaro. E: Transverse section of a control heart with Gli1 expression in the lungs (arrow), but not in membranous septum (asterisk) and AV valves. F: Transverse section of a DS no-AVSD heart with increased Gli1 expression in the membranous septum and AV valves (black arrows). RA = Right atrium; RV = right ventricle; LA = left atrium; LV = left ventricle; CS = coronary sinus; SVC = superior vena cava.

DISCUSSION

This study presents an overview of morphological findings in hearts of fetuses with DS without apparent cardiac malformations. This group showed: (1) a larger membranous septum, (2) a shorter ventricular septum, (3) dysplastic AV valves and (4) increased levels of Gli in the AV valves and membranous septum.

DS is associated with CHD, most frequently AVSDs, atrial septal defects, ventricular septal defects and tetralogy of Fallot [19] . AVSD has been described as a spectrum of disease [20] with varying levels of atrial and ventricular shunting. An inheritable shorter AV membranous septum, observed in families of patients with nonsyndromal AVSD, suggests a shorter membranous septum to be an intermediate phenotype towards AVSD [21] . In contrast, in other studies, patients with DS without a septal defect were suggested to have a long membranous septum, indicating a long membranous septum being a sliding scale towards AVSD [22] , which is in line with the findings in the current study. This discrepancy might partially be explained by the level in the heart where the largest membranous septum is observed in patients with a normal heart and in AVSD. It has been previously shown that in normal fetal hearts, in a plane equal to the echocardiographic four-chamber view and moving from the outflow tracts in the caudal direction towards the diaphragm, the distance between the insertion of the AV valves to the septum becomes smaller. The distance (i.e. the amount of differential insertion) is maximal in the four-chamber view just below the outflow tracts and smallest in the four-chamber view just above the diaphragm [16].

The larger membranous septum, based on microscopy, and shorter ventricular septum, based on echocardiography, in DS no-AVSD hearts in the current study, may reflect the end of the spectrum of a 'normal' heart in DS, which may form a sliding scale with an AVSD, as was postulated by Rosenquist and Sweeney [23]. A smaller inlet/outlet ratio is a feature of hearts with an AVSD, and a higher atrial to ventricular length ratio measured in a four-chamber view has been considered as a detection method for an AVSD [24] . The shorter ventricular septum in DS hearts with and without AVSD measured in our study supports this association. A shorter ventricular inlet septum, as was described previously [25], may hinder fusion of the endocardial cushions (which were shown to have a normal size in patients with an AVSD [26]) with the septum. Furthermore, we encountered in our study a fetal heart with an AVSD, in which a significant part of the membranous septum could still be distinguished. The central part of this fibrous tissue attached to the ventricular septum as well as to the atrial septum in the fourchamber view immediately beneath the aortic outflow tract (figure 1 e). Scrolling through the heart more caudally, this central part separated from the top of the ventricular septum and a common valve was visualized. We suggest that this centrally attached part could be regarded as a part of the membranous septum. However, in early pregnancy it is difficult to distinguish the membranous septum histologically from the annulus fibrosis and the valves because together they comprise the fibrous tissue of the heart [27, 28].

Several studies report valvular heart disease in patients with DS, including mitral valve prolapse in the majority of asymptomatic adults [11, 29, 30]. Tricuspid valve regurgitation has been suggested as a useful feature for detection of fetuses with DS [7, 8]. The increased prevalence of tricuspid valve regurgitation is considered to be related to the structural changes associated with DS: decreased number of myocytes, abnormal orientation of myocytes and myofibrils and abnormal connective tissue [31]. The observed dysplastic, plump AV valves in fetal hearts with DS confirm an abnormal development of the AV valves in patients with DS.

The high incidence of AVSD in DS suggests that genes on chromosome 21 are likely to be involved in the development of AVSD. However, not all patients with DS develop an AVSD, suggesting a multifactorial influence [32]. The observed SHH expression in the tendon of Todaro, a structure derived from the DMP and necessary for normal AV septation [33] , suggests a similar role of SHH in septation in humans as has previously been described in mice [12, 34] . We observed an increased expression of Gli1, a marker for SHH activity, in AV valves and the membranous septum in fetal hearts in DS without AVSD. Although numbers in the current study are too small to draw valid conclusions, it is tempting to speculate that the increased expression is a result of a previously suggested response deficit of SHH signaling in DS [35]. Increased Gli1 expression in fetuses with DS might also be caused by Yak1-related kinase (Dyrk), which induces Gli1 and is found on the DS critical region and is increased in patients with DS [36, 37]. The extensive Gli1 expression in the mesenchymal AV septum possibly influences cell fate, resulting in reduced myocardialization. Such a mechanism would implicate that inhibitors of Dyrk, currently experimentally used to improve cognitive function of DS patients, might be a focus for research concerning therapy of CHD in DS patients as well [38]. Further studies are required to investigate the role of SHH in heart development in fetuses with DS.

The current study is based on a unique collection of fetal specimens. This however causes limitations, including the small number and variable age of the observed hearts, inherent to the limited availability of human fetal material with known phenotype. Some stainings could not be performed in all hearts due to differences in the quality of the material.

In conclusion, hearts of patients with DS, even without overt CHD, appear to be abnormal in the majority of specimens examined. Hearts of fetuses with DS without septal defects have a different, elongated, membranous septum in comparison to hearts of fetuses with a normal karyotype and show abnormal dysplastic AV valves, which may explain the valve dysfunction observed both pre- and postnatally in patients with DS. Correlation with clinical data is necessary to explore if cardiac follow-up in patients with DS without overt CHD is warranted.

2.1

REFERENCES

1. Freeman SE, Turner RJ: A pharmacological study of the toxin in a Cnidarian, Chironex fleckeri South-cott. Br J Pharmacol 1969;35:510-520.

2. Paladini D, Tartaglione A, Agangi A, et al.: The association between congenital heart disease and Down syndrome in prenatal life. Ultrasound Obstet Gynecol 2000;15:104-108.

3. Briggs LE, Phelps AL, Brown E, et al.: Expression of the BMP receptor Alk3 in the second heart field is essential for development of the dorsal mesenchymal protrusion and atrioventricular septation. Circ Res 24-5-2013;112:1420-1432.

4. Allwork SP, Anderson RH: Developmental anatomy of the membranous part of the ventricular septum in the human heart. Br Heart J 1979;41:275-280.

5. Rosenquist GC, Sweeney LJ, McAllister HA: Relationships of the tricuspid valve to the membranous ventricular septum in Down's syndrome without endocardial cushion defect: study of 28 specimens, 14 with a ventricular septal defect. Am Heart J 1975;90:458-462.

6. Marino B, Papa M, Guccione P, et al.: Ventricular septal defect in Down syndrome. Anatomic types and associated malformations. Am J Dis Child 1990;144:544-545.

7. Ghaffari SR, Tahmasebpour AR, Jamal A, et al.: First-trimester screening for chromosomal abnormalities by integrated application of nuchal translucency, nasal bone, tricuspid regurgitation and ductus venosus flow combined with maternal serum free beta-hCG and PAPP-A: a 5-year prospective study. Ultrasound Obstet Gynecol 2012;39:528-534.

8. Khalil A, Nicolaides KH: Fetal heart defects: potential and pitfalls of first-trimester detection. Semin Fetal Neonatal Med 2013;18:251-260.

9. Geggel RL, O'Brien JE, Feingold M: Development of valve dysfunction in adolescents and young adults with Down syndrome and no known congenital heart disease. J Pediatr 1993;122:821-823.

10. Goldhaber SZ, Brown WD, Sutton MG: High frequency of mitral valve prolapse and aortic regurgitation among asymptomatic adults with Down's syndrome. JAMA 2-10-1987;258:1793-1795.

11. Currier DG, Polk RC, Reeves RH: A Sonic hedgehog (Shh) response deficit in trisomic cells may be a common denominator for multiple features of Down syndrome. Prog Brain Res 2012;197:223-236.

12. Hoffmann AD, Yang XH, Burnicka-Turek O, et al.: Foxf genes integrate tbx5 and hedgehog pathways in the second heart field for cardiac septation. PLoS Genet 2014;10:e1004604.

13. Gundersen HJ, Jensen EB: The efficiency of systematic sampling in stereology and its prediction. J Microsc 1987;147:229-263.

14. DeVore GR, Falkensammer P, Sklansky MS, et al.: Spatio-temporal image correlation (STIC): new technology for evaluation of the fetal heart. Ultrasound Obstet Gynecol 2003;22:380-387.

15. Goncalves LF, Lee W, Chaiworapongsa T, et al.:Four-dimensional ultrasonography of the fetal heart with spatiotemporal image correlation. Am J Obstet Gynecol 2003;189:1792-1802.

16. Adriaanse BM, Bartelings MM, van Vugt JM, et al.: The differential and linear insertion of the atrioventricular valves: a useful tool? Ultrasound Obstet Gynecol 10-2-2014.

17. Fredouille C, Piercecchi-Marti MD, Liprandi A, et al.: Linear insertion of atrioventricular valves without septal defect: a new anatomical landmark for Down's syndrome? Fetal Diagn Ther 2002;17:188-192.

18. Kim JS, Viragh S, Moorman AF, et al.: Development of the myocardium of the atrioventricular canal and the vestibular spine in the human heart. Circ Res 2-3-2001;88:395-402.

19. Irving CA, Chaudhari MP: Cardiovascular abnormalities in Down's syndrome: spectrum, management and survival over 22 years. Arch Dis Child 2012;97:326-330.

20. Craig B: Atrioventricular septal defect: from fetus to adult. Heart 2006;92:1879-1885.

21. Patel SS, Mahoney LT, Burns TL: Is a shorter atrioventricular septal length an intermediate phenotype in the spectrum of nonsyndromic atrioventricular septal defects? J Am Soc Echocardiogr 2012;25:782-789.

2.1

22. Gittenberger-de Groot AC, Bartram U, Oosthoek PW, et al.: Collagen type VI expression during cardiac development and in human fetuses with trisomy 21. Anat Rec A Discov Mol Cell Evol Biol 2003;275:1109-1116.

23. Rosenquist GC, Sweeney LJ: The membranous ventricular septum in the normal heart. Johns Hopkins Med J 1974;135:9-16.

24. Adachi I, Uemura H, McCarthy KP, et al.: Surgical anatomy of atrioventricular septal defect. Asian Cardiovasc Thorac Ann 2008;16:497-502.

25. Ebels T, Anderson RH, Devine WA, et al.: Anomalies of the left atrioventricular valve and related ventricular septal morphology in atrioventricular septal defects. J Thorac Cardiovasc Surg. 1990;99:299-307.

26. Wenink ACG, Zevallos JC., et al.: Human developmental stages of atrioventricular septal defect. in Clark EB., Takao A (eds): Developmental Cardiology: Morphogenesis and Function. New York, Futura, 1990, pp 593-603.

27. Lie-Venema H, Eralp I, Markwald RR, v et al.: Periostin expression by epicardium-derived cells is involved in the development of the atrioventricular valves and fibrous heart skeleton. Differentiation 2008;76:809-819.

28. van Gils FA: The fibrous skeleton in the human heart: embryological and pathogenetic considerations. Virchows Arch A Pathol Anat Histol 1981;393:61-73.

29. Goldhaber SZ, Rubin IL, Brown W, et al.: Valvular heart disease (aortic regurgitation and mitral valve prolapse) among institutionalized adults with Down's syndrome. Am J Cardiol 1-2-1986;57:278-281.

30. Hamada T, Kuroda M, Miyakoshi M, et al.: [Echocardiographic study in adult patients with Down's syndrome]. Rinsho Byori 1993;41:807-812.

31. Recalde AL, Landing BH, Lipsey AI: Increased cardiac muscle fiber size and reduced cell number in Down syndrome: heart muscle cell number in Down syndrome. Pediatr Pathol 1986;6:47-53.

32. Sailani MR, Makrythanasis P, Valsesia A, et al.: The complex SNP and CNV genetic architecture of the increased risk of congenital heart defects in Down syndrome. Genome Res 2013;23:1410-1421.

33. Snarr BS, Wirrig EE, Phelps AL, et al.: A spatiotemporal evaluation of the contribution of the dorsal mesenchymal protrusion to cardiac development. Dev Dyn 2007;236:1287-1294.

34. Goddeeris MM, Rho S, Petiet A, et al.: Intracardiac septation requires hedgehog-dependent cellular contributions from outside the heart. Development 2008;135:1887-1895.

35. Ahn S, Joyner AL: In vivo analysis of quiescent adult neural stem cells responding to Sonic hedgehog. Nature 2005;437:894-897.

36. Mao J, Maye P, Kogerman P, et al.: Regulation of Gli1 transcriptional activity in the nucleus by Dyrk1. J Biol Chem 2002;277:35156-35161.

37. Park J, Oh Y, Yoo L, J et al.: Dyrk1A phosphorylates p53 and inhibits proliferation of embryonic neuronal cells. J Biol Chem 2010;285:31895-31906.

38. De la Torre R, De Sol S, Pons M, et al.: Epigallocatechin-3-gallate, a DYRK1A inhibitor, rescues cognitive deficits in Down syndrome mouse models and in humans. Mol Nutr Food Res 2014;58:278-288.

Chapter 2.2

Imaging the first trimester heart: ultrasound correlation with morphology

Fenna A.R. Jansen*, Emmeline E. Calkoen*, Monique R.M. Jongbloed,
Margot M. Bartelings and Monique C. Haak
* Equal contribution

ABSTRACT

First trimester sonography is a widely used technique to examine the foetus early in pregnancy. The desire to recognise complex anatomy already in early developmental stages stresses the need for a thorough knowledge of basic developmental processes as well as recognition of cardiac compartments based on their morphology. In this paper, we describe the possibilities and limitations of sonographic assessment of the foetal heart between 10 and 14 weeks of gestation and correlate this to morphology. Examples of the most commonly detected congenital anomalies are atrioventricular septal defects, transposition of the great arteries, and hypoplastic left heart, which are shown in this paper.

INTRODUCTION

Heart development is a complex proces during which the heart needs to evolve from a single myocardial tube towards a fully septated heart with two atria, two ventricles, and a separated outflow tract. Figure 1 shows the cardiac events that must occur to achieve a normal circulation. These developmental processes do not occur sequentially, but largely overlap in time. It is therefore not surprising that maldevelopment during one timepoint might affect multiple processes. Correct remodelling of the heart most likely requires normal haemodynamics. Studies on chick and zebrafish demonstrate that reduced blood flow during heart development leads to impaired looping, incomplete septation, and abnormal valvulogenesis; [1,2] therefore, abnormal blood flow through the cardiovascular system during early embryonic stages can result in structural heart disease [3,4].

Congenital heart disease affects four to eight newborns per 1000 live births and is the most frequently encountered congenital malformation [5]. Congenital heart malformations are responsible for majority of infant deaths in the first year of life.5 Second trimester ultrasound screening programmes are routine pregnancy care in most developed countries. In the last 2 decades, ultrasound systems have improved rapidly, allowing the visualisation of the first trimester heart in detail. First trimester echocardiography is defined as an attempt to visualise foetal heart anatomy at a gestational age before 14 completed weeks (13^{+6}). The use of first trimester echocardiography to detect foetal anomalies at this early gestational age is increasingly gaining popularity, driven by the urge to detect foetal anomalies at very young stages. These examinations are conducted mainly in high-risk pregnancies, for example, in cases with increased nuchal

Figure 1. Schematic overview of the time span of development of the different cardiac components.
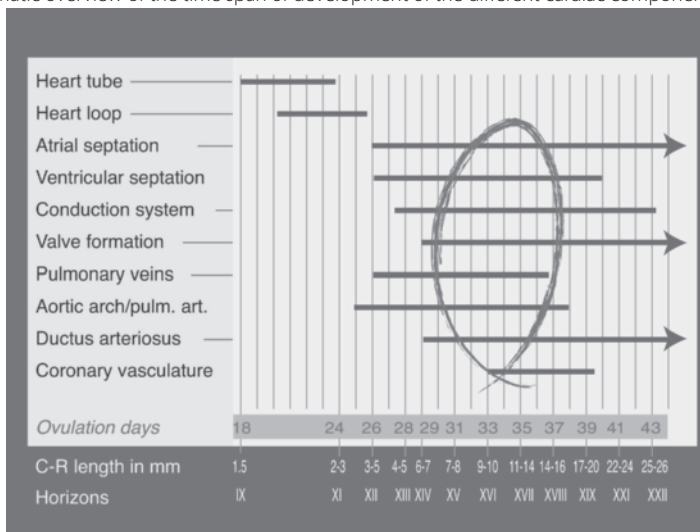
Modified after Jongbloed et al [87].

translucency or in patients with a positive family history for cardiac malformations [6]. At the same time, the desire to recognise complex anatomy already in these early developmental stages stresses the need for a thorough knowledge of basic developmental processes as well as recognition of cardiac compartments based on their morphology.

Despite several studies that stated that foetal heart examination could be incorporated in the first trimester examinations, its use is currently still limited to a few specialised centres. In the current paper, we aim to provide a comprehensive overview of the use first trimester echocardiography and the correlation with morphology. In addition, we give an overview of the current possibilities and limitations, and define the indications in which first trimester echocardiography could be offered.

VISUALISATION OF THE FOETAL HEART BEFORE 10 WEEKS OF GESTATIONAL AGE: ULTRASOUND VERSUS MORPHOLOGY

Organogenesis occurs in the first 8 weeks after conception. In this relatively short period, which corresponds to 10 completed weeks of gestation, all major organ systems develop. At the end of this period, most organs have reached a size that can be visualised by ultrasound.

The cardiovascular system begins to develop within the lateral intra-embryonic mesoderm at 4 weeks gestational age [7]. At this time, the primitive heart tube is formed and starts pulsating after 5 completed weeks of gestation, that is, day 22 after conception [8]. This single tube pro-pulses the blood initially in a peristaltic manner. The primitive myocardial heart tube undergoes a process of looping, remodelling, and septation, thereby transforming the single lumen into the four chambers of the definitive heart with a separated out- flow tract. This forms the basis for the separation of the pulmonary and systemic circulations at birth [8]. The final closure of the ventricular septum and ultimate formation of the atrioventricular valves is finished at 10 completed weeks of gestation [9,10]. After development, the different cardiac compartments can be distinguished based on their morphological characteristics [11].

Ultrasonographic studies on the foetal heart, before a gestational age of 10 completed weeks, have to take into account that heart morphology is not definitive yet. Therefore, examinations before this gestational age are studies on the developing embryo, rather than a diagnostic tool. Timor-Tritsch et al described embryonic development in 38 well-dated pregnancies [12]. He observed that foetal heartbeats could be visualised from 5+5 weeks gestational age. In a similar study, the ventricular septum was seen at 9+1 weeks and the four chambers were identified at 14 weeks [13]. With the use of 7.5 MHz transvaginal probes, more detailed structures of the foetal heart could be identified [14] The atrial and ventricular walls were visualised at the end of week 8, and the atrioventricular valves at the end of week 10 by Blaas et al. In this study, reference curves for the diameter of the foetal heart at this early gestation were constructed [15] Allan et al compared the results of echocardiographic studies at 5–12 weeks gestational age,

using transvaginal ultrasonography, with the anatomy of microdissected hearts [16] Before a gestational age of 9 weeks, cardiac morphology could not be visualised by ultrasound. The results in the study by Johnson et al, agree with these findings [17]. At 9 weeks gestational age, Allan found the foetal heart to be centrally positioned in the foetal chest, directionally opposite the foetal spine [16] The pulmonary trunk could be visualised in the B-mode, in contrast to the ascending aorta, which could only be identified with colour Doppler. At 10 weeks gestational age, they found the heart's position changing to a more left-sided orientation, as is typical later in pregnancy. Figure 2 shows an example of first trimester echocardiography and the correlation to morphology.

2.2

ECHOCARDIOGRAPHY IN LATE FIRST TRIMESTER FOETUSES

From 10 completed weeks of gestation onwards, the foetal heart has reached its definitive anatomy for foetal life. The final closure of the foramen ovale and the occlusion of the ductus arteriosus occur after birth and results in the definitive separation of the systemic and pulmonary circulation.

In the ultrasonographic examination of the foetal heart from 10 weeks gestational age onwards, a predefined strategy can be applied, similar to the way mid-gestational cardiac examination is conducted. Owing to the increased axial (0.3–0.4 mm) and lateral resolution of the modern broadband probes, the foetal heart and its detailed structures up to 1 mm can be readily visualised. Initially, the majority of early first trimester echocardiographic studies were conducted using transvaginal probes. More recent studies showed that modern high-frequency abdominal probes could reach a sufficient level of imaging quality [18–23]. Transabdominal scanning has the advantage that the imaging plane can be acquired in more angles compared with transvaginal ultrasound. In a review by Rasiah et al [24], it was stated that regarding specificity, transabdominal approach appears superior to transvaginal approach, but Gembruch et al stated that at lower gestational age transvaginal approach has better feasibility [25]. Considering these limitations it seems advisable to master both methods, to be able to individualise the approach according to the goal of the ultrasound, detecting or excluding/reassuring, and technical factors such as patient stature and size of the foetus).

The first published studies on the diagnosis of heart malformations in the first trimester foetus were case reports [26–28], published up to 4 years before Dolkart and Reimers [29] systematically described the possibilities of examining the normal foetal heart in this early period of gestation. Following these case reports, larger series of diagnosed malformations were published by several authors. Table 2 provides an overview of the structural heart defects that have been described to be accurately diagnosed in the first trimester.

THE FOUR-CHAMBER VIEW

The transverse section through the foetal heart at the inflow level, called "the four-chamber view", is incorporated in routine second trimester obstetric scanning in nearly every centre. In this ultrasonographic plane, the size and position of the heart, two equally sized ventricles and atria, the opening and closure of the mitral and tricuspid valves, and an intact ventricular septum up to the cardiac crux are evaluated (Figure 2e). Allan et al and later Copel et al described that a normal "four-chamber view" ruled out the majority of foetal heart malformations in midgestational foetuses [30,31].

An attempt to visualise the four-chamber view in first trimester foetuses proved feasible in several articles, as reviewed by Haak et al. [32] In the past few decades, the visualisation of this plane has increased to 90% of the examinations from 12 weeks gestational age onwards. Furthermore, a shift towards earlier gestational ages in which the four-chamber view can be visualised is observed. These improvements in early foetal echocardiography are probably because of the development of new transvaginal and transabdominal probes. Higher frequencies are used nowadays, and the increased variety in postprocessing possibilities produce a very high image quality, leading to more detailed visualisation of small structures [33,34]. The most frequently reported congenital heart defects in first trimester echocardiography are those with an abnormal four-chamber view, such as atrioventricular defects or defects with asymmetrical or disproportional ventricles. In most cases, follow-up ultrasounds are necessary to determine additional details and definitive diagnosis of the abnormalities and state the correct diagnosis, or sporadically conclude that there is a normal cardiac anatomy [6,22].

OUTFLOW TRACTS

During development, the outflow tract of the heart needs to develop from a single tube to a situation where the aorta and pulmonary trunk are separated and connect to the proper ventricle. During this process, a lengthening of the pulmonary part of the outflow tract will occur, whereas the aorta will stay relatively short [35] After normal development, the great arteries are located ventrally, wedged in between both atrial appendages. In the normal heart, the aorta has a right posterior position with respect to the pulmonary trunk (Fig 3a).

Although the four-chamber view is a potent plane to screen for major heart defects, it is not sufficient to rule out heart defects concerning the outflow tracts. To detect outflow tract anomalies with a normal four-chamber view, several planes have to be added to the examination [36]. The position and size of the ascending aorta is the first plane cranial to the fourchamber view. This is a relatively difficult plane to achieve, because the probe has to be rotated and slightly tilted.

Figure 2. Normal echocardiography versus morphology.

2.2
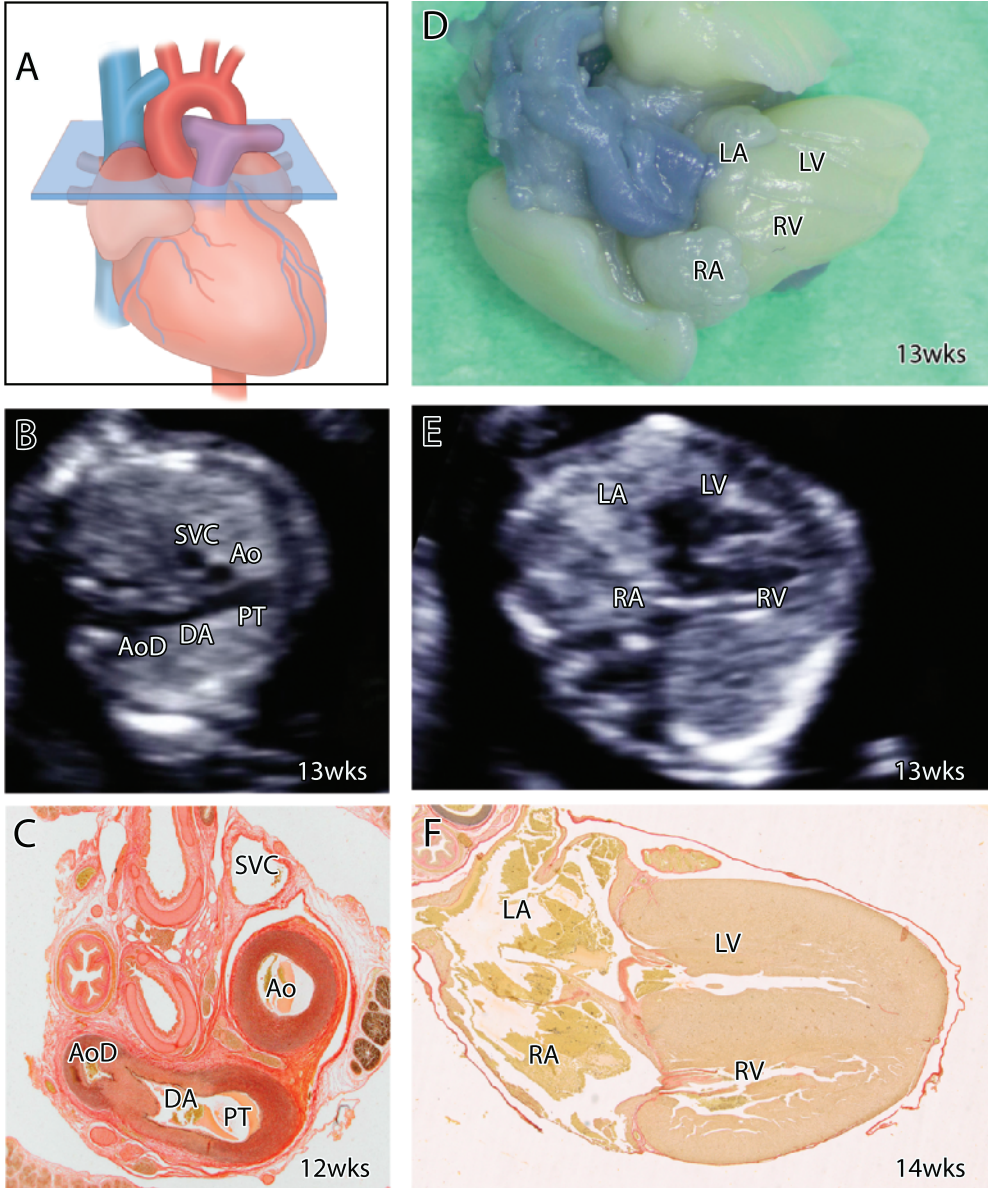
The transverse plane of the three-vessel view is depicted by the square (a). First trimester ultrasound (b) and a histo-logical (c) section of the three-vessel view clearly show the superior vena cava (SVC), aorta (Ao), pulmonary trunk (PT), ductus arteriosus (DA), descending aorta (AoD). Plane (d) depicts a normal foetal heart, corresponding to ultrasound (e), and histological (f) sections of the four-chamber view showing the left ventricle (LV), right ventricle (RV), left atrium (LA), and right atrium (RA). Spine (S) marks the dorsal side of the foetus on the ultrasound plane.

Figure 3. Echocardiography and morphology of a foetal heart with transposition of the great arteries.
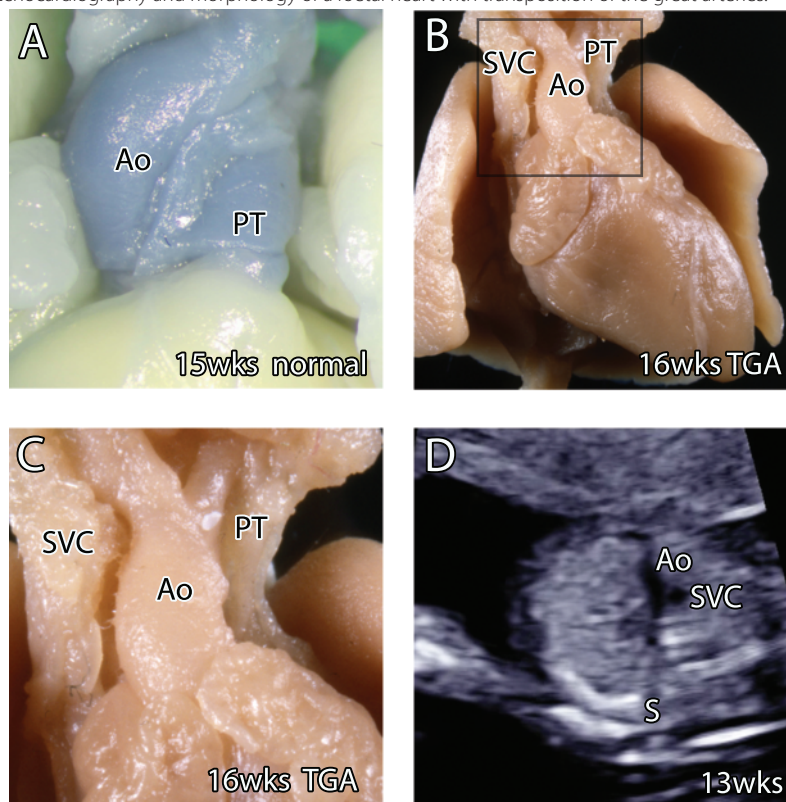
The aorta has, compared with the normal posterior position (a), in transposition of the great arteries, a right anterior position (panel (b) and enlargement (c)). On a transverse section through the foetal chest at the level of the "three-vessel view" (d), only the aorta (Ao) and superior vena cava (SVC) can be observed, owing to the caudal position of the pulmonary trunk. Spine (S) marks the dorsal side of the foetus on the ultrasound plane.

Just above the four-chamber view, above the outflow of the aorta, both the pulmonary trunk and the aorta can been seen in their spatial relationship in a transverse plane through the foetal chest. The superior caval vein is visible next to the aorta. This "three-vessel view" is not difficult to acquire and easy to teach to ultrasonographers (Figure 2a–c). It is generally accepted to be of great benefit in screening programmes, as it is abnormal in several heart malformations with abnormal position of the great vessels.

In the first trimester foetuses, the ascending aorta and pulmonary trunk measure about 1–2 mm at the valve annulus [25,37]. Haak et al [32] observed an increase in the visualisation of the outflow tracts in the past few decades up to 95% at gestational age of 13 weeks, confirmed by later studies [38]. Table 1 provides an overview of the visualisation rates of both the outflow tracts and the four-chamber view.

Table 1. Visualization of both four chamber view as well as the outflow tract, obtained by different studies.

Authors	Visualization rates in % (number of fetuses)			
	10+0 -10+6	11+0- 11+6	12+0- 12+6	13+0- 13+6
Johnson, 1992 [17]	0 (26)	0 (33)	31 (51)	43 (61)
Gembruch, 1993[73]	-	67 (15)	80 (30)	100 (51)
Gembruch, 2000[25]	44 (9)	75 (16)	93 (15)	100 (16)
Haak, 2002[37]	-	20 (85)	60 (85)	92 (85)
Vimpelli, 2006[74]	-	60 (53)	67 (201)	72 (330)
Smrcek, 2006[75]	67 (9)	100 (22)	98 (41)	100 (24)

   Reports on diagnosis of malformations solely affecting the outflow tracts, before 14 weeks gestational age, are increasingly being published, but mainly in the last decade. This suggests that these types of defects are more difficult to diagnose in the first trimester. Table 2 summarises several examples of outflow tract malformations detectable by echocardiography. Possibly, the most important of these is transposition of the great arteries, which is one of the most frequently missed severe heart defects, and could possibly benefit the most from prenatal detection [39] (Figure 3, transposition of the great arteries is further described below).

SENSITIVITY AND SPECIFICITY OF ECHOCARDIOGRAPHY IN FIRST TRIMESTER FOETUSES

As discussed, echocardiography in first trimester foetuses has been proven feasible. More recent studies have assessed the reliability and accuracy for detecting or excluding congenital heart disease. In a systematic review by Rasiah et al [24] a high sensitivity (85%) and specificity (99%) were reported in a pooled group of foetuses predominantly with a high risk for congenital heart defects such as increased nuchal translucency, previous child with cardiac defect, and cardiotoxic medication. These studies had all been conducted by specialised obstetricians in tertiary care hospitals. Large population-based studies concerning second trimester screening of low-risk pregnancies have demonstrated the limited accuracy regarding the detection of congenital heart defects. Specialised tertiary centres markedly showed higher detection rates [40]. It is therefore probable that considering first trimester echocardiography in population-based screening programmes will achieve lower reliability. A large randomised control trial41 demonstrated a low detection rate in a 12-week scan policy (11%). This did not differ significantly from an 18-week scan policy (15%), likely reflecting the level of training and experience of the ultrasonographers in this programme. Evidence regarding first trimester screening for congenital heart defects of low-risk mothers is scarce42 and does not assess cardiac anatomy only, but focuses on first trimester detection of structural defects in general [43–45]. The results of these pioneering studies are conflicting and no systematic reviews are available yet.

Table 2. Overview of heart anomalies detected by first-trimester sonography (up to 14 weeks of gestational age). HLHS=hypoplastic left heart syndrome.

Structural anomalies	Detected in first trimester - published by
Left persisting superior caval vein	Volpe 2011[42]
Atrioventricular defect	Gembruch 1990[27], Areias 1998[76], Carvalho 1998[18], Gembrug 1993[73], Achiron 1994[77], Carvalho 1998[18], Baschat 1999[78], Haak 2002[79], Huggon 2002[80], Comas 2002[81], Galindo 2003[82], McAuliffe 2005[38], Becker 2006[83], Weiner 2008[61], Bellotti 2010[23], Persico 2011[22], Hartge 2011[62], Volpe 2011[42], Eleftheriades 2012[63]
Left Isomerism	Huggon 2002[80,21],
Ventricular septal defect	DeVore 1987[26], Bronshtein 1991[84], Haak 2002[79], Huggon 2002[80], Comas 2002[81], McAuliffe 2005[38], Weiner 2008[61], Persico 2011[22], Hartge 2011[62], Eleftheriades 2012[63]
Univentricular heart	Gembruch 1993[73], Becker 2006[83], Hartge 2011[62]
Ebstein's anomaly	Huggon 2002[80], Eleftheriades 2012[63]
Tricuspid atresia / hypoplastic right heart	Comas 2002[81], Galindo 2003[82], Carvalho 2004 [21], Weiner 2008[61], Bellotti 2010[23], Hartge 2011[62], Eleftheriades 2012[63]
Hypoplastic left heart	Bronshtein 1991[84], Haak 2002[79], Huggon 2002[80], Comas 2002[81], Carvalho [21], McAuliffe 2005[38], Weiner 2008[61], Bellotti 2010[23], Persico 2011[22], Hartge 2011[62], Volpe 2011[42], Eleftheriades 2012[63]
Aortic stenosis (developing HLHS)	Axt-Fliedner 2006[85], Hartge 2011[62], Volpe 2011[42], Eleftheriades 2012[63]
Interrupted aortic arch	Carvalho 1998[18], Volpe 2011[42]
Vascular ring/right aortic arch	Volpe 2011[42]
Truncus arteriosus	Achiron 1994[77], Huggon 2002[80], Weiner 2008[61], Hartge 2011[62]
Double outlet right ventricle	Gembruch 1993[73], Baschat 1999[78], Haak 2002[79], Comas[81] 2002, Carvalho 2004[6], McAuliffe 2005[38], Belotti 2010[23], Hartge 2011[62]
Transposition of the great arteries	Baschat 1999[78], Galindo 2003[82], Carvalho [21], Weiner 2008[61], Bellotti 2010[23], Persico 2011[22], Volpe 2011[42]
Tetralogy of Fallot (Ventricular septal defect and overriding aorta)	Bronshtein 1990[28], Achiron 1994[77], Comas 2002[81], Galindo 2003[82], Weiner 2008[61], Persico 2011[22], Hartge 2011[62], Volpe 2011[42]
Pulmonary stenosis	Gembruch 1993[73], Baschat 1999[78], Hartge 2011[62], Volpe 2011[42]
Pulmonary atresia	Huggon 2002[80], Persico 2011[22], Hartge 2011[62]
Uhl's disease	Achiron 1994[77]
Ectopia cordis	Achiron 1994[77], Comas 2002[81], McAuliffe 2005[38], Bellotti 2010[23], Hartge 2011[62]
Cardiacdiverticle	Prefumo 2005[86], McAuliffe 2005[38]α

EXAMPLES OF CARDIAC MALFORMATIONS DETECTABLE WITH FIRST TRIMESTER ULTRASOUND; ULTRASOUND VERSUS MORPHOLOGY

The following section describes three examples of congenital malformations in the first trimester.

In transposition of the great arteries, there is a concordant atrio-ventricular connection in combination with ventriculo-arterial discordance. The aorta connects to the morphological right ventricle and the pulmonary trunk connects to the morphological left ventricle. There is often a

Figure 4. Echocardiography and morphology of a foetal heart with an atrioventricular septal defect.
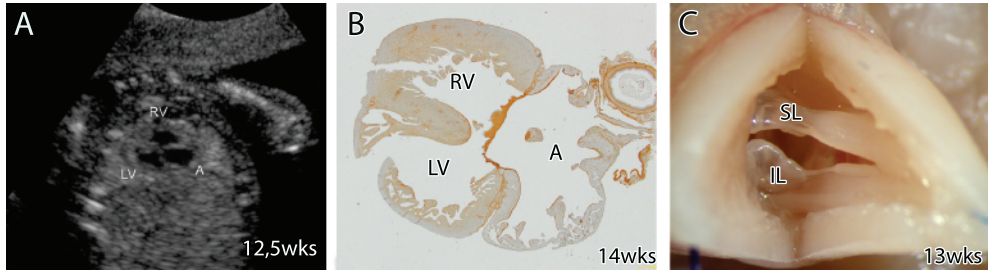
The common valve between the atria (a) and ventricles (RV and LV) can be recognised on the ultrasound four-chamber view (A; printed with permission of Ultrasound in Obstetrics and Gynaecology. Please note that this figure displays an oblique plane through the thorax. Owing to persistent foetal position, a correct fourchamber view was not obtainable) and histological section (b). On plane C, the common valve is seen from the left ventricle. IL = inferior bridging leaflet; SL= superior bridging leaflet.

Figure 5. Echocardiography and morphology of a hypoplastic left heart.
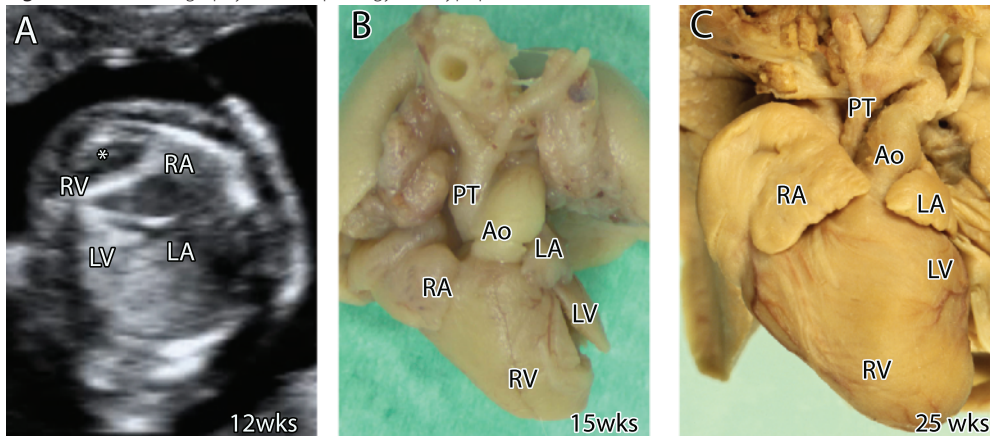
On ultrasound at 12 weeks gestational age (a), disbalance between the right ventricle (RV) and left ventricle (LV) can be observed. Foetal specimens of 13 (b) and 25 (c) weeks also show hypoplasia of the ascending aorta. Right atrium (RA), left atrium (LA), aorta (Ao), pulmonary trunk (PT). *Shows pericardial fluid.

parallel course of the great arteries, with a right anterior position of the aorta with respect to the pulmonary orifice [46] (Figure 3b–c). There is usually a fibrous continuity of the mitral valve and pulmonary valve, whereas the aortic valve is separated from the tricuspid valve by a muscular infundibulum. In transposition of the great arteries, both the aortic valve and the pulmonary valve are often situated at the same level, in contrast to normal hearts where the aortic valve is situated at a lower level than the pulmonary valve. In about 50% of the cases of transposition of the great arteries, a ventricular septal defect is present [47].

Transposition of the great arteries is frequently missed during routine second trimester anomaly scans [48] This is probably owing to the normal four-chamber view in this defect. In transposition of the great arteries the vessel that arises from the left ventricle branches in a

transverse plane. This is called "laterally branching", which identifies the pulmonary artery. The vessel that arises from the right ventricle is the aorta, which gives rise to the neck vessels (superiorly branching). Easier to recognise is the fact that the "three-vessel view" described above cannot be achieved in transposition of the great arteries. In transposition of the great arteries, the vessel that arises from the right ventricle produces a "two-vessel view". These two vessels are the aortic arch and the superior caval vein. Figure 3d illustrates that it is possible to diagnose transposition of the great arteries, even at an early gestational age. The images are comparable to those encountered in the second trimester transposition of the great arteries.

Another example of a congenital malformation that may be detected during first trimester echocardiography is atrioventricular septal defect. Atrioventricular septal defects cover a spectrum of heart malformations resulting in a common atrioventricular junction and common atrioventricular valve (Figure 4). The extent of the incomplete development of the atrioventricular septum varies and is used to categorise atrioventricular septal defects. A complete atrioventricular septal defect includes an ostium primum defect of the atrial septum, as well as a defect in the inflow portion of the ventricular septum. In incomplete or partial atrioventricular septal defect, the common atrioventricular annulus and valve are combined with an atrial septal defect – only shunting at the atrial level – or, less commonly, a ventricular septal defect – shunting only at the ventricular level. Extreme disbalance of the ventricles may result in hypoplastic right heart, in cases of left ventricular predominance, or hypoplastic left heart, if the right ventricle is predominant) [49–51].

In echocardiography, atrioventricular septal defects can be recognised in the four-chamber view (Figure 4a) by the absence of the crux and a common atrioventricular valve. As the four-chamber view is the most basic plane to screen for heart defects, atrioventricular septal defects, especially complete atrioventricular septal defects with moderate to large ventricular septal defects, are usually not missed, even in the first trimester scanning. As balanced complete atrioventricular septal defects carry a risk of around 60–80% for Down syndrome, karyotyping has to be offered. A careful examination of other organs is furthermore warranted, as 75% of cases with atrioventricular septal defects have anomalies in other organ systems [49]. A high prevalence of atrioventricular septal defects is also observed in patients with heterotaxy syndrome [52,53].

The final example is the hypoplastic left heart, in which aortic atresia or aortic stenosis is combined with either mitral atresia or mitral stenosis. The left side of the heart is underdeveloped, with a left ventricle of about 1/3 or less of its regular size, and there is hypoplasia of the ascending aorta and left atrium. When inflow of blood into the heart exceeds the outflow, a profound intimal thickening called fibro-elastosis can be observed. Whereas this intimal thickening can be readily observed during later development stages, this is usually not observed during first trimester echocardiography yet. A profound disbalance of the ventricles can be visible already during first trimester echocardiography (Figure 5). However, this disbalance may also occur only later in development, so that the observation of equal-sized ventricles does not always rule out the hypoplastic left heart. Follow-up studies are mandatory.

LIMITATIONS FOR FOETAL CARDIAC EVALUATION DURING FIRST TRIMESTER

The most important disadvantage and therefore the major limitation of first trimester echocardiography is the intrauterine development of congenital heart disease at later gestation [54,55]. Several malformations, such as mild pulmonary [56,57] and aortic stenosis or coarctation58 or even the hypoplastic left heart [59] can develop in second or third trimester foetuses. Furthermore, some heart lesions such as cardiac rhabdomyoma or cardiomyopathy may not be present in the first or second trimester and can evolve in later gestation or even after birth [60]. Therefore, it is important to clarify to parents that some lesions could be missed in early pregnancy, even after detailed examination, and that, however rarely, a serious defect can develop after the mid-trimester. This statement is also supported by reports of heart defects, being missed in the first trimester ultrasonography [6,38,42,61–63]. Thus, after the first trimester echocardiography, a follow-up examination on the second trimester of pregnancy should always be conducted. The knowledge that ventricular septal defects usually remain undetected in second trimester echocardiography [64,65], probably because the size of these defects are beyond the resolution of the currently available ultrasound devices, makes it a neglectable aspect of first trimester examination, at which time this technical limitation is even more severe.

Another disadvantage of the first trimester echocardiography is the possible detection of defects that could resolve spontaneously in later pregnancy, such as muscular ventricular septal defects [66]. This could result in unnecessary anxiety of the parents. If the first trimester echocardiography is performed transvaginally, the direction of probe manipulation is limited. If the foetal position is consistently unfavourable, the technique does not provide sufficient images of the foetal heart. Transvaginal scanning, however, produces images with detail comparable to the second trimester abdominal scanning. In our opinion, transvaginal scanning should therefore be the preferred approach, despite the fact that specific training is needed. Finally, probably the most significant reason that first trimester echocardiography (abdominal or transvaginal) is still a rarely applied method is the need for highly skilled staff with several years of experience in second trimester echocardiography, and the use of high-end ultrasound equipment with high-frequency (transvaginal) probes [67].

CONCLUSION

Although the advantages of first trimester transvaginal echocardiography seem of considerable value for couples at risk for having offspring with cardiac defects, this method is nowadays still limited to a few specialised centers. The numerous reports on the poor performance of mid-gestational sonography, regarding the detection of cardiac abnormalities, as well as the aforementioned limitations, could be the reason that centres are discouraged to extend echocardiography to the first trimester. Furthermore, high-end ultrasound facilities are needed, as

2.2

well as operators that are experienced and have a particular interest in echocardiography. These factors, as well as the need for a follow-up examination at 20 weeks, are probably responsible for the limited utilisation of first-trimester echocardiography, and its restricted use in foetuses at a high risk of cardiac abnormalities. In short, it seems clear that the capacity of highfrequency transvaginal probes is sufficient to perform echocardiographic examination in the late first trimester of pregnancy. However, the capability to detect and correctly diagnose heart defect is highly dependent on the operator, as is the case in the second trimester echocardiography.

REFERENCES

1. Hove JR, Koster RW, Forouhar AS, et al. Intracardiac fluid forces are an essential epigenetic factor for embryonic cardiogenesis. Nature 2003;421:172–177.

2. Broekhuizen ML, Hogers B, DeRuiter MC, et al. Altered hemodynamics in chick embryos after extraembryonic venous obstruction. Ultrasound Obstet Gynecol 1999;13:437–445.

3. Vermot J, Forouhar AS, Liebling M, et al. Reversing blood flows act through klf2a to ensure normal valvulogenesis in the developing heart. PLoS Biol 2009;7:e1000246.

4. Slough J, Cooney L, Brueckner M. Monocilia in the embryonic mouse heart suggest a direct role for cilia in cardiac morphogenesis. Dev Dyn 2008;237:2304–2314.

5. Allan L, Benacerraf B, Copel JA, et al. Isolated major congenital heart disease. Ultrasound Obstet Gynecol 2001;17:370–379.

6. Carvalho JS. Fetal heart scanning in the first trimester. Prenat Diagn 2004; 24: 1060–1067.

7. Gittenberger-de Groot AC, Poelmann RE. Normal and abnormal cardiac development. In: Moller JH, Hoffman JIE (eds). Pediatric Cardiovascular Medicine. Churchill Livingstone, Philadelphia, 2000:3–20.

8. Larsen WJ. Development of the heart. In: Sherman LS, Potter SS, Scott WJ (eds). Human Embryology. Churchill Livingstone, New York, 1999:157–180.

9. Schoenwolf GC, Bleyl SB, Brauer PR, Francis-West PH. Larsen's Human Embryology. Churchill Livingstone, New York,2008.

10. Cook AC, Yates RW, Anderson RH. Normal and abnormal fetal cardiac anatomy. Prenat Diagn 2004;24:1032–1048.

11. Anderson RH, Yen Ho S. Sequential segmental analysis – description and categorisation for the millennium. Cardiol Young 1997;7:98–116.

12. Timor-Tritsch IE, Farine D, Rosen MG. A close look at early embryonic development with the high-frequency transvaginal transducer. Am J Obstet Gynecol 1988;159:676–681.

13. Timor-Tritsch IE, Peisner DB, Raju S. Sonoembryology: an organ-oriented approach using a high-frequency vaginal probe. J Clin Ultrasound 1990;18:286–298.

14. D'Amelio R, Giorlandino C, Masala L, et al. Fetal echocardiography using transvaginal and transabdominal probes during the first period of pregnancy: a comparative study. Prenat Diagn 1991;11:69–75.

15. Blaas HG, Eik-Nes SH, Kiserud T, et al. Early development of the abdominal wall, stomach and heart from 7 to 12 weeks of gestation: a longitudinal ultrasound study. Ultrasound Obstet Gynecol 1995;6:240–249.

16. Allan LD, Santos R, Pexieder T. Anatomical and echocardiographic correlates of normal cardiac morphology in the late first trimester fetus. Heart 1997;77:68–72.

17. Johnson P, Sharland G, Maxwell D, et al. The role of transvaginal sonography in the early detection of congenital heart disease. Ultrasound Obstet Gynecol 1992;2:248–251.

18. Carvalho JS, Moscoso G, Ville Y. First-trimester transabdominal fetal echocardiography. Lancet 1998;351:1023–1027.

19. Simpsom JM, Jones A, Callaghan N, et al. Accuracy and limitations of transabdominal fetal echocardiography at 12–15 weeks of gestation in a population at high risk for congenital heart disease. BJOG 2000;107:1492–1497.

20. Huggon IC, DeFigueiredo DB, et al. Tricuspid regurgitation in the diagnosis of chromosomal anomalies in the fetus at 11–14 weeks of gestation. Heart 2003;89:1071–1073.

21. Carvalho JS, Moscoso G, Tekay A, et al. Clinical impact of first and early second trimester fetal echocardiography on high risk pregnancies. Heart 2004;90:921–926.

22. Persico N, Moratalla J, Lombardi CM, et al. Fetal echocardiography at 11–13 weeks by transabdominal high-frequency ultrasound. Ultrasound Obstet Gynecol 2011;37:296–301.

23. Bellotti M, Fesslova V, De GC, et al. Reliability of the firsttrimester cardiac scan by ultrasound-trained obstetricians with high-frequency transabdominal probes in fetuses with increased

2.2

nuchal translucency. Ultrasound Obstet Gynecol 2010;36:272–278.

24.   Rasiah SV, Publicover M, Ewer AK, et al. A systematic review of the accuracy of first-trimester ultrasound examination for detecting major congenital heart disease. Ultrasound Obstet Gynecol 2006;28:110–116.

25.   Gembruch U, Shi C, Smrcek JM. Biometry of the fetal heart between 10 and 17 weeks of gestation. Fetal Diagn Ther 2000;15:20–31.

26.   DeVore GR, Steiger RM, Larson EJ. Fetal echocardiography: the prenatal diagnosis of a ventricular septal defect in a 14-week fetus with pulmonary artery hypoplasia. Obstet Gynecol 1987;69:494–497.

27.   Gembruch U, Knopfle G, Chatterjee M, et al. First-trimester diagnosis of fetal congenital heart disease by transvaginal two-dimensional and Doppler echocardiography. Obstet Gynecol 1990;75:496–498.

28.   Bronshtein M, Siegler E, Yoffe N, et al. Prenatal diagnosis of ventricular septal defect and overriding aorta at 14 weeks' gestation, using transvaginal sonography. Prenat Diagn 1990;10:697–702.

29.   Dolkart LA, Reimers FT. Transvaginal fetal echocardiography in early pregnancy: normative data. Am J Obstet Gynecol 1991;165:688–691.

30.   Allan LD, Crawford DC, Chita SK, et al. Prenatal screening for congenital heart disease. Br Med J (Clin Res Ed) 1986;292:1717–1719.

31.   Copel JA, Pilu G, Green J, et al. Fetal echocardiographic screening for congenital heart disease: the importance of the four-chamber view. Am J Obstet Gynecol 1987;157:648–655.

32.   Haak MC, Van Vugt JM. Echocardiography in early pregnancy: review of literature. J Ultrasound Med 2003;22:271–280.

33.   Votino C, Jani J, Verhoye M, et al. Postmortem examination of human fetal hearts at or below 20 weeks' gestation: a comparison of high-field MRI at 9.4T with lower-field MRI magnets and stereomicroscopic autopsy. Ultrasound Obstet Gynecol 2012;40:437–444.

34.   Timor-Tritsch IE, Fuchs KM, Monteagudo A, et al.Performing a fetal anatomy scan at the time of first-trimester screening. Obstet Gynecol 2009;113:402–407.

35.   Scherptong RW, Jongbloed MR, Wisse LJ, et al. Morphogenesis of outflow tract rotation during cardiac development: the pulmonary push concept. Dev Dyn 2012;241:1413–1422.

36.   Sklansky MS, Berman DP, Pruetz JD, et al. Prenatal screening for major congenital heart disease: superiority of outflow tracts over the 4-chamber view. J Ultrasound Med 2009;28:889–899.

37.   Haak MC, Twisk JW, Van Vugt JM. How successful is fetal echocardiographic examination in the first trimester of pregnancy? Ultrasound Obstet Gynecol 2002;20:9–13.

38.   McAuliffe FM, Trines J, Nield LE, et al. Early fetal echocardiography – a reliable prenatal diagnosis tool. Am J Obstet Gynecol 2005;193:1253–1259.

39.   Blyth M, Howe D, Gnanapragasam J, et al. The hidden mortality of transposition of the great arteries and survival advantage provided by prenatal diagnosis. BJOG 2008; 115: 1096–1100.

40.   Sharland G. Fetal cardiac screening: why bother? Arch Dis Child Fetal Neonatal Ed 2010;95:F64–F68.

41.   Westin M, Saltvedt S, Bergman G, et al. Routine ultrasound examination at 12 or 18 gestational weeks for prenatal detection of major congenital heart malformations? A randomised controlled trial comprising 36,299 fetuses. BJOG 2006;113:675–682.

42.   Volpe P, Ubaldo P, Volpe N, et al. Fetal cardiac evaluation at 11–14 weeks by experienced obstetricians in a low-risk population. Prenat Diagn 2011;31:1054–1061.

43.   Grande M, Arigita M, Borobio V, et al. First-trimester detection of structural abnormalities and the role of aneuploidy markers. Ultrasound Obstet Gynecol 2012;39:157–163.

44.   Syngelaki A, Chelemen T, Dagklis T, et al. Challenges in the diagnosis of fetal non-chromosomal abnormalities at 11–13 weeks. Prenat Diagn 2011;31:90–102.

45.   Rissanen A, Niemimaa M, Suonpaa M, et al. First trimester Down's syndrome screening shows high detection rate for trisomy 21, but poor performance in structural abnormalities – regional outcome results. Fetal Diagn Ther 2007;22:45–50.

46. Bartelings MM, Gittenberger-de Groot AC. Morphogenetic considerations on congenital malformations of the outflow tract. Part 2: complete transposition of the great arteries and double outlet right ventricle. Int J Cardiol 1991;33:5–26.

47. Liebman J, Cullum L, Belloc NB. Natural history of transpositon of the great arteries. Anatomy and birth and death characteristics. Circulation 1969;40:237–262.

48. Pinto NM, Keenan HT, Minich LL, et al. Barriers to prenatal detection of congenital heart disease: a population-based study. Ultrasound Obstet Gynecol 2012;40:418–425.

49. Christensen N, Andersen H, Garne E, et al. Atrioventricular septal defects among infants in Europe: a population-based study of prevalence, associated anomalies, and survival. Cardiol Young 2012:1–8.

50. Cohen MS, Jacobs ML, Weinberg PM, et al. Morphometric analysis of unbalanced common atrioventricular canal using two-dimensional echocardiography. J Am Coll Cardiol 1996;28:1017–1023.

51. Yildirim G, Gungorduk K, Yazicioglu F, et al. Prenatal diagnosis of complete atrioventricular septal defect: perinatal and neonatal outcomes. Obstet Gynecol Int 2009: 958496.

52. Peoples WM, Moller JH, Edwards JE. Polysplenia: a review of 146 cases. Pediatr Cardiol 1983;4:129–137.

53. Irving CA, Chaudhari MP. Cardiovascular abnormalities in Down's syndrome: spectrum, management and survival over 22 years. Arch Dis Child 2012;97:326–330.

54. Allan LD. Development of congenital lesions in mid or late gestation. Int J Cardiol 1988;19:361–362.

55. Allan LD. Evolution of echocardiographic findings in the fetus. Circulation 1997;96:391–392.

56. Todros T, Presbitero P, Gaglioti P, et al. Pulmonary stenosis with intact ventricular septum: documentation of development of the lesion echocardiographically during fetal life. Int J Cardiol 1988;19:355–362.

57. Rice MJ, McDonald RW, Reller MD. Progressive pulmonary stenosis in the fetus: two case reports. Am J Perinatol 1993;10:424–427.

58. Allan LD, Crawford DC, Tynan M. Evolution of coarctation of the aorta in intra-uterine life. Brit Heart J 1984;52:471–473.

59. Allan LD, Sharland G, Tynan MJ. The natural history of the hypoplastic left heart syndrome. Int J Cardiol 1989;25:341–343.

60. Yagel S, Weissman A, Rotstein Z, et al. Congenital heart defects: natural course and in utero development. Circulation 1997;96:550–555.

61. Weiner Z, Weizman B, Beloosesky R, et al. Fetal cardiac scanning performed immediately following an abnormal nuchal translucency examination. Prenat Diagn 2008;28:934–938.

62. Hartge DR, Weichert J, Krapp M, et al. Results of early foetal echocardiography and cumulative detection rate of congenital heart disease. Cardiol Young 2011;21:505–517.

63. Eleftheriades M, Tsapakis E, Sotiriadis A, et al. Detection of congenital heart defects throughout pregnancy; impact of first trimester ultrasound screening for cardiac abnormalities. J Matern Fetal Neonatal Med 2012;25:2546–2550.

64. Garne E, Stoll C, Clementi M. Evaluation of prenatal diagnosis of congenital heart diseases by ultrasound: experience from 20 European registries. Ultrasound Obstet Gynecol 2001;17:386–391.

65. Jaeggi ET, Sholler GF, Jones OD, Cooper SG. Comparative analysis of pattern, management and outcome of pre- versus postnatally diagnosed major congenital heart disease: a populationbased study. Ultrasound Obstet Gynecol 2001;17:380–385.

66. Paladini D, Palmieri S, Lamberti A, et al. Characterization and natural history of ventricular septal defects in the fetus. Ultrasound Obstet Gynecol 2000;16:118–122.

67. Rustico MA, Benettoni A, D'Ottavio G, et al. Early screening for fetal cardiac anomalies by transvaginal echocardiography in an unselected population: the role of operator experience. Ultrasound Obstet Gynecol 2000;16:614–619.

68. Stoll C, Alembik Y, Dott B, et al. Evaluation of prenatal diagnosis of congenital heart disease. Prenat Diagn 1998;18:801–807.

69. Queisser-Luft A, Stopfkuchen H, Stolz G, et al. Prenatal diagnosis of major malformations: quality control of routine ultrasound examinations based

on a five-year study of 20,248 newborn fetuses and infants. Prenat Diagn 1998;18:567–576.

70.   Todros T, Faggiano F, Chiappa E, et al. Accuracy of routine ultrasonography in screening heart disease prenatally. Gruppo Piemontese for Prenatal Screening of Congenital Heart Disease. Prenat Diagn 1997;17:901–906.

71.   Kirk JS, Comstock CH, Lee W, et al. Sonographic screening to detect fetal cardiac anomalies: a 5-year experience with 111 abnormal cases. Obstet Gynecol 1997;89:227–232.

72.   Queisser-Luft A, Stolz G, Wiesel A, Schlaefer K, Spranger J. Malformations in newborn: results based on 30,940 infants and fetuses from the Mainz congenital birth defect monitoring system (1990–1998). Arch Gynecol Obstet 2002;266:163–167.

73.   Gembruch U, Knopfle G, Bald R, Hansmann M. Early diagnosis of fetal congenital heart disease by transvaginal echocardiography. Ultrasound Obstet Gynecol 1993;3:310–317.

74.   Vimpelli T, Huhtala H, Acharya G. Fetal echocardiography during routine first-trimester screening: a feasibility study in an unselected population. Prenat Diagn 2006; 6:475–482.

75.   Smrcek JM, Berg C, Geipel A, et al. Early fetal echocardiography: heart biometry and visualization of cardiac structures between 10 and 15 weeks' gestation. J Ultrasound Med 2006;25:173–182.

76.   Areias JC, Matias A, Montenegro N, et al. Early antenatal diagnosis of cardiac defects using transvaginal Doppler ultrasound: new perspectives? Fetal Diagn Ther 1998;13:111–114.

77.   Achiron R, Rotstein Z, Lipitz S, et al. First trimester diagnosis of fetal congenital heart disease by transvaginal ultrasonography. Obstet Gynecol 1994;84:69–72.

78.   Baschat AA, Gembruch U, Knopfle G, et al. First trimester fetal heart block: a marker for cardiac anomaly. Ultrasound Obstet Gynecol 1999;14:311–314.

79.   Haak MC, Bartelings MM, Gittenberger-de Groot AC, et al. Cardiac malformations in first-trimester fetuses with increased nuchal translucency: ultrasound diagnosis and postmortem morphology. Ultrasound Obstet Gynecol 2002;20:14–21.

80.   Huggon IC, Ghi T, Cook AC, et al. Fetal cardiac abnormalities identified prior to 14 weeks' gestation. Ultrasound Obstet Gynecol 2002;20:22–29.

81.   Comas GC, Galindo A, Martinez JM, et al. Early prenatal diagnosis of major cardiac anomalies in a high-risk population. Prenat Diagn 2002;22:586–593.

82.   Galindo A, Comas C, Martinez JM, et al. Cardiac defects in chromosomally normal fetuses with increased nuchal translucency at 10–14 weeks of gestation. J Matern Fetal Neonatal Med 2003;13:163–170.

83.   Becker R, Wegner RD. Detailed screening for fetal anomalies and cardiac defects at the 11–13-week scan. Ultrasound Obstet Gynecol 2006;27:613–618.

84.   Bronshtein M, Zimmer EZ, Milo S, et al. Fetal cardiac abnormalities detected by transvaginal sonography at 12–16 weeks' gestation. Obstet Gynecol 1991;78:374–378.

85.   Axt-Fliedner R, Kreiselmaier P, Schwarze A, et al. Development of hypoplastic left heart syndrome after diagnosis of aortic stenosis in the first trimester by early echocardiography. Ultrasound Obstet Gynecol 2006;28:106–109.

86.   Prefumo F, Bhide A, Thilaganathan B, et al. Fetal congenital cardiac diverticulum with pericardial effusion: two cases with different presentations in the first trimester of pregnancy. Ultrasound Obstet Gynecol 2005;25:405–408.

87.   Jongbloed MR, Mahtab EAF, Blom NA, et al. Development of the cardiac conduction system and the possible relation to predilection sites of arrhythmogenesis. Scientific World Journal 2008;8:239–269.

Chapter 2.3

Echocardiographic assessment of embryonic and fetal mouse heart development: a focus on haemodynamics and morphology

Nathan D. Hahurij*, Emmeline E. Calkoen*, Monique R.M. Jongbloed, Arno A. W. Roest,
Adriana C. Gittenberger-de Groot, Robert E. Poelmann, Marco C. De Ruiter,
Conny J. van Munsteren, Paul Steendijk and Nico A. Blom
* Equal contribution

ABSTRACT

Background
Heart development is a complex process, and abnormal development may result in congenital heart disease (CHD). Currently, studies on animal models mainly focus on cardiac morphology and the availability of hemodynamic data, especially of the right heart half, is limited. Here we aimed to assess the morphological and hemodynamic parameters of normal developing mouse embryos/fetuses by using a high-frequency ultrasound system.

Methods
A timed breeding program was initiated with a WT mouse line (Swiss/129Sv background). All recordings were performed transabdominally, in isoflurane sedated pregnant mice, in hearts of sequential developmental stages: 12.5, 14.5, and 17.5 days after conception (n = 105).

Results
Along development the heart rate increased significantly from 125 ± 9.5 to 219 ± 8.3 beats per minute. Reliable flow measurements could be performed across the developing mitral and tricuspid valves and outflow tract. M-mode measurements could be obtained of all cardiac compartments. An overall increase of cardiac systolic and diastolic function with embryonic/ fetal development was observed.

Conclusion
High-frequency echocardiography is a promising and useful imaging modality for structural and hemodynamic analysis of embryonic/fetal mouse hearts.

INTRODUCTION

Heart development is a complex process during which the heart will form from a single myocardial heart tube to a full septated four-chambered heart with functional atrioventricular (AV) and ventriculoarterial valves and a separated outflow tract. The primary heart tube is derived from the splanchnic mesoderm in the embryonic plate and initially consists mainly of a left ventricle (LV) and AV canal. During further development, significant contributions to the heart tube will continue to be made from the mesenchyme situated behind the heart, the so-called second heart field (SHF). The cells of the SHF will form the right ventricle (RV) and outflow tract at the arterial pole of the heart as well as myocardial and vascular structures at the venous pole of the heart [1].

Abnormal heart development results in congenital heart disease (CHD), the most common birth defect with an estimated incidence of six per 1000 live born children [2]. In the last decade, knowledge regarding genes, growth and transcription factors important in heart development has dramatically increased, which has led to the generation of specific genetically mutated mouse models to study the etiology of CHD [3]. Up till now description of both normal and abnormal heart development in these mouse models mainly focused on the morphology of the heart, whereas functional data like hemodynamics and *in vivo* imaging are limited. Furthermore, functional parameters and their course at subsequent stages of normal mouse heart development have only been described in a few studies [4-7]. Specifically, knowledge regarding RV inflow and myocardial function during embryonic development is scarce.

In clinical practice ultrasound is the most frequently used minimally invasive imaging modality at pre- and postnatal stages of heart development. Clinical ultrasound machines have also been used for imaging of embryonic mouse hearts, however, ultrasound frequencies (8-15MHz) are not sufficient for a detailed morphological and hemodynamic analysis. Recently developed high-frequency ultrasound systems (30-50MHz) are able offer sufficient spatial-temporal resolution for detailed and reliable imaging of embryonic mouse hearts. Thus far, there are only limited studies describing the hemodynamic and morphological changes at subsequent stages of heart development using such ultrasound systems [4;6;8].

Hemodynamics play an important role in normal heart development by the activation of shear-stress dependent signaling pathways. During development genes like Klf-2 [9] and periostin [10] are expressed in regions of the heart that are known to be subjected to high mechanical/hemodynamical stress. It has also been demonstrated that artificial alterations in hemodynamics throughout heart development result in aberrant activation of genes at the endocardial surface of the heart [11], which might lead to disturbed cardiogenesis, i.e. CHD. A first step in the interpretation of hemodynamic parameters during development is the acquisition of a reliable reference series during normal heart development.

In the current study we aim to provide an overview of hemodynamic and morphological changes during embryonic and fetal stages of normal mouse heart development using a high-

2.3

frequency ultrasound system. Knowledge of these functional parameters is highly relevant for the interpretation of results obtained in genetically mutated mouse models. We expect that knowledge of how echocardiographic parameters shift over development will eventually contribute to the early detection of CHD during human pregnancy.

MATERIAL AND METHODS

Animals

Animal experiments were approved by the local animal welfare committee (DEC no:10177) of the Leiden University Medical Center. A timed breeding program was initiated with a WT (Swiss/129Sv background) mouse line. The day after breeding was considered to be 0.5 days post conception (dpc). All pregnant mice (n=11) were subjected to high-frequency ultrasound recordings at 3 subsequent stages of embryonic/fetal development, being 12.5, 14.5 and 17.5dpc. At 12.5dpc, the pregnant mother mouse was anaesthetized using Isoflurane (induction 5%, maintenance during assessment 1.5%), the most commonly used anesthetic in mouse experiments [6;12]. Subsequently, the sedated mouse was placed in the experimental setup (VisualSonics Vevo770 system, Toronto, Canada), which includes a heated table and rectal probe for maintenance and control of body temperature (36.5-37.5^{0}C). Electrodes were attached to the paws for monitoring the maternal electrocardiogram, heart and breathing rate during the experiments.

Abdominal hair was removed using a commercially available chemical hair remover followed by application of ultrasound transmission gel (Aquasonic, Parker Laboratories, Fairfield, NY, USA). The ultrasound recordings were performed with a high-frequency ultrasound system (30MHz, VisualSonics Vevo 770 system, Toronto, Canada) with an axial resolution of 55μm, a focal length of 12.7mm and a maximal field of view of 20mm. Scanning time was kept as short as possible according to the ALARA principle[13]. Between the three subsequent developmental stages that were assessed the pregnant mice were housed in cages in the animal facility.

Ultrasound recording protocol

All ultrasound recordings were performed by NDH and EEC. During the ultrasound recordings the two laterally located uterus horns were scanned for the presence and position of the embryos/fetuses (n=105). In individual embryos/fetuses, the left and right side was established to identify the position of the heart including the individual cardiac compartments and structures. At 12.5dpc these compartments included the left atrium (LA), right atrium (RA), LV, RV, the common AV canal (cAVC) encompassing the future mitral valve (MV) and tricuspid valve (TV) orifices, common outflow tract (cOFT), developing inter-ventricular septum (IVS) and the inter-ventricular foramen i.e. the continuity between the LV and RV before completion of ventricular

septation. At later stages (14.5 and 17.5dpc) the MV and TV orifices, aorta (Ao) and pulmonary trunk (PT) were identified.

Pulsed-wave Doppler recordings

The methods that were used for pulsed-wave Doppler flow recordings are summarized in Table 1. For flow measurements automatic Doppler angle corrections were accepted up to 45 degrees. Flow recordings across the cAVC (12.5dpc: future MV n=1;future TV n=11) and developing MV and TV orifices (14.5dpc: MV n=17, TV n=20;17.5dpc: MV n=16, TV n=14) were performed to assess the peak-E (Early/passive ventricular filling by ventricular relaxation in early diastole) and peak-A wave velocities (active ventricular filling due to atrial contraction), hence the E/A-ratios

2.3

Table 1. The methods used for performing Doppler flow recordings per gestational age. DFT = diastolic filling time, IVRT = isovolumetric relaxation time, IVCT = isovolumetric contraction time, ET = ejection time, VTI = velocity time integral, cAVC = common atrioventricular canal, cOFT = common outflow tract, LVOT = left ventricular outflow tract, RVOT = right ventricular outflow tract. MV = mitral valve, TV tricuspid valve, Ao = aorta, PT = pulmonary trunk, IVS = interventricular septum.

Age (dpc)	Location	Parameter (unit)	View	Doppler beam: position and alignment
12.5	Future MV	E-wave (m/s)	4 chambers	cAVC, parallel to flow direction at left side of the developing IVS
		A-wave (m/s)		
		DFT (ms)		
		IVCT (ms)		
		IVRT (ms)		
		ET (ms)		
	Future TV	E-wave (m/s)	4 chambers	cAVC, parallel to flow direction at the right side of the developing IVS
		A-wave (m/s)		
	cOFT, future Ao/PT	Peak flow (m/s)	5 chambers/ OFT	Proximal part cOFT, parallel to flow direction
		VTI (mm)		
14.5 and 17.5	MV	E-wave (m/s)	4 chambers	LV below (developing) MV annulus, parallel to flow direction at left side of the IVS
		A-wave (m/s)		
		DFT (ms)		
		IVCT (ms)		
		IVRT (ms)		
		ET (ms)		
	TV	E-wave (m/s)	4 chambers	RV below (developing) TV annulus, parallel to flow direction at right side of IVS
		A-wave (m/s)		
	Ao	Peak flow (m/s)	5 chambers/ LVOT	Ao above (developing) valve annulus, VTI (mm) parallel to flow direction
	PT	Peak flow (m/s)	RVOT	PT above (developing) valve annulus, parallel to flow direction

were calculated. The recordings across the cAVC and developing MV orifice were also used to evaluate the embryonic heart rate (HR) in beats per minute (BPM), cardiac cycle length (RR-interval), diastolic ventricular filling time (DFT;12.5dpc *n*=11, 14.5dpc *n*=17 and 17.5dpc *n*=16), ejection time (ET;12.5dpc *n*=11, 14.5dpc *n*=17 and 17.5dpc *n*=16), isovolumetric contraction time (IVCT;12.5dpc *n*=7, 14.5dpc *n*=17 and 17.5dpc *n*=16) and isovolumetric relaxation time (IVRT;12.5dpc *n*=7, 14.5dpc *n*=17 and 17.5dpc *n*=16) of the LV (Figure 1a). The myocardial performance index (MPI;12.5dpc *n*=5;14.5dpc *n*=17;17.5dpc *n*=16) i.e. Tei-index that evaluates the combined LV systolic and diastolic function was calculated using the following formula: (IVRT+IVCT)/ET [14].
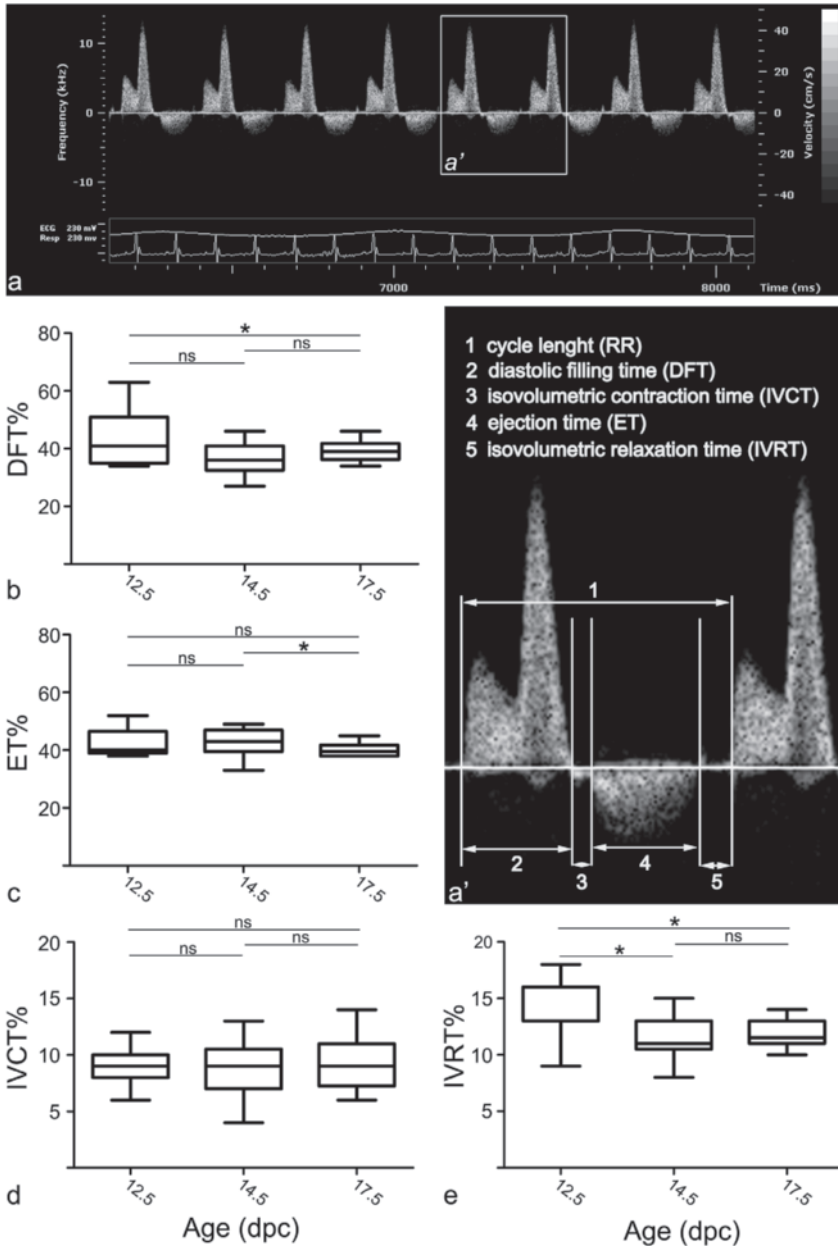
Pulsed-wave Doppler recordings were also performed in the cOFT at 12.5dpc (*n*=15) and Ao and PT at 14.5dpc (*n*=18 and *n*=12) and 17.5dpc (*n*=12 and *n*=4;Table 1). Furthermore, the velocity time integral (VTI) i.e. the area under the Doppler velocity envelope for one heart beat was determined (12.5dpc *n*=15;14.5dpc Ao *n*=18 and PT *n*=12;17.5dpc Ao *n*=12 and PA *n*=4) and the diameters of the cOFT (*n*=2) and Ao (14.5dpc *n*=3 and 17.5dpc *n*=2) were evaluated from B-mode echo-loops in order to calculate the mean stroke volume (SV) per developmental stage according to the following formula: mean SV=mean TVI x (mean diameter of Ao or cOFT/2)^2 x π. Hence, the mean cardiac output (CO) was calculated (mean CO=mean SV x mean HR) for the three developmental stages.

M-mode measurements

For morphological assessment M-mode measurements in short or a long-axis views of the ventricles were performed, to evaluate the end-systolic and end-diastolic ventricular inner diameter of the LV (LVID;12.5dpc *n*=9, 14.5dpc *n*=11 and 17.5dpc *n*=14) and RV (RVID;12.5dpc *n*=9, 14.5dpc *n*=10 and 17.5dpc *n*=12) and IVS diameter (12.5dpc *n*=4, 14.5dpc *n*=6 and 17.5dpc *n*=9). Cardiac fractional shortening (FS%) for the LV and RV were calculated using the formula: (VIDdiastole–VIDsystole)/VIDdiastole x 100%. Due to the size of the hearts at 12.5dpc, the resolution often limited the possibility to discriminate the epicardial, myocardial and endocardial layer of the ventricular free wall. Therefore, at this stage the distances from the epicardial layer to the IVS in end-systole and end-diastole were used to calculate the FS%.

Although a complete hemodynamic and morphological assessment for each heart was aimed for (Table 2 for overview), imaging possibilities were regularly limited by the position of the embryo/fetus. All echocardiographic recordings were stored for off-line data analysis by NDH and EEC, inter-observed analysis demonstrated a high level of consistency (*r*=0.8-1.0;*P*<0.05). Flow parameters were calculated by the average of pulsed-wave Doppler complexes of three consecutive beats, similar methods were applied for M-mode recordings and diameter calculations on B-mode echo-loops.

Figure 1. Development of left ventricular inflow patterns.

(a) Shows an example of a pulsed-wave Doppler recording across the MV at 17.5dpc. (a') Indicates the magnification of the boxed area in (a) in which the individual time intervals are indicated i.e. RR, DFT, IVCT, ET and IVRT. (b) Through (e) indicates the course of the DFT, ET, IVCT and IVRT respectively, throughout embryonic/fetal life. All values in (b-e) are expressed as percentage of the RR.

Table 2. Summary of the assessment of embryonic and fetal hearts.

Method	Parameter	Unit	Structure (abbreviation) / Definition	Formula
2D ultrasound B-mode echo loops	Morphological assessment position and diameters of cardiac compartments.	mm	right atrium (RA), left atrium (LA), right ventricle (RV), left ventricle (LV), common outflow tract (cOFT), pulmonary trunk (PT), aorta (Ao), inter ventricular septum (IVS), common atrioventricular canal (cAVC), mitral valve (MV), tricuspid valve (TV)	
	Peak-E	m/s	early, diastolic ventricular filling	
	Peak-A	m/s	active, diastolic ventricular filling	
	E/A-ratio		Peak-E / Peak-A	
	RR interval	ms	cycle length/ evaluation of heart rate	
	DFT	ms	diastolic filling time	
	IVRT	ms	isovolumetric relaxation time	
Pulsed-wave Doppler	IVCT	ms	isovolumetric contraction time	
	ET	ms	ejection time	
	MPI/Tei index		myocardial performance index	IVRT + IVCT / ET
	Peak velocities cOFT, Ao, PT	m/s		
	VTI	mm	velocity time integral	
	SV	mm	stroke volume	TVI x (Ao or cOFT diameter/2)^2 x π
	CO	ml/min	cardiac output	
	VID	mm	ventricular inner diameter	
	LVIDd	mm	end diastolic left ventricular inner diameter	
	LVIDs	mm	end systolic left ventricular inner diameter	
	RVIDd	mm	end diastolic right ventricular inner diameter	
M-mode	RVIDs	mm	end systolic right ventricular inner diameter	
	IVSd	mm	end diastolic interventricular septum diameter	
	IVSs	mm	end systolic interventricular septum diameter	
	FS	%	fractional shortening	(VIDd-VIDs)/VIDd x 100%

Table 3. The parameters used for calculation of the mean CO per gestational age.

Parameter	12.5 dpc (cOFT)	14.5 dpc (Ao)	17.5 dpc (Ao)
VTI (mm)	33.9±1.37	42.3±2.0	29.2±2.05
Mean diameter (mm)	0.23	0.18	0.48±0.03
Mean HR (bpm)	134±11.2	148±6.1	206±9.8
Mean CO (mL/min)	0.19	0.16	0.96

Cardiac morphology and three-dimensional reconstructions

After the experiments, the pregnant mouse was sacrificed by cervical dislocation and embryos/fetuses were extracted. We refer to previous publications for details regarding embryonic/fetal processing, sectioning, immunohistochemistry with MLC2a specific antibodies and preparation of the three-dimensional AMIRA reconstructions (AMIRA software package, Template Graphics Software, San Diego, USA) [15].

Statistics

All statistics were performed with the statistical package for the social sciences 15.0 (SPSS Inc, Chicago Ill, USA) and GraphPad Prism (GraphPad Software, La Jolla CA, USA). A *P*<0.05 (2-tailed) was considered to be significant, all values are given as mean±SEM. All boxplots indicate the upper and lower quartile of the median, which is indicated by the horizontal bar. The whiskers indicate max/min range of the values.

RESULTS

Cardiac morphology

Reliable imaging of hearts as small as 2 mm was feasible in all stages examined. Representative examples are shown in online Movie 1 (available online at http://dx.doi.org/10.1155/2014/531324.) At embryonic stages (12.5dpc) ventricular septation has been initiated but is not completed resulting in a primitive inter-ventricular foramen that directly connects the lumen of LV and RV. M-mode recordings at these stages show a mean systolic IVS diameter of 0.20±0.045mm. Figure 2a shows a reconstruction of a 12.5dpc embryonic heart, in which the lumen of the four cardiac chambers, inter-ventricular foramen and the OFT can be identified. The atrial and ventricular chambers are connected via the cAVC that harbors large AV cushions, which will contribute to formation of the MV and TV. The AV canal is still partly positioned above the LV at this stage. The developing OFT is still positioned completely above the RV and contains cushion tissue that will form the semilunar valves of the Ao and PT. They will further form the basis for the muscular subpulmonary infundibulum and will contribute to the membranous part of the IVS. Consequently, the blood from the LV runs via the primitive inter-ventricular foramen into the cOFT i.e. future Ao and PT.

2.3

Figure 2. Cardiac morphology and shortening fraction calculation.
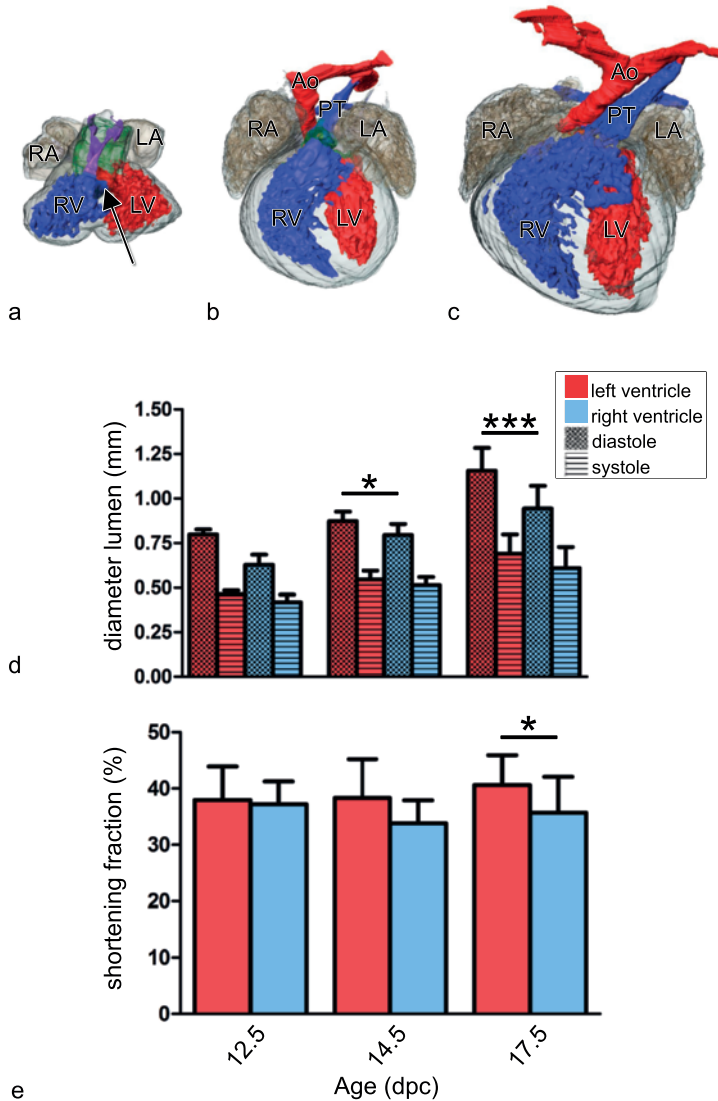
(a) Shows a reconstruction of anterior view of an embryonic heart of 12.5dpc. The myocardium is indicated in grey transparent. The LA and RA are indicated in transparent dark grey. The left ventricular (LV) and right ventricular (RV) lumen are indicated in red and blue, respectively. Note that the outflow tract lumen (purple) is positioned completely above the future RV, which is surrounded by large outflow tract cushions (green transparent). At these stages development of the interventricular septum (IVS) has not yet completed leading to a direct connection between the LV and RV via the inter-ventricular foramen (arrow). (b) Anterior view of an early fetal heart of 14.5dpc. At this stage IVS development has completed and four separate cardiac chambers can be identified. The outflow tract consists of a separate aorta (Ao) and pulmonary trunk (PT) including their valve apparatus, which at these stages mainly consist of cushion tissue (green transparent). (c) Anterior view of a late fetal heart of 17.5dpc. At this stage the heart shows a mature morphological phenotype. (d) Schematic representation of LV and RV diameters and (e) shortening fraction at the three consecutive stages of development. RA = right atrium. LA = left atrium.

Figure 3. Development of left ventricle and right ventricle inflow patterns.
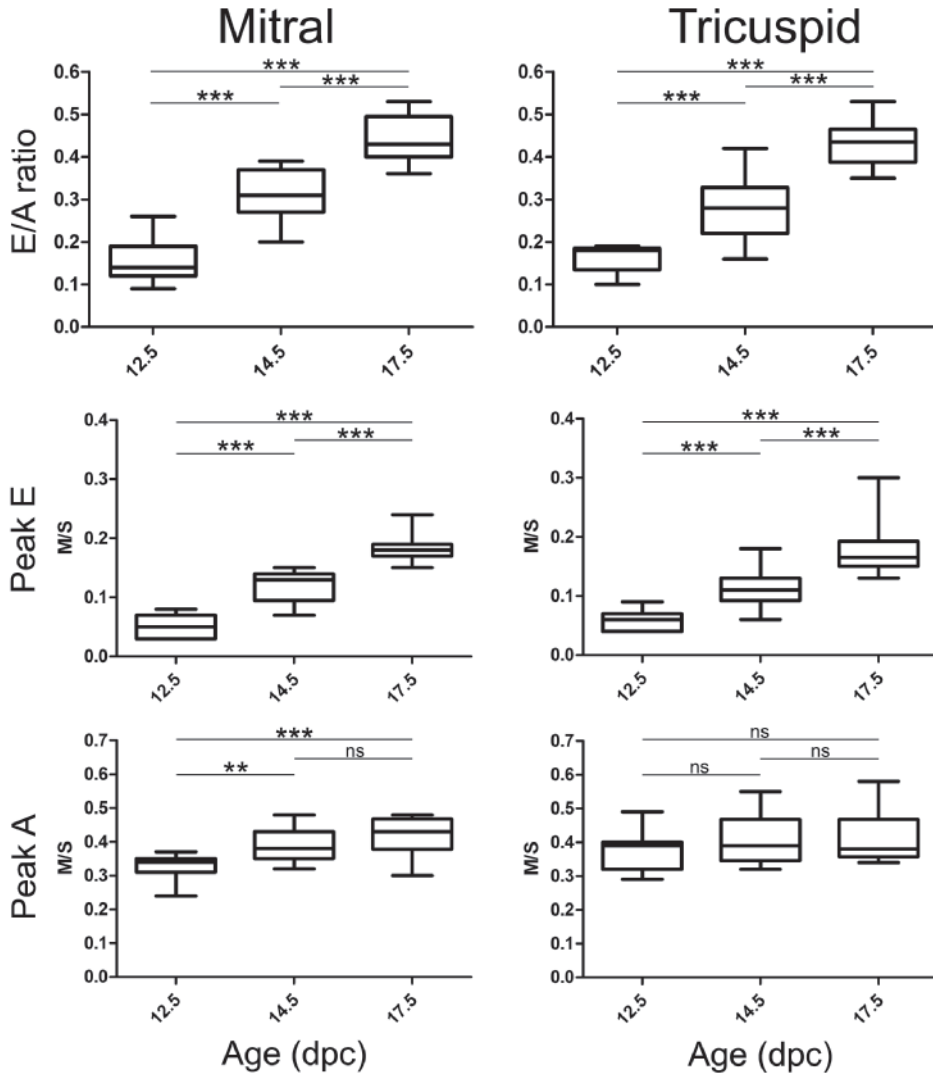
The graphs represent the course of the E/A-ratio (a,b), Peak-E wave (c,d) and Peak-A wave (e,f) across the developing mitral valve and tricuspid valve at the three subsequent developmental stages.

At early fetal stages 14.5dpc the heart has increased in size (Figure 2b) and ventricular septation is now complete. The systolic diameter of the IVS has increased (0.24±0.018mm). In the AVC the TV orifice has expanded and is now situated entirely above the RV. Also the MV orifice can be identified as well as the developing AV valves. The cardiac OFT now consists of a separate Ao and PT connecting to the LV and RV, respectively. The Ao and pulmonary valves still show immaturity and consist of cushion tissue.
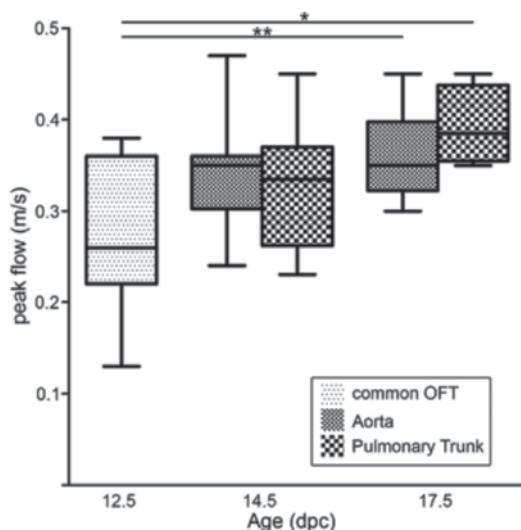
Figure 4. Pulsed wave Doppler flow measurements.

Pulsed wave Doppler flow measurements in the common outflow tract (OFT), Aorta and Pulmonary Trunk. The graph demonstrates the significant increase of the peak blood flow measured in the cOFT at 12.5 and Aorta and Pulmonary trunk at 14.5 and 17.5dpc.

At late fetal stages (17.5dpc) the size of the RV and LV and IVS (0.39±0.009mm) has increased significantly (Figure 2c). Mature valves are present at the levels of the in- and outflow part of both ventricles.

Diastolic and Systolic function

During embryonic and fetal development the HR increases significantly ($P<0.0001$) from 125±9.5 up to 219±8.3BPM. Ventricular inflow patterns across the developing MV and TV annulus were studied by pulsed-wave Doppler imaging. The DFT corrected for the RR-interval (DFT/RR) did not differ significantly at the three stages assessed (Figure 1b). LV and RV filling was dominated by the peak-A wave. Between 12.5 and 17.5dpc the peak-A wave of the developing MV annulus increased significantly (0.33±0.001m/s vs 0.42±0.014m/s;$P<0.0001$) whereas that of the TV also showed an increasing trend, albeit not significant (0.37±0.018m/s vs 0.41±0.019m/s;P=NS). The peak-E wave also increased significantly for both the LV (0.05±0.006m/s vs 0.18±0.005m/s;P=<0.0001) and RV (0.06±0.006m/s vs 0.18±0.012m/s;P=<0.0001), and showed a relatively greater increase than the peak-A wave during development. As a resultant, the E/A-ratio, a measure for the ventricular diastolic function, showed a significant increase for both the LV (0.16±0.015 vs 0.44±0.013;P=<0.0001) and RV (0.16±0.010 vs 0.44±0.014;P=<0.0001) (Figure 3a-f).

The IVRT, one of the measures for diastolic LV function, corrected for the RR-interval (IVRT/RR) demonstrated a significant (P=0.037) decrease between 12.5 (0.15±0.011) and 14.5dpc (0.12±0.004), and remained stable at later fetal stages 17.5dpc (0.12±0.003) (Figure 1e), indicating that LV myocardial relaxation remains stable after completion of IVS development during fetal life.

The systolic function of the developing ventricles was assessed through studying the course of the FS%, IVCT/RR and ET/RR. Throughout embryonic and fetal development the FS% remained constant for both ventricles and values ranged between ≈30-40%. Furthermore, except for 17.5dpc (LV: 40.6%, RV 35.7%;P=0.046) no significant differences were observed between the FS% of the LV and RV (Figure 2d,e). The mean IVCT/RR remained stable during all three stages ≈0.09%, the ET/RR showed no changes between 12.5dpc (0.42±0.015) and 14.5dpc (0.43±0.010) but significantly decreased at 17.5dpc (0.40±0.006;P=0.017) (Figure 1c,d).

A combined assessment of LV systolic and diastolic function was performed by calculating the MPI. At embryonic pre-septated stages (12.5dpc), the MPI was 0.64±0.012 and decreased to 0.49±0.017 (P=0.0002) after closure of the IVS at 14.5dpc. At late fetal stages (17.5dpc) the MPI did not change significantly (0.53±0.022;P=NS).

2.3

Outflow tract and Cardiac output

The pulsed-wave Doppler recordings performed in the cOFT demonstrated a peak-flow of 0.27±0.021m/s at pre-septated stages. As from 14.5dpc two individual ventricular outflow tracts could be discriminated, especially the high echo-density of the blood at these stages enabled to discriminate the flow in the Ao (0.34±0.013m/s) and PT (0.33±0.021m/s) that are closely related to each other. As can be observed in Figure 4, the peak flow increased significantly in the Ao (from 0.27±0.021m/s to 0.36±0.016m/s;P=0.010) and PT (0.27±0.021m/s to 0.44±0.030m/s;P=0.003) along fetal life.

Table 3 summarizes the HR, VTI and the diameters of the cOFT and Ao that were used to calculate the mean CO at the three developmental stages. Between 12.5 and 14.5dpc the CO remained stable, where after it increased to 0.96ml/min at 17.5dpc.

DISCUSSION

Heart development is a complex process, which has been extensively studied in both WT and genetically mutated mouse models [3]. It is only in the last decades that modern imaging techniques like ultrasound enable the assessment of real-time hemodynamic and morphological changes that occur during mouse heart development [4-6;8;16-18]. Knowledge regarding these functional parameters is essential since abnormal flow in the developing heart might lead to CHD through aberrant activation of shear-stress responsive genes important in cardiogenesis [9;11]. In early reports describing the course of functional parameters during heart development major variability exists in measured values. This is most likely related to the relatively low ultrasound frequencies of clinical ultrasound machines used to image the small hearts of mouse embryos/fetuses [16], and externalization of uterus horns during ultrasound assessment [18], which influences embryonic/fetal physiology. Isoflurane anesthesia, used in this study, only has a minimal effect on hemodynamics and diastolic function in adult mice and effect on embryos

is supposed to be marginal [6]. In the current study we aimed to provide an overview of hemo-dynamic parameters and changes that occur at subsequent stages of heart development, using a high-frequency ultrasound system.

Compared with other reports in mouse using similar ultrasound techniques we did not only focus on development of the future LV but also on that of the RV. Key findings of our study are: 1. A reliable assessment of LV and RV in- and outflow patterns can be performed from 12.5dpc to term; 2. A significant improvement occurs in the diastolic and systolic function of both LV and RV; 3. Over the developmental period of 12.5dpc to 17.5dpc, the ratio between RV and LV size, as well as the FS% of both ventricles did not change significantly.

Knowledge regarding the functional parameters of the RV is important since the RV is commonly affected in CHD. During development, the RV including the TV annulus develops subsequent to the LV by addition of SHF derived cells to the developing heart [1]. Many genes have been identified that have an important role in the SHF contribution to the developing heart and mutations in these genes may lead to CHD [19].

At early embryonic stages endocardial cushion tissue is positioned in the primitive AVC and OFT, which later on will contribute to formation of the TV and MV and Ao and PT semilunar valves. Some clinical studies argued that AV valve regurgitation is a common phenomenon during the first trimester of pregnancy [20]. Our study, in accordance with several others in mouse [4;6] and human [13] did not show signs of regurgitation at both early and late stages of heart development. Pulsed-wave Doppler recordings across the cAVC at 12.5dpc and MV and TV at 14.5dpc demonstrated that the AV cushions mimic the function of normal AV valves at 17.5dpc. In our opinion especially the flow in the cOFT at early embryonic stages, which is completely positioned above the RV (see Figure 2a) might wrongly be identified as regurgitation of the developing AV valves/cushions. This stresses the importance of detailed knowledge regarding the rapid morphological changes the heart undergoes at especially the very early developmental stages.

Regarding growth of the heart we demonstrated that there was a 31% increase of LVID, 34% of RIVD and 35% of IVS diameter from 12.5 up to17.5dpc. We showed a trend towards a smaller RVID as compared with the LVID at all stages, which was not mentioned in other studies.

Diastolic and systolic function during heart development.

Improvement of ventricular systolic and diastolic function occurs throughout the length of embryonic and fetal development. With respect to the diastolic function we demonstrated a significant increase of E/A-ratio across the developing MV and TV orifices, which was related to an increase of the peak-E wave, i.e. the fraction of diastolic ventricular filling that is defined by ventricular relaxation. These data are in accordance with the study of Zhou and colleagues, who demonstrated that the E/A-ratio is increasing during development, which seems to continue up to approximately 3 weeks after birth [6]. Around day four after birth, the peak-E wave measured across the MV becomes more dominant than the peak-A wave indicating an improvement of

cardiac compliance and that LV filling becomes dominated by passive ventricular relaxation. Remarkably, these changes were not observed for the RV inflow patterns, where the peak-A wave remains dominant [6]. Human embryonic and fetal hearts show the same maturation course of E/A-ratios across the developing MV and TV as was demonstrated in multiple studies [21-25]. An abnormal course of E/A-ratio i.e. a decreasing [25;26] or an increasing trend [27] along development has been related to the presence of CHD.

With respect to systolic ventricular function, the FS% remained stable (≈30-40%) for both ventricles throughout development. We did find a significant difference favoring the LV FS% as compared with the RV FS% at 17.5dpc. Interestingly, the same phenomenon of FS% difference between LV and RV has been reported in a study of human fetal hearts between 14 and 40 weeks of pregnancy . However, as in mouse, differences between human LV and RV FS% is subtle, [28] and whether a decreased or decreasing FS is a predictor of CHD remains unknown. Furthermore, we did not find a decreasing trend of both LV and RV FS as was recently demonstrated during human fetal life [28;29]. With respect to the CO we noticed no change around the proces of ventricular septation (between 12.5 and 14.5 dpc), where after a major increase occured to 0.96mL/min near term (17.5 dpc). The initial CO decrease might be related to the fact that the mean diameter of the unseptated cOFT diameter was used at 12.5dpc compared with the isolated Ao diameter at 14.5dpc. The subsequent CO increase is mostly related to the dramatic increase of HR along fetal life.

The MPI or Tei-index [14] is a measure for combined systolic and diastolic cardiac function and can be calculated for both ventricles. In order to assess the MPI three different time intervals are needed, the IVCT, IVRT and ET. For the LV these parameters can be easily obtained, since all three parameters can be assessed at once by placing the Doppler ultrasound beam across the developing MV orifice. Noticeably, in literature there is less data regarding RV MPI and its course along development, which might be related to the fact that for the RV not all three time intervals can be assessed in one view as was also suggested in a recent review by Godfrey et al [14]. The current study demonstrated a significant decrease of LV MPI between 12.5 and 14.5dpc, which might be related to the rapid morphological changes the heart goes through including completion of IVS leading to altered hemodynamic conditions in the developing heart. It is however also important to notice that at pre-septation stages not always the IVCT and IVRT can be identified separately so that calculation of the MPI is frequently not possible at very early stages of embryonic development. Between 14.5 and 17.5dpc we noticed a slight increase of the MPI suggesting that cardiac function improves at subsequent fetal stages; similar results have also been demonstrated in mouse [4] and human [30]. However, discussion remains regarding the exact course of the MPI, IVCT, IVRT and ET and whether isolated changes of one of the factors is a predictor for fetal demise and CHD. Interestingly with respect to IVRT% we observed a decreasing trend near completion of the IVS (between 12.5 and 14.5) whereafter it more or less remained stable throughout fetal life. A similar course was observed in a recent ultrasound study

2.3

in embryonic/fetal C57Bl6 mice [4]. Human embryos also showed a decreasing course of the IVRT% [13;21], and an elevated IVRT% has been implicated as a predictor of CHD [13].

CONCLUSION

We demonstrated the course of several morphologic and hemodynamic parameters along embryonic and fetal life. Our data show that a reliable assessment can be made not only of the left, but also of right ventricular function during embryonic/fetal stages. We demonstrate an overall improvement of cardiac diastolic and systolic function of both LV and RV along heart development. The implementation of high-frequency ultrasound in embryonic/fetal mouse heart development is a promising and useful tool. The data presented in this study might be useful as reference values in future studies in genetic mutated mouse models of CHD.

REFERENCES

1. R. G. Kelly, Molecular inroads into the anterior heart field, Trends in CardiovascularMedicine, 2005;15,51–56.

2. J. I. E. Hoffman, S. Kaplan, The incidence of congenital heart disease, Journal of theAmericanCollege of Cardiology, 2002;39:890–1900.

3. D. Srivastava, Genetic assembly of the heart: implications for congenital heart disease, Annual Review of Physiology, 2001;63;451–469.

4. N. Corrigan, D. P. Brazil, F. M. Auliffe, High-frequency ultrasound assessment of the murine heart from embryo through to juvenile, Reproductive Sciences, 2010;17:147–157.

5. C. F. Spurney, C.W. Lo, L. Leatherbury, Fetal mouse imaging using echocardiography: a review of current technology, Echocardiography, 2006;23:891–899.

6. Y.Q. Zhou, F. S. Foster, R. Parkes, et al, Developmental changes in left and right ventricular diastolic filling patterns in mice, American Journal of Physiology, 2003;285:H1563–H1575.

7. Q. Yu, L. Leatherbury, X. Tian, et al., Cardiovascular assessment of fetal mice by in utero echocardiography, Ultrasound in Medicine and Biology, 2008;34:741–752.

8. C. K. L. Phoon, Imaging tools for the developmental biologist:ultrasound biomicroscopy of mouse embryonic development, Pediatric Research, 2006;60:14–21.

9. J. S. Lee, Q. Yu, J. T. Shin et al., Klf2 is an essential regulator of vascular hemodynamic forces in vivo, Developmental Cell, 2006;11:845–857.

10. R. A. Morris, B. Damon, V. Mironov et al., Periostin regulates collagen fibrillogenesis and the biomechanical properties of connective tissues, Journal of Cellular Biochemistry, 2007;101:695–711.

11. B. C.W. Groenendijk, B. P. Hierck, J. Vrolijk et al., Changes in shear stress-related gene expression after experimentally altered venous return in the chicken embryo, Circulation Research, 2005;96:1291–1298.

12. C. J. Zuurbier, V. M. Emons, C. Ince, Hemodynamics of anesthetized ventilated mouse models: aspects of anesthetics, fluid suort, and strain, American Journal of Physiology, 2002;282:H2099–H2105.

13. A.Włoch,W. Rozmus-Warcholinska, B. Czuba et al., Doler study of the embryonic heart in normal pregnant women, Journal of Maternal-Fetal and Neonatal Medicine, 2007;20:533–539.

14. M. E. Godfrey, B. Messing, S. M. Cohen, et al., Functional assessment of the fetal heart: a review, Ultrasound in Obstetrics and Gynecology, 2012;39:131–144.

15. M. R. M. Jongbloed, M. C. E. F. Wijffels, M. J. Schalij et al., Development of the right ventricular inflow tract and moderator band: a possible morphological and functional explanation for Mahaim tachycardia, Circulation Research, 2005;96:776–783.

16. Y.-H.Gui, K. K. Linask, P z.Khowsathit, et al., Doppler echocardiography of normal and abnormal embryonic mouse heart, Pediatric Research, 1996;40:633–642.

17. C. F. Spurney, L. Leatherbury, C. W. Lo, High-frequency ultrasound database profiling growth, development, and cardiovascular function in C57BL/6J mouse fetuses, Journal of the American Society of Echocardiography, 2004;17:893–900.

18. R. P. Ji, C. K. L. Phoon, O. Aristizabal, et al., Onset of cardiac function during early mouse embryogenesis coincides with entry of primitive erythroblasts into the embryo proper, Circulation Research, 2003;92:133–135.

19. M. R. Jongbloed, S. R. Vicente, N. D. Hahurij et al., Normal and abnormal development of the cardiac conduction system, implications for conduction and rhythm disorders in the child and adult, Differentiation, 2012;84:131–148.

20. K.Makikallio, P. Jouila, J. Rasanen, Human fetal cardiac function during the first trimester of pregnancy, Heart, 2005;91:334–338.

21. W. Rozmus-Warcholinska, A. Wloch, G. Acharya et al., Reference values for variables of fetal cardiocirculatory dynamics at 11-14 weeks of gestation, Ultrasound in Obstetrics and Gynecology, 2010;35:540–547.

22. G. Tulzer, P. Khowsathit, S. Gudmundsson et al., Diastolic function of the fetal heart during second

and third trimester: a prospective longitudinal Doppler-echocardiographic study, European Journal of Pediatrics, 1994;153:151–154.

23. M.C.Leiva, J.E.Tolosa, C. N. Binotto et al., Fetal cardiac development and hemodynamics in the first trimester, Ultrasound in Obstetrics and Gynecology, 1999;14:169–174.

24. I. P. Van Splunder, J. W. Wladimiroff, Cardiac functional changes in the human fetus in the late first and early second trimesters, Ultrasound in Obstetrics and Gynecology, 1996;7:411–415.

25. S. A. Clur, R. K. Oude, B. W. Mol, et al., Fetal cardiac function between 11 and 35 weeks' gestation and nuchal translucency thickness, Ultrasound in Obstetrics and Gynecology, 2011;37:48–56.

26. G. Rizzo, A. Muscatello, E. Angelini, et al. Abnormal cardiac function in fetuses with increased nuchal translucency. Ultrasound in obstetrics and gynecology. 2003;21:539-542.

27. F. Crispi, E. Hernandez-Andrade, M. M. A. L. Pelsers et al., Cardiac dysfunction and cell damage across clinical stages of severity in growth-restricted fetuses, American Journal of Obstetrics and Gynecology, 2008;199:254–258.

28. S. Luewan, Y. Yanase, F. Tongprasert, et al., Fetal cardiac dimensions at 14-40 weeks' gestation obtained using cardio-STIC-M, Ultrasound in Obstetrics and Gynecology, 2011;37:416–422.

29. T. Tongsong, C. Wanapirak, W. Piyamongkol et al., Fetal ventricular shortening fraction in hydrops fetalis, Obstetrics and Gynecology, 2011;117:84–91.

30. E. Hernandez-Andrade, H. Figueroa-Diesel, C. Kottman et al., Gestational-age-adjusted reference values for the modified myocardial performance index for evaluation of fetal left cardiac function, Ultrasound in Obstetrics and Gynecology, 2007;29:321–325.

Chapter 2.4

Abnormal sinoatrial node development resulting from disturbed Vascular Endothelial Growth Factor signaling

Emmeline E. Calkoen, Rebecca Vicente-Steijn*, Nathan D. Hahurij *,
Conny van Munsteren, Arno A.W. Roest, Marco C. DeRuiter, Paul Steendijk,
Martin J. Schalij, Adriana C. Gittenberger de Groot,
Nico A. Blom and Monique R.M. Jongbloed.
* Equal contributions

ABSTRACT

Background

Sinus node dysfunction is frequently observed in patients with congenital heart disease (CHD). Variants in the Vascular Endothelial Growth Factor-A (VEGF) pathway are associated with CHD. In Vegf$^{120/120}$ mice, overexpressing VEGF$_{120}$, a reduced sinoatrial node (SAN) volume was suggested. Aim of the study is to assess the effect of VEGF over-expression on SAN development and function.

Methods

Heart rate was measured in Vegf$^{120/120}$ and wildtype (WT) embryos during high frequency ultrasound studies at embryonic day (E)12.5, 14.5 and 17.5 and by optical mapping at E12.5. Morphology was studied with several antibodies. SAN volume estimations were performed, and qualitative-PCR was used to quantify expression of genes in SAN tissues of WT and Vegf$^{120/120}$ embryos.

Results

Heart rate was reduced in Vegf$^{120/120}$ compared with WT embryos during embryonic echocardiography (52 ± 17 versus 125 ± 31 beats per minute (bpm) at E12.5, $p < 0.001$; 123 ± 37 vs 160 ± 29 bmp at E14.5, $p=0.024$; and 177 ± 30 vs 217 ± 34 bmp, at E17.5 $p=0.017$) and optical mapping (81 ± 5 vs 116 ± 8 bpm at E12.5; $p=0.003$). The SAN of mutant embryos was smaller and more vascularized, and showed increased expression of the fast conducting gap junction protein, Connexin43.

Conclusions

Over-expression of VEGF$_{120}$ results in reduced heart rate and a smaller, less compact and hyper-vascularized SAN with increased expression of Connexin43. This indicates that VEGF is necessary for normal SAN development and function.

ABBREVIATIONS

CX	Connexin
DFT	Diastolic filling time
ET	Ejection Time
HCN	Hyperpolarization-activated cyclic nucleotide-gated channel
ISL-1	Insulin gene enhancer protein
IVCT	Isovolemetric Contraction Time
IVRT	Isovolemetric Relaxation Time

MPI	Myocardial performance index
NKX2.5	Homeobox protein 2.5
PDGFR-alfa	Platelet-derived growth factor receptor- alfa
SAN	Sinoatrial node
SSS	Sick sinus syndrome
TBX	T-box transcription factor
SHOX2	Short stature homeobox 2
VEGF	Vascular endothelial growth factor

2.4

INTRODUCTION

Sinus node (SAN) dysfunction, or sick sinus syndrome (SSS), can cause sudden cardiac death and is a frequent cause of pacemaker implantations [1]. SSS increases with age, but can be present in newborns and young patients in association with congenital heart disease (CHD) [2, 3]. The mechanism of SSS is not always surgery related and can be detected already in embryonic life in many CHD patients [4].

The SAN develops from the fifth week of development in humans (around embryonic day (E) 10.5 in mouse) from the sinus venosus myocardium, which expresses many genes including *TBX18*, *TBX3*, *SHOX2*, *HCN4*, *ISL-1* and *PDGFR-alpha* [5]. The mature SAN consists of a head and tail and is vascularized by a SAN artery, in 65% of the cases arising from the right coronary artery, in 22% from the circumflex branch of the left coronary artery, and from both arteries in 10% [1].

In humans, genetic variants in the Vascular Endothelial Growth Factor-A (*VEGF-A* or *VEGF*) pathway have been associated with CHD like persistent truncus arteriosus [6], tetralogy of Fallot [7] and atrioventricular septal defects (AVSD) [8].

$VEGF_{121}$, $VEGF_{165}$ and $VEGF_{189}$ are the three main isoforms of VEGF in humans, represented by $Vegf_{120}$, $Vegf_{164}$ and $Vegf_{188}$ in mouse. Mutant $Vegf^{120/120}$ mouse embryos over-express $VEGF_{120}$ and do not express $VEGF_{164}$ and $VEGF_{188}$ [9], causing a local increase of VEGF and NOTCH expression [10]. Previous studies in the $Vegf^{120/120}$ mouse focused on abnormalities of the outflow tract and coronary arteries [10, 11]. Compared with studies in humans with VEGF mutations [8], there are no studies in mouse describing the abnormalities of the inflow tract of the heart comprising the sinus venosus, pulmonary and cardinal veins (putative superior caval vein and coronary sinus), atria, and atrioventricular connection. Interestingly, $Vegf^{120/120}$ mice have a reduced heart rate [9]. Moreover, the SAN was suggested to be hypoplastic in $Vegf^{120/120}$ embryos, this was however not investigated in detail [12] and no data are available on the cardiac function of $Vegf^{120/120}$ embryos. Furthermore, in-vitro studies revealed that VEGF can increase the expression of the gap junction protein, Connexin43 (CX43), thereby altering the conduction properties of the cardiac muscle [13, 14]. Additionally, Notch, which can be stimulated by VEGF through activation of VEGFR2, is suggested to keep cardiomyocyte precursors in a primitive state and promotes the expressions of NKX2.5 and HCN1 [15, 16].

New techniques, such as embryonic echocardiography [17, 18] and optical mapping [19] allow the assessment of cardiac function and hemodynamic consequences as early as E12.5 in mouse embryos [18]. In the current study, these techniques were used to establish the role of the VEGF signaling pathway on SAN and inflow tract development and function in the $Vegf^{120/120}$ mouse model.

METHODS

All experiments were approved by the local animal welfare committee (DEC no: 10177) of the Leiden University Medical Center and performed according to institutional guidelines. SAN function and cardiac development were studied in wildtype (WT) and $Vegf^{120/120}$ embryos. Heart rate and hemodynamic parameters were assessed at E12.5, E14.5 and E17.5 with high frequency ultrasound, enabling the study of the heart in vivo, thus reducing the effect of autonomic denervation. Heart rate was additionally analyzed with ex vivo optical mapping at E12.5, during which no Isoflurane anesthesia was used. SAN morphology (E12.5 till E17.5) was studied and volume estimations (E12.5 and E17.5) were performed. The expression profiles of genes in the SAN were studied with q-PCR in the samples of E17.5 collected with lasercapture microdissection.

2.4

Generation of $Vegf^{120/120}$ embryos

A routine breeding program was performed with mice heterozygous for the 120-isoform of the $Vegf$ gene ($Vegf^{+/120}$) kindly received form Professor Carmeliet [9], more than 10 times backcrossed. This resulted in WT ($Vegf^{+/+}$), heterozygous ($Vegf^{+/120}$) and mutant embryos with the over-expression of the Vegf 120-isoform ($Vegf^{120/120}$) and no expression of $Vegf_{164}$ and $Vegf_{188}$ as described previously [10]. The day after the breeding was considered E0.5.

Ultrasound recording protocol

Ultrasound recordings were performed using the Vevo770 ultrasound system (VisualSonics, Toronto, Canada), with a 40 MHz transducer. The embryos were studied longitudinally at E14.5 and 17.5. The ultrasound examination at E12.5 was performed separately in pregnant mice as examination at this stage resulted in embryonic mortality at E17.5. In order to trace back an individual embryo at subsequent stages (E14.5 and E17.5) of development the maternal bladder was used as reference point. The first embryos positioned next to the left and right sides of the bladder were assessed.

The ultrasound protocol was performed as described previously [18]. In short, Pregnant $Vegf^{+/120}$ mice were anesthetized with 1.5% Isoflurane (induction with 5% Isoflurane) via a cone-shaped nose mask. During the experiments maternal vital signs were monitored continuously. Echodoppler recordings over the atrioventricular valves of the embryos were performed to evaluate fetal heart rates (Figure 1A). Additionally, functional data were derived on passive or early filling (E-peak), atrial contraction or late filling (A-peak), diastolic filling time (DFT), isovolumetric contraction time (IVCT), ejection time (ET) and isovolumetric relaxation time (IVRT). Myocardial performance index (MPI) was calculated as (IVRT + IVCT)/ET.

Ultrasound assessments were completed <30 min to limit a possible negative effect of Isoflurane on the function of the embryonic heart. Following the ultrasound experiment of E12.5 or E17.5 the pregnant mouse was sacrificed by cervical dislocation and the embryos were harvested.

Offline analyses of the echocardiographic recordings were performed blindly using Visual Sonics analytical software. The ultrasound measurements were performed in 28 WT embryos (E12.5: N = 11, E14.5 = 15, E17.5 = 12) and 14 $Vegf^{120/120}$ embryos (E12.5 N=4, E14.5 = 6, E17.5 = 7). WT embryos in this study were also included in the previously published reference series [18]. Heterozygous embryos did not show differences compared with WT in morphology or echocardiographic parameters and were therefore excluded from further analysis.

Optical mapping

Optical mapping was performed at E12.5. To exclude any effect of anesthesia, optical mapping was also performed in a series of embryos that did not undergo previous anaesthesia during echocardiography (WT N=8 and $Vegf^{120/120}$, N=7). Prior to optical mapping, embryos were decapitated and the thoracic region containing the heart was stained with the voltage sensitive dye di-4-ANNEPS for 5 min in Tyrode solution as described previously [20, 21]. Briefly, hearts were allowed to equilibrate in warm (37 ±0.5°C) oxygenated Tyrode solution before mapping using the Ultima-L mapping setup (SciMedia, Costa Mesa, CA, USA). Analysis of the recordings was performed using the BV-Analyzer software (Brain Vision). The time point of the maximum upstroke velocity determined the activation time points, which were defined as dF/dt$_{MAX}$. The initial atrial activation point was determined by analyzing the total activation pattern of the atria and determining the location of the first atrial signal. The same was done for the ventricular activation pattern. The RR-interval was calculated as the time in milliseconds (ms) between two initial atrial activation points (Figure 1B). With this interval, heart rate in beats per minute (bpm) was calculated. Atrioventricular (AV) conduction time was determined by subtracting the first activation time point in the atria from the same point in the ventricles and then subtracting the total atrial activation time.

## Harvesting of Vegf$^{120/120}$ embryos

After fetal ultrasound and optical mapping, embryos were harvested and their tails collected for routine genotyping procedures as described previously [10]. Thoraxes were fixed in 4% paraformaldehyde phosphate (PFA) buffer pH7.4 for 24-48 h, after which they were stored in 70% alcohol and embedded in paraffin, followed by the preparation of 5 μm sections for immunohistochemistry and 10 μm sections for lasercapture and quantitative real time-polymerase chain reaction (qPCR) analysis

Immunohistochemistry

Routine immunohistochemical staining procedures were performed as described previously [22] using antibodies against Troponin-I, isoform 2 (TNNI2) (1/800, SC-15368, Santa Cruz Biotechnology Inc., Dallas, USA) and NKX2.5 (1/4000, SC-12514 Santa Cruz Biotechnology Inc., Dallas, USA) to study myocardial contributions; HCN4 (1/1000,APC-052 , Alomone Labs, Jerusalem, Israel) the highest expressed sodium/potassium channel in the SAN [23]; the gap junction

channels Connexin40 (1/100, SC-20466, Santa Cruz Biotechnology Inc., Dallas, USA), Connexin43 (1/250, C-6219, Sigma-Aldrich Chemie) and Connexion45 (1/250, SC-7676, Biotechnology Inc., Dallas USA); the autonomic nerve markers Tyroxin Hydroxylase (1/500, PA-14679, Fisher Emergo BV, Landsmeer, The Netherlands) and Ncam (1/8000, AB-5032, Chemicon, Temecula, USA); the endothelial marker Pecam-1/CD31 (1/4000, Sc-1506-R, Santa Cruz Biotechnology Inc., Dallas, USA). The secondary antibodies used were either 1/200 goat anti-rabbit biotin (BA-1000, Vector Laboratories, Burlingame, USA) and 1/66 goat serum (S1000, Vector Laboratories, Burlingame, USA) in PBS-Tween-20 or 1/200 horse anti-goat biotin (BA-9500, Vector Laboratories, Burlingame, USA), and 1/66 horse serum (S-2000, Vector Laboratories, Burlingame, USA) in PBS-Tween-20. For immunofluorescent stainings, Alexa Fluor 488 Donkey Anti-Rabbit IgG (1/200, A-21206, Invitrogen, Molecular Probes, Eugene, USA, A-21206) and Alexa Fluor 555 Donkey Anti-Goat IgG (1/200, A-21432, Life technologies Carlsbad, California, USA, A-21432) were used. To amplify non-fluorescent stainings ABC-reagent (PK-6100, Vector Laboratories, Brunschwig Chemie) was used

2.4

Figure 1. Lower heart rate in Vegf$^{120/120}$ compared with Wild type embryos.
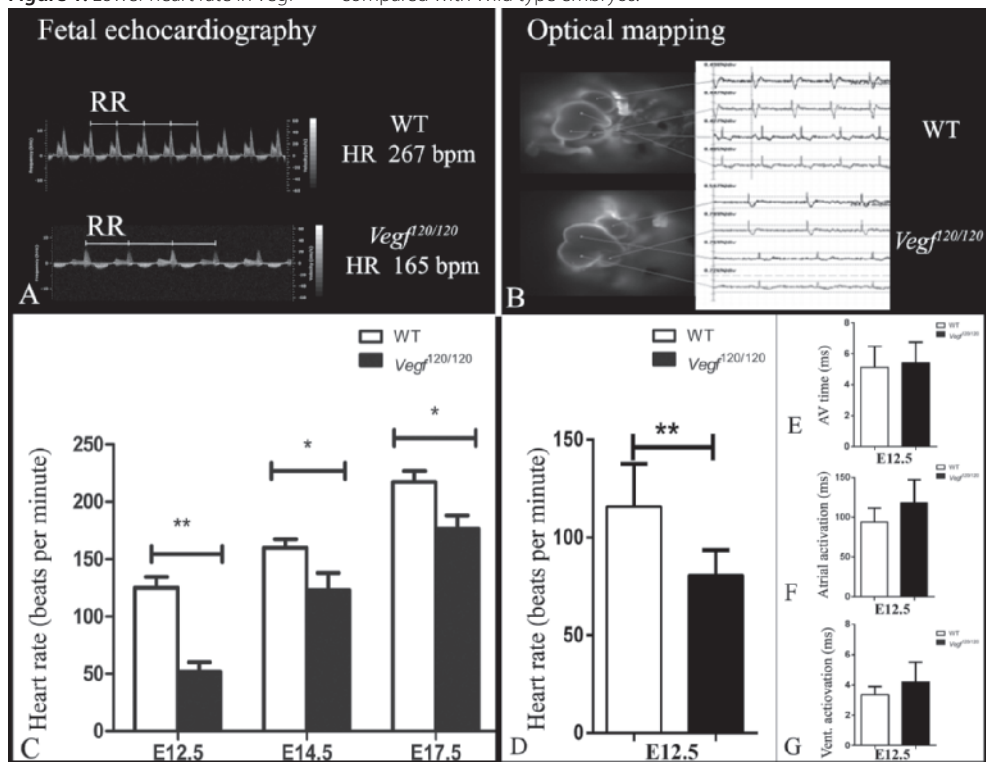
Blindly analyzed measurements of fetal echocardiography (A) and optical mapping (B). A significantly lower heart rate was observed in Vegf$^{120/120}$ compared with wild type (WT) embryos with echocardiography at E12.5, E14.5 and E17.5 (C). Optical mapping analysis at E12.5 confirmed the lower heart rate (D), with a trend towards a longer atrio-ventricular (AV) time (E) and no difference in atrial (F) and ventricular (Vent.) activation times (G). MS = milliseconds.

and for visualization, 3-3'di-aminobenzidin tetrahydrochloride (DAB, Sigma-Aldrich Chemie, USA) was used. Counterstaining was performed with 0.1% haematoxylin (Merck, Darmstadt, Germany). For fluorescent staining, nuclei were stained with DAPI (1/1000, Life technologies, Carlsbad, California, USA) and the slides were mounted with Prolong gold (Life technologies, Carlsbad, California, USA).

Morphometry of the sinoatrial node

SAN volume estimations were performed in 4 WT and 4 *Vegf120/120* embryos at E12.5 and in 4 WT and 10 *Vegf120/120* embryos at E17.5. Morphometry was based on the Cavelieri's principle as described by Gunderson and Jensen in 1987 [42] and applied in our previous studies [24]. Briefly, regular spaced ($49mm^2$) points were randomly placed on the TNNI2 and HCN4 positive and NKX2.5 negative stained SAN cells. The distance between the subsequent slices was 0.025mm in E12.5 embryos and 0.035mm in E17.5 embryos. Olympus microscope was used with a 400× magnification objective for E12.5 embryos and 200× for E17.5 embryos. To assess a possible effect of VEGF$_{120}$ over-expression on cardiac size and to relate SAN volume changes to myocardial volume changes, the total ventricular myocardial volumes were estimated at E12.5 and E17.5, with distances between the subsequent slices ranging from 0.075mm to 0.150mm, $100mm^2$ points and a 40× magnification objective. The SAN myocardium / ventricular myocardium ratio was calculated to exclude an effect on overall myocardial volume change. Furthermore, the sinus venosus myocardium, i.e. the NKX2.5 negative myocardium [25, 26], was calculated at E12.5, using 0.025mm slice distance, $100mm^2$ points and a 400x magnification.

Lasercapture microdissection and qPCR of sinoatrial node

To study the genetic profile of the SAN, quantitative real time-polymerase chain reaction (qPCR) was performed using the SAN tissue of E17.5 embryos. The material was collected using laser-capture microdissection with a PALM microlaser system (PALM MCB, Bernried, Germany). After fixation for 24 h in 4% PFA and embedding in paraffin, sections of 10μm were cut, mounted on polyethylene naphthalate membrane-coated slides (Zeiss, Gottingen, Germany) and immediately dehydrated with xylene for 10 min. SAN and ventricular tissues were dissected and collected in adhesive caps (Zeiss, Gottingen, Germany). The SAN was defined as the bulging structure at the medial side of the entrance of the cardinal vein into the right atrium, containing a SAN artery (supplemental Figure 1). Six to eight sections with the SAN material of one embryo were collected. RNA was isolated from the tissue using the RecoverAll Total Nucleic Acid Isolation Kit from Ambion (Foster City, California, USA, 1975) according to the manufacturer's protocol. cDNA was synthesized by using the iScript cDNA synthase kit from Biorad (Berkely, California, USA, 170-8891). For internal negative control no Reverse Transcriptase reactions were carried out, all according to protocol. qPCR was performed in 5 WT and 5 mutant samples (*Vegf120/120*) for *Hcn4, Hcn1, Tbx5, Tbx3, Nkx2.5, Vegf, Cx40, Cx43* and *Cx45*, with RT[2] SYBR® Green qPCR Mastermix (330500) using the CFX96 Fast Real-Time PCR System with the use of Bio-Rad CFX Manager 3.1

software. Each reaction was carried out in triplicate for each sample. All samples were processed using a nested qPCR approach. In short, samples underwent a first round of PCR using the first primer set for 15 cycles at 55°C for product-specific pre-amplification. Then, a second round of amplification was carried out using one of the previous primers with a newly designed primer specific for the pre-amplified product. A list of the gene-specific primers used is provided in the data supplementary 2. Relative gene expression was normalized to *Gapdh* to compensate for the differences in the RNA input.

Statistics

The SPSS software program (version 20.0 IBM SPSS, Chicago, Illinois) was used for statistical analysis. Data are presented as mean ± standard deviation. Differences between WT and *Vegf[120/120]* embryos were analyzed with the independent sample *t*-test in case of normal distribution and with the non-parametric Mann-Whitney U-test when data was not normally distributed. A *P*<0.05 was considered to be statistically significant.

2.4

RESULTS

Experiments were aimed to detect differences in function and morphology of the developing cardiac inflow tract including the SAN between WT and *Vegf[120/120]* embryos. Below firstly observations in function and morphology of the SAN in wild type (WT) versus *Vegf[120/120]* embryos are shown. Subsequently other inflow tract abnormalities are described. The main quantitative parameters are presented in Table 1.

Table 1. Quantitative measured parameters (with N) at different stages.

		WT	*Vegf[120/120]*	Significance
Heart rate (bpm) (high frequency ultrasound)	E12.5	125±31 (11)	52±17 (4)	p<0.001
	E14.5	160±29 (15)	123±37 (6)	p=0.024
	E17.5	217±34 (12)	177±30 (7)	p=0.017
Heart rate (bpm) (optical mapping)	E12.5	116±8 (8)	81±5 (7)	p=0.003
SAN volume (mm³) (morphometry)	E12.5	0.0018±0.00017 (4)	0.0011±0.00014 (4)	p=0.029
	E17.5	0.006±0.0008 (4)	0.003±0.0007 (10)	p=0.002

Functional assessment of the sinoatrial node: results obtained from high frequency ultrasound and optical mapping

Heart rate was assessed with high frequency ultrasound during developmental stages. Figure 1C shows that heart rates were lower in *Vegf[120/120]* as compared with WT at all stages examined: E12.5 (52±17 bpm versus 125±31 bpm, p<0.001), E14.5 (123±37 bpm vs 160±29 bmp p=0.024) and E17.5 (177±30 vs 217±34 bmp, p=0.017). No irregular heart rhythms were observed during

echocardiographic studies. As VEGF is involved in the promotion of sympathetic innervation [27], differences in heart rate may be attributed to a disturbed autonomic innervation of the SAN. Based on TH, expressed in the sympathetic nerve system and NCAM, a more general nerve marker no differences between *Vegf120/120* and WT embryos were observed in size and number of the autonomic ganglia as well as the peripheral nerve patterns (Supplementary 3). To further exclude potential autonomic effects and a possible role of Isoflurane anesthesia, optical mapping was performed in ex vivo hearts at E12.5. The decreased heart rate in *Vegf120/120* embryos compared with the WT was confirmed with optical mapping (81±5 bpm vs 116±8 bpm; p=0.003, Figure 1D). No differences in heart rate were observed between embryos that underwent embryonic echocardiography with anesthesia and those that were directly used for optical mapping. Additionally, the measurements showed a tendency towards a prolonged atrioventricular (AV) interval in *Vegf120/120* embryos when compared with WT (119±12 ms vs 94±6 ms; p=0.072) (Figure 1E). Total atrial activation times and patterns were not disturbed in *Vegf120/120* embryos as compared with WT (5.4±0.54 ms vs 5.1±0.48ms; p=0.713, Figure 1F). Total ventricular activation times and patterns were also normal in *Vegf120/120* embryos (4.2±0.53 ms vs 3.4±0.18 ms; p=0.126, Figure 1G).

Morphological analysis of the sinoatrial node: results obtained from histological examination and morphometry

To assess possible causes of the reduced heart rate observed by echocardiography and optical mapping, the morphology of the SAN was studied ex-vivo. Myocardialization of the sinus venosus progresses during development and at E12.5 in WT embryos the myocardial sleeve around the cardinal veins covers nearly (± 90%) of the circumferential wall. There is a large putative right SAN (TNNI2 and HCN4 positive, NKX2.5 negative) at the entrance of the right cardinal vein and also a smaller left SAN at the entrance of the left cardinal vein, as described previously [25]. In *Vegf120/120* mutant embryos at E12.5 the myocardial sleeve and the right SAN are also present. No evident difference in the length of the sleeves covering the cardinal vein was observed and total sinus venosus myocardium volume, was not significantly different between *Vegf120/120* and WT (E12.5 0.0055±0.001 mm^3 vs 0.0079±0.002 mm^3, p=0.179). At stages E14.5 and E17.5, when ventricular septation is completed, a clear right-sided SAN could be detected in WT with a single SAN artery. In *Vegf120/120* embryos at E17.5 the SAN was shortened and positioned more cranial compared with WT embryos. The expression patterns of TNNI2 (Figure 2D and 2G), and HCN4 (Figure 2E and 2H) were unaffected, as in previous stages. Strikingly, PECAM staining showed large vascular structures in the SAN of mutant embryos, as compared with the single SAN artery in WT embryos (Figure 2F and 2I**)**.

   As the SAN in the *Vegf120/120* embryos appeared smaller during morphological examination, morphometry was performed. The SAN in the *Vegf120/120* embryos were significantly smaller at E12.5 (0.0011±0.00014 mm^3 vs 0.0018±0.00017 mm^3 p=0.029) and at E17.5 (0.003±0.0007 mm^3 vs 0.006±0.0008 mm^3 p=0.002) compared with WT (Figure 2A). Additionally, the ventricular myo-

cardial volume measurements were performed to exclude an overall decrease of myocardium. At E12.5 no significant difference was observed between *Vegf^120/120* and WT embryos (0.23±0.03 mm³ vs 0.26±0.02 mm³). At E17.5 a non-significant trend towards a smaller volume of the *Vegf^120/120* embryos was seen (1.53±0.35 mm³ vs 1.32±0.14 mm³) (Figure 2B). However compared with WT the SAN myocardium/ventricular myocardium-ratio was smaller in *Vegf^120/120* embryos at E12.5 (0.0081±0.0002 vs 0.0044±0.0003, p=0.029) and E17.5 (0.0041±0.0017 vs 0.0023±0.0004, p=0.004) (Figure 2C).

Examination of cellular coupling in the sinoatrial node: results of immunostaining and qPCR

The next step in the analysis was aimed at studying the expression profile of the SAN, with emphasis on connexins. As VEGF can increase the fast conducting CX43[13], the expression

2.4

Figure 2. Smaller volume and less compact sinoatrial node with extensive vasculature in Vegf^120/120 embryos.
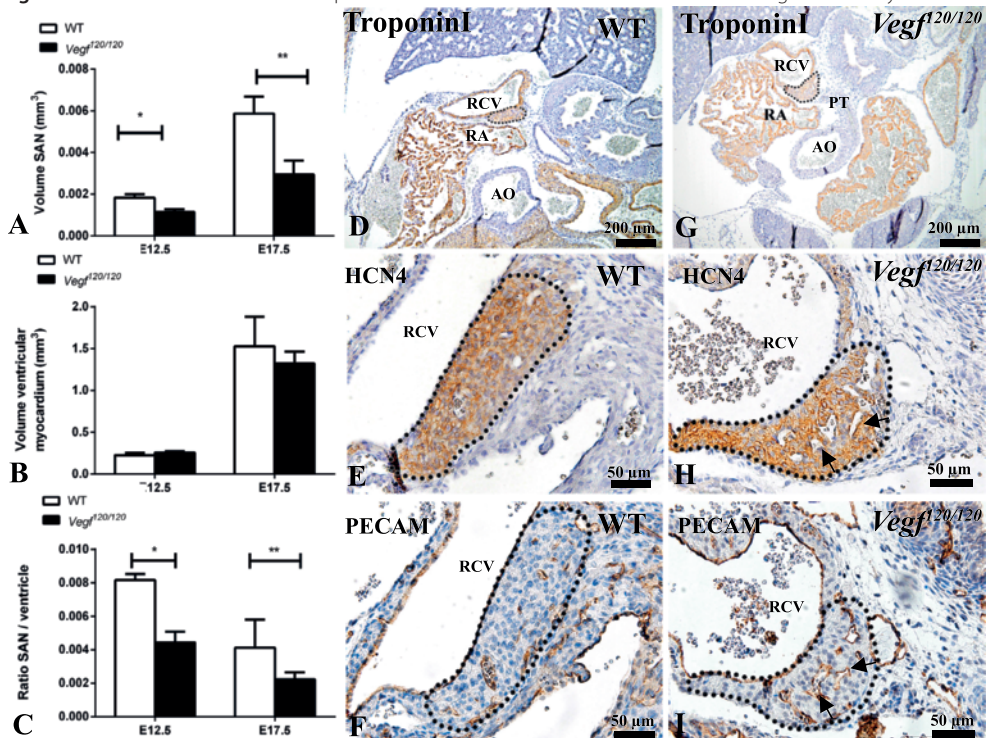
Morphometric analysis showed a smaller sinoatrial node (SAN) volume at E12.5 and E17.5 (A) and no difference in ventricular myocardial volume at E12.5 and E17.5 (B). The ratio between SAN and ventricular myocardium was significantly smaller in Vegf^120/120 embryos at E12.5 and E17.5 (C). Morphologic analysis of the SAN with staining for TroponinI, HCN4 and PECAM. The SAN (black dotted line) is situated at the medial side of the entrance of the right cardinal vein (RCV) into the right atrium (RA). The SAN appears less compact with extensive vasculature (black arrows) in Vegf^120/120 embryos (G-I) compared with WT control (D-F). * = p <0.05, ** = p <0.01. AO = aorta, PT = pulmonary trunk.

of CX43 in *Vegf* mutants was studied. In both WT and *Vegf*[120/120] embryos CX43 was clearly expressed in the ventricles (Figure 3). In E17.5 WT embryos CX43 was also expressed in the atria and myocardium surrounding the cardinal veins, but not in the SAN itself, that was separated from the working myocardium by a TNNI2 negative zone of tissue, corresponding to the previously described fibrotic conduction barrier [28] (Figure 3). By contrast, in *Vegf*[120/120] embryos C43 expression extended over this conduction barrier and was observed in the caudal part of the SAN (Figure 4).

In order to endorse the observed result, qPCR at E17.5 SAN tissues was performed. The primers for several known genes mandatory for SAN development *Hcn4, Hcn1, Nkx2.5, Tbx3* and *Tbx5*, were included, as well as primers for *Connexin40 (Cx40)*, *Cx43* and *Connexin45 (Cx45)* (Figure 5). One *Vegf* [120/120] sample was excluded because of the presence of *Nkx2.5*, suggesting that atrial myocardium was dissected instead of the SAN. The other samples were used for analysis, and showed no significant difference in the SAN markers *Hcn4*, *Hcn1*, and *Tbx3*, or in *Tbx5* (Figure
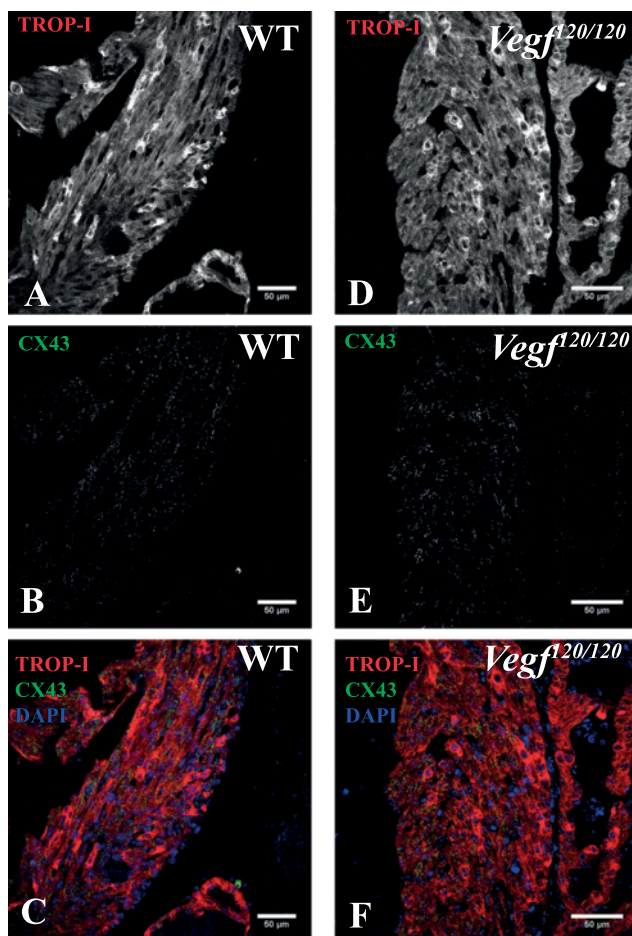

Figure 3. Unaffected Connexin43 expression in ventricular myocardium.

No difference was observed in expression level of Connexin43 in the ventricle of wild type (A-C) and mutant (D-E) embryos (E17.5). In C and F Troponinl (TropI) is stained red, Connexin43 (Cx43) white and nuclei (DAPI) blue.

5). Interestingly, *Cx43* was detected in 40% of WT and in 100% of the *Vegf*^{120/120} embryos and levels of *Cx43* were distinctly increased in *Vegf*^{120/120} embryos. The *Cx43* level in the ventricle was the same in mutants and WT embryos in accordance with the observed protein expression patterns (Figure 3B and E). *Cx40* was equally expressed in WT and mutant embryos. *Cx45* showed

2.4
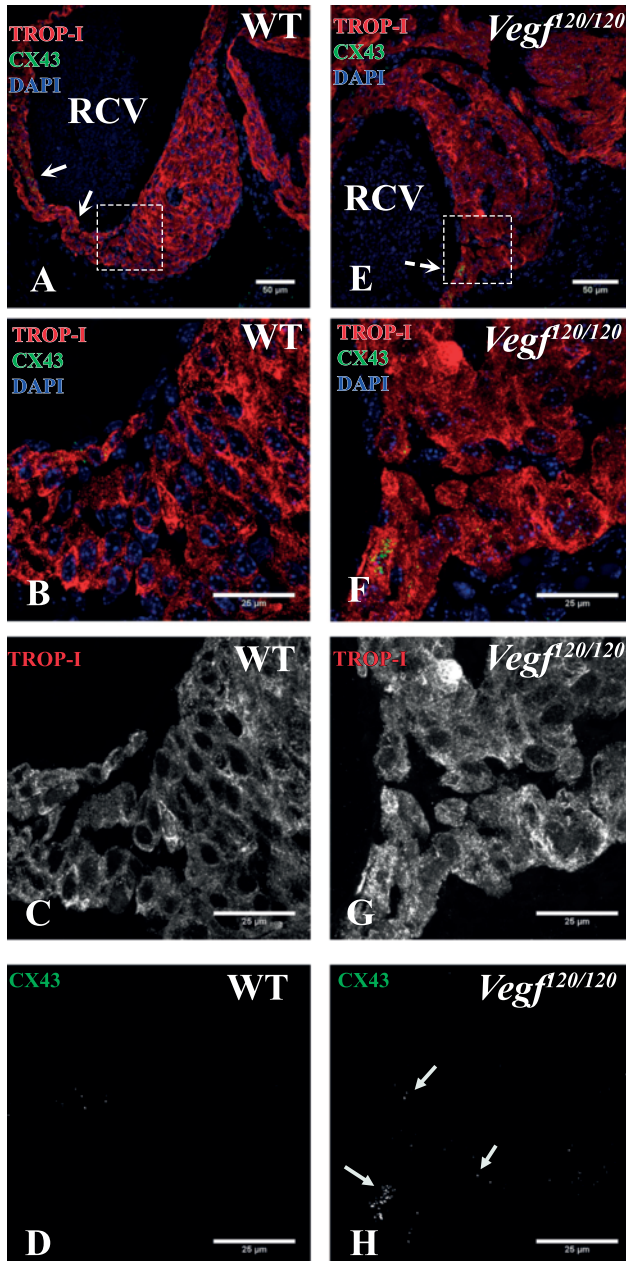
Figure 4. Overexpression of Connexin43 expression in the sinoatrial node of Vegf^{120/120} embryos.

In a E17.5 wild type embryo CONNEXIN43 (CX43) is expressed in the wall of the cardinal vein (white arrow in A), but not in the SAN (B-D), whereas in a Vegf^{120/120} embryo the CX43 continues from the cardinal vein wall into the caudal part of the SAN (E-H). Troponin (Trop-I) is stained red, Connexin43 (Cx43) white and nuclei (DAPI) blue. White arrows in H point at CX43 expression in the SAN.
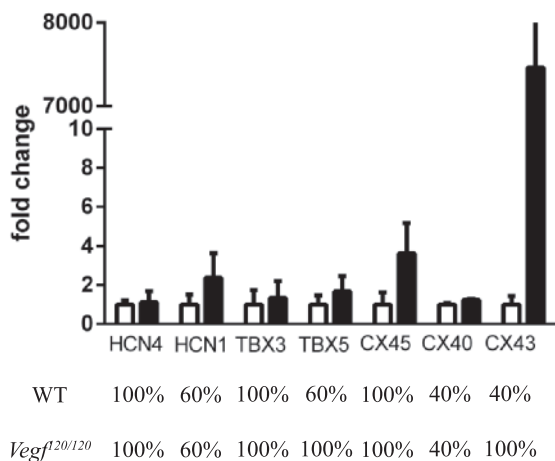
Figure 5. q-PCR of genes in SAN reveals an increase of Connexin43 in Vegf[120/120] versus wild type embryos

Q-PCR of genes in SAN samples of wild type and Vegf[120/120]. Error bars depict standard error of the mean. Values given under the graph show the percentages of samples in which expression of the gene was detected.

	HCN4	HCN1	TBX3	TBX5	CX45	CX40	CX43
WT	100%	60%	100%	60%	100%	40%	40%
Vegf[120/120]	100%	60%	100%	100%	100%	40%	100%

Figure 6. Underdeveloped atrioventricular cushion in Vegf[120/120] embryos.
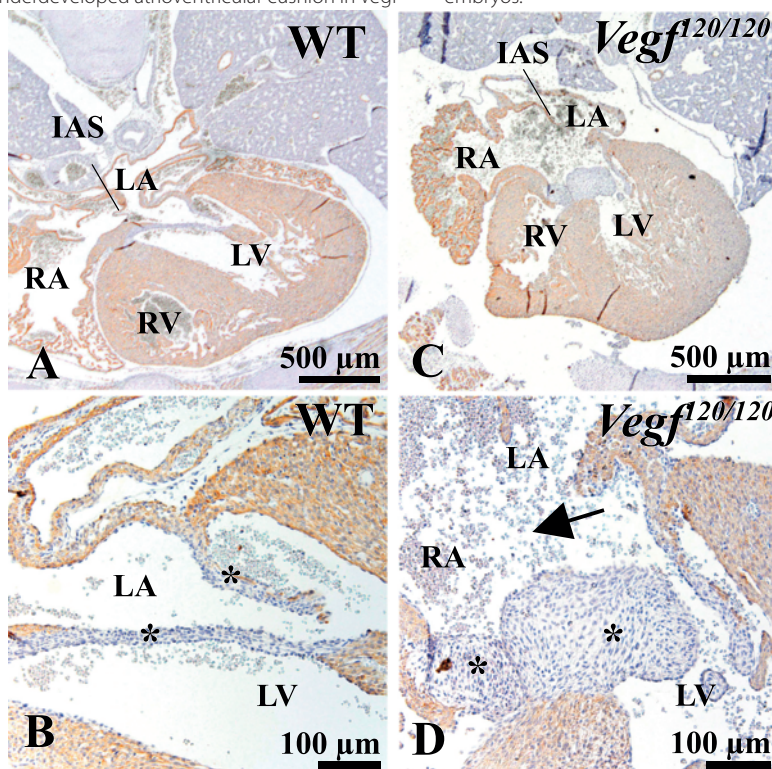
In a WT embryo at E17.5 the leaflets of the left atrioventricular valve have developed into thin structures (asterisks in B), whereas the AV valve in the Vegf[120/120] embryo is plump (asterisks in D). Moreover a partial AVSD is seen in the Vegf[120/120] embryo (black arrow in D). RA= Right Atrium, RV = Right Ventricle, LA = Left Atrium, LV = Left Ventricle IAS= interatrial septum.

variability in both WT and mutant embryos. Samples with high expression of *Cx43* showed low expression of *Cx45* and vice versa.

As local differences in VEGF levels have been described in *Vegf¹²⁰/¹²⁰* embryos [10], the total VEGF expression (i.e. the sum of all isoforms) was also studied. With immunohistochemistry stainings no detectable differences in VEGF staining in the SAN was observed between mutants

Table 2. Phenotype of *Vegf¹²⁰/¹²⁰* embryos in which ultrasound was performed at both E14.5 and 17.5. AV= atrioventricular; AVSD=atrioventricular septum defect; E=embryonic day; PT=pulmonary trunk; VSD=ventricular septum defect

	N
Total analyzed	9
Sub-aortal VSD, overriding aorta and small PT	4
Sub-aortal VSD, overriding aorta, normal PT	2
Absent ductus arteriosus	5
Plump AV valve	5
AVSD	1

Figure 7. Working model: proposed mechanism of bradycardia in Vegf¹²⁰/¹²⁰ embryos.
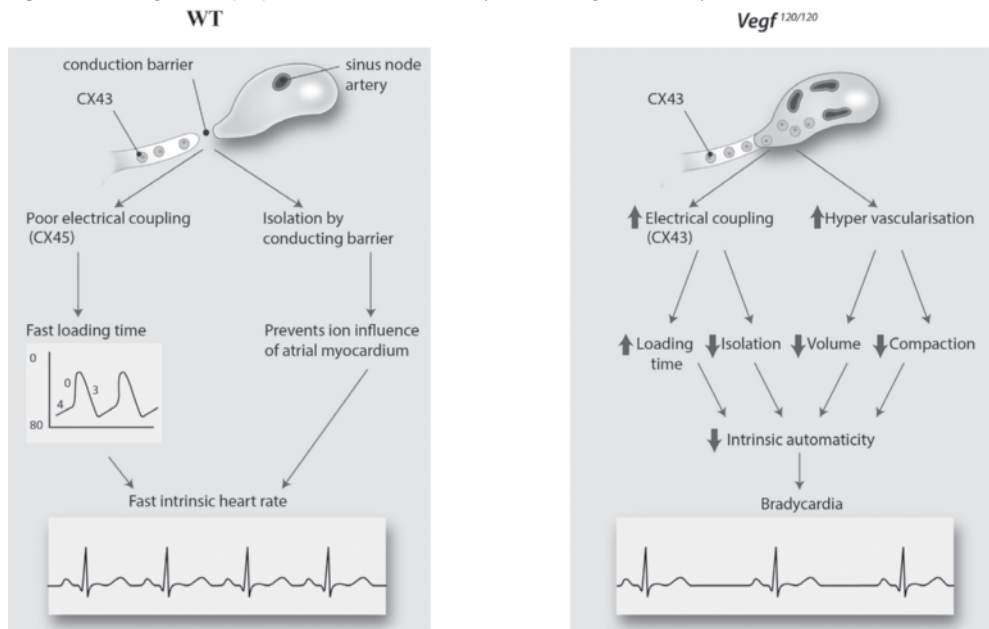
In Vegf¹²⁰/¹²⁰ embryos, increased Connexin43 causes more electrical coupling and ionic shift between neighboring cells in the sinoatrial node (SAN). This results in prolongation of the loading time (i.e. time to depolarization) of the SAN cells. Connexin43 crossing the conduction barrier also results in reduced isolation (and increased electrical coupling) of the SAN from atrial myocardium. The prolonged loading time of cells in the SAN and reduced isolation of the SAN, may lead to bradycardia. Moreover, the increased vascularization causes reduced volume and compaction of the SAN, which may also lead to reduced intrinsic automaticity and bradycardia.

and WT embryos. With qPCR total *Vegf* expression was detectable in one out of five WT embryos and in four out of five mutants, suggesting a net overexpression of VEGF.

Analysis of congenital anomalies at the inflow tract of the heart in Vegf$^{120/120}$ embryos

To assess structural cardiac abnormalities specifically at the inflow tract of the heart, serial sections were examined. As previously described [10], at the level of the outflow tract (OFT), *Vegf$^{120/120}$* embryos showed phenotypes varying from normal to a tetralogy of Fallot (Table 2). At the level of the inflow tract, large and dysplastic atrioventricular valves were observed in five embryos and a partial AVSD in one case (Table 2, Figure 6). Pulmonary veins drained at a normal position in all mutant embryos. Although the interventricular foramen should have closed at stage E14.5, VSDs could be visualized by echo at both E14.5 and E17.5 in *Vegf$^{120/120}$* embryos (Supplementary movie 1). The E/A ratio, a diastolic function parameter reflecting the flow over the AV valve caused by passive (E) and active (A, reflecting atrial contraction) filling of the ventricles, was studied. The embryo with an AVSD and plump AV valves had a lower E and A peak velocities compared with WT controls at E17.5 (Figure 1A). In normal hearts, the E/A ratio over the mitral and tricuspid valves increases between E14.5 and E17.5 [18], reflecting an improvement of ventricular relaxation (diastolic function). The flow over the mitral valve was unaltered in *Vegf$^{120/120}$* embryos. In contrast, the E/A ratio over the TV did not show the same increase as was seen in the WT embryos (*Vegf$^{120/120}$* embryos from 0.31±0.05 to 0.34±0.07 between E14.5 and E17.5 versus and increase from 0.31±0.04 to 0.48±0.05 in WT, p=0.03 at E17.5), indicating impaired right ventricular relaxation. The MPI, suggested to be an early marker of diastolic and systolic dysfunction [29], of *Vegf$^{120/120}$* embryos fell in the normal range of WT embryos (data not shown). The *Vegf$^{120/120}$* embryo that died between E14.5 and E17.5, had a low MPI (0.32 versus 0.49±0.07 in WT), suggesting that the MPI is indeed a marker for poor prognosis.

DISCUSSION

Congenital heart disease is often associated with conduction disorders, such as sinus node dysfunction, both before and after surgical correction[30, 2, 3, 4]. Furthermore, normal blood flow hemodynamics are required for cardiac development and a reduced heart rate may result in abnormal valve development in zebrafish [31]. Therefore normal function of the cardiac conduction system ensuring proper blood flow during early development is essential for cardiogenesis. In the current study, the role of VEGF in embryonic development of the inflow part of the heart was studied with emphasis on the function and morphology of the developing SAN.

Key findings of this study are: 1) *Vegf$^{120/120}$* embryos have a lower heart rate as detected by echocardiography and optical mapping; 2) the SAN in *Vegf$^{120/120}$* embryos is hypervascularized, with smaller volume, and shows aberrant expression of gap junction channels with high

conduction velocity; and 3) besides the known OFT defects, *Vegf120/120* embryos show abnormal inflow tract development including AVSDs and aberrant AV valve inflow patterns.

A role for VEGF in sinoatrial node function

Even though the anatomical shape of the SAN differs between species, in all species adequate function of the SAN requires: 1) Cells with pacemaker potential, expressing potassium/sodium channels, gap junction channels with low conductance (Cx45, Cx30.2 and Cx30) [32], lack of expression of high conductance gap junctions (Cx43) and specific intracellular Ca^{2+} dynamics [33] 2) Anatomical isolation of the SAN from the atrial myocardium by coronary arteries and connective tissue to prevent depression of the pacemaker automaticity from the resistive load of the atrial myocardium [28] 3) Autonomic innervation including sympathetic and parasympathetic innervation, which in large mammals (human) is dominated by vagal tone and in mice by adrenergic stimulation [34] and 4) Presence of adequate pacemaker volume and both the head and tail components of the SAN. The latter is important, as both components have a different pacemaker potential (head is a faster pacemaker compared with the tail) and a shift in leading pacemaker activity can cause heart rhythm differences [28]. In the current study, impaired SAN function in *Vegf120/102*, reflected by a low heart rate observed with two independent techniques, suggests a role for VEGF in SAN development. The optical mapping data, confirming the lower heart rate, indicate that abnormalities in the conduction system of *Vegf120/120* embryos are restricted to the SAN.

Bradycardia in Vegf120/120 embryos due to less compact, hypervascularized node with a smaller volume

In human elderly patients a decrease in theSAN volume has been suggested to contribute to a higher incidence of SSS [35], nevertheless little is known about the minimum volume required for an adequate pacemaker function. The reduction of the SAN volume can be caused by either diminished growth or increased decomposition of the SAN cells. Mutant mouse models of genes expressed in the posterior second heart field (including the *Shox2*, *Podoplanin*, *Id2*, *Tbx3* and *Pdgf-alpha* mutant mouse embryos [5]), largely share a phenotype with hypoplasia of the cardinal (putative caval) vein myocardium, hypoplasia of the SAN, aberrant expression patterns of Connexins and NKX2.5 and sinus node bradycardia. VEGF is expressed in the sinus venosus myocardium, however in *Vegf120/120* mutants no overt hypoplasia of sinus venosus myocardium was observed. Consequently a reduced contribution of the sinus venosus myocardium most likely is not the only cause of a smaller SAN volume.

The extensive vascularization in the SAN of *Vegf120/120* embryos is in line with previously described irregular, tortuous and dilated capillaries in *Vegf* mutants [9] and with the fact that overexpression of $VEGF_{120}$ induces irregular and dilated vessels [36, 11]. As these vascular structures were not included in the measurements of the SAN volume, they could explain the decrease in the SAN volume. In the elderly a reduction in the SAN volume due to ischemia and fibrosis and a

change in the expressions of ion channels and gap junctions are considered a cause of SSS [37]. A similar effect may play a role in the *Vegf^120/120* embryos (Figure 7). Furthermore a prolonged corrected sinus nodal recovery time has been described in patients with SSS and a coronary anomaly [38], suggesting an impact of abnormal coronary distribution on the SAN. The abnormal coronary arterial supply described in *Vegf^120/120* embryos might contribute to diminished development of the SAN.

Bradycardia in Vegf^120/120 embryos due to over-expression of Connexin43

In the initial study reporting *Vegf^120/120* embryos, a decrease in *Cx43* levels was observed in the ventricles of postnatal mutants with ischemic cardiomyopathy [9], which we did not observe. Possibly, a decrease in *Cx43* in the ventricle only becomes present when ischemia escalates after birth. Total VEGF mRNA has been shown to be indifferent in *Vegf^120/120* embryos , but a local increase of VEGF has been observed in a.o. the OFT [10]. Even though the mRNA levels of VEGF were too low to detect in all embryos, the higher percentage of mutant embryos in which VEGF could be detected, suggest a net over-expression of VEGF in the SAN of mutants. Human $VEGF_{165}$ is known to increase CX43 in vitro [13, 14]. Possibly, $VEGF_{120}$ has a similar effect on *Cx43* in *Vegf^120/120* mutants. The effect might also be due to decreased expression of $Vegf_{164}$ and $Vegf_{188}$ in *Vegf^120/120* mutants. Gap junctions consist of connexin protein complexes and play a role in communication and conduction between neighboring cells. The spontaneous depolarization of pacemaker cells (phase 4) is caused by the slow inward depolarization of the cell via "funny" currents. The slow velocity gap junctions (*Cx45*) cause poor electrical coupling to other cells in the SAN which is essential for fast repolarization and thus allows for high frequency depolarization, which keeps the cells in the lead. The poor electrical coupling to the surrounding myocardium is essential for the spontaneous depolarization, because the trigger is then only due to the funny current (channel related) and not due to ionic fluxes from the myocardium (gap junction related) [40]. *Cx43* is a gap junction protein associated with fast conduction, mainly expressed in the working myocardium [41], which has a lower intrinsic automaticity as compared with the SAN. We propose that the increase of *Cx43,* observed in this study, improves electrical coupling in the SAN, causing a lower resistance for ions to move from one cell to another. This increases the loading time needed to repolarize individual SAN cells and thus decreases the frequency of depolarization (Figure 7).

This finding in mice is in agreement with a recent large genome-wide association study in human, where a genetic variant near the *Cx43* gene is associated with variations in the resting heart rate [39], suggesting a role of *Cx43* on the heart rate. Moreover conduction barriers to prevent the suppression of the pacemaker activity by the atrium, described as a sudden break of *Cx43* expression, are important for the normal SAN function, and in humans with the SAN dysfunction, areas of nodal to atrial continuity have been detected [40]. Expansion of *Cx43* into the SAN, as observed in the *Vegf* mutants, can disturb this conduction barrier. Further electrophysiological

investigation of the SAN using high resolution optical mapping or micro-electrode arrays [41] is required to investigate a shift of pacemaker initiation within the SAN.

### Abnormal development of the cardiac inflow tract

In humans, VEGF has been associated with in- and outflow tract defects and the *Vegf[120/120]* mouse model has previously been described with a tetralogy of Fallot phenotype. In the current study abnormalities in the endocardial cushion and atrioventricular valve development of *Vegf[120/120]* embryos, as well as AVSD, resembling the human phenotype, were observed. Of interest, sinus dysfunction is related to congenital heart diseases and has been described in patients with a.o. tetralogy of Fallot [3]. The same combination of CHD and sinus node dysfunction is observed in the VEGF mutant. Whether the impaired heart rate observed in our study contributes to abnormal valve development, as suggested in earlier studies conducted in zebra fish [31], requires further investigation.

Limitations

Although the results of the current study suggest an influence of VEGF on the SAN molecular composition and function, it must be emphasized that the study is of a descriptive nature and future studies are required to investigate the exact cellular and molecular mechanism underlying the bradycardia in *Vegf[120/120]* embryos. Morphometry showed a smaller SAN at both early (E12.5) and late (E 17.5) developmental stages. Although it is likely that this is not different at E14.5, in the current study these measurements were not performed. qPCR was only performed at E17.5 due to limitations with sample size with the techniques used. Despite relatively small numbers, the sample size for analysis of the main outcome parameters (lower heart rate, smaller SAN size and expression of SAN proteins) was sufficient. Due to the positioning of the embryo it was not possible to measure Doppler flow over all four valves in all measured embryos. Therefore this study was insufficiently powered to draw a definite conclusion of valvular flow patterns.

CONCLUSION

In conclusion, the results of the current study indicate a role of VEGF signaling in murine SAN development. The over-expression of VEGF results in bradycardia caused by a hypervascularized SAN with small myocardial volume and compaction, overexpressing the fast conducting Connexin43 that is normally expressed in working myocardium (Figure 7). These observations indicate that VEGF is necessary for normal SAN development and function in mice. Although caution should be taken when extrapolating data from mouse study to human, disturbed VEGF signaling may as well explain the common occurrence of manifest or silent sinus node dysfunction in humans, as observed in selected groups of CHD patients.

2.4

Supplement figure 1. Lasercapture micro-dissection.
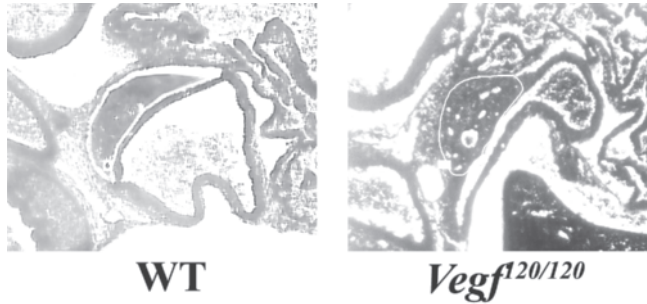
Examples are given of the drawn lasercapture border in a wild type (left) and mutant embryo (right).

Supplement figure 2. supporting information: primers used for q-PCR

Primers used for qualitative PCR

HCN4 F	5'- CTTCTGCTGTGTCACTGGGA-3'
HCN4 R	5'- ATACTGCTTCCCCCAGGAGT-3'
HCN4 nested	5'- TTGATGGACACCCAGCAGTC-3'
HCN1 F	5'- TTGCTAACGCCGATCCCAAT-3'
HCN1 R	5'- GTGATAACGCCAGCAACACC-3'
HCN1 nested	5'- CCCACAGCTCCTTCTCGAAT-3'
Tbx3 F	5'- GAACCCGAAGAAGACGTAGAAC-3'
Tbx3 R	5'- AGAGCACCTCACTTTAAACGG-3'
Tbx3 nested	5'- GAGGCCAAGGAACTTTGGGA-3'
Tbx5 F	5'- AGCCCACTGGATGCGACAA-3'
Tbx5 R	5'- ACGCAGTGTTCTTTGAACCGAACC-3'
Tbx5 nested	5'- ACCTGGACCCGTTTGGACACATTA-3'
Cx45 F	5'- TCATCCTGGTTGCAACTCCC-3'
Cx45 R	5'- AGGTTTTGGTTGGCTCTGCT-3'
Cx45 nested	5'- GCATGGCATAGGGTTTGCTC-3'
Cx40 F	5'- CGTAGGCCAGTACCTCCTCT-3'
Cx40 R	5'- TGGTAGAGTTCAGCCAGGCT-3'
Cx40 nested	5'- GAGGCCCACGGAGAAGAATG-3'
Cx43 F	5'- AGGAGTTCCACCACTTTGGC -3'
Cx43 R	5'- CCCCAGGAGCAGGATTCTGA-3'
Cx43 nested	5'- ACAAGGTCCAAGCCTACTCCA -3'
Vegf-A F	5'- GTCCGATTGAGACCCTGGTG-3'
Vegf-A R	5'- CATCTGCTGTGCTGTAGGAA-3'
Vegf-A nested	5'- GTCAGAGAGCAACATCACCA-3'
Nkx2.5 F	5'- GTCCGGCCTGGCAGAG-3'
Nkx2.5 R	5'- GGCTTTGTCCAGCTCCACT-3'
Nkx2.5 nested	5'- CAAGTGCTCTCCTGCTTTCC-3'

Supplement figure 3. Autonomic innervation.
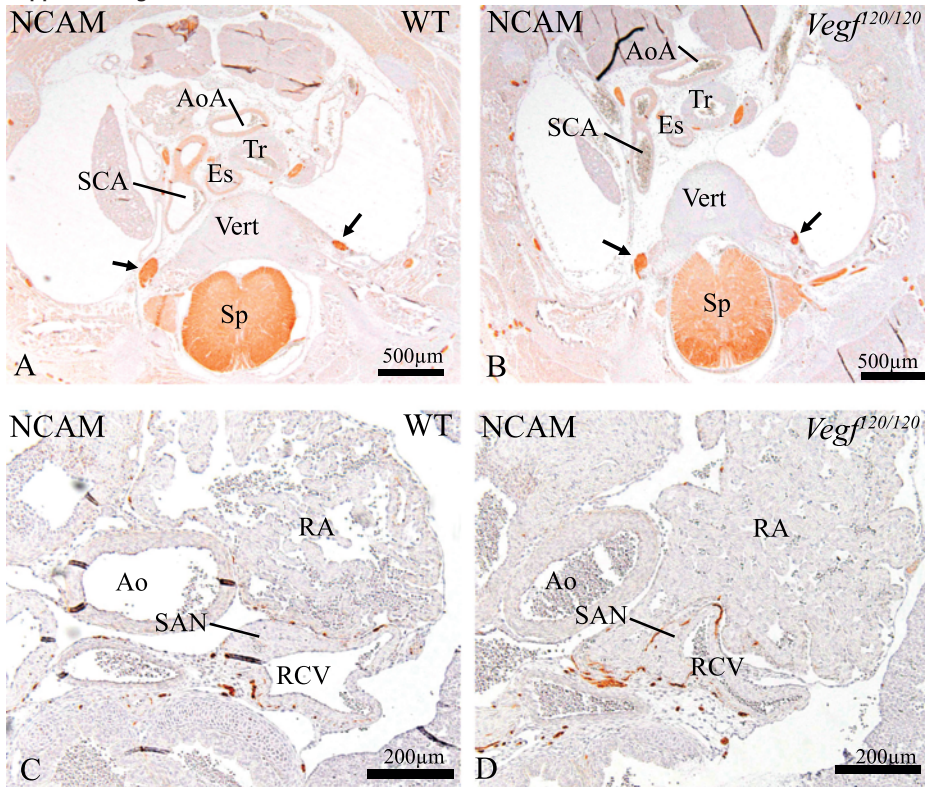
NCAM stainings show similar appearance of the stellate ganglion (black arrows) in WT (A) and Vegf[120/120] (B). Peripheral innervation of the sinoatrial node (SAN) appears similar in WT (C) and Vegf[120/120] (D). AoA= Aortic arch, Ao=Aorta, Es=Esophagus, RA= right atrium, RCV= right cardinal vein, SCA=subclavian artery, Sp=Spine, Tr=Trachea, Vert=Vertebrae

REFERENCES

1. Mangrum JM, DiMarco JP: The evaluation and management of bradycardia. N.Engl.J.Med. 2000;342:703-709.

2. Rathore KS, Agrawal SK, Kapoor A: Restrictive physiology in tetralogy of Fallot: exercise and arrhythmogenesis. Asian Cardiovasc.Thorac.Ann. 2006;14:279-283.

3. Nakazawa M, Shinohara T, Sasaki A, et al.: Arrhythmias late after repair of tetralogy of Fallot: a Japanese Multicenter Study. Circ.J. 2004;68:126-130.

4. Maeno Y, Hirose A, Kanbe T, et al.: Fetal arrhythmia: prenatal diagnosis and perinatal management. J.Obstet.Gynaecol.Res. 2009;35:623-629.

5. Jongbloed MR, Vicente SR, Hahurij ND, et al.: Normal and abnormal development of the cardiac conduction system; implications for conduction and rhythm disorders in the child and adult. Differentiation 2012;84:131-148.

6. Stalmans I, Lambrechts D, De Smet F, et al.: VEGF: a modifier of the del22q11 (DiGeorge) syndrome? Nat.Med. 2003;9:173-182.

7. Lambrechts D, Devriendt K, Driscoll DA, et al.: Low expression VEGF haplotype increases the risk for tetralogy of Fallot: a family based association study. J.Med.Genet. 2005;42:519-522.

8. Ackerman C, Locke AE, Feingold E, et al.: An Excess of Deleterious Variants in VEGF-A Pathway Genes in Down-Syndrome-Associated Atrioventricular Septal Defects. Am.J.Hum.Genet. 2012;91:646-659.

9. Carmeliet P, Ng Y-S, Nuyens D, et al.: Impaired myocardial angiogenesis and ischemic cardiomyopathy in mice lacking the vascular endothelial growth factor isoforms $VEGF_{164}$ and $VEGF_{188}$. Nat. Med. 1999;5:495-502.

10. Van Den Akker NM, Molin DG, Peters PP, et al.: Tetralogy of fallot and alterations in vascular endothelial growth factor-A signaling and notch signaling in mouse embryos solely expressing the VEGF120 isoform. Circulation Research 2007;100:842-849.

11. Van Den Akker NM, Caolo V, Wisse LJ, et al.: Developmental coronary maturation is disturbed by aberrant cardiac vascular endothelial growth factor expression and Notch signalling. Cardiovasc. Res. 2008;78:366-375.

12. Van Den Akker NM, Caolo V, Molin DG: Cellular decisions in cardiac outflow tract and coronary development: an act by VEGF and NOTCH. Differentiation 2012;84:62-78.

13. Pimentel RC, Yamada KA, Kleber AG, et al.: Autocrine regulation of myocyte Cx43 expression by VEGF. Circulation Research 2002;90:671-677.

14. Iyer RK, Odedra D, Chiu LL, V et al.: Vascular endothelial growth factor secretion by nonmyocytes modulates Connexin-43 levels in cardiac organoids. Tissue Eng Part A 2012;18:1771-1783.

15. Rentschler S, Yen AH, Lu J, Petrenko NB, et al.: Myocardial Notch signaling reprograms cardiomyocytes to a conduction-like phenotype. Circulation 2012;126:1058-1066.

16. Nakashima Y, Yanez DA, Touma M, et al.: Nkx2-5 suppresses the proliferation of atrial myocytes and conduction system. Circulation Research 2014;114:1103-1113.

17. Corrigan N, Brazil DP, Auliffe FM: High-frequency ultrasound assessment of the murine heart from embryo through to juvenile. Reprod.Sci. 2010;17:147-157.

18. Hahurij ND, Calkoen EE, Jongbloed MR, R et al.: Echocardiographic assessment of embryonic and fetal mouse heart development: a focus on haemodynamics and morphology. ScientificWorldJournal. 2014;2014:531324-

19. Myers DC, Fishman GI: Molecular and functional maturation of the murine cardiac conduction system. Trends Cardiovasc.Med. 2003;13:289-295.

20. Sankova B, Benes J, Jr., Krejci E, et al.: The effect of connexin40 deficiency on ventricular conduction system function during development. Cardiovasc. Res. 2012;95:469-479.

21. Vicente-Steijn R, Kolditz DP, Mahtab EA, et al.: Electrical activation of sinus venosus myocardium and expression patterns of RhoA and Isl-1 in the chick embryo. J.Cardiovasc.Electrophysiol. 2010;21:1284-1292.

22. Mahtab EA, Vicente-Steijn R, Hahurij ND, J et al.: Podoplanin deficient mice show a Rhoa-related hypoplasia of the sinus venosus myo-

cardium including the sinoatrial node. Dev.Dyn. 2009;238:183-193.

23. Liu J, Dobrzynski H, Yanni J, et al.: Organisation of the mouse sinoatrial node: structure and expression of HCN channels. Cardiovasc.Res. 2007;73:729-738.

24. Jongbloed MR, Vicente-Steijn R, Douglas YL, et al.: Expression of Id2 in the second heart field and cardiac defects in Id2 knock-out mice. Dev.Dyn. 2011;240:2561-2577.

25. Gittenberger-de Groot AC, Mahtab EAF, Hahurij ND, et al.: Nkx2.5 negative myocardium of the posterior heart field and its correlation with podoplanin expression in cells from the developing cardiac pacemaking and conduction system. Anat Rec 2007;290:115-122.

26. Christoffels VM, Mommersteeg MT, Trowe MO, P et al.: Formation of the venous pole of the heart from an Nkx2-5-negative precursor population requires Tbx18. Circulation Research 2006;98:1555-1563.

27. Marko SB, Damon DH: VEGF promotes vascular sympathetic innervation. Am.J.Physiol Heart Circ. Physiol 2008;294:H2646-H2652.

28. Fedorov VV, Glukhov AV, Chang R: Conduction barriers and pathways of the sinoatrial pacemaker complex: their role in normal rhythm and atrial arrhythmias. Am.J.Physiol Heart Circ.Physiol 2012;302:H1773-H1783.

29. Godfrey ME, Messing B, Cohen SM, et al.: Functional assessment of the fetal heart: a review. Ultrasound Obstet.Gynecol. 2012;39:131-144.

30. Norozi K, Wessel A, Alpers V, et al.: Chronotropic incompetence in adolescents and adults with congenital heart disease after cardiac surgery. J.Card Fail. 2007;13:263-268.

31. Hove JR, Koster RW, Forouhar AS, et al.: Intracardiac fluid forces are an essential epigenetic factor for embryonic cardiogenesis. Nature 2003;421:172-177.

32. Christoffels VM, Smits GJ, Kispert A, et al.: Development of the pacemaker tissues of the heart. Circulation Research 2010;106:240-254.

33. Lakatta EG, maltsev VA, Vinogradova TM: A coupled SYSTEM of intracellular Ca2+ clocks and surface membrane voltage clocks controls the timekeeping mechanism of the heart's pacemaker. Circulation Research 2010;106:659-673.

34. Adachi T, Shibata S, Okamoto Y, et al.: The mechanism of increased postnatal heart rate and sinoatrial node pacemaker activity in mice. J.Physiol Sci. 2013;63:133-146.

35. Shiraishi I, Takamatsu T, Minamikawa T, et al.: Quantitative histological analysis of the human sinoatrial node during growth and aging. Circulation 1992;85:2176-2184.

36. Cheng SY, Nagane M, Huang HS, et al.: Intracerebral tumor-associated hemorrhage caused by overexpression of the vascular endothelial growth factor isoforms VEGF121 and VEGF165 but not VEGF189. Proc.Natl.Acad.Sci.U.S.A 1997;94:12081-12087.

37. Dobrzynski H, Boyett MR, Anderson RH: New insights into pacemaker activity: promoting understanding of sick sinus syndrome. Circulation 2007;115:1921-1932.

38. Liu PY, Chao TH, Tsai WC, et al.: Sick sinus syndrome in a patient with single coronary artery anomaly. J.Formos.Med.Assoc. 2000;99:785-788.

39. Deo R, Nalls MA, Avery CL, et al.: Common genetic variation near the connexin-43 gene is associated with resting heart rate in African Americans: a genome-wide association study of 13,372 participants. Heart Rhythm. 2013;10:401-408.

40. Demoulin JC, Kulbertus HE: Histopathological correlates of sinoatrial disease. Br.Heart J. 1978;40:1384-1389.

41. Yi T, Wong J, Feller E, et al.: Electrophysiological mapping of embryonic mouse hearts: mechanisms for developmental pacemaker switch and internodal conduction pathway. J.Cardiovasc. Electrophysiol. 2012;23:309-318.

42. H.J. Gunderson, E.B. Jensen: The efficiency of systematic sampling in stereology and its prediction, J. Microsc. 1987;147:229–263.

2.4

Part 3

Long-term follow-up after
atrioventricular septal
defect correction

Chapter 3.1

Cardiovascular function and flow by
4-dimensional magnetic resonance
imaging techniques: new applications

Emmeline E. Calkoen, Arno A. Roest, Rob J. van der Geest,
Albert de Roos and Jos J.M. Westenberg

SUMMARY

Acquisition techniques related to 4D flow Magnetic Resonance Imaging (MRI) improved rapidly over the last three decades. Most importantly, a major improvement was the acceleration of the acquisition which resulted in a clinically feasible scan duration and led to more comprehensive use of 4D flow MRI in clinical research. This resulted in various new applications of 4D flow MRI for the evaluation of various physiologic and pathologic cardiovascular flow patterns. Visualization tools aim at displaying the direction and magnitude of blood flow velocity from 4D flow data, by using for instance a vector glyph or streamline representation or by constructing pathlines from particle tracing. Such tools are applied to provide insight in the temporal distribution of the three-dimensional flow velocity and enable the quantification of hemodynamic markers. These hemodynamic markers play an important role in the quantitation of abnormalities in cardiovascular blood flow patterns and the characterization of vascular and myocardial remodelling which can possibly be used to predict pathology such as heart failure, aortic dissection or aneurysm or thrombus formation. This review focuses on the clinical use of 4D flow MRI and presents an overview of new applications of visualisation and quantification tools to describe physiologic and pathologic cardiovascular blood flow.

3.1

INTRODUCTION

Over the last three decades, technology in cardiovascular magnetic resonance imaging (MRI) developed remarkably which contributed to the evolution of four-dimensional (4D) flow MRI from an imaging tool strictly limited to research environments into a clinically practical modality providing valuable disease-specific information. 4D flow acquisitions allow visualization and quantification of intra-cardiac blood flow and blood flow in the great arteries and veins, providing new insights in normal and pathologically altered blood flow patterns that were previously only suggested by computational fluid dynamics or in vitro simulations. In the current review, we will address important technical developments in cardiovascular MRI that contributed to the evolution of 4D flow, discuss the latest advances in acquisition tools and present an overview of current clinical applications in vascular, valvular and intra-cardiac blood flow visualization and quantification.

DEVELOPMENT OF FLOW ASSESSMENT WITH MRI: TOWARDS FAST AND ACCURATE 4D FLOW

After the commercial introduction of whole-body MRI scanners in the early 1980s, Moran was the first to describe in vivo two-dimensional (2D) imaging with one-directional velocity informa-

tion for each voxel [1], by adding velocity-sensitive and velocity-compensated gradients to a standard gradient-echo pulse sequence. Bryant et al. [2] and van Dijk [3] demonstrated the use of motion-induced phase shifts to encode the magnitude and direction of blood flow velocity. The principle of velocity-encoding or phase-contrast imaging relies on manipulating the phase signal of spins moving in the direction along a magnetic field gradient in contrast to the phase of stationary spins, in such a way that the difference in phase between moving and stationary spins is proportional to the velocity of those moving spins. A velocity-sensitive gradient induces a phase shift proportional to the velocity, but other factors than motion (i.e., magnetic field inhomogeneity, eddy currents, concomitant gradient effects) which depend on B_0 (i.e., the static magnetic field), induce additional phase shifts. By performing a subtraction of echoes from acquisitions using alternating velocity-sensitive and velocity-compensated gradient schemes, these additional phase shifts are eliminated and only phase shifts related to velocity remain. After image reconstruction, the accustomed phase images from phase-contrast MRI are obtained, in which the grey value is linearly related to the velocity of blood flow. Typically, imaging is performed in a time-resolved manner [4], resulting in multiple phases during one average cardiac cycle. Data collection extends over multiple cardiac cycles and is synchronized to the patient's ECG signal using either prospective [5] or retrospective gating [6]. With prospective gating, a trigger signal starts off data acquisition and data is collected over multiple heart beats at predefined time points of the cardiac cycle. Prior to acquisition, the heart beat interval is set in the acquisition protocol, determining the start of each trigger. Variations in the true heart beat during the acquisition may result in inaccurate acquisition timing, leading to inaccuracies especially in late diastolic flow assessment, or even missing flow assessment in this part of the cardiac cycle. With retrospective gating, data collection is performed continuously throughout the cardiac cycle and stored with the trigger signal. During image reconstruction, this recorded trigger signal is used to retrospectively assign the collected data to subsequent timings in the cardiac cycle. Since velocity-encoded imaging is not real-time and velocity images are reconstructed from data acquired over multiple heart beats, therefore representing average velocities at specific time points in the cardiac cycle, alterations in the velocity over multiple heart beats cannot be picked up.

Nowadays, 2D cine MRI with one-directional through-plane velocity-encoding is widely used in clinical protocols to assess the function of cardiac chambers and heart valves by evaluation of trans-valvular blood flow [7,8]. Intra-cardiac blood flow, however, is a complex three-dimensional and highly-dynamically-changing phenomenon which requires multi-dimensional imaging. 4D flow MRI is the term used for time-resolved three-dimensional (3D) three-directional velocity-encoded MRI with data collected during several minutes but represented as one average heartbeat. From this acquisition, the blood flow velocity is acquired in a 3D volume (e.g., covering the heart or the great thoracic vessels) by encoding the three individual vector components consecutively [9]. Visualization tools are required to display the multi-dimensional data such as

the time-dependent velocity vector field and quantification algorithms have been developed for hemodynamic analysis.

The first 4D flow MRI protocols involved a along acquisition time, which is the major drawback for introducing this technique in clinical practice [10,11]. Several improvements led to acquisition protocols which can provide good quality data acquired in less than 10-15 minutes. Accelerated acquisition techniques using parallel imaging [12] or undersampling in k-t domain (k-t BLAST Broad-use Linear Speed-up Technique) [13] vastly reduced acquisition time. In contrast to conventional Cartesian read-out methods, algorithms for data read-out using Echo Planar Imaging (EPI) [14] or implementing radial [15] or spiral read-out trajectories [16] further contributed to the reduction of acquisition times towards a clinically acceptable scan duration. The introduction of radial undersampling, known as VIPR (vastly undersampled isotropic projection reconstruction) [15] revealed the advantage of a larger area coverage, higher spatial resolution and improvement of hemodynamic analysis.

Because scan time still exceeds a breath hold and respiratory motion may significantly degrade image quality, specific techniques have been developed to minimize breathing artefacts. Commonly used techniques are bellows reading [17], that corrects via registration of the excursion of the abdominal circumference, and navigator gating [18], based on diaphragm movement. In both cases, collected data are only included for image reconstruction when acquired during the time in the respiratory cycle when breathing motion is minimal. Rejection of data can be reduced to 20-40 % with adaptive k-space recoding [19]. The drawbacks of these types of respiratory compensation are that these methods are based on abdominal or long-liver movement instead of relying on heart movement, and the inaccuracy caused by the time delay between signal and movement [20]. To overcome these disadvantages respiratory self-gating is introduced, where k-space data of the heart is used to provide information about its movement [21].

Due to mentioned developments, it is currently possible to acquire whole-heart 4D flow data in under 10-15 minutes, with echo time 2-4 ms, repetition time 5-7 ms, spatial resolution 2-3 mm and temporal resolution 30-40 ms [22]. The implementation of these acceleration techniques however, led to a negative trade-off: increasing inaccuracies in velocity quantitation. Most notably are local phase offset errors, caused by eddy currents [23], Maxwell terms [15] and gradient field nonlinearity [24]. 4D flow acquisition implies volume coverage with consequently a larger anatomical area included than for conventional 2D flow acquisitions. Therefore, measurements are performed in areas further from the iso-center of the magnet where they are more prone to offset errors. During pre-processing, the major source of these errors should be taken into account and additional background correction methods have been developed, either by a phantom correction [25] or by using a plane-fitting correction algorithm based on the phase signal sampled in areas inside the acquired 3D volume with no velocity, in order to correct the position-dependent velocity offset [26,27].

3.1

VISUALIZATION TECHNIQUES

4D flow data represents the pulsatile time-resolved three-directional velocity distribution inside a 3D volume (i.e., the heart or great arteries and veins). Several image processing techniques are available to present this multi-dimensional data for qualitative visual interpretation, usually projecting velocity or flow as animations onto anatomical images presented in cine mode. Figure 1 illustrates three available and often-used visualization methods. A glyph (graphic symbol) display of the velocity vector field represents the magnitude and direction of the velocity measured inside each voxel. Color coding or adjustment of the size of the vector glyph may be used to represent the velocity magnitude. Streamlines [28] are lines instantaneously tangent to the local velocity vector in each position at a specific time point and connected to all points along the direction of this line. Therefore, streamlines can be used to visualize the flow direction

Figure 1. Three types of 4D flow visualization.
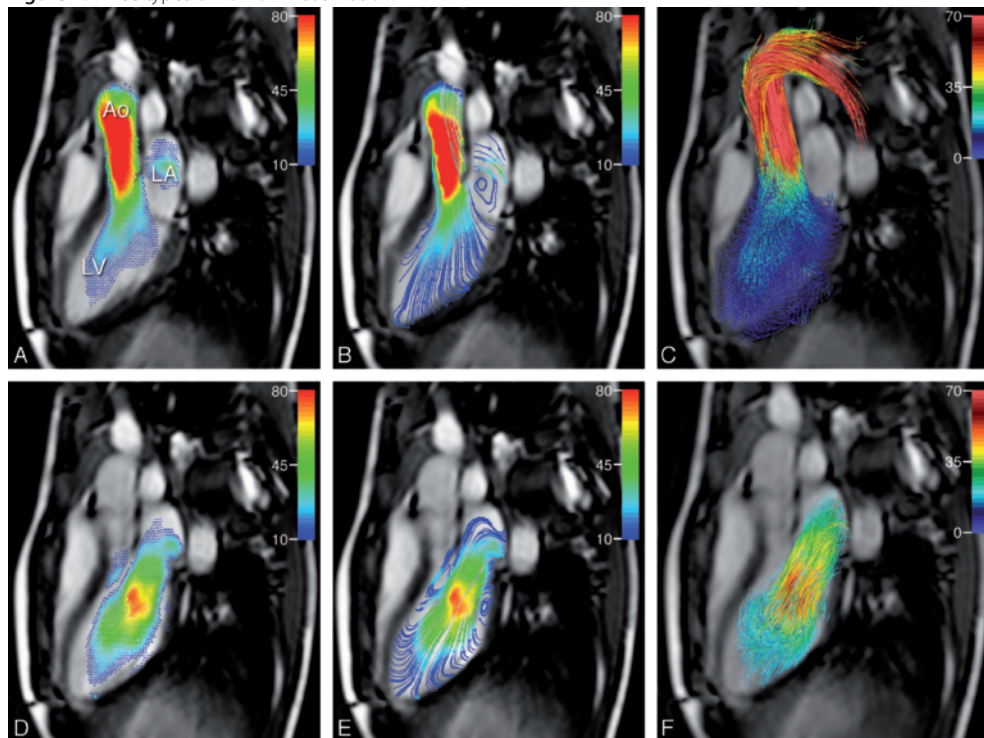
3-chamber orientation with velocity color coding (in cm/s). In panel A and D velocity vector glyph representation, in panel B and E streamline representation and in panel C and F pathline representation after forward (C) and backward (F) particle tracing. 4D flow MRI data was obtained with a 3T MRI scanner in a 9 year old healthy girl (informed consent was obtained from the parents) with a heart rate of 89 beats per minute. A-C represent the same mid-systolic phase (i.e., 136 ms after R-peak), D-F represent the same early diastolic phase (i.e., 409 ms after R-peak). In C and F, respectively forward and backward tracing was performed with particles being released in the left ventricle at end diastole. LV left ventricle, LA left atrium, Ao aorta.

only at this specific instant in time and do not represent the true pathlines of flow over time. Color coding can again be used to display the velocity magnitude [29].

Particle tracing is an often-used visualization tool to display the true pathline of flowing blood over time [30]. In particle tracing, virtual particles are positioned at a predefined position and time and subsequently released inside the 3D velocity field and then followed over time. The trajectory of the particles is calculated by either forward or backward tracing, by using the local velocity at each position and time point and calculating the next or previous position of this particle. Pathlines can be displayed over time with color coding either representing velocity magnitude or labelling the origin or destination of the particles in the flow field. The discretization in time and space in combination with the quality of data defines the accuracy of particle tracing. When uncorrected, a particle near a physical border may dissipate through this border if the local velocity at a specific time point directs this particle towards the border and the distance covered over the time step exceeds the distance to the border. To check the quality of particle tracing, agreement in the particle count entering and leaving a volume should be verified [31].

3.1

Another line representation that is used for displaying flow is the streakline [32]. This line is constructed similarly to a pathline, with a virtual particle being released from a seed point inside a flow field. With streaklines, however, particles will be released continuously over time from the same seed point. At an instant in time, the positions of all consecutively released particles from the same seed point are connected to construct the streakline. Since streaklines are not representatives of the true pathline or velocity of blood flow, this type of visualization has not found widespread use in physiological hemodynamics. Isosurfaces are used as a visualization tool to cluster and segment flow structures. For example, vortical or helical flow can be displayed with an isosurface, clustering blood with identical vorticity or helicity together inside the flow field [33].

QUANTIFICATION TECHNIQUES

Visualization techniques as described above aid in the qualitative interpretation of flow patterns in 4D flow data. In addition, quantification tools have been developed to assess hemodynamic markers from 4D flow data. Using particle tracing, a four-component evaluation of the intracardiac blood flow has been introduced [31]. According to the moment of passing the LV relative to the cardiac cycle, the blood volume inside the LV at end diastole can be subdivided into four functional components: 1. direct flow, which is the amount of blood that enters the LV during diastole and is subsequently ejected through the aorta in the next systole; 2. retained inflow, which is the amount of blood that enters the LV during diastole but is not ejected in the next systole; 3. delayed ejected flow, which is part of the blood already present inside the LV during diastole but leaves the LV during the next systole; 4. residual volume, which is the amount of

blood that was not part of the blood entering during diastole and is not ejected in the next systole, and therefore resides in the LV for more than two cardiac cycles. Using particle tracing and color coding, the four components in intra-cardiac blood flow are labelled and the distribution can be followed over time [31].

From local velocity and flow rate, the kinetic energy of flowing blood can be calculated. Stroke volume multiplied by the blood density represents the mass m of flowing blood. The kinetic energy of this blood flow is then calculated by $0.5mv^2$, with v being the mean velocity. Another parameter representing energy of blood flow that is often used is the turbulent kinetic energy [34]. Turbulence is characterized by incoherent flow and rapid fluctuations in velocity, which cannot be picked up by the magnitude of velocity encoding. However, the standard deviation of the velocity distribution within each voxel can be assessed and this parameter is related to the turbulent kinetic energy. Another hemodynamic marker that is of high interest is the wall shear stress (WSS), as this shear stress affects vascular remodelling through its act on endothelial cells. WSS can be quantified [35,36] based on the assumption that a laminar condition exist in the boundary layer of the blood vessel, in which WSS is calculated by the wall shear rate multiplied by the blood viscosity, with the wall shear rate being the derivative of local velocity at the vascular wall.

The aortic pulse wave velocity (PWV, i.e., the speed of the systolic pulse propagating through the aorta) is being used as a surrogate marker for aortic stiffness. PWV is calculated by measuring the transit time of wave propagation over a predefined segment of the aorta (Figure 2). Although temporal resolution in 4D flow is limited, global PWV assessment in the total aorta using 4D flow has been described [37]. High temporal resolution, required for accurate regional PWV assessment, can be achieved by combining multiple one-directional velocity-encodings [38].

Diastolic vortices are important phenomena in intra-ventricular blood flow patterns that can be evaluated with 4D flow (Figure 3). Vorticity describes the local rotation of fluid particles. A vortex represents a compact region of vorticity and forms when boundary layers separate, for instance distal to valve leaflets. Due to variance in speed in the shear layer, blood swirls and may separate from the boundaries, forming a compact vortex [39]. During early (E) and late (A) filling, a circular vortex ring is formed from the tips of the mitral and tricuspid valve leaflets, causing minimal loss in kinetic energy [40]. The vortex ring formed in the left ventricle is suggested to form a channel that prevents spreading of the inflow jet and loss of momentum to convective deceleration [41]. Additionally, the vortex ring contributes to the redirection of flow towards the aorta and possibly aids mitral valve closure [42] and prevents thrombus formation [43]. Various parameters have been suggested to characterize vortices and their association with systolic and diastolic function. With Echocardiographic studies (using contrast or vector flow mapping) found a relation between abnormal left ventricular function and vortex size, intensity and position [44,45]. The vortex formation time (VFT), introduced by Gharib et al. [46], is a parameter computed from the equations for trans-mitral flow and ejection fraction and has been proposed as an indicator for cardiac health and diastolic function with suggested prognostic value in

predicting heart failure [47]. In contrast, Stewart et al. demonstrated no association between VFT and diastolic function [48]; they postulated that the vortex pinches off the mitral valve already before E-peak, leading to an abrupt deceleration of the velocity propagation. Since VFT is based on the assumption that the vortex is only completely formed at E-peak, they concluded that VFT is not useful as an indicator for cardiac function.

**Figure 2.** Regional aortic pulse wave velocity assessment.
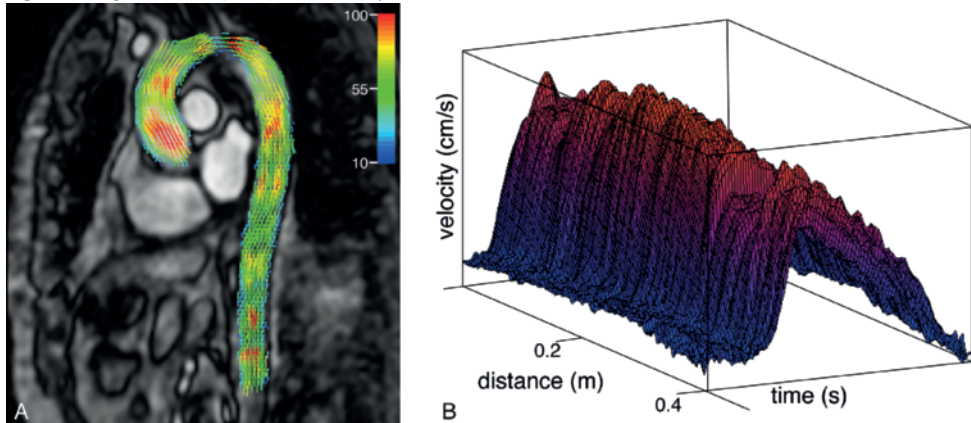
Two combined high-temporal one-directional in-plane velocity-encoded MRI acquisitions, performed with 3T MRI scanner in a 44 year old healthy male volunteer (informed consent was obtained). In A, in-plane velocity is displayed in a mid-systolic phase of a double-oblique sagittal view of the aorta, using a velocity vector glyph representation with color coding (cm/s). In B, velocity-time curves are displayed, sampled at 200 equidistantly-spaced positions along the 40 cm long centerline of the aorta, starting from the aortic valve to the abdominal aorta. From these velocity-time curves, the relation between sampling position and the transit-time for velocity wave propagation can be obtained, which defines the regional pulse wave velocity.

Figure 3. Visualization of the diastolic vortex in the left ventricle distal to the mitral valve.
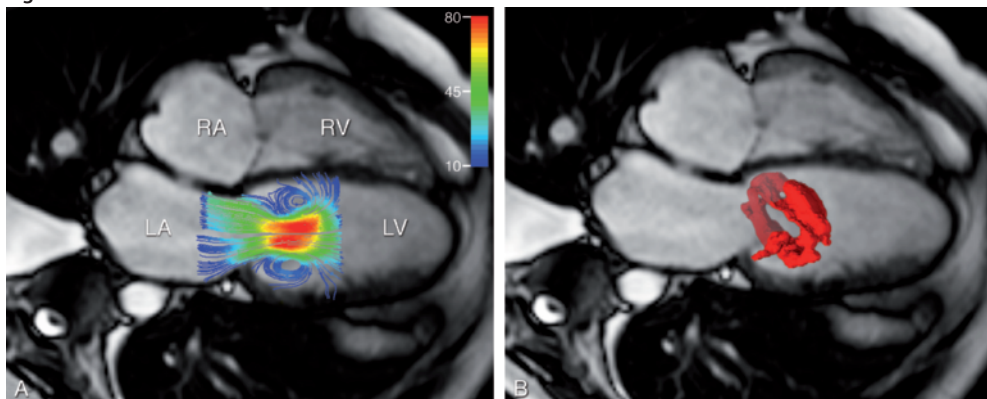
Obtained with a 1.5T MRI scanner in a 45 year old male patient with ischemic cardiomyopathy (informed consent was obtained). In A, a 4-chamber orientation with streamline representation and velocity color coding (in cm/s) is presented and in B, a vorticity isosurface display, segmenting the ring-like structure of the vortex. LV left ventricle, LA left atrium, RV right ventricle, RA right atrium.

Figure 4. Streamline visualization of left ventricular inflow.
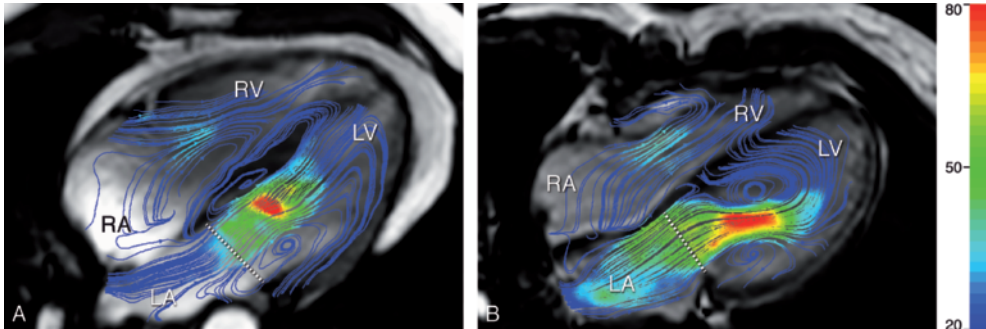
Velocity color coding (in cm/s) of 4D flow MRI data, displaying the early diastolic inflow in a 4-chamber orientation, obtained with a 3T MRI scanner in a 33 year old healthy male volunteer (A) and a 30 year old female patient with a corrected atrioventricular septum defect (B) (informed consent was obtained in both subjects). The dotted line represents the anatomical annulus of the left atrioventricular valve. In A, an apically-directed inflow is visualized, in contrast to the laterally-directed inflow (B) in the patient, due to restricted opening of the valve. Peak inflow velocity is visualized 1-2 cm distal to the anatomical annulus, at the location of the valve leaflets. LV left ventricle, LA left atrium, RV right ventricle, RA right atrium.

Figure 5. Streamline representation of atrioventricular regurgitation.
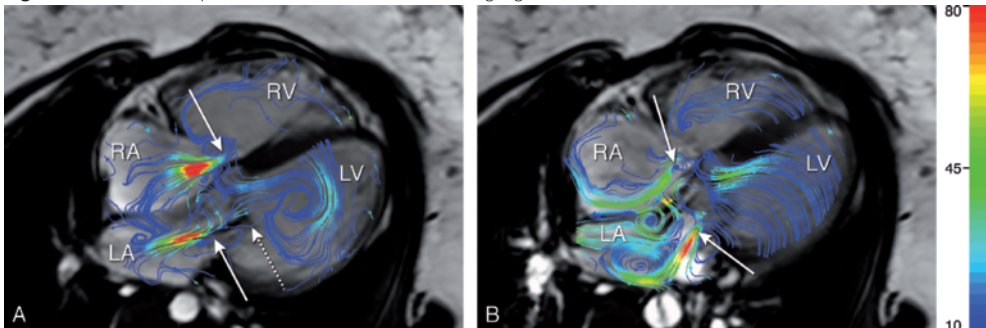
Velocity color coding (in cm/s) of 4D flow MRI data in a 4-chamber orientation, obtained with a 3T MRI scanner in a 16 year old female patient with a corrected atrioventricular septum defect and recurrent regurgitation in both left and right atrioventricular valves (solid arrows) during follow-up (informed consent was obtained from the patient and parents). A represents an early systolic phase (i.e., 34 ms after R-peak at heart rate of 61 beats per minute) and B represents mid-systolic phase (i.e., 201 ms after R-peak). Note the dynamically-changing direction of the regurgitant jets, illustrating the need for dynamical adaptation of measurement planes to the flow direction throughout the cardiac cycle. Due to turbulence at the regurgitant orifice, intra-voxel spin coherence is absent leading to dispersion of phase signal, especially notable at early systole at the left atrioventricular valve (A, dotted arrow). Therefore, quantification of regurgitant flow is usually performed 1.5 – 2 cm proximal to the valve, inside the atrium. Retrospective valve tracking at left and right atrioventricular valve resulted in an assessment of mean effective forward flow volume of 95 ml per cardiac cycle, and regurgitant fractions of 11% at the left atrioventricular valve and 15% at the right atrioventricular valve. LV left ventricle, LA left atrium, RV right ventricle, RA right atrium.

From intra-cardiac blood flow, transvalvular stroke volumes and regurgitation can be assessed, describing valve and chamber function. Retrospective valve tracking was introduced to transvalvular velocity mapping, with the measurement plane following the valve plane and the angulation adapting to the blood flow direction, to accurately quantify blood flow through any of the four heart valves obtained from one single 4D flow acquisition [49,50].The high velocity regurgitation jet is usually analyzed in a plane inside the atrium distal to the valve plane, in order to avoid underestimation of regurgitation velocity due to phase dispersion from turbulent flow. This 4D flow approach with retrospective valve tracking was proven to be more accurate for transvalvular velocity mapping than conventional 2D one-directional velocity-encoded (VE) MRI using a fixed acquisition plane [49,50]. From transvalvular velocity mapping, parameters such as cardiac output, ejection fraction, the effective forward flow volume, peak flow rate, peak velocity, retrograde flow and regurgitation fraction can be assessed.

Besides quantification of flow volume, the trans-atrioventricular flow rate graph allows assessment of diastolic function analysis. From the flow rate graph, usually the following diastolic function parameters are determined: early (E) and late or atrial (A) filling rates, E/A ratio, E-peak acceleration and E-peak deceleration duration. When 4D flow data extents to the left atrium, wave form analysis of pulmonary venous inflow, another indicator for diastolic function, may be assessed when velocity sensitivity and temporal resolution allow [51].Kumar et al. defined the fractional propagation parameter as the ratio between the longest jet stream of early diastole to the length of the entire ventricle [52]. The flow propagation velocity V_{prop} is another marker used for classifying diastolic function; V_{prop} describes the speed of the early filling wave propagation, which is driven by a pressure gradient between atrium and apex [53]. From the intra-ventricular inflow in combination with streamline visualization, the inflow propagation can be evaluated [54], albeit no 4D flow approach has been able to provide sufficiently high temporal resolution, required for assessing the transit time of blood flow waves over a relatively short propagation distance inside the left ventricle.

Moreover, retrospective positioning of measurement planes in a 4D flow dataset of thoracic vessels allows accurate flow quantification, giving access to various hemodynamic parameters such as, antegrade and retrograde flow, peak velocity, wall shear stress and kinetic energy. With this approach, the pressure drop over a valve stenosis can be estimated using the equation of Bernoulli and accurate peak velocity assessment at both sides of the valve. However, accurate velocity depiction in a high-grade stenosis might be difficult, as phase dispersion due to turbulent flow makes assessment of high peak velocities impossible. Furthermore, pressure gradients can be estimated from the intra-cardiac velocity field when using the Navier-Strokes equation. In this approach, it is assumed blood to be an incompressible Newtonian fluid and velocity to have zero variation (i.e., no turbulence) [55].

3.1

APPLICATIONS

In the following section, we will review the current status of 4D flow applications in clinical research and discuss promising results already obtained by applying the visualization and quantification tools that were described above. We will review first applications of 4D flow for evaluating intra-cardiac flow patterns in the atria and ventricles, followed by blood flow quantification across atrioventricular valves and finally, in the thoracic vessels.

Flow patterns in the atria

The left atrium is a conduit and reservoir which directs the inflow of blood from the four pulmonary veins towards the mitral valve during diastole and collects blood during systole. Visualization of 4D flow data revealed vortical flow in the left atrium during systole and diastole. This vortical flow is mainly formed from blood coming from the left pulmonary veins, while the blood from the right pulmonary veins passes along the vortex [56]. In the right atrium, a vortex is formed, rotating in an anti-clockwise direction [57]. In healthy volunteers, more and longer vortices and higher velocities were found in younger than in older individuals [58], which could be related to a decreased atrial compliance and late active (A-peak) filling becoming more dominant with ageing. The increased risk factor for thrombosis and systemic embolisms in patients with atrial fibrillation might partly be caused by disturbed flow. Preliminary results from Fluckiger et al. using 4D flow showed that patients with atrial fibrillation have lower atrial flow velocities and patients after treatment may reach similar velocities compared with age-matched controls [59]. In patients with mitral regurgitation, atrial vortices did not originate from the inflow through the (left) pulmonary vein, but from the regurgitation jet. Furthermore, a relation between mitral regurgitation fraction and left atrium turbulent kinetic energy loss was found [60].

Flow patterns in the left ventricle

Visualization techniques such as particle tracing have contributed to knowledge on the pathway of blood entering the ventricle through the atrioventricular valve and exiting through the aorta [57]. This pathway is assumed to be energy efficient and depends on multiple factors such as chamber shape, LV pressure, myocardial function and valve function. Changes in the cardiac flow pathway may influence cardiac function. Using computational fluid dynamics, simulated changes in flow direction have shown to reduce the heart pumping efficiency by 10% [40]. Moreover, it is suggested that changed hemodynamic forces act upon cardiac adaption through epigenetic mechanisms [61]. In an early study by Mohiaddin and colleagues, 4D flow was used to describe altered flow patterns in patients with dilated left ventricles. In normal subjects, the diastolic inflow through the mitral valve is directed towards the apex while in patients with dilated left ventricles, the inflow is directed towards the lateral wall, giving rise to a well-developed circular flow pattern [62]. Another study using 4D flow to describe LV inflow in patients with diastolic dysfunction showed that the high velocity inflow did not reach as far into the ventricle

as in healthy controls [52]. Figure 4 shows a laterally directed inflow in a patient who underwent correction for atrioventricular septum defect at early age, compared with a healthy control. The four-component evaluation of the intra-cardiac blood flow (i.e., direct flow, retained flow, delayed ejected flow and residual volume) in combination with particle tracing has provided unique insight in altered systolic and diastolic flow in patients with heart failure [63]. In patients with compensated heart failure, not only a decreased amount direct flow was observed, but also the kinetic energy of direct flow at end diastole was reduced. Furthermore, in a patient with a dilated cardiomyopathy, increased retained flow was described and related to increased kinetic energy loss of the retained flow [64]. The amount of residual volume potentially may predict intra-chamber thrombus formation.

Despite the high potential of 4D flow for evaluating intra-cardiac flow patterns, not much has been reported yet on vortex analysis in left ventricular flow patterns using 4D flow MRI. Foll et al. [58] used 4D flow with particle tracing and velocity vector fields to semi-quantitatively calculate vortex numbers and measure vortex duration and area based on the 2- and 4-chamber view and they observed smaller vortices in the base of the LV in women compared with men. Further-more, Toger et al. quantified vortex volume [65] extracted from 4D flow and described smaller volumes in patients with ischemic cardiomyopathy. Further studies using 4D flow are required to standardize vortex description and quantification and detect clinical relevant parameters.

3.1

Flow patterns in the right ventricle

Despite the increasing interest in the right ventricular function, particularly in congenital heart disease, little is known about right ventricular (RV) fluid dynamics. This is mainly due its complex anatomy and function and difficulties to visualize the RV in 3D with echocardiography. Only recently, a computational fluid dynamics model was suggested to simulate right ventricular flow [66]. Fredriksson et al. [67]used 4D flow in combination with particle tracing and four-component evaluation to describe differences in LV and RV blood flow distribution and kinetic energy in healthy volunteers. Diastolic characterization of RV vortices has been so far only reported in vivo using echocardiography in dogs [68]. Kheradvar and Pedrizetti [39] depicted the complexity of the vortex in the right ventricle. In patients with a corrected Tetralogy of Fallot (TOF), more, and pathological vortices were observed in the right atrium and ventricle using 4D flow [69,70].

Transvalvular flow quantification

As was described above, 4D flow allows reliable and reproducible transvalvular flow assessment at each of the four heart valves when retrospective valve tracking is implemented [50]. Accurate quantification of valve regurgitation is clinically important as the regurgitation fraction is an indicator for morbidity and mortality and therefore a determinant for surgical decision making. Assessment of regurgitation with 2D one-directional through-plane VE MR is still routine clini-cal practice, however, correlation between flow volumes at consecutive valves is lacking. With a 4D flow approach, conservation of mass has been described between the inlet and outlet

of cardiac chambers, a requirement for accurate quantitation of regurgitant volumes [71,72]. Several studies applied 4D flow with retrospective valve tracking in various patient groups, such as patients with functional mitral [73,74] or aortic valve insufficiency [75], patients with ischemic cardiomyopathy [76] and patients after correction of TOF [71]. These studies compared their flow results either with Doppler echocardiography or MRI planimetry, and concluded that 4D flow with retrospective valve tracking was superior to conventional 2D one-directional VE MRI for assessment of valve patency, regurgitation fraction and effective forward flow. Especially, quantification of eccentric jets is challenging with echocardiography [77]. Figure 5 shows an example of a 16 year old patient, corrected for atrioventricular septum defect at early age, who underwent a 4D flow evaluation as a part of follow-up cardiovascular MRI examination. Streamline visualization revealed multiple eccentric regurgitant jets over the atrioventricular valve, dynamically changing its orientation during systole. With 4D flow, multiple measurement planes were adjusted perpendicular to the regurgitation jet(s) throughout systole allowing reliable quantification of the regurgitation fraction.

While the gold standard in detecting intra-cardiac shunt remains echocardiography, a new visualization technique (i.e., volume-rendered stereoscopic velocity fusion visualization) based on 4D flow showed improvement of detection of shunts with MRI [78]. Moreover, volumes of shunts can be more accurately estimated when using 4D retrospective valve tracking approach in describing the forward flow through the cardiac chambers.

Classification of diastolic filling parameters obtained from trans-atrioventricular flow rate graphs in patients with ischemic heart failure using 4D flow showed excellent agreement with Doppler echocardiography, superior to conventional 2D one-directional VE MRI [79]. It should be taken into account that temporal resolution (0.8 ms) used in echocardiography is vastly superior to MRI. This might interfere with accurate assessment of peak velocity. Furthermore, with MRI, flow rate graphs are usually used for diastolic function testing in contrast to the velocity-time graphs with echocardiography. Also, with echocardiography, diastolic parameters are assessed at the tip of atrioventricular valves and measurement performed at annulus level, as done in MRI calculations, are known to result in changes in E/A ratio [80]. Therefore, new reference values for classifying various types of diastolic dysfunction should be defined and applied when using 4D flow.

Flow patterns in the thoracic vessels

Early 4D flow MRI studies have contributed to understanding blood flow in the aorta [81,82]. During systole, the normal blood flow in the aorta forms an anti-clockwise helix in the ascending aorta and clockwise helix in the aortic arch. Quantification of helicity is possible by combining velocity vectors with vorticity [83]. The highest velocity is found in the ascending aorta. During diastole, mild retrograde flow is visualized, which is important for perfusion of the coronary arteries. Regional differences of wall shear stress and oscillatory shear index are found in the healthy aorta, which might explain why specific locations are vulnerable for atherosclerotic

Figure 6. 4D flow visualization of a type A aortic dissection in a 50 year old male patient with Marfan syndrome.
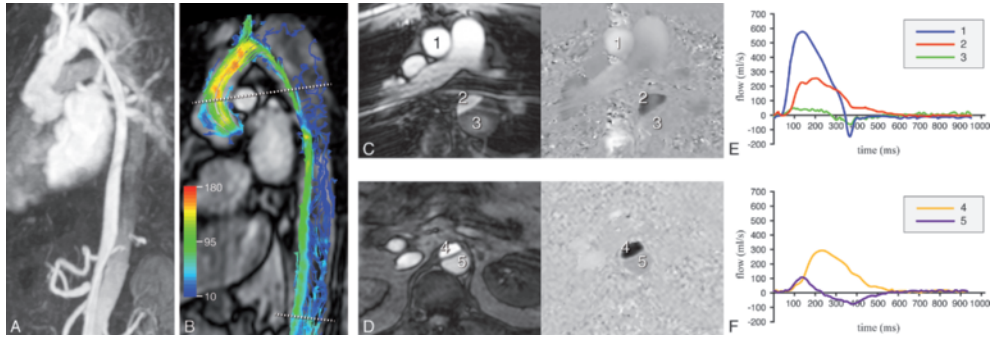
Obtained with 1.5T MRI. In A, a double-oblique sagittal maximal intensity projection of a contrast-enhanced magnetic resonance angiogram of the aorta is presented (i.e., first-pass imaging of 25 mL contrast bolus Dotarem (Guerbet, Gorinchem, the Netherlands) with a molarity of 0.5 mmol/mL, intravenously injected at an infusion rate of 2 mL/s). The dissection is visualized from the aortic arch to the abdominal aorta. In B, 4D flow MRI data of a mid-systolic phase is presented with velocity color coding (in cm/s) in velocity vector glyph representation. In the descending aorta, the true lumen is displayed with high flow velocity and the false lumen with low velocity. Through-plane velocity mapping is performed at ascending (labeled by 1) and proximal descending aorta (labeled by 2 and 3) at the level of the pulmonary trunk (in C and E) and at the abdominal aorta (labeled by 4 and 5 in D and F). The true lumen (labeled by 2 and 4) presents high pulsatile flow while the false lumen (labeled by 3 and 5) presents low flow.

3.1

plaque formation or for dissection [84]. Several studies using 4D flow MRI revealed pathological blood flow in diseased aortas, such as coarctation of the aorta [85] or dissection (Figure 6). Furthermore, 4D flow can be used to describe pathology and hemodynamics within the abnormal vessel due to valvular pathology. Patients with bicuspid aortic valves, who frequently develop aortic aneurysms, show aberrant helical flow patterns in the ascending aorta [83]. Whether this abnormal flow leads to aneurysm formation or whether the abnormal flow is a consequence of abnormal aorta wall structure and luminal size remains a debate. Other studies on aberrant helical flow in aortic aneurysms suggest additional value of 4D flow in prediction and prevention of aneurysms [86,87]. Sigovan et al. found a correlation between eccentric flow jets in patients with aortic valve diseases and local increased wall shear stress and aortic dilatation [88]. Figure 7 gives an example of a patient with aortic valve stenosis leading to an eccentric outflow jet, helical flow and aberrant laminar velocity and wall shear stress. Furthermore, in patients with aortic stenosis, the turbulent kinetic energy is high at the site of the stenosis and can be related with irreversible pressure loss [89]. When the stiffness of the aorta increases due to atherosclerosis, hypertension or connective tissue disorder such as the Marfan syndrome, an increased pulse wave velocity has been described as a precursor of aortic disease and related to end-organ damage [90,91]. Abnormal flow with altered wall shear stress has been described in these patients at relatively early stages of disease [92]. In patients with Marfan syndrome, multi-directional velocity-encoding has been proposed for accurate PWV assessment regionally in the aorta [38], relating lumen dilatation to increased PWV [93]. Another application for 4D flow of the aorta is the evaluation of abnormal retrograde flow, which can lead to retrograde embolization into the branches of the

aorta causing embolic stroke [94]. Early detection of retrograde flow might become a prognostic factor for embolization.

Using 4D flow, the normal blood flow pattern in the pulmonary circulation revealed two counter rotating helices in the left and right pulmonary artery [95]. In contrast, this helical flow was not found in a patient with corrected transposition of the great arteries and aberrant in a patient with correction of abnormal venous return. From 4D flow data obtained in patients after correction of a Tetralogy of Fallot, an increased peak systolic velocity in the pulmonary trunk and abnormal vertical flow in the main pulmonary artery were revealed [70,71]. A recent 4D flow study presented a patient with pulmonary regurgitation and pulmonary artery stenosis, who had a larger pressure drop and energy loss in the pulmonary artery branches [96]. Although some retrograde pulmonary flow is normal, increased backward flow has been described in pulmonary hypertension. Furthermore, presence of vorticity in the pulmonary flow pattern was

**Figure 7.** 4D flow visualization of the aortic outflow with different visualization techniques.
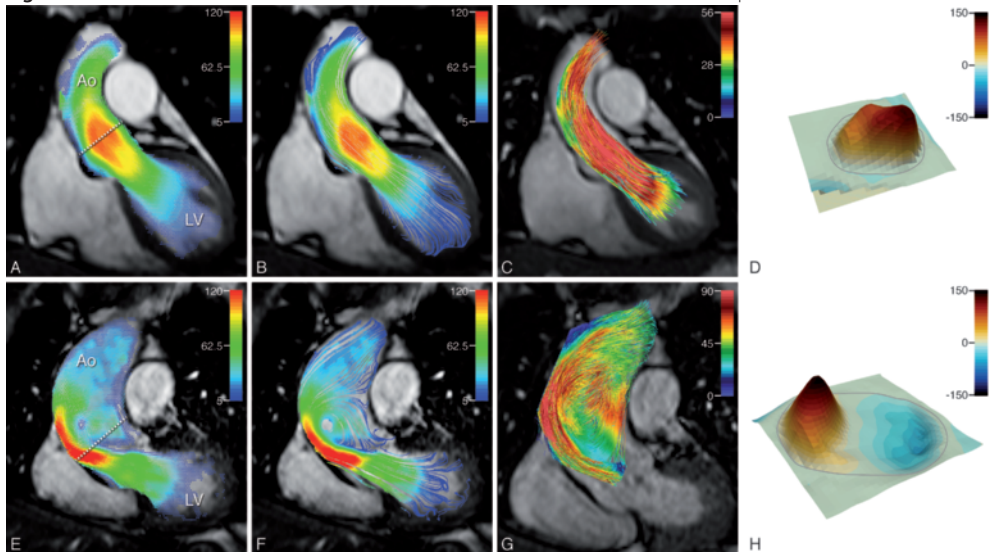
Velocity color coding (in cm/s) of the aortic outflow, by a velocity vector glyph representation (A and E), streamline representation (B and F) and pathline representation after forward particle tracing (C and G). 4D flow MRI data was obtained with a 3T MRI scanner in a 23 year old healthy female volunteer (A-C) (informed consent was obtained) and a 56 year old male patient with aortic valve stenosis and dilated aortic root, clinically referred for MRI. In the patient, 4D flow visualization revealed an eccentric aortic outflow jet distal to the valve stenosis (E-G) with an area of recirculating flow in the ascending aorta. Particle tracing revealed a strong helical flow pattern in the ascending aorta (G). The through-plane velocity profile was retrospectively reformatted at the level of the sinotubular junction (dotted line in A and E), and presented for a mid-systolic phase in panels D (volunteer) and H (patient). For the volunteer in D, an approximately laminar velocity profile was obtained, presenting a skewed parabolic profile with the maximal velocity shifted towards the inner curve (i.e., the left wall). The wall shear rate at the left wall was calculated at 37 s-1 and at the right wall 80 s-1. For the patient, backward flow was visualized in the dilated ascending aorta at the left wall, with a calculated wall shear rate of −144 s-1 and at the right wall of 241 s-1. LV left ventricle, Ao aorta.

correlated with pulmonary hypertension and the duration of this abnormal pattern has been correlated with mean pulmonary artery pressure [97].

A unique patient group for the clinical application of 4D flow MRI constitute patients with a Fontan palliation of their congenital heart defect. The Fontan procedure is the treatment for patients with a univentricular heart where biventricular repair is not possible. Several surgical approaches have been developed to create the connection of the superior and inferior vena cava with the right and left pulmonary artery: the total cavopulmonary connection (TCPC). However, late complications frequently occur. Etiology and risk factors for complications, including protein losing entropathy (PLE), development of pulmonary arteriovenous malformations (PAVMs), thrombosis, stenosis and aneurysms, are largely unknown. Understanding of flow patterns in the Fontan circulation might advance knowledge in the etiology of these risk factors and contribute to improvement of surgical techniques. Recent work has successfully employed 4D flow for visualizing and quantifying the distribution of caval flow towards the right and left pulmonary artery [98,99]. An unequal distribution of blood flow is associated with pulmonary arteriovenous malformations [100]. Moreover, it is possible to demonstrate kinetic energy loss due to helical flow formation in the pulmonary arteries. As can be seen in Figure 8, altered flow patterns with

3.1

Figure 8. 4D flow streamline visualization of the Fontan circulation.
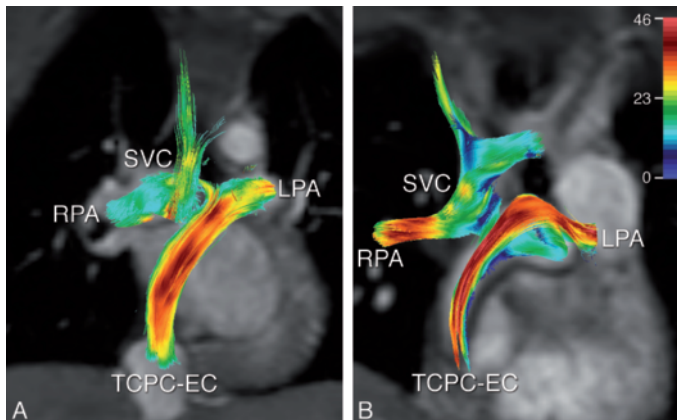
Two patients who underwent surgery at the age of 5, during which a total cavopulmonary connection with an extra cardiac conduit (TCPC-EC) was made to connect the inferior (IVC) and superior vena cava (SVC) to both the left (LPA) and right pulmonary artery (RPA). In A, a 13 year old female patient is presented, with normal distribution of blood flow through the conduit without loss of kinetic energy. Stroke volumes and kinetic energy per heart beat: SVC 12 ml and 0.12 mJ, IVC 18 ml and 0.09 mJ, LPA 16 ml and 0.10 mJ, RPA 15 ml and 0.12 mJ. Total volume at the inlet of the connection was 30 ml with a kinetic energy of 0.21 mJ, and the total volume at outlet was 31 ml with kinetic energy of 0.22 mJ. In B, a 15 year old female patient is presented, with an area of recirculating flow present in the connection, proximal to the LPA, resulting in significant kinetic energy loss. Stroke volumes and kinetic energy per heart beat: SVC 21 ml and 0.25 mJ, IVC 34 ml and 2.0 mJ, LPA 26 ml and 0.41 mJ, RPA 29 ml and 0.18 mJ. Total volume at the inlet was 55 ml with kinetic energy of 2.25 mJ, total volume at outlet was 55 ml with kinetic energy of 0.59 mJ, resulting in a total kinetic energy loss of 1.66 mJ. Prior to MRI, informed consent was obtained from the patients and their parents.

related kinetic energy loss can be observed in patients with a similar extra cardial TCPC, possibly due to differences in geometry of the connection of the conduit to the pulmonary arteries.

CONCLUSION AND FUTURE PROSPECTIVE

4D flow MRI acquisition techniques improved rapidly over the last three decades. Shorter scan duration made 4D flow applicable for clinical use. The concomitant development of visualization tools such as streamlines and particle tracing enriched knowledge on blood flow hemodynamics. Intra-cardiac blood flow patterns (e.g., vortices) may possibly add to the diagnosis of diastolic dysfunction. Moreover, as increasing evidence arises that hemodynamics play an important role in vascular and myocardial remodelling, altered blood flow patterns can possibly be used to predict pathology such as aneurysm or thrombus formation and early therapy can be aimed at prevention of these pathologies. Besides qualitative interpretation of 4D flow data by visualization techniques, quantitative tools are increasingly used. Further studies are required to evaluate which hemodynamic markers will be clinically relevant and in what way 4D flow can help to improve early detection of pathology and identify response to treatment.

ACKNOWLEDGEMENTS

REFERENCES

1. Moran PR. A flow velocity zeugmatographic interlace for NMR imaging in humans. Magn Reson Imaging 1982;1:197-203.

2. Bryant DJ, Payne JA, Firmin DN, et al. Measurement of flow with NMR imaging using a gradient pulse and phase difference technique. J Comput Assist Tomogr 1984;8:588-593.

3. van Dijk EJ. Direct cardiac NMR imaging of heart wall and blood flow velocity. J Comput Assist Tomogr 1984;8:429-436.

4. Atkinson DJ, Edelman RR. Cineangiography of the heart in a single breath hold with a segmented turboFLASH sequence. Radiology 1991;178:357-360.

5. van Dijk P. ECG-triggered NMR imaging of the heart. Diagn Imaging Clin Med 1984;53:29-37.

6. Lenz GW, Haacke EM, White RD. Retrospective cardiac gating: a review of technical aspects and future directions. Magn Reson Imaging 1989;7:445-455.

7. Chai P, Mohiaddin R. How we perform cardiovascular magnetic resonance flow assessment using phase-contrast velocity mapping. J Cardiovasc Magn Reson 2005;7:705-716.

8. Carr JJ, Hendel RC, White RD, et al. 2013 appropriate utilization of cardiovascular imaging: a methodology for the development of joint criteria for the appropriate utilization of cardiovascular imaging by the American College of Cardiology Foundation and American College of Radiology. J Am Coll Cardiol 2013;61:2199-2206.

9. Pelc NJ, Bernstein MA, Shimakawa A, et al. Encoding strategies for three-direction phase-contrast MR imaging of flow. J Magn Reson Imaging 1991;1:405-413.

10. Bogren HG, Mohiaddin RH, Kilner PJ, J et al. Blood flow patterns in the thoracic aorta studied with three-directional MR velocity mapping: the effects of age and coronary artery disease. J Magn Reson Imaging 1997;7:784-793.

11. Wigstrom L, Sjoqvist L, Wranne B. Temporally resolved 3D phase-contrast imaging. Magn Reson Med 1996;36:800-803.

12. Thunberg P, Karlsson M, Wigstrom L. Accuracy and reproducibility in phase contrast imaging using SENSE. Magn Reson Med 2003;50:1061-1068.

13. Baltes C, Kozerke S, Hansen MS, et al. Accelerating cine phase-contrast flow measurements using k-t BLAST and k-t SENSE. Magn Reson Med 2005;54:1430-1438.

14. Firmin DN, Klipstein RH, Hounsfield GL, et al. Echo-planar high-resolution flow velocity mapping. Magn Reson Med 1989;12:316-327.

15. Gu T, Korosec FR, Block WF, et al. PC VIPR: a high-speed 3D phase-contrast method for flow quantification and high-resolution angiography. AJNR Am J Neuroradiol 2005;26:743-749.

16. Sigfridsson A, Petersson S, Carlhall CJ, et al. Four-dimensional flow MRI using spiral acquisition. Magn Reson Med 2012;68:1065-1073.

17. McConnell MV, Khasgiwala VC, Savord BJ, et al. Comparison of respiratory suppression methods and navigator locations for MR coronary angiography. AJR Am J Roentgenol 1997;168:1369-1375.

18. Baltes C, Kozerke S, Atkinson D, et al. Retrospective respiratory motion correction for navigated cine velocity mapping. J Cardiovasc Magn Reson 2004;6:785-792.

19. Markl M, Harloff A, Bley TA, et al. Time-resolved 3D MR velocity mapping at 3T: improved navigator-gated assessment of vascular anatomy and blood flow. J Magn Reson Imaging 2007;25:824-831.

20. Nehrke K, Bornert P, Manke D, et al. Free-breathing cardiac MR imaging: study of implications of respiratory motion--initial results. Radiology 2001;220:810-815.

21. Buehrer M, Curcic J, Boesiger P, et al. Prospective self-gating for simultaneous compensation of cardiac and respiratory motion. Magn Reson Med 2008;60:683-690.

22. Markl M, Kilner PJ, Ebbers T. Comprehensive 4D velocity mapping of the heart and great vessels by cardiovascular magnetic resonance. J Cardiovasc Magn Reson 2011;13:7.

23. Walker PG, Cranney GB, Scheidegger MB, et al. Semiautomated method for noise reduction and background phase error correction in MR phase

velocity data. J Magn Reson Imaging 1993;3:521-530.

24.   Markl M, Bammer R, Alley MT, et al. Generalized reconstruction of phase contrast MRI: analysis and correction of the effect of gradient field distortions. Magn Reson Med 2003;50:791-801.

25.   Gatehouse PD, Rolf MP, Bloch KM, et al. A multi-center inter-manufacturer study of the temporal stability of phase-contrast velocity mapping background offset errors. J Cardiovasc Magn Reson 2012;14:72.

26.   Lorenz R, Bock J, Snyder J, et al. Influence of eddy current, Maxwell and gradient field corrections on 3D flow visualization of 3D CINE PC-MRI data. Magn Reson Med 2013;72:33-40.

27.   Holland BJ, Printz BF, Lai WW. Baseline correction of phase-contrast images in congenital cardiovascular magnetic resonance. J Cardiovasc Magn Reson 2010;12:11.

28.   Napel S, Lee DH, Frayne R, et al. Visualizing three-dimensional flow with simulated streamlines and three-dimensional phase-contrast MR imaging. J Magn Reson Imaging 1992;2:143-153.

29.   Nordmeyer S, Riesenkampff E, Messroghli D, et al. Four-dimensional velocity-encoded magnetic resonance imaging improves blood flow quantification in patients with complex accelerated flow. J Magn Reson Imaging 2013;37:208-216.

30.   Buonocore MH. Visualizing blood flow patterns using streamlines, arrows, and particle paths. Magn Reson Med 1998;40:210-226.

31.   Eriksson J, Carlhall CJ, Dyverfeldt P, et al. Semi-automatic quantification of 4D left ventricular blood flow. J Cardiovasc Magn Reson 2010;12:9.

32.   Weinkauf T, Theisel H. Streak lines as tangent curves of a derived vector field. IEEE Trans Vis Comput Graph 2010;16:1225-1234.

33.   Kohler B, Gasteiger R, Preim U, et al. Semi-Automatic Vortex Extraction in 4D PC-MRI Cardiac Blood Flow Data using Line Predicates. IEEE Trans Vis Comput Graph 2013;19:2773-2782.

34.   Dyverfeldt P, Sigfridsson A, Kvitting JP, et al. Quantification of intravoxel velocity standard deviation and turbulence intensity by generalizing phase-contrast MRI. Magn Reson Med 2006;56:850-858.

35.   Oyre S, Paaske WP, Ringgaard S, et al. Automatic accurate non-invasive quantitation of blood flow, cross-sectional vessel area, and wall shear stress by modelling of magnetic resonance velocity data. Eur J Vasc Endovasc Surg 1998;16:517-524.

36.   Stalder AF, Russe MF, Frydrychowicz A, et al. Quantitative 2D and 3D phase contrast MRI: optimized analysis of blood flow and vessel wall parameters. Magn Reson Med 2008;60:1218-1231.

37.   Wentland AL, Wieben O, Francois CJ, et al. Aortic pulse wave velocity measurements with under-sampled 4D flow-sensitive MRI: comparison with 2D and algorithm determination. J Magn Reson Imaging 2013;37:853-859.

38.   Westenberg JJ, de Roos A., Grotenhuis HB, et al. Improved aortic pulse wave velocity assessment from multislice two-directional in-plane velocity-encoded magnetic resonance imaging. J Magn Reson Imaging 2010;32:1086-1094.

39.   Kheradvar A, Pedrizzetti G. Vortex formatin in the cardiovascular system. London UK, Springer-Verlag; 2012.

40.   Pedrizzetti G, Domenichini F. Nature optimizes the swirling flow in the human left ventricle. Phys Rev Lett 2005;95:108101.

41.   Charonko JJ, Kumar R, Stewart K, et al. Vortices formed on the mitral valve tips aid normal left ventricular filling. Ann Biomed Eng 2013;41:1049-1061.

42.   Bellhouse BJ. Fluid mechanics of a model mitral valve and left ventricle. Cardiovasc Res 1972;6:199-210.

43.   Ghosh E, Shmuylovich L, Kovacs SJ. Vortex formation time-to-left ventricular early rapid filling relation: model-based prediction with echocardiographic validation. J Appl Physiol 2010;109:1812-1819.

44.   Hong GR, Pedrizzetti G, Tonti G, et al. Characterization and quantification of vortex flow in the human left ventricle by contrast echocardiography using vector particle image velocimetry. JACC Cardiovasc Imaging 2008;1:705-717.

45.   Zhang H, Liu L, Chen L, et al. The evolution of intraventricular vortex during ejection studied by using vector flow mapping. Echocardiography 2013;30:27-36.

46. Gharib M, Rambod E, Kheradvar A, et al. Optimal vortex formation as an index of cardiac health. Proc Natl Acad Sci U S A 2006;103:6305-6308.

47. Kheradvar A, Assadi R, Kheradvar A, et al. Assesment of transmitral vortex formation in patients with diastolic dysfunction. J Am Soc Echocardiogr 2012;25:220-227.

48. Stewart KC, Charonko JC, Niebel CL, et al. Left ventricular formation time is unaffected by diastolic impairment. Am J Physiol Heart Circ Physiol 2012;303:H1255-1262.

49. Westenberg JJ, Roes SD, Ajmone MN, et al. Mitral valve and tricuspid valve blood flow: accurate quantification with 3D velocity-encoded MR imaging with retrospective valve tracking. Radiology 2008;249:792-800.

50. Roes SD, Hammer S, van der Geest RJ, et al. Flow assessment through four heart valves simultaneously using 3-dimensional 3-directional velocity-encoded magnetic resonance imaging with retrospective valve tracking in healthy volunteers and patients with valvular regurgitation. Invest Radiol 2009;44:669-675.

51. Westenberg JJ. CMR for Assessment of Diastolic Function. Curr Cardiovasc Imaging Rep 2011;4:149-158.

52. Kumar R, Charonko J, Hundley WG, et al. Assesment of left ventricular diastolic function using 4-dimensional phase-contrast cardiac magnetic resonance. J Comput Assist Tomogr 2011;35:108-112.

53. Garcia MJ, Thomas JD, Klein AL. New Doppler echocardiographic applications for the study of diastolic function. J Am Coll Cardiol 1998;32:865-875.

54. van den Boogaard PJ, Ajmone MN, Bax JJ, et al. Left ventricular inflow propagation velocity for diastolic function testing: head-to-head comparison between velocity-encoded MRI and color M-mode Doppler echocardiography. J Cardiovasc Magn Reson 2013;15(Suppl 1):P54.

55. Ebbers T, Wigstrom L, Bolger AF, et al. Noninvasive measurement of time-varying three-dimensional relative pressure fields within the human heart. J Biomech Eng 2002;124:288-293.

56. Fyrenius A, Wigstrom L, Ebbers T, et al. Three dimensional flow in the human left atrium. Heart 2001;86:448-455.

57. Kilner PJ, Yang GZ, Wilkes AJ, et al. Asymmetric redirection of flow through the heart. Nature 2000;404:759-761.

58. Foll D, Taeger S, Bode C, et al. Age, gender, blood pressure, and ventricular geometry influence normal 3D blood flow characteristics in the left heart. Eur Heart J Cardiovasc Imaging 2013;14:366-373.

59. Fluckiger JU, Goldberger JJ, Lee DC, et al. Left atrial flow velocity distribution and flow coherence using four-dimensional FLOW MRI: A pilot study investigating the impact of age and Pre- and Postintervention atrial fibrillation on atrial hemodynamics. J Magn Reson Imaging 2013;38:580-587.

60. Dyverfeldt P, Kvitting JP, Carlhall CJ, et al. Hemodynamic aspects of mitral regurgitation assessed by generalized phase-contrast MRI. J Magn Reson Imaging 2011;33:582-588.

61. Pasipoularides A. Diastolic filling vortex forces and cardiac adaptations: probing the epigenetic nexus. Hellenic J Cardiol 2012;53:458-469.

62. Mohiaddin RH. Flow patterns in the dilated ischemic left ventricle studied by MR imaging with velocity vector mapping. J Magn Reson Imaging 1995;5:493-498.

63. Eriksson J, Bolger AF, Ebbers T, et al. Four-dimensional blood flow-specific markers of LV dysfunction in dilated cardiomyopathy. Eur Heart J Cardiovasc Imaging 2013;14:417-424.

64. Bolger AF, Heiberg E, Karlsson M, et al. Transit of blood flow through the human left ventricle mapped by cardiovascular magnetic resonance. J Cardiovasc Magn Reson 2007;9:741-747.

65. Toger J, Kanski M, Carlsson M, et al. Vortex ring formation in the left ventricle of the heart: analysis by 4D flow MRI and Lagrangian coherent structures. Ann Biomed Eng 2012;40:2652-2662.

66. Mangual JO, Domenichini F, Pedrizzetti G. Describing the highly three dimensional Right Ventricle flow. Ann Biomed Eng 2012;40:1790-1801.

67. Fredriksson AG, Zajac J, Eriksson J, et al. 4-D blood flow in the human right ventricle. Am J Physiol Heart Circ Physiol 2011;301:H2344-H2350.

3.1

68.   Pasipoularides A, Shu M, Shah A, et al. Diastolic right ventricular filling vortex in normal and volume overload states. Am J Physiol Heart Circ Physiol 2003;284:H1064-H1072.

69.   Francois CJ, Srinivasan S, Schiebler ML, et al. 4D cardiovascular magnetic resonance velocity mapping of alterations of right heart flow patterns and main pulmonary artery hemodynamics in tetralogy of Fallot. J Cardiovasc Magn Reson 2012;14:16.

70.   Geiger J, Markl M, Jung B, et al. 4D-MR flow analysis in patients after repair for tetralogy of Fallot. Eur Radiol 2011;21:1651-1657.

71.   van der Hulst AE, Westenberg JJ, Kroft LJ, et al. Tetralogy of fallot: 3D velocity-encoded MR imaging for evaluation of right ventricular valve flow and diastolic function in patients after correction. Radiology 2010;256:724-734.

72.   Westenberg JJ, Doornbos J, Versteegh MI, et al. Accurate quantitation of regurgitant volume with MRI in patients selected for mitral valve repair. Eur J Cardiothorac Surg 2005;27:462-466.

73.   Shanks M, Siebelink HM, Delgado V, et al. Quantitative assessment of mitral regurgitation: comparison between three-dimensional transesophageal echocardiography and magnetic resonance imaging. Circ Cardiovasc Imaging 2010;3:694-700.

74.   Marsan NA, Westenberg JJ, Ypenburg C, et al. Quantification of functional mitral regurgitation by real-time 3D echocardiography: comparison with 3D velocity-encoded cardiac magnetic resonance. JACC Cardiovasc Imaging 2009;2:1245-1252.

75.   Ewe SH, Delgado V, van der Geest R, et al. Accuracy of three-dimensional versus two-dimensional echocardiography for quantification of aortic regurgitation and validation by three-dimensional three-directional velocity-encoded magnetic resonance imaging. Am J Cardiol 2013;112:560-566.

76.   Marsan NA, Westenberg JJ, Roes SD, et al. Three-dimensional echocardiography for the preoperative assessment of patients with left ventricular aneurysm. Ann Thorac Surg 2011;91:113-121.

77.   Biner S, Rafique A, Rafii F, et al. Reproducibility of proximal isovelocity surface area, vena contracta, and regurgitant jet area for assessment of mitral regurgitation severity. JACC Cardiovasc Imaging 2010;3:235-243.

78.   Hsiao A, Lustig M, Alley MT, et al. Evaluation of valvular insufficiency and shunts with parallel-imaging compressed-sensing 4D phase-contrast MR imaging with stereoscopic 3D velocity-fusion volume-rendered visualization. Radiology 2012;265:87-95.

79.   Brandts A, Bertini M, van Dijk EJ, et al. Left ventricular diastolic function assessment from three-dimensional three-directional velocity-encoded MRI with retrospective valve tracking. J Magn Reson Imaging 2011;33:312-319.

80.   Appleton CP, Jensen JL, Hatle LK, et al. Doppler evaluation of left and right ventricular diastolic function: a technical guide for obtaining optimal flow velocity recordings. J Am Soc Echocardiogr 1997;10:271-292.

81.   Bogren HG, Buonocore MH. 4D magnetic resonance velocity mapping of blood flow patterns in the aorta in young vs. elderly normal subjects. J Magn Reson Imaging 1999;10:861-869.

82.   Kilner PJ, Yang GZ, Mohiaddin RH, F et al. Helical and retrograde secondary flow patterns in the aortic arch studied by three-directional magnetic resonance velocity mapping. Circulation 1993;88:2235-2247.

83.   Lorenz R, Bock J, Barker AJ, et al. 4D flow magnetic resonance imaging in bicuspid aortic valve disease demonstrates altered distribution of aortic blood flow helicity. Magn Reson Med 2013;71:1542-53.

84.   Frydrychowicz A, Stalder AF, Russe MF, et al. Three-dimensional analysis of segmental wall shear stress in the aorta by flow-sensitive four-dimensional-MRI. J Magn Reson Imaging 2009;30:77-84.

85.   Grotenhuis HB, de Roos A. Structure and function of the aorta in inherited and congenital heart disease and the role of MRI. Heart 2011;97:66-74.

86.   Hope MD, Meadows AK, Hope TA, et al. Clinical evaluation of aortic coarctation with 4D flow MR imaging. J Magn Reson Imaging 2010;31:711-718.

87.   Frydrychowicz A, Arnold R, Hirtler D, et al. Multidirectional flow analysis by cardiovascular magnetic resonance in aneurysm development following repair of aortic coarctation. J Cardiovasc Magn Reson 2008;10:30.

88. Sigovan M, Hope MD, Dyverfeldt P, et al. Comparison of four-dimensional flow parameters for quantification of flow eccentricity in the ascending aorta. J Magn Reson Imaging 2011;34:1226-1230.

89. Dyverfeldt P, Hope MD, Tseng EE, et al. Magnetic resonance measurement of turbulent kinetic energy for the estimation of irreversible pressure loss in aortic stenosis. JACC Cardiovasc Imaging 2013;6:64-71.

90. van Elderen SG, Westenberg JJ, Brandts A, et al. Increased aortic stiffness measured by MRI in patients with type 1 diabetes mellitus and relationship to renal function. AJR Am J Roentgenol 2011;196:697-701.

91. Brandts A, van Elderen SG, Westenberg JJ, et al. Association of aortic arch pulse wave velocity with left ventricular mass and lacunar brain infarcts in hypertensive patients: assessment with MR imaging. Radiology 2009;253:681-688.

92. Geiger J, Markl M, Herzer L, et al. Aortic flow patterns in patients with Marfan syndrome assessed by flow-sensitive four-dimensional MRI. J Magn Reson Imaging 2012;35:594-600.

93. Kroner ES, Scholte AJ, de Koning PJ, et al. MRI-assessed regional pulse wave velocity for predicting absence of regional aorta luminal growth in marfan syndrome. Int J Cardiol 2013;167:2977-2982.

94. Harloff A, Simon J, Brendecke S, et al. Complex plaques in the proximal descending aorta: an underestimated embolic source of stroke. Stroke 2010;41:1145-1150.

95. Bachler P, Pinochet N, Sotelo J, et al. Assessment of normal flow patterns in the pulmonary circulation by using 4D magnetic resonance velocity mapping. Magn Reson Imaging 2013;31:178-188.

96. Lee N, Taylor MD, Hor KN, et al. Non-invasive evaluation of energy loss in the pulmonary arteries using 4D phase contrast MR measurement: a proof of concept. Biomed Eng Online 2013;12:93.

97. Reiter G, Reiter U, Kovacs G, et al. Magnetic resonance-derived 3-dimensional blood flow patterns in the main pulmonary artery as a marker of pulmonary hypertension and a measure of elevated mean pulmonary arterial pressure. Circ Cardiovasc Imaging 2008;1:23-30.

98. Bachler P, Valverde I, Pinochet N, et al. Caval blood flow distribution in patients with Fontan circulation: quantification by using particle traces from 4D flow MR imaging. Radiology 2013;267:67-75.

99. Markl M, Geiger J, Kilner PJ, et al. Time-resolved three-dimensional magnetic resonance velocity mapping of cardiovascular flow paths in volunteers and patients with Fontan circulation. Eur J Cardiothorac Surg 2011;39:206-212.

100. Srivastava D, Preminger T, Lock JE, et al. Hepatic venous blood and the development of pulmonary arteriovenous malformations in congenital heart disease. Circulation 1995;92:1217-1222.

3.1

Chapter 3.2

Characterization and improved quantification of left ventricular inflow using streamline visualization with 4DFlow MRI in healthy controls and patients after atrioventricular septal defect correction

Emmeline E. Calkoen, Arno A.W. Roest, Lucia J.M. Kroft, Rob J. van der Geest, Monique R.M. Jongbloed, Pieter J. van den Boogaard, Nico A. Blom, Mark G. Hazekamp, Albert de Roos and Jos J.M. Westenberg

ABSTRACT

Purpose
To evaluate trans-left atrioventricular valve (LAVV) blood flow and optimize left ventricular inflow quantification in healthy controls and patients after atrioventricular septal defect (AVSD) correction.

Materials and Methods
Twenty-five patients after AVSD correction and 25 controls underwent 4DFlow MRI. Using streamline visualization in four- and two-chamber views, inflow direction at early and late filling was defined at the annulus level and at the peak inflow velocity (PIV) level. Trans-LAVV flow volume and velocity were assessed from a static 2D-multiplanar-reformat (MPR), a 4D-MPR tracking LAVV annulus and a 4D-MPR tracking the PIV-level, angulated perpendicular to the inflow.

Results
In patients, on average 9 more laterally directed inflow was found at the PIV-level compared with controls. In controls, 4DFlow velocity mapping with LAVV annulus tracking resulted in lower absolute error with aortic flow (3 (1–8) mL) than with static 2D-MPR (7 (4–16) mL, P ¼ 0.001). In patients, 4D-MPR tracking the PIVlevel, resulted in lower absolute error with aortic flow (2 (1–4) mL) than with 4D-MPR LAVV annulus tracking (6 (2–10) mL, P = 0.003).

Conclusion
Streamline visualization of 4DFlow MRI data revealed dynamic trans-LAVV inflow and more lateral flow after AVSD correction. Streamline visualization improved trans-LAVV flow quantification as the positioning and angulation of the measurement plane was optimized, allowing an accurate assessment of left ventricular inflow.

INTRODUCTION

Quantification of blood flow over the atrioventricular valve (AVV) is essential in the evaluation of valve function and ventricular filling [1]. Left atrioventricular valve (LAVV) dysfunction and diastolic dysfunction are both indicators of cardiovascular morbidity and mortality [2]. Moreover, disturbances of ventricular inflow have been shown to reduce the effi- ciency of the heart pump [3]. After correction of an atrioventricular septal defect (AVSD), LAVV morphology is changed substantially [4], but limited data are available on the physiological consequences of altered ventricular inflow.

Time-resolved 3D magnetic resonance imaging (MRI) with three-directional velocity-encoding (VE), termed 4DFlow, can be applied to obtain timedependent distribution of blood flow veloci- ties in the cardiac chambers during the whole cardiac cycle. Streamlines are lines representing the blood flow direction at one instant in time, as these lines are tangent to the local velocity vectors, connecting at all points along the direction of these lines [5]. Moreover, they can be presented with color-coding according to velocity magnitude [6] and therefore allow localiza- tion of the peak inflow velocities.

Blood flow over the atrioventricular valves can be quantified using a static 2D plane, which is commonly used in a clinical setting, but this approach has been shown to overestimate flow vol- ume as the annulus plane moves through the static measurement plane [7]. With 4D retrospec- tive valve tracking, blood flow over the atrioventricular valves can be quantified more accurately, with the measurement plane adapting to the valve motion, as was validated in phantoms and volunteers [8]. In these reports, valve tracking was used to follow the anatomical annular plane, assuming blood flow to be orthogonal to the annulus during LV filling. Errors in the location and angulation of the reformatting plane may affect flow assessment [9]. Furthermore, changes in inflow direction during the cardiac cycle may also affect the assessment of diastolic parameters derived from AVV flow, measured with echocardiography and MRI [10].

We hypothesize that knowledge of the LV inflow pattern, depicted with streamline visual- ization in healthy controls and patients after AVSD correction, will aid the retrospective valve tracking procedure: by locating the peak inflow velocity near the tips of the LAVV leaflets and aligning the measurement plane perpendicular to the inflow direction, flow quantification may be improved.

Subsequently, the purpose of our study was to characterize trans-LAVV blood forward flow in healthy controls and patients after AVSD correction using 4DFlow MRI with streamline visualiza- tion and to assess the effect of optimal positioning of the measurement plane to assess the LAVV forward flow.

3.2

MATERIAL AND METHODS

Study Population

The study was approved by the local Ethics Committee and written informed consent was obtained from all participants or their parents. Between October 2012 and July 2013, 28 patients with a history of corrected AVSD were prospectively and consecutively enrolled in the study from an available surgical database [11]. Patients younger than 8 years, with pacemaker dependency and/or Down syndrome were excluded. Twenty-five controls with a similar age with no history of cardiac disease were included for comparison.

MRI

Whole-heart 4DFlow was obtained using a 3T-MRI scanner (Ingenia, Philips Medical Systems, Best, The Netherlands) with maximal gradient amplitude of 45 mT/m for each axis and a slew rate of 200 T/m/sec. A combination of FlexCoverage Posterior coil in the tabletop with a dStream Torso coil was used, providing up to 32 coil elements for signal reception. In the majority of patients (21 out of 25), gadolinium contrast agent (0.015 mmol/kg body weight, Dotarem, Guerbet, Aulnay-sous-Bois, France) was administrated just before the 4DFlow acquisition. Velocity encoding of 150 cm/s was used in all three directions, spatial resolution 2.3×2.3×3.0–4.2mm, flip angle 10 °, echo time (TE) 3.2 msec, and repetition time (TR) 7.7 msec, resulting in a maximal true temporal resolution of 4 x TR = 31 msec. Parallel imaging was performed using SENSE with factor of 2 and echo planar imaging with factor 5 was used for acquisition acceleration. The commercially available concomitant gradient correction and local phase correction filter were applied. The 4DFlow acquisition time was, for a typical heart rate of 60–80 beats per minute, on average 8–10 minutes. Furthermore, a two-chamber view of the left ventricle, a four-chamber view as well as a short-axis stack of slices, to measure left ventricular volumes and compute the ejection fraction (EF), were acquired with a steady-state free-precession sequence with TE/TR 1.5/3.0; 350mm field of view, 8 mm section thickness; 45 ° flip angle; spatial resolution 1.0×1.0×8.0mm, three signal averages and parallel imaging with SENSE factor 2. Manual contour segmentation of LV volume was performed on the short axis stack to compute EF (EF = LV end diastolic volume – LV end systolic volume / LV end diastolic volume). During all scans, free breathing was allowed and no respiratory compensation was performed, retrospective vectorcardiogram-gating was performed, and for all acquisitions 30 phases were reconstructed representing one average cardiac cycle.

Image Analysis: Characterization of LAVV Forward Flow

Image analysis was performed using in-house developed Mass software. 2D streamlines were generated based on image pixels within the LV cavity exceeding a minimum velocity of 10 cm/s, defined as candidate seed points. Streamlines were computed by applying a simple Euler integration method in both forward and backward directions using a step size of 1 pixel dimension

and using bilinear image interpolation. Integration was terminated when either the velocity was below 10 cm/s, or the trace length reached a length of 80 screen pixels. To avoid visual cluttering of the generated streamlines, images were displayed enlarged on the computer monitor and the distance between seed points was forced to be 20 screen pixels at minimum. Three angles were measured in the twoand four-chamber view to characterize the valve morphology and the inflow pattern: the angle between the annulus and long-axis (Fig. 1A, angle 1), the angle between annulus and inflow direction at annulus level (Fig. 1B, angle 2) and the angle between the inflow direction and a plane parallel to the annulus at the level of peak inflow velocity (PIV) (Fig. 1B, angle 3). Angle 1 and angle 2 were measured at E-peak and Apeak, while angle 3 was measured only at E-peak, as the highest inflow velocity appeared at the E-peak. The timepoints of E- and A-peak were defined based on the flow-time curve calculated from velocity mapping after retrospective valve tracking. Finally, to combine the effect of annulus movement and flow direction through the annulus, we calculated the inflow angle defined as

Figure 1. Inflow angles.
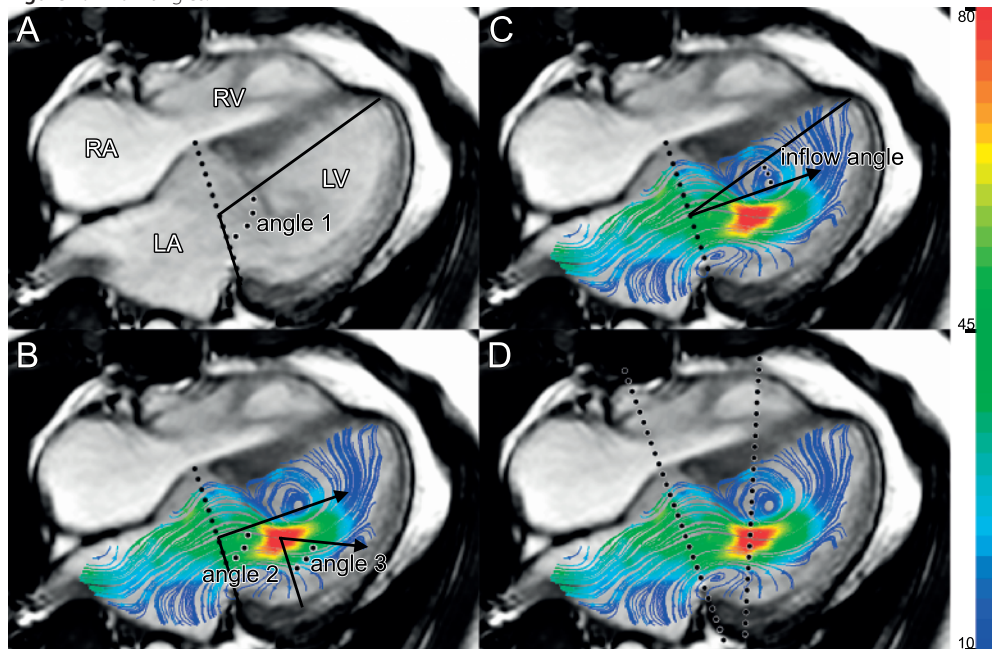
Streamline representation with velocity color coding (in cm/s) of LV inflow pattern illustrates the measured angles in the four-chamber view. A: The angle between annulus and long-axis (angle 1), where the annulus was manually identified as the line between the septal and lateral attachment of the LAVV and the long-axis was recognized as the line through the center of the annulus and the apex. B: The angles between annulus and inflow at the annulus level (angle 2) and peak inflow velocity level (angle 3). C: The inflow angle calculated as the difference between long-axis and inflow (angle 1 – angle 2), at the annulus level in this example. D: The positioning of the two reformat planes are shown at the annulus level and at the PIV-level, angulated perpendicular to the inflow. Left ventricle (LV), right ventricle (RV), left atrium (LA), and right atrium (RA).

the angle between long-axis and inflow at both levels (angle 1 – angle 2 and angle 1 – angle 3) (Fig. 1C). For these calculations, a positive value designates lateral inflow relative to the longaxis on the four-chamber view and anterior inflow relative to the long-axis on the two-chamber view. Intra- and interobserver variation of these angle measurements was tested by repeated analysis in 10 randomly selected controls and 10 patients. Two observers (E.C. with 2 years of cardiac MRI experience and J.W. with over 15 years of cardiac MRI experience) performed these analyses blinded for each other, with one observer (E.C.) performing the analyses twice with an interexamination time of 3 weeks.

Image Analysis: Quantification of LAVV Forward Flow

LAVV velocity mapping was performed retrospectively. For comparison with the clinically used 2D technique, a static fixed MPR was defined retrospectively as described previously on the annulus at the moment of end systole by an MRI technician (P.v.d.B.) with over 20 years of experience. For 4DFlow quantification, two MPR measurement planes were positioned retrospectively: one on the anatomical annulus and one at the level of PIV distal to the annulus and angulated perpendicular to the inflow direction, using streamline visualization (Fig. 1D). The 4DFlow quantification analysis was performed by one observer (E.C.) with 2 years of experience in cardiac MRI and verified by one experienced observer with more than 15 years of experience in cardiac MRI (J.W.). Solely during systole, the reformat plane was positioned as previously described, either at the closed valve or, in case of regurgitation, 1–1.5 cm proximal to the valve inside the atrium, perpendicular to the jet [12]. Transvalvular flow velocity was calculated by subtraction of myocardial velocity in the throughplane direction, sampled in nearby myocardium, from the mean inflow velocity. Transvalvular flow volume was subsequently calculated by integrating the transvalvular velocity over the inflow area (ie, the flow rate) and then integrating over the cardiac cycle. Because we aimed to evaluate quantification approaches of left ventricular inflow only, the same regurgitation volume during systole as most optimally quantified was included in all three measurements. Finally, the flow volume at the aortic valve was assessed from the same 4DFlow MRI data aligned on a coronal and sagittal aorta view [12], to evaluate correlation and agreement with trans-LAVV effective forward flow.

Statistical Analysis

Data analysis was performed using SPSS Statistics (v. 20.0 IBM SPSS, Chicago, IL) software. Variables were tested for normal distribution using the Shapiro–Wilk test. Continuous variables are expressed as mean ± standard deviation or median with interquartile range (IQR) where appropriate. Differences between patients and controls were determined using an unpaired T-test or Mann-Whitney-U-test. Differences in angles at E- and A-peak were tested with paired T-tests or Wilcoxon-Signed-Rank-test. Linear regression analysis and Bland-Altman analysis [13] were used to assess relation and agreement between LAVV effective forward flow and aortic flow. Intra- and interobserver variation was determined by the significance of differences be-

tween measurements and the intraclass correlation coefficient for absolute agreement and the coefficients of variance. A p-value<0.05 was considered as statistically significant. For statistical nonsignificant results (P > 0.05), the mean difference and 95% confidence interval (CI) of the difference are given.

RESULTS

Subject Characterization

Of 28 scanned patients, two were excluded because they had a restrictive LAVV ring placed around the annulus, made of paramagnetic material, which resulted in distortion of the MRI signal. One other patient was diagnosed with left isomerism and was excluded to avoid influence on inflow direction, due to atrial isomerism and different position of the heart. 4DFlow scans of the remaining 25 patients and 25 controls were visually inspected to be free from imaging artifacts and approved to be of adequate quality for image analysis. In all these patients and controls streamline visualization and trans-valvular flow quantification was possible. Patient and control characteristics are given in Table 1. Fifteen (60%) patients underwent correction of a partial AVSD and 10 (40%) of a complete AVSD. Correction of the AVSD involved closure of the cleft of the LAVV in 21 (84%) patients. Ejection fraction was significantly lower in patients compared with controls (55% (IQR 53–58) versus 61% (IQR 58–66), P < 0.001) and regurgitation volume was higher in patients compared with controls (8 mL (IQR 5–12) versus 1 mL (IQR 0–2), P < 0.001).

Table 1. Patient characteristics: Data are presented as mean ± standard deviation or median with interquartile range where appropriate. * indicates p<0.001. BSA = Body surface area, LVED = Left ventricular end diastolic volume, EF = Ejection fraction, AVSD = Atrioventricular septal defect, LAVV = Left atrioventricular valve.

	Controls (N=25)	Patients (N=25)
Age (yrs)	17 (IQR 12–28)	22 (IQR 16–31)
Male (N, %)	10 (40)	7 (28)
BSA (m^2)	1.6 ± 0.3	1.7 ± 0.4
LVED/BSA (mL/m^2)	87 ± 11	89 ± 16
EF (%)	61 (IQR 58–66)	55 (IQR 53–58)*
Regurgitation volume LAVV (mL)	1 (IQR 0–2)	8 (IQR 5–12)*
Time after surgical correction of AVSD (years)		19 ± 8

Healthy Controls

The angle measurements are presented in Table 2. On the four-chamber view, the inflow angle was larger during A-peak, implicating a more lateral inflow direction (E-peak 12±9° versus A-peak 17±7°, p=0.021). The difference in inflow angle between A- and E-peak ranged between –13 and 22. The difference between A- relative to E-peak correlated with age (R 0.573, P = 0.003).

Table 2. Inflow angles: angle measurements in the four-chamber view and two-chamber view in degrees at early (E) and late (A) filling. * (p < 0.05) and ** (p < 0.01) indicating statistical significant differences between patients and controls. Data are presented as mean ± standard deviation or median with interquartile range where appropriate.

		Four-chamber		Two-chamber	
		Controls	Patients	Controls	Patients
E	Annulus - long axis (angle 1)	95 ±3	98 ± 9	94 ± 6	101 ± 8**
	Annulus - inflow at annulus (angle 2)	83 ±9	88 ± 8	89 ± 10	94 ± 8*
	Inflow angle at annulus level (angle 1-2)	12 ± 9	10 ± 10	6 ± 9	7 ± 9
	Distance between annulus and PIV-level (mm)	14 ± 6	15 ± 6	13 ± 5	16 ± 6
	Annulus - inflow at PIV-level (angle 3)	84 (80–90)	77 (65–82)**	90 ± 7	92 ± 8
	Inflow angle at PIV-level (angle 1-3)	10 ± 8	19 ± 11**	5 ± 7	9 ± 9
A	Annulus - long axis (angle 1)	94 ± 4	102 ± 8**	98 ± 5	101 ± 8
	Annulus - inflow at annulus (angle 2)	77 ± 8	85 ± 12**	89 ± 10	100 ± 8**
	Inflow angle at annulus level (angle 1-2)	17 ± 7	16 ± 15	9 ± 10	2 ± 11*

On the two-chamber view, the inflow was more anterior relative to the long-axis at the A-peak (E-peak 6±9° versus A-peak 9±10°, p=0.034), with an intersubject range in difference from –14 to 13. The difference between inflow angle at PIV-level and annulus level was not statistically significant (mean difference 1.8 with 95% CI –0.6-4.5°, P =0.145). Velocities and flow volumes are provided in Table 3. In controls, high correlation was found between aortic flow volume and LAVV effective forward flow volume assessed with the 4DFlow MPR tracking the annular level (R^2 0.949, P < 0.001) and the 4DFlow MPR tracking the PIV-level and angulated perpendicular to inflow (R^2 0.949, P < 0.001), while correlation with static 2D MPR was lower (R^2 0.877, P < 0.001). The absolute error with aortic flow in volunteers was smaller when 4D MPR tracking the annulus (3 (1–8) mL, P = 0.001) and tracking PIV-level angulated on the inflow (3 (2–5) mL, P < 0.001) were used compared with the measurements with static 2D MPR (7 (4–16) mL). The mean difference between aortic flow volume and LAVV flow volume with 4D MPR tracking the annulus was 0.14 6 6.4 mL; 95% limit of agreement –12.4-12.7 mL and with 4D MPR tracking the PIVlevel and angulated on the inflow was –0.8 ± 4.6 mL; 95% limit of agreement –9.7-8.1 mL. The mean difference between aorta flow volume an LAVV flow from the static 2D MPR was higher with a mean difference of –10.1 ± 10.2 mL; 95% limit of agreement –30.0-9.9 mL (Fig. 2).

Patients

The inflow angle measurements performed in the patients are presented in Table 2. On the four-chamber view, the difference in inflow angle between E-peak and A-peak at annulus level was not statistically significant (mean difference 3.5° 95% CI –12.9– 1.5°, P = 0.113); however, a large interpatient variation was observed (range –40° to 38°). On the two-chamber view, inflow direction relative to the longaxis was more posterior during the A-peak (E-peak 7±9° versus A-peak 2±11°, p=0.009). In patients, the inflow direction at the PIV-level was more lateral compared with the inflow angle at annulus level (annulus 10±10° versus PIV-level 19±11°, p=0.003). In the

Table 3. Comparison of velocities and flow volumes: differences between trans- left atrioventricular valve (LAVV) velocity mapping using the static 2D MPR during diastole and a 4D MPR tracking the annulus and tracking the Peak inflow velocity (PIV)-level and angulated perpendicular to the inflow direction. Data are presented as mean ± standard deviation or median with interquartile range where appropriate, with * (p < 0.01) and ** (p < 0.001) indicating statistical significance between measurements with static 2D MPR and on the 4D MPR tracking the annulus level compared with the measurements with 4D MPR tracking the PIV-level and angulated perpendicular to the inflow direction. LAVV= left atrioventricular valve, PIV = Peak inflow velocity.

Reformat plane	Controls			Patients		
	Static 2D	4D annulus	4D PIV and angulated	Static 2D	4D annulus	4D PIV and angulated
LAVV flow volume (mL)	87 ± 26**	77 ± 20	78 ± 20	72 ± 21	65 ± 19**	70 ± 20
Absolute error LAVV flow with aortic flow (mL)	7 (4–16) **	3 (1–8)	3 (2–5)	4 (1–9) *	6 (2–10) *	2 (1–4)
Correlation LAVV flow with aortic flow (R²)	0.877	0.950	0.949	0.823	0.877	0.972
Aortic flow (mL)		77 ± 20			71 ± 20	

two-chamber view, the difference in inflow angle between the two planes was not statistically significant (mean difference −2.3°, 95% CI −5.1–0.4°, P = 0.091). Flow volumes and velocities obtained at the two measurement positions are presented in Table 3. In patients, a higher correlation was found between aortic flow and LAVV flow measurements performed at the PIV-level with 4D MPR angulated perpendicular to inflow direction (R^2 0.972, P < 0.001) and with 4D MPR tracking the annulus (R^2 0.877, P < 0.001) rather than with the static 2D MPR (R^2 0.823, P < 0.001). The absolute error between LAVV forward flow and aorta flow was smaller in the angulated MPR at the PIV–level (2 (1–4) mL), compared with MPR tracking the annulus (6 (2–10) mL, P = 0.003) and the static 2D MPR (4 (1–9) mL, P = 0.004). The mean difference between aortic flow and LAVV flow was smaller when the angulated MPR on PIV-level was used (0.2±3.4 mL; 95%-limit of agreement -6.9-6.4mL), compared with the MPR tracking the annulus (4.4 ±7.2mL; 95%-limit of agreement -9.6-18.5mL) and the static 2D MPR (-3.0±9.0 mL; 95%-limit of agreement -20.7-14.77mL).

Differences Between Patients and Healthy Controls

Differences in angle measurements between patients and healthy controls are given in Table 2. At the annulus level, the difference in inflow direction between patients and controls was not statistically significant (mean difference 2.0°, 95% CI −3.6-7.5°, P = 0.483). However, at the PIV-level, inflow direction was significantly more lateral (controls 10 ± 8° versus patients 19 ± 11°, P = 0.002) (Fig. 3). On the two-chamber view, the difference in inflow angle was not statistically significant between patients and controls during E-peak at both measurement levels (annulus mean difference 1.1°, 95% CI −6.1–3.9°, P = 0.668 and the PIV-level mean difference −4.1°, 95% CI −8.6–0.4°, P = 0.072), but the inflow was more posterior in the patients during Apeak (controls 9 ± 10° versus patients 2 ± 11°, P = 0.019).

Table 4. inter-observer and intra-observer analysis of angle measurements performed in the four- chamber view (4ch) and two-chamber view (2ch) during early (E) and late (A) filling. chamber view (4ch) and two-chamber view (2ch) during early (E) and late (A) filling. Ch = chamber.

	Inter-observer					Intra-observer				
	Intraclass correlation coefficient	Mean difference	p value	95% - Confidence interval	Coefficient of variation	Intraclass correlation coefficient	Mean difference	p value	95% - Confidence interval	Coefficient of variation
4ch angle 1 E peak	0.95 (p<0.001)	-0.1	0.932	-1.3, 1.2	3%	0.87 (p<0.001)	-1.5	0.069	-3.2, 0.1	4%
4ch angle 2 E peak	0.94 (p<0.001)	-0.3	0.685	-1.8, 1.2	4%	0.94 (p<0.001)	-1.3	0.069	-2.7, 0.1	4%
4ch angle 3 E peak	0.90 (p<0.001)	-1.9	0.127	-4.4, 0.6	7%	0.95 (p<0.001)	-1.5	0.096	-3.4, 0.3	5%
4ch angle 1 A peak	0.84 (p<0.001)	0.6	0.480	-1.2, 2.4	4%	0.89 (p<0.001)	0.15	0.830	-1.4, 1.7	3%
4ch angle 2 A peak	0.86 (p<0.001)	0.1	0.965	-2.4, 2.5	8%	0.90 (p<0.001)	0.0	1.000	2.1, 2.1	5%
2ch angle 1 E peak	0.92 (p<0.001)	-1.4	0.072	-2.9, 0.2	3%	0.77 (p<0.001)	-1.5	0.199	-3.9, 0.9	5%
2ch angle 2 E peak	0.93 (p<0.001)	0.2	0.811	-1.5, 1.9	4%	0.88 (p<0.001)	-0.3	0.783	-2.5, 2.0	6%
2ch angle 3 E peak	0.92 (p<0.001)	-1.2	0.192	-2.9, 0.6	4%	0.82 (p<0.001)	-0.3	0.798	-2.7, 2.1	7%
2ch angle 1 A peak	0.93 (p<0.001)	-1.9	0.005	-3.1, -0.6	3%	0.89 (p<0.001)	-0.6	0.453	-2.2, 1.0	3%
2ch angle 2 A peak	0.97 (p<0.001)	-1.3	0.129	-2.9, 0.4	4%	0.93 (p<0.001)	0.0	1.000	-2.1, 2.1	4%

Inter- and Intraobserver Variation

Interobserver coefficient of variation for angle measurements ranged between 3% and 8%, with an intra-class correlation coefficient higher or equal to 0.85 (P < 0.001). The mean differences ranged between 0.1° and 1.9° and none of these were statistically significant, except for the assessment of the angle between two-chamber view annulus and long-axis (mean difference 1.9 ± 2.7°, P = 0.005). The intraobserver coeffi- cient of variation ranged between 3% and 7%, with an intraclass correlation coefficient higher or equal to 0.77 (P < 0.001) and differences ranged between 0° and 1.5° (Table 4).

Figure 2. Agreement between left atrioventricular valve (LAVV) forward flow and aorta flow using three approaches for MPR placement.
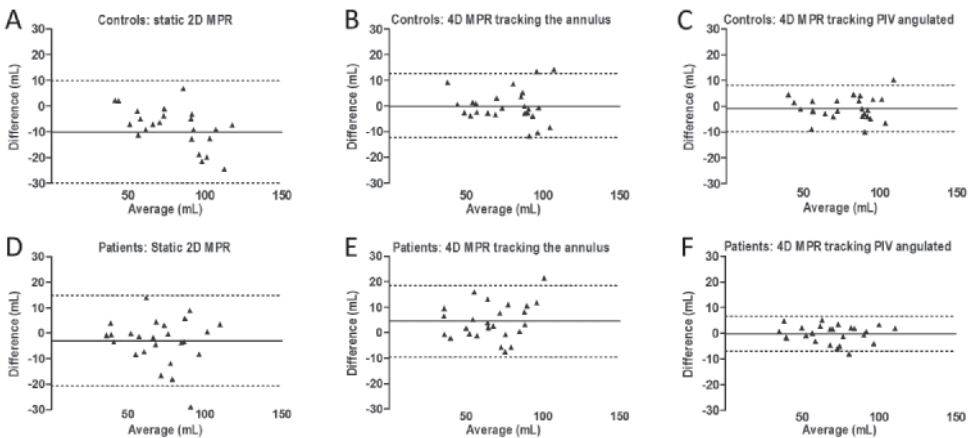

Bland–Altman graphs depicting agreement between aortic flow and effective forward flow over the LAVV with static 2D MPR (A,D), 4D MPR tracking the annulus (B,E) and 4D MPR tracking peak inflow velocity (PIV)-level and angulated perpendicular to the inflow (C,F), measured both in controls (A–C) as well as in corrected atrioventricular septal defect (AVSD) patients (D–F).

DISCUSSION

In this study, streamline visualization of 4DFlow MRI data was used to characterize and improve the quantification of trans-LAVV forward flow in healthy controls and patients after AVSD correction. The main findings of the current study are as follows: First, streamline visualization revealed a change in inflow direction between E- and A-peak in healthy controls and patients and a more laterally directed LV inflow in patients with corrected AVSD. Second, streamline visualization aids in optimizing the positioning and angulation of the measurement plane (ie, at peak inflow velocity level and perpendicular to inflow direction) during retrospective valve tracking procedure, resulting in a more reliable assessment of trans-LAVV forward flow volume in patients.

Quantification and characterization of transatrioventricular valve flow is important in the evaluation of ventricular and valvular function. In the healthy subjects, we observed a difference in

Figure 3. Lateral inflow after AVSD correction.
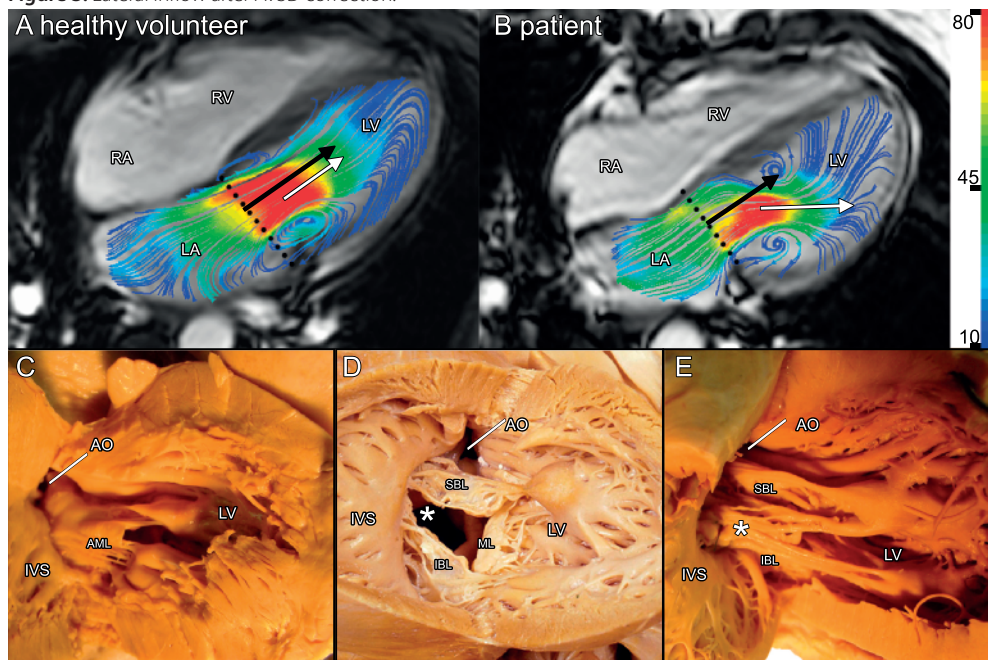
Streamline representation with velocity color coding (in cm/s) of the LV inflow pattern, illustrating the difference in inflow direction at E-peak inflow between a healthy volunteer (A) and a corrected AVSD patient (B), which presents with a more lateral inflow. The dotted line represents the annulus. Black arrow points in the direction of the inflow at the annulus level and the white arrow depicts the inflow direction at the peak inflow velocity (PIV)-level. C: A normal mitral valve with supple anterior leaflet of the mitral valve (AML). D: An AVSD before surgery with the ridged superior bridging leaflet (SBL), inferior bridging leaflet (IBL), and mural leaflet (ML); *the cleft. E: An AVSD heart after correction; the cleft between the SBL and IBL was closed (*). Left ventricle (LV), right ventricle (RV), left atrium (LA) and right atrium (RA), aorta (AO), interventricular septum (IVS).

inflow angle at E- and A-peak in both the four-chamber as well as the two-chamber orientation, which is most likely explained by the incomplete opening of the LAVV during A-peak phase [14]. Our observations are in line with Fyrenius et al [10] and extend their observations by quantification of the inflow angle. The high degree of intersubject variability correlated with age, where in younger patients the A-peak inflow was relatively more lateral compared with the E-peak. To investigate this further, a larger number of subjects and a broader age range is required. The intersubject variation in inflow angle, the difference between inflow angle at E- versus A-peak in both four- and two-chamber view implies that adjustment of the reformatting plane with 4DFlow MRI in each patient and during the whole cardiac cycle is relevant for quantification and characterization of trans-atrioventricular valve flow.

The observed dynamic changes in inflow direction during E- versus A-peak in healthy subjects were statistically significant but small, with substantial intersubject variation. The clinical relevance of these findings needs to be investigated in future studies. The PIV-level was found on

average 15–16 mm distal to the annulus, corresponding with approximately half of the diameter of the LAVV, suggesting that the measured peak velocity may be found near or at the tip of the LAVV leaflets. At this PIV-level, the inflow direction in patients was directed significantly more laterally. The altered inflow is presumably caused by the abnormal annulus shape and attachment of the anterolateral papillary muscle as described in a previous echocardiography study in corrected AVSD patients [4] and by the restrictive mobility of the septal leaflet caused by the cleft closure during correction (Fig. 3). Future studies are needed to investigate whether regurgitation of the LAVV effects the inflow direction.

Lateral inflow was previously found in patients with dilated LVs [15] and the altered flow pattern in patients with dilated cardiomyopathy was related to an increased loss in kinetic energy [16]. In simulations with computational fluid dynamics, changes in eccentricity of the inflow jet have been shown to reduce the efficiency of the heart pump by 10% [3]. Further studies are required to investigate whether the aberrant inflow pattern after correction of AVSD, indeed, in addition to other factors, contributes to less efficient LV function. These insights may be valuable in changing surgical techniques to minimize leaflet restriction and, subsequently, the effect on LV function. The more lateral inflow direction in patients with a corrected AVSD should also be taken into account during Doppler echocardiography. Appleton et al [14] observed that in patients with a dilated LV, the inflow can be directed up to 20 more lateral, leading to changes in inflow velocity recording without proper alignment of the echo Doppler beam to peak velocity direction and level. This report and our observation of a more lateral inflow in patients after AVSD correction stresses the need for proper adjustment to the inflow direction using echocardiography. The higher flow volume measured in controls, using the static 2D MPR approach, confirms previously described overestimation of LAVV when a static plane is used, due to movement of the atrioventricular valve [17]. The overestimation of flow was not observed in the patients, which can be explained by reduced throughplane movement of the AV valve but, more important, a concomitant increased misalignment due to the observed angulated flow, which compensates the overestimation.

Furthermore, in patients we found a higher accuracy in trans-LAVV flow quantification when measurements were performed at the PIV-level angulated to the inflow, with an underestimation of flow when the measurement plane was tracking the annulus. This is possibly caused by the difficulty in defining the exact anatomical position and angulation of the annulus in patients with corrected AVSD and the increased deviation of the inflow angle in these patients. Furthermore, while the effect of intravoxel phase dispersion and partial volume on the measured vector components contributing to the velocity mapping procedure will not change when the reformatting plane is adjusted in a 4DFlow dataset, higher accuracy can still be achieved by reducing the number of voxels with such inaccurate velocity within the region of interest due to a better alignment of the measurement plane perpendicular to the flow [9]. The higher accuracy stresses the importance of streamline visualization in 4DFlow quantification to optimize

3.2

positioning of the measurement plane. Further studies are required to investigate the impact of optimal positioning of the measurement plane in other congenital and acquired heart disease.

Our study has some limitations. Streamline visualization of 4DFlow MRI data is projected onto two- and four-chamber views and subsequently used for manual angle measurements and adjustment of measurement planes and, therefore, anatomical information and streamline data originate from different scans. Streamlines are a representation of the instantaneous flow velocity field and do not visualize the actual timecontinuous pathway of blood particles as pathlines do. In the present study we aimed to use the streamline visualization of the inflow direction at each specific timepoint during diastole and use this to position the measurement plane (assessing flow volume as through-plane velocity times cross-sectional area) at each of these timepoints. However, future studies may focus on differences between streamline and pathline visualization and their effect on measurement plane positioning. Differences in heart rate and respiratory rate might have caused some inaccuracy. In the future, automatic positioning and adjustment of measurement planes to the inflow direction from single scan data might improve the reliability and reproducibility of inflow assessment. All scans were performed with free-breathing and 4DFlow acquisition was performed without navigator gating in order to minimize acquisition time, because children were included in the study. However, image quality was adequate in all studies to perform offline velocity mapping and any possible effect of overestimation in flow volume due to area enlargement from breathing motion may be assumed to be equal in patients and controls. Local phase offset errors, which may lead to small systematic errors, should be taken into account [18]. During data reconstruction, the commercially available concomitant gradient correction and local phase correction filter were applied. Furthermore, measurements of peak velocity at the annulus level and at the PIVlevel were obtained from the same dataset at sampling positions relatively close to each other and, therefore, we may assume that a potential systematic error in velocity is almost equal for both sampling positions. Furthermore, for LAVV flow quantification, transvalvular velocity is calculated from local blood flow velocity relative to through-plane myocardial velocity and is therefore corrected for potential phase offset errors.

CONCLUSION

Streamline visualization of 4DFlow MRI data confirmed different inflow angle at early versus late filling in healthy controls, with substantial intersubject variation and a more laterally orientated LV inflow after AVSD correction. Using this visualization for optimizing the position of the measurement plane, assessment of trans-LAVV blood flow proved to be more accurate and resulted in related changes in blood flow characteristics. Our findings have implications for the assessment of trans-LAVV flow, as they stress the importance of careful adjustment of echocardiography Doppler beam or MRI measurement plane in the assessment of the dynamic ventricular inflow and taking into account alterations caused by AVSD correction.

REFERENCES

1. Bella JN, Palmieri V, Roman MJ, et al. Mitral ratio of peak early to late diastolic filling velocity as a predictor of mortality in middle-aged and elderly adults: the Strong Heart Study. Circulation 2002;105:1928–1933.

2. Little WC, Oh JK. Echocardiographic evaluation of diastolic function can be used to guide clinical care. Circulation 2009;120:802–809.

3. Pedrizzetti G, Domenichini F. Nature optimizes the swirling flow in the human left ventricle. Phys Rev Lett 2005;95:108101.

4. Takahashi K, Mackie AS, Thompson R, et al. Quantitative realtime three-dimensional echocardiography provides new insight into the mechanisms of mitral valve regurgitation post-repair of atrioventricular septal defect. J Am Soc Echocardiogr 2012;25: 1231–1244.

5. Napel S, Lee DH, Frayne R, Rutt BK. Visualizing threedimensional flow with simulated streamlines and threedimensional phase-contrast MR imaging. J Magn Reson Imaging 1992;2:143–153.

6. Nordmeyer S, Riesenkampff E, Messroghli D, et al. Four-dimensional velocity-encoded magnetic resonance imaging improves 8 Calkoen et al.blood flow quantification in patients with complex accelerated flow. J Magn Reson Imaging 2013;37:208–216.

7. Westenberg JJ, Danilouchkine MG, Doornbos J, et al. Accurate and reproducible mitral valvular blood flow measurement with three-directional velocity-encoded magnetic resonance imaging. J Cardiovasc Magn Reson 2004;6:767–776.

8. Westenberg JJ, Roes SD, Ajmone MN, et al. Mitral valve and tricuspid valve blood flow: accurate quantification with 3D velocityencoded MR imaging with retrospective valve tracking. Radiology 2008;249:792–800.

9. Lotz J, Meier C, Leppert A, et al. Cardiovascular flow measurement with phase-contrast MR imaging: basic facts and implementation. Radiographics 2002;22:651–671.

10. Fyrenius A, Wigstrom L, Bolger AF, et al. Pitfalls in Doppler evaluation of diastolic function: insight from 3-dimensional magnetic resonance imaging. J Am Soc Echocardiogr 1999;12:817–826.

11. Hoohenkerk GJ, Bruggemans EF, Rijlaarsdam M, et al. More than 30 years' experience with surgical correction of atrioventricular septal defects. Ann Thorac Surg 2010;90:1554–1561.

12. Roes SD, Hammer S, van der Geest RJ, et al. Flow assessment through four heart valves simultaneously using 3-dimensional 3- directional velocity-encoded magnetic resonance imaging with retrospective valve tracking in healthy volunteers and patients with valvular regurgitation. Invest Radiol 2009;44:669–675.

13. Bland JM, Altman DG. Statistical methods for assessing agreement between two methods of clinical measurement. Lancet 1986;1:307–310.

14. Appleton CP, Jensen JL, Hatle LK, et al. Doppler evaluation of left and right ventricular diastolic function: a technical guide for obtaining optimal flow velocity recordings. J Am Soc Echocardiogr 1997;10:271–292.

15. Mohiaddin RH. Flow patterns in the dilated ischemic left ventricle studied by MR imaging with velocity vector mapping. J Magn Reson Imaging 1995;5:493–498.

16. Eriksson J, Bolger AF, Ebbers T, et al. Four-dimensional blood flow-specific markers of LV dysfunction in dilated cardiomyopathy. Eur Heart J Cardiovasc Imaging 2013;14:417–424.

17. Kilner PJ, Gatehouse PD, Firmin DN. Flow measurement by magnetic resonance: a unique asset worth optimising. J Cardiovasc Magn Reson 2007;9:723–728.

18. Gatehouse PD, Rolf MP, Graves MJ, et al. Flow measurement by cardiovascular magnetic resonance: a multi-centre multi-vendor study of background phase offset errors that can compromise the accuracy of derived regurgitant or shunt flow measurements. J Cardiovasc Magn Reson 2010;12:5.

3.2

Chapter 3.3

Disturbed intracardiac flow organization after atrioventricular septal defect correction as assessed with 4D Flow magnetic resonance imaging and quantitative particle tracing

Emmeline E. Calkoen, Patrick J.H. de Koning, Nico A. Blom, Lucia J.M. Kroft, Albert de Roos, Ron Wolterbeek, Arno A.W. Roest and Jos J.M. Westenberg

ABSTRACT

Objectives

Four-dimensional (3 spatial directions and time) velocity-encoded flow magnetic resonance imaging with quantitative particle tracing analysis allows assessment of left ventricular (LV) blood flow organization. Corrected atrioventricular septal defect (AVSD) patients have an abnormal left atrioventricular valve shape. We aimed to analyze flow organization in corrected AVSD patients and healthy controls.

Methods

A total of 32 patients (age, 25 ± 14 years), 21 after partial AVSD correction and 11 after complete/intermediate AVSD correction, and 30 healthy volunteers (26 ± 12 years) underwent whole-heart four-dimensional velocityencoded flow magnetic resonance imaging. Particle tracing in the 16-segment LV cavity model was used to quantitatively evaluate blood flow organization discriminating multiple components.

Results

Patients showed a smaller percentage of direct flow compared with controls (30% ± 9% vs 44% ± 11%; P < 0.001). In patients, more inflow was observed in the basal inferior segment (22% ± 11% vs controls, 17% ± 5%; P = 0.005), with less direct but more retained inflow (ie, part of inflow that is not ejected from LV in subsequent systole). In patients, more inflow reached the midventricular level (68% ± 13% vs controls, 58% ± 9%; P < 0.001), most notably as retained inflow in the lateral segments. Subsequently, in patients, more (mostly retained) inflow reached the apex (23% ± 13% vs 14% ± 7%; P < 0.001), which correlated with early peak filling velocity (r = 0.637, P < 0.001). Patients with a corrected complete or intermediate AVSD presented with less direct flow (24% ± 8% vs 33% ± 8%; P = 0.003) and more apical inflow (30% ± 14% vs 18% ± 12%; P = 0.014) compared with a corrected partial AVSD.

Conclusion

Multicomponent particle tracing combined with 16-segment analysis quantitatively demonstrated altered LV flow organization after AVSD correction, with less direct and more retained inflow in apical and lateral LV cavity segments, which may contribute to decreased cardiac pumping efficiency.

INTRODUCTION

Atrioventricular septal defect (AVSD) covers a spectrum of heart anomalies with a common atrio-ventricular junction and is generally corrected early in life. Patients with a corrected AVSD have an abnormal atrioventricular valve with different leaflets and position of the papillary muscles [1;2], influencing left ventricular (LV) inflow. The normal pathway of blood flowing through the LV, from inflow through the mitral valve towards ejection into the aorta, optimizes the efficiency of cardiac pumping [3]. MRI based streamline evaluation in corrected AVSD patient revealed a more lateral inflow direction [4], which may disturb the most efficient intra-ventricular blood flow organization [5] and may also affect cardiac pumping efficiency and eventually lead to ventricular remodeling [6;7]. An evaluation of the organization of intra-cardiac blood flow is possible with particle tracing [8] from four-dimensional (three spatial directions and time) velocity-encoded magnetic resonance imaging (4DFlow MRI). Particle tracing is a visualization approach based on calculation of pathlines of virtual particles seeded in a flow velocity field and followed over time and can be used as a tool to display LV blood flow organization [8]. Eriksson et al. [9] introduced a quantitative four-component analysis of LV flow discriminating 1) direct flow entering and exiting the LV within the analyzed diastole and systole, 2) retained inflow entering during diastole but remaining in the LV during the following systole, 3) delayed ejection flow already present in LV prior to diastole but exiting the LV during the following systole and 4) residual volume present and remaining in the LV during the analyzed diastole and systole cardiac cycle. These functional distinct components are used to describe the blood flow organization [10] and were found disturbed in patients with heart failure [11]. As LV blood flow is a fundamental aspect of the cardiac function and plays a role in remodeling [12], further understanding of blood flow organization is paramount.

We aimed to use multi-component analysis from 4DFlow MRI and extend this with the 16-segment model introduced by the American Heart Association (AHA) [13] to quantitatively describe regional blood flow through the LV in healthy controls and patients after correction of a partial, intermediate or complete AVSD. Our hypothesis is that an altered inflow direction such as in corrected AVSD patients will disturb intra-cardiac flow organization.

3.3

MATERIALS AND METHODS

Study population
The study was approved by the local medical ethical committee and written informed consent was obtained from all participants or their parents. Thirty-four patients with a corrected AVSD, without contraindication for MRI, were prospectively enrolled from a surgical databases [14]. At our institution partial AVSD is corrected with a single patch and a complete and intermediate AVSD with two patches. One of the 32 patients had an associated aortic coarctation, which

was corrected with an end-to-end anastomosis during correction of the (intermediate) AVSD . In one other patient a small commissurotomy was performed in the pulmonary vein during surgical correction of the (complete) AVSD. All patients had a balanced ventricular anatomy. Two patients were excluded from analysis as these patients underwent left atrial ventricular valve (LAVV) replacement with a Carpentier ring which will result in severe imaging artifacts on MRI. Twenty-one patients had a partial AVSD with shunt at atrial level and 11 patients a complete or intermediate AVSD with a shunt at atrial and ventricular level. For comparison 30 healthy controls within a similar age range and without history of cardiac disease were included. Patients and volunteers in this study were also included in a study reporting on quantification of flow over the left atrioventricular valve [4],vortex core analysis [15] and quantification of regurgitation [16] . Patients underwent echocardiography and ECG details were analyzed.

MRI acquisition

Between October 2012 and November 2013 all patients and healthy subjects underwent whole-heart 4DFlow MRI on a 3Tesla MRI (Ingenia, Philips Medical Systems, Best, The Netherlands) with maximal gradient amplitude of 45mT/m for each axis and a slew rate of 200T/m/sec with the use of a combination of a FlexCoverage Posterior coil in the table top and a dStream Torso coil, providing up to 32 coil elements for signal reception. Typical volume for a whole-heart acquisition was 396mm (Right - Left) × 336mm (anterior-posterior) × 117mm (feet-head). Scans were performed with three-directional velocity-encoding of 150cm/s in all directions, spatial resolution 2.3×2.3×3.0-4.2mm3, flip angle 10°, echo time (TE) 3.2ms, repetition time (TR) 7.7ms, true temporal resolution 31ms, sensitivity encoding (SENSE) factor 2 in anterior-posterior direction and Echo Planar Imaging (EPI) was performed with a factor 5 and 30 phases reconstructed over one cardiac cycle. The temporal footprint was 14 seconds for a subject with a heartbeat of 60bpm [17]. 4DFlow acquisition duration was on average 8 minutes (range 5-12 minutes). Commercially-available concomitant gradient correction and local phase correction were applied from the software available on MRI system (Ingenia 3T MRI with Software Stream 4.1.3.0). Trans-LAVV flow analysis was performed using through-plane velocity mapping with the use of retrospective valve tracking as described previously [4]. Peak velocity during E-peak filling and A-peak filling was determined from the trans-LAVV velocity-time curves. A cine multi-2D short-axis image set was acquired using steady-state free-precession sequence with TE/TR 1.5/3.0, 350mm field-of-view, 45° flip angle, acquisition resolution 1.0×1.0×8.0mm3, which was used to obtain the LV volume after segmentation of the LV contours. Retrospective gating was used with 30 phases reconstructed to represent one cardiac cycle. Free breathing was allowed without using motion compensation or respiratory triggering, and three signal averages were taken to suppress effects of breathing motions.

Particle tracing

The workflow of the multi-component particle tracing evaluation of the LV flow organization is presented in Figure 1. The endocardial contours of the LV were manually traced in all slices at the phases of the largest and smallest LV volume, marked as respectively end-diastole (ED) and end-systole (ES). Sphericity index of the LV was calculated as $EDV/(\pi/6 \times \text{long-axis at end-diastole}^3)$ [18], with EDV representing end-diastolic volume. The contours were transferred to the 4DFlow data set. To reduce a possible translation of the subject between the cine short-axis acquisition and the whole-heart 4DFlow acquisition, image registration was performed between the cine data set and the magnitude image of the 4DFlow data set for a single phase that visually showed the best depiction of the LV in the magnitude image. The registration was restricted to translation only. This registration result was then applied to all phases.

   The 3D velocity data of the whole-heart 4DFlow acquisition was used for particle tracing algorithm, using 4th order Runge-Kutta numerical integration to create pathlines. Each voxel inside the LV at the moment of end-diastole was considered to represent one seed point (i.e., one particle), with the exception of the voxels from the outermost layer at the endocardial border, which were removed to avoid any boundary effects. Pathlines of the particles were calculated by integration of velocity data over time: backward over the diastole and forward over systole. The positions of the particles were stored every 10 ms. Particles exiting the LV other than into the aorta or the left atrium were excluded from analysis. Next, the four-component evaluation was performed as introduced by Eriksson, however, in patients, particles exiting the LV and entering the atrium during systole (i.e., the regurgitation) were classified as a fifth component.

3.3

Figure 1. Workflow of particle tracing.
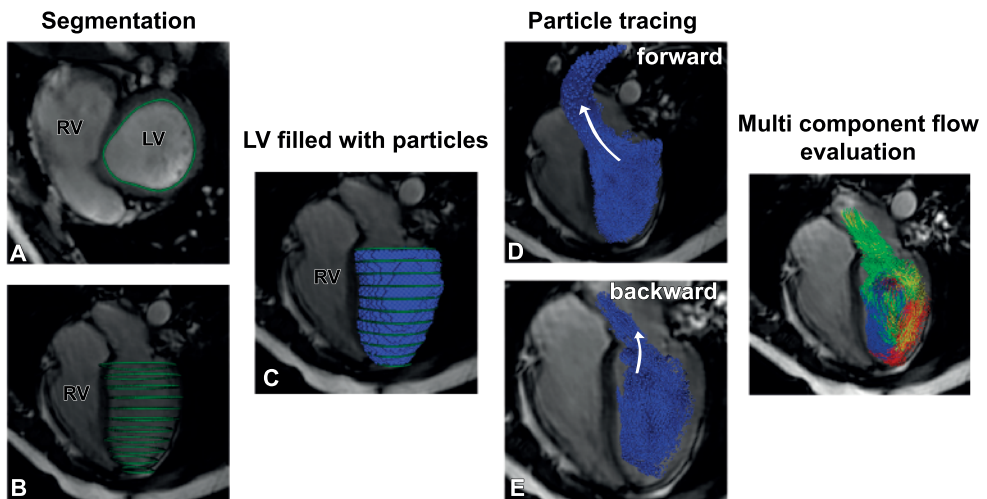
Contours of the left ventricle (LV) are manually segmented (green lines) on the short-axis images (A) in all slices (B). Subsequently, the LV is filled with particles at end-diastole (C). Forward (D) and backward (E) tracing are used to detect the components of left ventricular flow (F).

We compared the amount of particles part of the LV inflow with the amount of particles part of the outflow of the LV to evaluate the consistency of the particle tracing. To evaluate regional LV blood flow, the LV cavity was subdivided into 16 segments similar to the AHA model (i.e. six segments at both basal and mid-ventricular level and four segments at apical level) [13]. Segments were created automatically after setting a reference point manually at the insertion point between LV and right ventricle in each slice, with the endocardial circumference of each segment per level equal in size. Subsequently, the pathway of all particles contributing to diastolic inflow (i.e. direct flow and retained flow) was assessed. For each segment, the amount of inflow particles entering a segment from an upper level segment was counted relative to the total amount of inflow particles. Besides the total inflow, the distribution of direct flow (i.e. direct flow particles in a segment relative to total amount of direct flow particles) and retained flow (i.e. retained inflow particles in a segment relative to the total amount of retained inflow) was computed. Manual segmentation of contours took 7-12 minutes, subsequently the automated particle tracing procedure and automated quantification took 5-8 minutes per subject.

To evaluate whether the absolute error between inflow and outflow or the number of particles that were excluded, influenced the particle organization, the correlations between outcome parameters (i.e. componental proportions and percentage of particles in a segment) and the absolute error and the number of excluded particles were analyzed.

Statistical analysis

Data analysis was performed using SPSS Statistics (version 20.0 IBM SPSS, Chicago, Illinois) software. Variables are expressed as mean ± standard deviation. We used mixed models to evaluate the differences between controls and patients to take account of the within-subject correlation

Table 1. Subject characteristics. Data is presented as mean ± standard deviation. BSA = body surface area, BP = blood pressure, LVEDV = Left ventricular end-diastolic volume. * indicates significant difference between patients and controls p<<0.001.

	Controls	Patients partial AVSD (N = 21)	Patients complete AVSD (N=11)
Age (years)	25 ± 14	29 ± 12	18 ± 8
BSA (m²)	1.7 ± 0.3	1.8 ± 0.3	1.6 ± 0.5
Heart rate (bpm)	70 ± 13	74 ± 12	78 ± 15
Systolic BP (mmHg)	112 ± 13	122 ± 20	113 ± 18
Diastolic BP (mmHg)	67 ± 9	69 ± 12	59 ± 7
Sphericity index	0.37 ± 0.06 *	0.56 ± 0.14	0.58 ± 0.14
LVEDV (mL)	146 ± 42	154 ± 27	158 ± 43
LVEDV / BSA (mL/m²)	87 ± 13	88 ± 15	97 ± 14
Stroke volume (mL)	89 ± 23	86 ± 17	85 ± 24
Ejection fraction (%)	61 ± 4*	56 ± 4	54 ± 8
Regurgitation fraction (%)	-	12 ± 7	17 ± 11

of the components, the 3 layers or 16 segments respectively. Subject groups and components/layers/segments were modelled as fixed and subjects were modelled as a random effect (random intercept). A first mixed model analysis was performed to compare differences in the four componential percentages between patients and controls. A second mixed model analysis was performed to assess the difference between controls and patients in particle percentage entering the three levels (i.e. basal, mid and apical). Third, a mixed model analysis was performed to analyze the distribution over the 16 segments. Mixed model analyses for layers and segments were performed for total inflow as well as direct flow and retained inflow.

RESULTS

Study population
Patient characteristics are presented in Table 1. Patients were similar in age, heart rate and LV stroke volume when compared with the controls. All patients were in NYHA class 1 or 2. On echocardiography none were diagnosed with mitral stenosis. 14 (44%) patients presented with a right bundle branch block and six (19%) with some form of left bundle branch block

Validation
After exclusion of particles that secede from the LV other than into the aorta or LA, 79 ± 9% of the particles remained available for analysis. A significant, but small difference was observed between in- and outflow volume (inflow 59 ± 18 mL versus outflow 55 ± 15 mL, p=0.005, 95% confidence interval of difference 1.2 to 6.5 mL). There was no difference in absolute error between in- and outflow volume between controls (8.2 ± 8.7 mL) and patients (7.8 ± 6.4 mL) (p=0.851, 95% confidence interval of difference -3.5 to 4.2 mL). No correlations were observed between componential proportions and absolute error or number of excluded particles. Similarly, no correlation was observed between percentage of particles per segment and absolute error or number of excluded particles.

Inflow analysis
Patients had a smaller percentage of direct flow compared to controls (30±9% versus 44±11%, p<0.001), but a larger percentage of delayed ejection flow (22±6% versus 17±7%, p=0.014) and residual volume (21±7% versus 16±6%, p=0.004) (Figure 2). In patients 4±4% of particles was computed as regurgitation volume, no regurgitation was quantified in controls. Examples of multi-component analysis are shown in Figure 2 and supplemental Movie 1. Lower ejection fraction was related to higher residual volume (volunteers r = -0.561 p=0.001 and patients r = -0.617 p<0.001) and lower direct flow (volunteers r = 0.258 p=0.169 and patients r = 0.370 p = 0.037).

As shown in Figure 3, in controls and in patients the majority of all inflow particles enter the LV via the basal inferior, basal infero-lateral and basal antero-lateral segments. In patients a lower
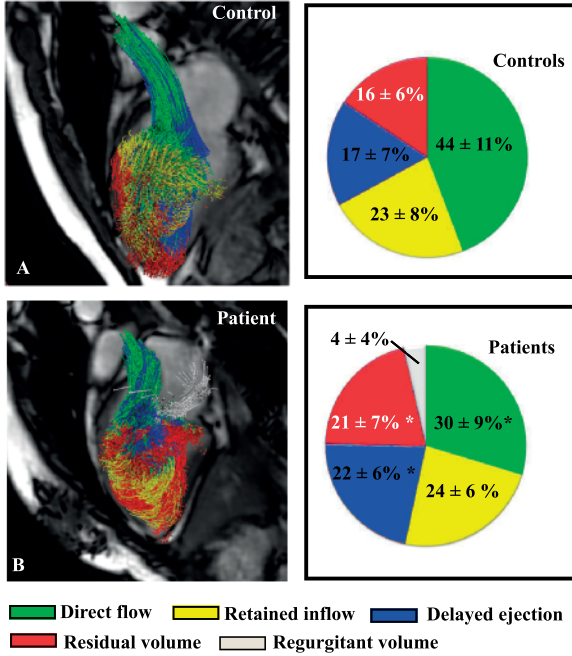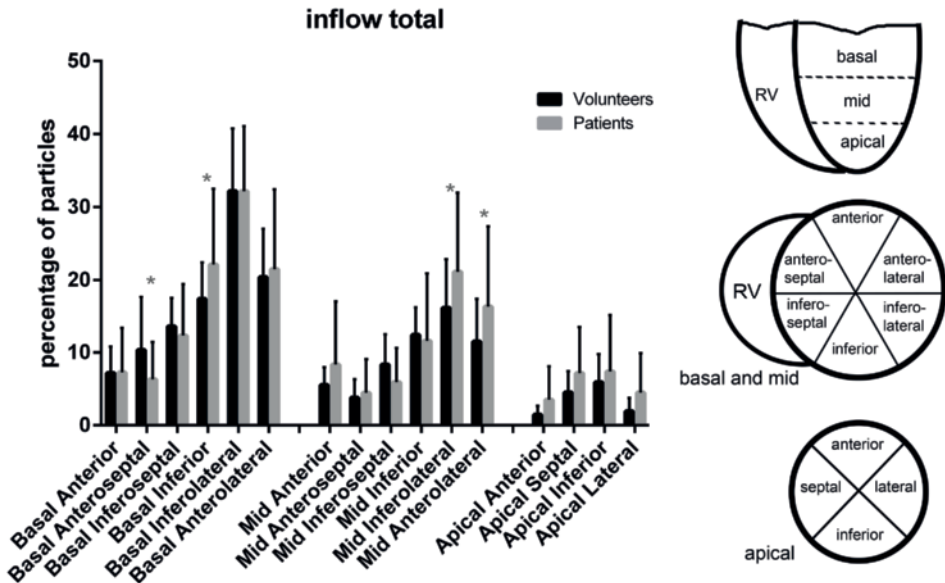
Figure 2. Example of left ventricular flow components in a healthy control (A) and a corrected AVSD patient (B).

Pie charts of the componential proportions (%) in controls and patients with * indicating significant difference (p<0.05) between controls and patients.

Figure 3. Particle percentage per segment relative to the total inflow.

* indicates significant (p<0.05) difference between patients (gray bar) and controls (black bar) based on mixed model analysis. The 16-segment model is presented in the right panels. RV = right ventricle.

percentage of inflow particles was observed in the basal antero-septal segment (6±5% versus 10±7%, p=0.018) and a higher percentage of inflow particles in the basal inferior segment (22±11% versus 17±5%, p=0.005). Dividing inflow into direct flow and retained inflow revealed that in patients the percentage of direct flow was lower in the basal level, especially in infero-lateral and antero-lateral segments compared to controls (Figure 4 and Figure 5). In contrast, in patients the percentage of retained inflow was higher in the basal and mid infero-lateral and antero-lateral segments (Figure 5).

In patients, of all particles entering the LV during diastole, 68 ± 13% reached into the mid ventricular level, compared to 58 ± 9% in controls (p<0.001). In controls, at the mid-ventricular level, particles were more evenly distributed over all six segments. At mid-ventricular level in patients, the percentage of inflow particles was higher in the infero-lateral (21±11% versus 16±7%, p=0.003) and antero-lateral (16±11% versus 11±6%, p=0.005) segments.

Subsequently, in the patients a higher percentage of inflow particles reached into the apex (23±13% versus 14±7%, p<0.001). Direct flow into the apex was not significantly different between patients and controls, whereas the retained inflow into the apex was significantly higher in patients (14±6% versus 7±3%, p=0.005). An example of a patient with increased lateral and apical flow compared to a healthy control is shown in Figure 4 and supplemental movie 2 and 3.

Patients with a corrected complete or intermediate AVSD presented with a lower percentage of direct flow (24±8% versus 33±8%, p=0.003) and more apical inflow (30±14% versus 18±12%, p=0.014) when compared to patients with a corrected partial AVSD. In patients no correlation was observed between sphericity index or LVEDV and componential proportions. The increased inflow into the apex correlated with early peak filling velocity (r = 0.637, p<0.001) in patients. In patients total apical flow correlated with delayed ejection flow (r = 0.631, p <0.001).

3.3

DISCUSSION

The current study introduces multi-component particle tracing in the LV using 16 AHA segments [13] and applies this technique in patients that underwent atrioventricular valve surgery. In patients after correction of an AVSD we observed altered intra-cardiac blood flow as compared to healthy controls. Key findings of the study are 1) the direct flow fraction is significantly lower in patients compared to controls, whereas the percentage of delayed ejection flow and residual volume are larger; 2) In patients versus controls a larger percentage of retained inflow is directed towards the lateral segments, whereas the inflow in the basal lateral segments contains more direct flow in controls versus patients; 3) In patients versus controls more (retained) inflow is directed towards the apex during diastole. Finally, after correction of an intermediate or complete AVSD a lower percentage of direct inflow was observed as compared to patients with a corrected partial AVSD.

Figure 4. Flow component organization in the left ventricle during diastole.
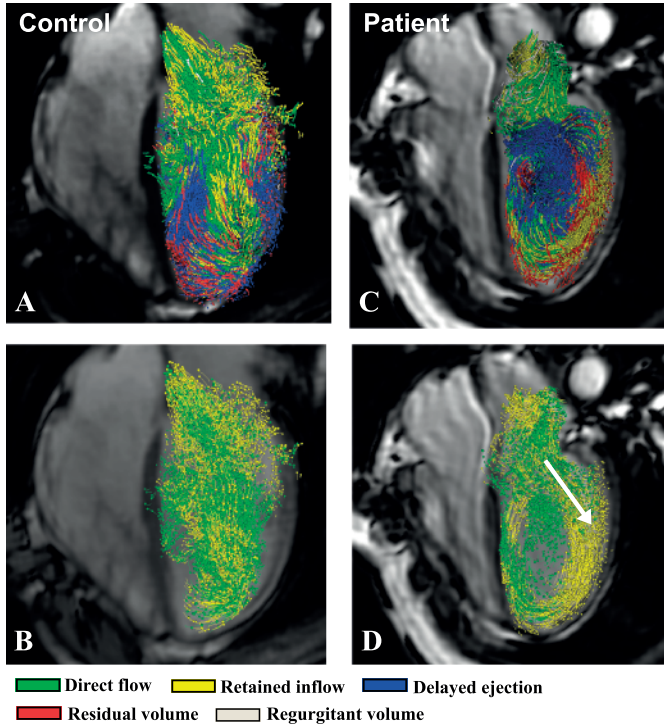
In a healthy control (A and B) and a patient (C and D). In A and C all components are presented, in B and D only the inflow components. More lateral and apical (retained) inflow is observed in a patient after AVSD correction (D) compared to the healthy control (B).

Figure 5. Particle percentage per segment relative to the total direct inflow and retained flow.
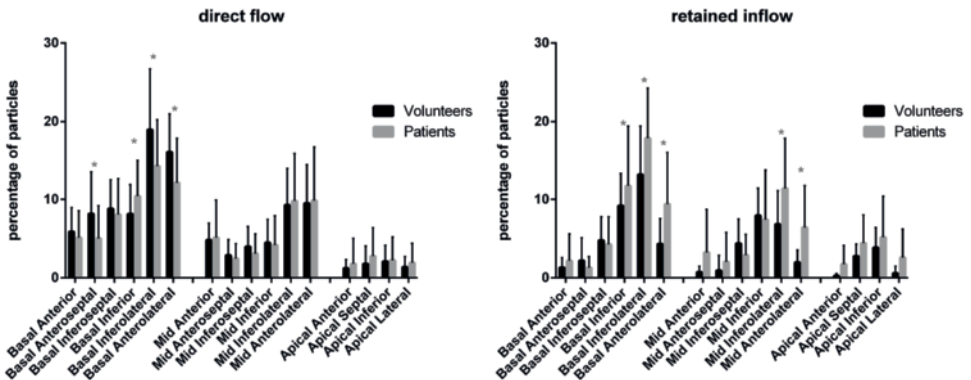
* indicates significant (p<0.05) difference between patients (black bar) and controls (gray bar) based on mixed model analysis.

The LAVV in AVSD has a different leaflet shape and papillary muscle position [1;2]. Furthermore, during AVSD correction a 'cleft' in the anterior leaflet of the LAVV is closed, which prevents regurgitation, but can cause restricted opening of the valve [1;2;19]. Using 2D streamline visualization, a previous cardiac magnetic resonance (CMR) study showed a more lateral inflow direction in corrected AVSD patients [4]. Based on these observations, we aimed to study the effect of this altered inflow after AVSD correction on intra-cardiac flow organization. Particle tracing allows visualization of the pathlines of blood flow over time [8]. The multi-component analysis proposed and validated by Eriksson et al. [9] extended visualization of 4DFlow MRI by specifying destination and timing of flow. Combining the 16 AHA segment model to the multi-component 4DFlow method enables quantification of the organization of the separate blood flow components regionally within the LV.

Healthy controls

Compared to previous studies, direct flow percentage in our volunteers (i.e. 44%) was slightly higher as observed in earlier studies from the same research group reporting on 6-12 healthy controls with age range 19-62 (i.e. 35-38%) [9;11;20]. Retained inflow was slightly higher, delayed ejection flow was similar and residual volume was lower (current study 16% versus 29-33% [9;11;20]). These studies were performed on a 1.5 Tesla MRI with Venc 100cm/s and other differences in acquisition protocol were a slightly larger echo time (3.7ms) and shorter repetition time (6.3ms) but a lower spatial resolution (3x3x3mm3) and true temporal resolution (50.4ms) than in our acquisition protocol. Additionally, no echo planar imaging was used but instead segmented k-space readout was used. Furthermore, navigator gating was used to compensate for breathing motion. These differences in acquisition protocol may contribute to the differences in componential proportions in healthy volunteers. Furthermore, the younger age of our patients might be a factor in the differences in results.Töger et al. used volume tracking of early filling blood at mid-diastole and end-diastole and observed a variety in inflow blood organization in the LV cavity, with a small percentage entering the apical level in healthy subjects [21]. Considering the complete diastole, for controls we obtained a similar result, with only $14 \pm 7\%$ of inflow entering the apical level. Vortex ring formation at the tip of the LAVV might play an important role in redirecting the flow towards the aorta [22]. Furthermore, a recent study showed pressure difference, not only between apical and basal level, but also between contralateral segments in healthy volunteers, which possibly influences blood, flow pathways [23]. The high percentage of particles in inferior, infero-lateral and anterolateral segments is in line with visually described flow patterns in the LV as reported by Eriksson et al. [9].

Corrected AVSD Patients

Patients with corrected AVSD had a reduced percentage of direct flow but increased delayed ejection flow, resulting in a similar stroke volume as in healthy controls, as was also observed in patients with dilated cardiomyopathy [11]. The increased portion of (mainly retained) inflow par-

3.3

ticles flowing through the mid antero- and infero-lateral segments is in line with our previous re-port using 2D streamline visualization, describing more lateral inflow in corrected AVSD patients [4] and can be explained by the restricted opening of the valve due to 'cleft' closure. Additionally, the offset between the inter-atrial and inter-ventricular septum in AVSD hearts may influence inflow direction. However numbers in current study were too small to study subgroups with different off-sets. A possible effect of the left bundle branch block observed in 6 patients cannot be ruled out, but we expect that this will predominantly influence ejection and not the inflow. Next to the lateral inflow, patients presented with an increase of inflow into the apical segments, which may be a result of lateral inflow. Possibly, abnormal formation of the vortex ring, which is suggested to redirect flow towards the aorta [22], at the tip of the LAVV in patients allows blood to propagate towards the apex. To further analyze the consequences of these altered intra-cardiac flow patterns we divided the inflow into direct flow and retained flow components and observed an increased percentage of particles entering the mid lateral segments. Also, the apical level contained significantly more retained inflow particles, i.e. particles that do not exit the LV during the next systole, which indicates that this lateral and apical flow is less efficient.

Patients with a corrected partial AVSD showed fewer abnormalities in flow organization compared to patients with a corrected complete or intermediate AVSD. This suggests that the morphology of the common atrioventricular valve or the more comprehensive surgery needed to correct a complete or intermediate AVSD, requiring correction with 2 patches, enhances abnormal LV blood flow organization.

Clinical implications

Blood flow in the LV should be directed from atrium towards aorta in order to pump in an ef-ficiently [3;10]. In-vitro studies showed that abnormal lateral inflow, due to LAVV manipulation, resulted in over 10% less efficient cardiac pumping [5]. In the current study the abnormal blood flow was not related to LVEDV nor sphericity index, which suggests that the affected blood flow is most likely related to valve abnormalities instead of LV shape. During AVSD correction the surgeon has to close the cleft in the LAVV and sometimes performs approximation of the leaflets to prevent LAVV regurgitation. Aberrant blood flow after AVSD correction indicates that the surgeon should be aware that LAVV leaflet shape can influence blood flow organization. Furthermore, the increased apical flow in patients was related to increased early peak filling velocity, which implicates that care should be taken not to restrict the LAVV opening too much as this will result in higher peak velocities and subsequent altered intra-cardiac flow pattern.

Little is known about cardiac function long-term after AVSD correction and long-term follow-up of these patients is needed to show the effect of disturbed LV blood flow organization on cardiac remodeling [6;7] and subsequent cardiac function. Our study was conducted in patients in NYHA class I or II with preserved systolic function, however already marked changes could be observed in intra-cardiac flow organization suggesting less efficient LV flow. The abnormal intra-cardiac flow organization without clinical signs or symptoms observed in the current

study, suggests that flow organization may be used as a subclinical parameter of impaired LV function. However, studies during stress or after serial follow-up are still needed to assess the consequences of this disturbed flow organization.

In the adult population, mitral valve abnormalities are common and mitral valve surgery is advocated in asymptomatic patients with moderate to severe mitral valve regurgitation [24]. Recently examples of aberrant inflow and vortex formation after mitral valve replacement or repair were shown in vivo using 2D echocardiography [25]. 3D particle tracing using flow component analysis with the 16-segment model as performed in the current study, may give further insight in the consequences of different types of LAVV surgery and its effect on LV flow organization and cardiac function.

Limitations

4DFlow acquisition was performed without navigator gating in order to minimize acquisition time, because children were included in the study. The particle tracing approach is considered to represent the true pathlines of blood flow over time, however changes in velocity magnitude and direction faster than the temporal and spatial resolution can detect, cannot be represented in the tracing algorithm. Moreover, free breathing without respiratory gating as applied in our acquisition protocol in combination with a low EPI readout to allow a higher temporal resolution in contrast to segmented k-space acquisition with navigator gating, may lead to errors in the position of all particles. However this error is expected to be similar in magnitude in patients and controls and the used 4DFlow acquisition with free breathing has been validated previously [26] and an earlier study in this patient group showed excellent internal validation between LV stroke volume from 4DFlow MRI and the LV stroke volume calculated with multi-slice cine balanced steady state free precession [16]. Also no imaging artefacts were observed from using EPI readout. Furthermore, data quality was considered adequate by comparing the inflow and outflow particle count. In each subject a number of particles was excluded in the evaluation as these particles seceded from the LV cavity. This might be due to inaccuracies in the LV contour segmentation or registration, or by the fact that during the tracing procedure, particles can 'cross' the myocardial wall due to the limited time step used in the integration procedure and the discretization of the acquired data. However, neither the difference between in- and outflow nor the number of excluded particles had a correlation with componential proportion or particle percentage per segment. Moreover, there was no difference observed in validation between controls and patients. To reduce the number of particles crossing the myocardial wall, one layer of particles was excluded before the analysis. This may have caused an underestimation of lateral flow quantification. As patients in current study were (nearly) asymptomatic it was not possible to relate abnormal flow patterns to clinical parameters. This study is limited to the flow patterns in the left ventricle, as most re-operations are needed because of abnormalities of the left atrioventricular valve and we have shown lateral inflow in the left ventricle in a previous study [4]. Furthermore, the widely used American Heart Association segmentation model of the left

ventricle enables assessment of regional flow distribution, which would be more challenging in the right ventricle which has a complex anatomy. In addition, the left ventricle is the systemic ventricle and one would expect disturbances of the left ventricular intracaviy flow organisation to have more profound impact on clinical status. Future studies are needed to evaluate the flow patterns in the right ventricle as well as right ventricle - left ventricle interaction.

CONCLUSION

The current study shows the feasibility of the segmental quantification of different flow components in the LV. This technique allows description of the normal inflow pathway and reveals more lateral and apical inflow in patients after AVSD correction. As retained inflow in the lateral and apical segments was significantly higher after AVSD correction, it is considered as less efficient. Whether the disturbed flow pattern has a negative effect on cardiac remodeling and cardiac function on the long-term remains to be established.

SUPPLEMENTAL MATERIAL

Supplemental digital contents are available for this chapter on www.investigativeradiology.com.

REFERENCES

1. Penkoske PA, Neches WH, Anderson RH et al. Further observations on the morphology of atrioventricular septal defects. J Thorac Cardiovasc Surg 1985;90:611-22.

2. Takahashi K, Mackie AS, Thompson R et al. Quantitative Real-Time Three-Dimensional Echocardiography Provides New Insight into the Mechanisms of Mitral Valve Regurgitation Post-Repair of Atrioventricular Septal Defect. J Am Soc Echocardiogr 2012;25:1231-44.

3. Kilner PJ, Yang GZ, Wilkes AJ et al. Asymmetric redirection of flow through the heart. Nature 200;404:759-61.

4. Calkoen EE, Roest AA, Kroft LJ et al. Characterization and improved quantification of left ventricular inflow using streamline visualization with 4DFlow MRI in healthy controls and patients after atrioventricular septal defect correction. J Magn Reson Imaging 2015;41:1512-20.

5. Pedrizzetti G, Domenichini F. Nature optimizes the swirling flow in the human left ventricle. Phys Rev Lett 2005;95:108101.

6. Pasipoularides A. Evaluation of right and left ventricular diastolic filling. J Cardiovasc Transl Res 2013;6:623-39.

7. Pasipoularides A. Diastolic filling vortex forces and cardiac adaptations: probing the epigenetic nexus. Hellenic J Cardiol 2012;53:458-69.

8. Buonocore MH. Visualizing blood flow patterns using streamlines, arrows, and particle paths. Magn Reson Med 1998;40:210-26.

9. Eriksson J, Carlhall CJ, Dyverfeldt P et al. Semi-automatic quantification of 4D left ventricular blood flow. J Cardiovasc Magn Reson 2010;12:9.

10. Bolger AF, Heiberg E, Karlsson M et al. Transit of blood flow through the human left ventricle mapped by cardiovascular magnetic resonance. J Cardiovasc Magn Reson 2007;9:741-7.

11. Eriksson J, Bolger AF, Ebbers T et al. Four-dimensional blood flow-specific markers of LV dysfunction in dilated cardiomyopathy. Eur Heart J Cardiovasc Imaging 2013;14:417-24.

12. Richter Y, Edelman ER. Cardiology is flow. Circulation 2006;113:2679-82.

13. Cerqueira MD, Weissman NJ, Dilsizian V et al. Standardized myocardial segmentation and nomenclature for tomographic imaging of the heart. A statement for healthcare professionals from the Cardiac Imaging Committee of the Council on Clinical Cardiology of the American Heart Association. Circulation 2002;105:539-42.

14. Hoohenkerk GJ, Bruggemans EF, Rijlaarsdam M et al. More than 30 years' experience with surgical correction of atrioventricular septal defects. Ann Thorac Surg 2010;90:1554-61.

15. Elbaz MS, Calkoen EE, Westenberg JJ et al. Vortex flow during early and late left ventricular filling in normal subjects: quantitative characterization using retrospectively-gated 4D flow cardiovascular magnetic resonance and three-dimensional vortex core analysis. J Cardiovasc Magn Reson 2014;16:78.

16. Calkoen EE, Westenberg JJ, Kroft LJ et al. Characterization and quantification of dynamic eccentric regurgitation of the left atrioventricular valve after atrioventricular septal defect correction with 4D Flow cardiovascular magnetic resonance and retrospective valve tracking. J Cardiovasc Magn Reson 2015;17:18.

17. Haider CR, Hu HH, Campeau NG et al. 3D high temporal and spatial resolution contrast-enhanced MR angiography of agn Reson Med 2008;60:749-60.

18. Kono T, Sabbah HN, Stein PD et al. Left ventricular shape as a determinant of functional mitral regurgitation in patients with severe heart failure secondary to either coronary artery disease or idiopathic dilated cardiomyopathy. Am J Cardiol 1991;68:355-9.

19. Ando M, Takahashi Y. Variations of atrioventricular septal defects predisposing to regurgitation and stenosis. Ann Thorac Surg 2010;90:614-21.

20. Eriksson J, Dyverfeldt P, Engvall J et al. Quantification of presystolic blood flow organization and energetics in the human left ventricle. Am J Physiol Heart Circ Physiol 2011;300:H2135-H2141.

21. Toger J, Carlsson M, Soderlind G et al. Volume Tracking: A new method for quantitative assessment and visualization of intracardiac blood

3.3

flow from three-dimensional, time-resolved, three-component magnetic resonance velocity mapping. BMC Med Imaging 2011;11:10.

22. Martinez-Legazpi P, Bermejo J, Benito Y et al. Contribution of the diastolic vortex ring to left ventricular filling. J Am Coll Cardiol 2014;64:1711-21.

23. Eriksson J, Bolger AF, Carlhall CJ et al. Spatial heterogeneity of four-dimensional relative pressure fields in the human left ventricle. Magn Reson Med 2014: in press.

24. Bonow RO, Carabello BA, Chatterjee K et al. 2008 focused update incorporated into the ACC/AHA 2006 guidelines for the management of patients with valvular heart disease: a report of the American College of Cardiology/American Heart Association Task Force on Practice Guidelines. J Am Coll Cardiol 2008;52:e1-142.

25. Sengupta PP, Narula J, Chandrashekhar Y. The dynamic vortex of a beating heart: wring out the old and ring in the new! J Am Coll Cardiol 2014;64:1722-4.

26. Westenberg JJ, Roes SD, Ajmone MN et al. Mitral valve and tricuspid valve blood flow: accurate quantification with 3D velocity-encoded MR imaging with retrospective valve tracking. Radiology 2008;249:792-800.

Chapter 3.4

High-temporal velocity-encoded MRI for the assessment of left ventricular inflow propagation velocity: comparison with color M-mode echocardiography

Emmeline E. Calkoen, Nina Ajmone-Marsan, Jeroen J. Bax , Pieter J. van den Boogaard, Arno A.W. Roest, Albert de Roos and Jos J.M. Westenberg.

ABSTRACT

Purpose

Left ventricular (LV) inflow propagation velocity (Vp) is considered a useful parameter in the complex assessment of LV diastolic function and is measured by Color M-mode echocardiography. The aim of current study was to develop an alternative method for Vp-assessment using high-temporal velocity-encoded magnetic resonance imaging (VE-MRI).

Methods

A total of 43 patients diagnosed with ischemic heart failure (61±11years) and 22 healthy volunteers (29±13years) underwent Color M-mode echocardiography and VE-MRI to assess the inflow velocity through the mitral valve (mean inter-examination time 14 days). (Temporal resolution of VE-MRI was 10.8–11.8 ms) Local LV inflow velocity was sampled along a 4 cm line starting from the tip of the mitral leaflets and for consecutive sample points the point-in-time was assessed when local velocity exceeded 30 cm/s. From the position-time relation, Vp was calculated by both the difference quotient (Vp-MRI-DQ) as well as from linear regression (Vp-MRI-LR).

Results

Good correlation was found between Vp-echo and both Vp-MRI-DQ (r=0.83 p<0.001) and Vp-MRI-LR (r=0.84 p<0.001). Vp-MRI showed a significant but small underestimation as compared to Vp measured by echocardiography (Vp-MRI-DQ: : 5.5±16.2 cm/s, p=0.008; Vp-MRI-LR: 9.9±15.2cm/s, p<0.001). Applying age-related cut-off values for Vp to identify LV impaired relaxation, Kappa-agreement with echocardiography was 0.72 (p<0.001) for Vp-MRI-DQ and 0.69 (p<0.001) for Vp-MRI-LR.

Conclusion

High-temporal VE-MRI represents a novel approach to assess Vp showing good correlation with Color M-mode echocardiography. In healthy subjects and patients with ischemic heart failure, this new methods demonstrated good agreement with echocardiography to identify LV impaired relaxation.

INTRODUCTION

Despite improvements in the treatment of cardiac diseases, the prevalence of systolic and dia-stolic heart failure (HF) continues to rise [1]. Particularly, presence of LV diastolic dysfunction, with or without a concomitant LV systolic dysfunction, is associated with increased morbidity and portends poor prognosis [2,3]. Furthermore, subclinical LV diastolic dysfunction has been shown to be related to a high risk of progression to symptomatic HF and therefore an early detection of LV impaired relaxation might have important clinical implications for patient management [1].

LV diastolic function is influenced by several factors, such as LV geometry and myocardial relaxation properties, left atrial function, pericardial restraint, heart rate and rhythm [4]. Direct measurement of the LV pressure-volume relation is considered the gold standard for diagnosis of diastolic function [5,6], but such assessment is invasive and not available for most patients. Current recommendations for the evaluation of LV diastolic function consider echocardiography the method of choice for a non-invasive evaluation in clinical practice and a combination of various parameters is proposed [7]. A useful marker for the assessment of LV diastolic function with echocardiography is the LV inflow propagation velocity (Vp), a relatively load-independent parameter that records velocity information along a scan line from the mitral valve into the ventricle during early LV filling [8-11]. Vp can be measured with Color M-mode echocardiography, which allows a high temporal resolution. It has been shown that the ratio of peak early filling velocity to Vp is directly proportional to LA pressure and therefore can be used to identify impaired LV relaxation by itself [12,13] or in combination with the isovolumic relaxation time [14]. Furthermore, while a Vp>50 m/sec is considered normal, in patients >30 year-old a Vp less than 45 cm/s has been suggested to identify LV impaired relaxation; in patients <30 year-old, this cut-off value is raised to 55 cm/s [10].

Recently, magnetic resonance imaging with high-temporal time-resolved velocity encoding (VE-MRI) has been also proposed for Vp evaluation [15], allowing for the assessment of the intra-cardiac blood flow velocities. The aim of the current study was to develop a high-temporal VE-MRI approach to measure Vp and to compare this method with Color M-mode echocardiography in patients with ischemic HF and healthy volunteers.

MATERIAL AND METHODS

Subjects

Forty-three patients with ischemic HF consecutively referred for cardiac MRI and 22 healthy volunteers were included in this study. Valvular stenosis or a repaired/replaced valve was an exclusion criterion. Data on New York Heart Association (NYHA) classification and percentage of LV scarring based on delayed contrast enhancement MRI [16] were obtained by patient status review. To allow evaluation of a wide range of LV diastolic function, the mean age of the

healthy volunteers was substantially younger as compared to patients. Mean inter-examination time between echocardiography and VE-MRI was 14 days. The study was approved by the local ethical committee and written informed consent was obtained from all patients and volunteers. Data of this patient population has been published before [17-21] however none was related to Vp-evaluation.

Echocardiography

Transthoracic echocardiography images were acquired in the left lateral decubitus position using a commercially available system equipped with a 3.5 MHz or M5S transducer (Vivid 7-9, GE-Vingmed Ultrasound, Horton, Norway). Vp was measured as described by Garcia et al. [10] by a cardiologist with 10 years of experience, (NA) blinded with regard to the MRI results. In the apical 4-chamber view, with the use of Color Doppler, the M-mode cursor was aligned along the mitral inflow stream to record the early flow propagation velocity into the LV. Baseline shift was performed as needed to obtain a distinct border of the propagation velocity into the LV cavity (usually Nyquist limit around 30-40 cm/sec). During off-line analysis, the slope of the first 'aliasing' velocity (red to blue) was traced from the mitral valve plane to 4 cm distal in the LV (Vp in cm/sec) (Figure 1). In some cases, the slope of the aliasing area in the M-mode image flattens towards the top. In such cases, the measurement line was positioned along the steepest part of the area of aliasing. For each subject, Vp-echo was calculated from an average of three measurements.

MRI acquisition

MRI patient data was collected using a 1.5 Tesla (T) MRI system (Intera, release 11 and 12; Philips Medical Systems, Best, the Netherlands) with 33 mT/m maximal gradient amplitude and 100 mT/m/ms slew rate. A five-element cardiac coil placed on the chest was used for signal reception. A series of survey scans which included cine 2- and 4-chamber views and a multi-slice multi-phase short-axis set were acquired to measure LV volume and compute the ejection fraction (LV EF = (LV end-diastolic volume - LV end-systolic volume) / LV end-diastolic volume) with a steady-state free-precession sequence with typical imaging parameters: slice thickness = 8 mm, field-of-view = 400×320 mm2, spatial resolution voxel size of 1.8×2.0×8.0 mm3, flip angle = 50°, echo time (TE) = 1.7 ms, repetition time (TR) = 3.4 ms, one number of signal averages (NSA) and no parallel imaging. Each slice was acquired using breath-holding in end-expiration. Retrospective gating was used, with 10% arrhythmia rejection, and for each slice, 1 average heart beat was reconstructed into 30 phases. Image analysis with manual contour segmentation for LV volume calculation was performed using in-house developed MASS software.

   Subsequent non-segmented VE-MRI was performed in a 4-chamber view with single-directional in-plane velocity encoding in phase encoding direction. This direction was visually angulated parallel to the LV inflow direction (i.e. parallel to the line from the opened mitral valve leaflets to the apex). The following typical imaging parameters were used: slice thickness = 8 mm, field-of-view = 370×320 mm2, spatial resolution voxel size of 2.8×2.5×8.0 mm3, flip angle =

10°, TE = 3.4 ms, TR = 5.4 ms, NSA = 4 and no parallel imaging was used. Velocity sensitivity was set to 20 cm/s and retrospective gating was used. Acquisition was performed with free breathing. The maximal number of phases was reconstructed, yielding an effective temporal resolution of approximately 6 ms (i.e., the true temporal resolution equals 2×TR = 10.8 ms).

Figure 1. Schematic representation of velocity propagation assessment with Color M-mode echo and velocity-encoded MRI.

3.4
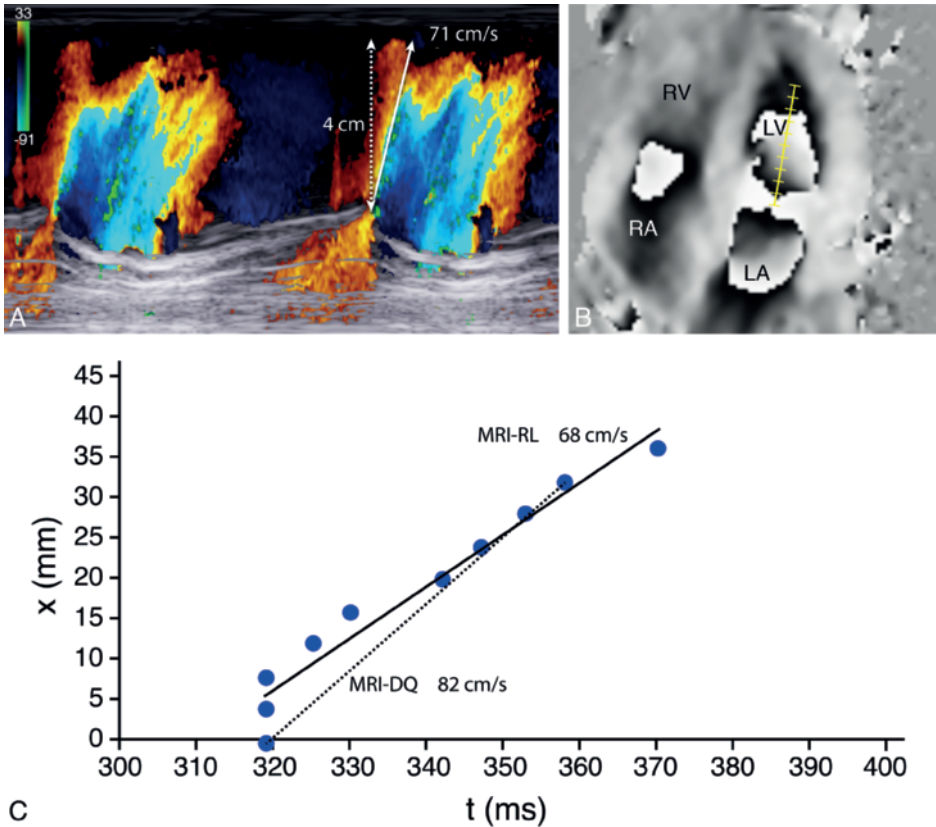
During offline analysis of echocardiography (panel A), the slope of the first 'aliasing' velocity (red to blue) is traced from the mitral valve plane to position 4 cm distal into the LV. On the velocity encoded MRI scan (panel B), a 4 cm scan line is defined starting from the position of the valve leaflets and in the direction of the LV inflow. 11 sample points (4 mm apart) are defined on this scan line and the point-in-time was recorded, starting from the onset of LV filling, when aliasing was reached for each consecutive sample point. The time points where aliasing occurs, are then displayed in a position-time graph (panel C). The slope of the line of the position-time relation, representing Vp, is calculated by two definitions: Vp-MRI-Difference Quotient (Vp-MRI-DQ), using the difference quotient (i.e. the slope of the straight line between the first point and the final recording that represents the inflow wave), and Vp-MRI-Lineair Regression (Vp-MRI-LR), using the slope which was calculated by linear regression from all included sample points along the scan line. Since the slope of the x-t relation flattens towards the top in this example, only measurement points along the steepest part of line are included and the last sample point most distally in the LV is disregarded. Due to the limited temporal resolution, consecutive sample points may present equal recorded times of aliasing in case of fast propagation, as is illustrated in the first 8mm distal to the valve (panel C).

Volunteer data was acquired using a 3.0T MRI system (Ingenia, Philips Medical Systems, The Netherlands) with 45 mT/m maximal gradient amplitude and 200 mT/m/ms slew rate. A combination of FlexCoverage Posterior coil in the table top with a dStream Torso coil was used, providing up to 32 coil elements for signal reception. Similar to the patient data acquisition, a series of survey scans and a multi-slice multi-phase short-axis set were acquired with a steady-state free-precession sequence with typical imaging parameters: slice thickness = 8 mm, field-of-view = 350×350 mm2, spatial resolution voxel size of 1.5×1.5×8.0 mm3, flip angle = 45°, TE = 1.5 ms, TR = 3.0 ms, NSA = 3 and parallel imaging with SENSE factor 2. Free breathing was allowed. VE-MRI was performed with typical imaging parameters: slice thickness = 8 mm, field-of-view = 320×260 mm2, spatial resolution voxel size of 2.5×2.5×8.0 mm3, flip angle = 10°, TE = 3.8 ms, TR = 5.9 ms (i.e., the true temporal resolution equals 2×TR = 11.8 ms), NSA = 1 and parallel imaging with SENSE factor 2. Velocity sensitivity was set to 30 cm/s and retrospective gating with 10% arrhythmia rejection, was used with maximal number of phases reconstructed and acquisition was performed with free breathing.

VP-QUANTIFICATION BASED ON VE-MRI

The approach of inflow propagation evaluation with MRI has been modelled to the Color M-mode approach, i.e. a position-time (x-t) graph was constructed which displays for each consecutive sample point along the scan line from mitral valve towards the apex, the point in time when local inflow velocity exceeds the aliasing value of 30 cm/s. Similar to Vp-echo assessment from Color M-mode echocardiography, the slope of the straight line constructed from the x-t relation then represents Vp. Therefore, in the 4-chamber view velocity images, a scan line of 4 cm was manually indicated from the tip of the valve leaflets into the LV, parallel to the inflow direction. The velocity scale was set to a maximal inflow velocity of 30 cm/s. For volunteers, this aliasing threshold already has been set at the acquisition. For patient data, however, the maximal velocity sensitivity at acquisition was 20 cm/s. Therefore, using the MASS software, the display range of velocity values was first shifted from -20 cm/s – 20 cm/s into -10 cm/s – 30 cm/s. Equidistantly along the scan line, 11 sample points were defined, 4 mm apart. Starting at the onset of LV filling, the point-in-time was recorded when aliasing was reached for each consecutive sample point along the scan line. These time points were then transported offline into MS Excel (version 2010) and displayed in a position-time graph. The slope of the line of the position-time relation, representing Vp, was calculated by two definitions: Vp-MRI-Difference Quotient (Vp-MRI-DQ), using the difference quotient (i.e., the slope of the straight line between the first point and the final recording that represented the inflow wave), and Vp-MRI-Linear Regression (Vp-MRI-LR), using the slope which was calculated by linear regression from all included sample points along the scan line. Similarly as in Color M-mode echocardiography in cases when the slope of the x-t relation flattens towards the top, only the measurement points along the steepest part of line

were included and sample points more distal in the LV were disregarded, both for Vp-MRI-DQ as well as for Vp-MRI-LR calculation.

Intra- and interobserver variation of MRI-DQ and MRI-LR were tested by repeated analysis in 10 randomly selected controls and 10 patients. Two observers (EC with 2 years of cardiac MRI experience and JW with over 15 years of cardiac MRI experience), performed these analyses blinded for each other and the analyses was performed twice by the initial observer with an inter-examination time of two weeks.

To compare the signal-to-noise ratio (SNR) in patients versus volunteers, one observer (JW) measured SNR in the VE-MRI magnitude images at the moment of end-diastole, by placing circular sampling regions-of-interest of approximately 1 – 1.5 cm2 in the left ventricle (at the position of the end of the scan line, 4 cm distal to the mitral valve) and in the air near to the anterior chest wall. SNR was calculated by the ratio between the mean signal intensity sampled in the LV and the standard deviation of the signal intensity measured in air.

Statistical analysis

Continuous data were expressed as mean ± standard deviation (SD). Vp from VE-MRI was compared with echo Doppler using paired t-test, Pearson correlation and Bland-Altman analysis with 95% limits of agreement. [22] When using the cut-off value for Vp of 45 cm/s for subjects >30 years and 55 cm/s for subject <30 years to classify LV impaired relaxation, a cross-table was constructed to determine weighted kappa agreement (Fleiss-Cohen weighting) between both modalities [23]. Correlation and agreement were classified as excellent (>0.95), strong (0.95 – 0.85), good (0.85 – 0.70), moderate (0.70 – 0.60) or fair (>0.60). Intra- and interobserver variation was determined by the significance of differences between measurements and the intraclass correlation coefficient for absolute agreement and the coefficients of variation. SPSS for Windows version 20 (SPSS Inc., Chicago, Illinois) was used for statistical analysis and $P < 0.05$ was considered significant.

3.4

RESULTS

Characteristics of the patients and healthy volunteers, with parameters for left ventricular volume measurement obtained by standard short-axis MRI evaluation, are presented in Table 1. Delayed enhancement analysis in 42 patients showed a mean infarct size of 23±16% of the total LV myocardial mass. Mean heart rate ± SD during VE-MRI for patients was 68 ± 14 bpm (range 45 – 104 bpm), which resulted in mean VE-MRI acquisition time of 4 minutes 7 seconds (range: 2 minutes 43 seconds – 5 minutes 17 seconds). For volunteers, mean heart rate ± SD during VE-MRI was 68 ± 13 bpm (range 53 – 103 bpm), which resulted in mean VE-MRI acquisition time of 1 minutes 22 seconds (range: 54 seconds – 1 minutes 46 seconds). Heart rates between examinations were very similar and not statistically significantly different: mean heart rate in patients during during

echocardiography 69 ± 15 bpm (for comparison with VE-MRI p = 0.65). For controls, mean heart rate during echocardiography 67 ± 13 bpm (for comparison with VE-MRI p = 0.46). Heart rates between patients and controls were also not statistically significantly different (p=0.46). Analysis time for Vp-assessment from VE-MRI was 1–2 minutes. SNR measured in VE-MRI in patients was 53 ± 36 versus 114 ± 77 in volunteers (p = 0.002).

In Figure 2, correlation between Vp-echo and both VE-MRI-assessed markers (Vp-MRI-DQ and Vp-MRI-RL) is presented. Good correlation between both modalities was observed: linear regression analysis between Vp-echo and Vp-MRI-DQ Y = aX + b, with regression coefficients a = 0.81±0.07 and b = 6.1±4.6, r = 0.83, p<0.001. Linear regression between Vp-echo and Vp-MRI-LR Y = aX + b, with regression coefficients a = 0.70±0.06 and b = 8.3±3.7, r = 0.84, p<0.001. Comparing both MRI markers, Vp-MRI-DQ showed significant but slightly higher values as compared to Vp-MRI-LR (mean difference 7.1±8.1cm/s, p<0.001), with excellent correlation: r = 0.941 (p<0.001). The agreement between Vp-echo and both VE-MRI markers is presented in Bland-Altman graphs in Figure 3. For both Vp-MRI-DQ and Vp-MRI-LR, a significant but small underestimation compared to Vp-echo was observed (Vp-MRI-DQ: 5.5±16.2 cm/s, p=0.008, 95% limits of agreement -26 to 37 cm/s; Vp-MRI-LR: 9.9±15.2cm/s, p<0.001, 95% limits of agreement -20 to 40 cm/s). As shown by the Bland-Altman graphs, the bias between Vp-echo and Vp-MRI becomes larger for higher values of Vp.

To identify LV impaired relaxation, age-related cut-off values were used (Vp<45 cm/s for subjects older than 30 years and Vp<55 cm/s for subjects younger than 30 years). A 26 year-old female volunteer showed a Vp-echo = 59 cm/s, a Vp-MRI-DQ = 48 cm/s and a Vp-MRI-LR = 45 cm/s. All other volunteers showed Vp>55cm/s for Vp-echo as well as for both VE-MRI markers. All patients were older than 30 years. Applying the age-related cut-off values, good agreement was found between Vp-echo and Vp-MRI-DQ: kappa ± standard error (SE) = 0.72 ± 0.09, p < 0.001;

Table 1. Population characteristics. EF: ejection fraction; LV: left ventricle, EDV: end-diastolic volume; ESV: end-systolic volume.

	Healthy volunteers	**Patients**
N	22	43
Age (years)	29 ± 13	61 ± 11
Weight (kg)	65 ± 15	80 ± 11
Gender	68% male	72% male
Heart rate (bpm)	68 ± 13	68 ± 14
LV EF %	60.9 ± 4.8	29.6 ± 11.4
LV EDV (mL)	161 ± 37	295 ± 85
LV ESV(mL)	63 ± 19	213 ± 82
NYHA class		9% class I 35% class II 47% class III 9% class IV

moderate agreement was found between Vp-echo and Vp-MRI-LR: kappa ± SE = 0.69 ± 0.09, p < 0.001 (Table 2). When using either VE-MRI measures of Vp to identify LV impaired relaxation, high values for sensitivity (Vp-MRI-DQ 88% with 95%-CI 71 – 96% and Vp-MRI-LR 88% with 95%-CI 71 – 96%) and specificity (Vp-MRI-DQ 85% with 95%-CI 70 – 93% and Vp-MRI-LR 82% with 95%-CI 67 – 91%) were found (Table 3).

Intra-observer analysis showed excellent intraclass correlation for both MRI-LR and MRI-DQ (0.97) with a coefficient of variation of 15% (Table 3). Mean difference in MRI-LR was -4.5cm/s 95%-CI -9.0 – -0.6, p=0.05 and in MRI- DQ -3.0cm/s 95%-CI -7.2 – 1.2, p=0.15. Inter-observer analysis showed strong intraclass correlation for both MRI-LR (0.92) and MRI-DQ (0.95) with a coefficient of variation of 26% for MRI-DQ and 20% for MRI-LR (Table 3). Mean difference in MRI-LR was 2.5cm/s 95%-CI -5.5 – -10.4, p=0.53 and in MRI- DQ 0.5cm/s 95%-CI -5.5 – 5.6, p=0.99.

Figure 2. Correlation between velocity propagation.
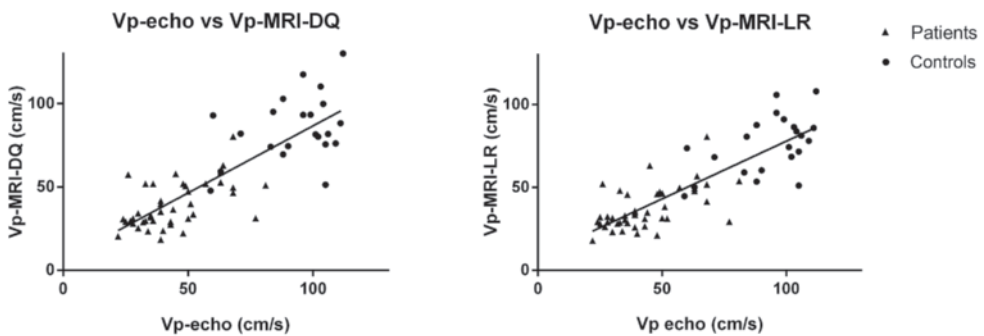
Measured with Color M-mode echocardiography (Vp-echo) and MRI difference quotient (Vp-MRI-DQ) and MRI linear regression (Vp-MRI-LR).

Figure 3. Agreement between velocity propagation.
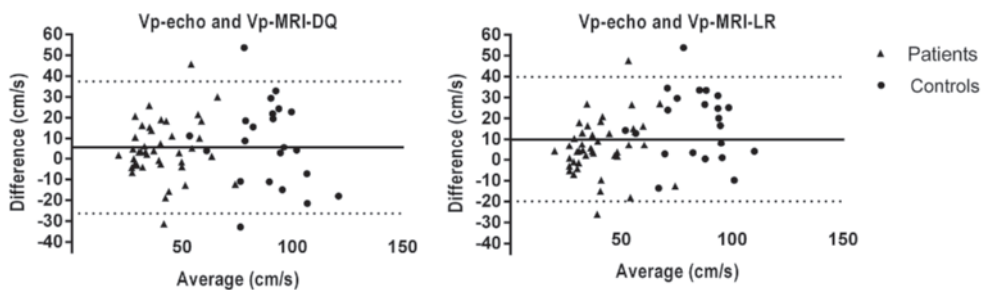
Measured with Color M-mode echocardiography (Vp-echo) and MRI difference quotient (Vp-MRI-DQ) and MRI linear regression (Vp-MRI-LR) presented in a Bland-Altman plot.

Table 2. Cross-tables determining weighted kappa agreement (Fleiss-Cohen weighting) between Vp-measurements with Color M-mode echocardiography (Vp-echo) and MRI difference quotient (Vp-MRI-DQ) and MRI linear regression (Vp-MRI-LR).

		Vp-MRI-DQ	
		< 45/55 cm/s	≥ 45/55 cm/s
Vp-echo	**< 45/55 cm/s**	23	6
	≥ 45/55 cm/s	3	33

		Vp-MRI-LR	
		< 45/55 cm/s	≥ 45/55 cm/s
Vp-echo	**< 45/55 cm/s**	23	7
	≥ 45/55 cm/s	3	32

Table 3. Intra- and inter-observer variability analysis. Vp-MRI-DQ = Velocity propagation MRI difference quotient, Vp-MRI-LR = Velocity propagation MRI linear regression.

	Intra-observer		Inter-observer	
	Vp-MRI-DQ	**Vp-MRI-LR**	**Vp-MRI-DQ**	**Vp-MRI-LR**
Intraclass correlation coefficient	0.97 (p<0.001)	0.97 (p<0.001)	0.92 (p<0.001)	0.95 (p<0.001)
Mean difference with 95%-CI (cm/s)	-4.5 (-9.0 – -0.6)	-3.0 (-7.2 – 1.2)	2.5 (-5.5 – 10.4)	0.1 (-5.5 – 5.6)
P value	0.05	0.15	0.53	0.99
Absolute difference (cm/s)	7.1 ± 7.9	5.8 ± 7.4	11.9 ± 12.3	8.9 ± 7.5
Coefficient of variation	15%	15%	26%	20%

DISCUSSION

In the current recommendations for LV diastolic function assessment, LV Vp is proposed as a relatively load-independent parameter to identify LV impaired relaxation [8,10,11] and is reproducibly measured by Color M-mode echocardiography [12]. Even when multiple echocardiographic tests of LV diastolic function may be available, Vp-assessment may be useful in the identification of impaired LV relaxation in case other Doppler indices appear to be inconclusive [24].

In the present study, a high-temporal VE-MRI method has been introduced to assess Vp and compared to Color M-mode echocardiography. More specifically, two different approaches of Vp measurement by VE-MRI were assessed; one based on the difference quotient, calculated from the LV inflow wave propagation between two measurement points; and one based on the slope determined with linear regression from the wave propagation along multiple measurement positions. The first approach reflects more closely the analysis by Color M-mode echocardiography, whereas the second approach has been tested as potentially less noise-sensitive. We chose to model the method for MRI-Vp-assessment on the Color M-mode echocardiography approach, rather than evaluating wave propagation similar to arterial pulse wave propagation approaches [25,26] as the short intra-ventricular distance that is covered and the limited spatial and temporal

resolution do not allow such evaluation. Vp-values obtained by both MRI approaches showed good correlation and agreement with Color M-mode echocardiography. However, Vp based on difference quotient calculation showed slightly better agreement and smaller bias when compared with echocardiography. This approach could be therefore proposed as a potential alternative method or as further confirmation to echocardiography in the assessment of LV diastolic function and identification of LV impaired relaxation.

Although echocardiography remains the method of choice for the assessment of LV diastolic function considering the high temporal and spatial resolution and the wide availability, VE-MRI could represent a valuable alternative in several patients referred for cardiac MRI for a comprehensive systolic and diastolic function evaluation. In patients with Duchenne muscular dystrophy for example, echocardiographic window may be poor in progressive disease, but Vp has been reported as an early marker of LV diastolic dysfunction [27]. Vp measured by VE-MRI could therefore serve as a useful tool in such cases when the echo measure is difficult to obtain. Similarly, Vp measured with Color M-mode echocardiography may be challenging in patients with dilated cardiomyopathy [13] or patients after atrioventricular valve surgery [28] due to lateral mitral valve inflow ; in these patients the MRI acquisition plane can be adjusted to the inflow direction and provide a potentially more accurate assessment. However, MRI is not feasible in all patients: claustrophobia is occasionally a problem, and absolute contraindications include pacemakers, defibrillators, and cerebral clips.

Several limitations of current study should be mentioned. VE-MRI is characterized by a lower temporal resolution as compared to Color M-mode echocardiography. Higher temporal resolution is possible by applying one-directional Fourier encoded M-mode [29], however, this technique was not available on our MRI platform. Especially for fast wave propagation, temporal resolution of VE-MRI may not be adequate to register Vp accurately. This explains the fact that agreement between MRI and Color M-mode echocardiography worsened for higher Vp values. However, around the proposed cut-off values of 45cm/s (>30 year-old) and 55cm/s (<30 year-old), VE-MRI performs well for the identification of impaired LV relaxation with a good kappa agreement and high sensitivity and specificity. With VE-MRI an average heart beat is constructed from several minutes of recording, consequently variety in heart rate might cause errors. The time-resolved imaging approach of MRI is not feasible for detecting small-scale fluctuations in the temporal domain. However, variety in heart rate was minimized during the acquisition by excluding heart beats with more than 10% deviation of the average. Furthermore, due to logistical reasons, patients and volunteers were scanned using different scanners and field strengths, resulting in minor differences among some scan parameters and a more than twofold higher SNR for VE-MRI in volunteers versus patients. However, SNR of VE-MRI in patients was still adequate for Vp-assessment. Furthermore, it is not expected that the method of Vp-assessment will be affected by scanning at different field strengths. Finally, in the current study, only patients with ischemic heart failure were included. Vp-assessment with VE-MRI should also be evaluated further in healthy controls to provide reference values and in different patient populations

3.4

such as heart failure patients with preserved ejection fraction, non-ischemic cardiomyopathy or congenital heart disease.

CONCLUSION

This study showed the feasibility of a high-temporal VE-MRI approach for Vp-assessment, with a direct comparison to Color M-mode echocardiography. Good correlation and agreement was found especially for lower Vp-values which are related to impaired LV relaxation. VE-MRI represents therefore a potential valuable approach in the assessment of LV diastolic function.

REFERENCES

1. Wan SH, Vogel MW, Chen HH. Pre-clinical diastolic dysfunction. J Am Coll Cardiol 2014;63:407-16.

2. Kitzman DW, Little WC, Brubaker PH, et al. Pathophysiological characterization of isolated diastolic heart failure in comparison to systolic heart failure. JAMA 2002;288:2144-50.

3. Redfield MM, Jacobsen SJ, Burnett JC Jr, et al. Burden of systolic and diastolic ventricular dysfunction in the community: appreciating the scope of the heart failure epidemic. JAMA 2003;289:194-202.

4. AlJaroudi WA, Thomas JD, Rodriguez LL, et al. Prognostic value of diastolic dysfunction: state of the art review. Cardiol Rev 2014;22:79-90.

5. Sagawa K. The end-systolic pressure-volume relation of the ventricle: definition, modifications and clinical use. Circulation 1981;63:1223-7.

6. Gilbert JC, Glantz SA. Determinants of left ventricular filling and of the diastolic pressure-volume relation. Circ Res 1989;64:827-52.

7. Nagueh SF, Appleton CP, Gillebert TC, et al. Recommendations for the evaluation of left ventricular diastolic function by echocardiography. J Am Soc Echocardiogr 2009;10:165-93.

8. Takatsuji H, Mikami T, Urasawa K, et al. A new approach for evaluation of left ventricular diastolic function: spatial and temporal analysis of left ventricular filling flow propagation by color M-mode Doppler echocardiography. J Am Coll Cardiol 1996;27:365-71.

9. Brun P, Tribouilloy C, Duval AM, et al. Left ventricular flow propagation during early filling is related to wall relaxation: a color M-mode Doppler analysis. J Am Coll Cardiol 1992;20:420-32.

10. Garcia MJ, Thomas JD, Klein AL. New Doppler echocardiographic applications for the study of diastolic function. J Am Coll Cardiol 1998;32:865-75.

11. Garcia MJ, Smedira NG, Greenberg NL, et al. Color M-mode Doppler flow propagation velocity is a preload insensitive index of left ventricular relaxation: animal and human validation. J Am Coll Cardiol 2000;35:201-8.

12. Garcia MJ, Ares MA, Asher C, et al. An index of early left ventricular filling that combined with pulsed Doppler peak E velocity may estimate capillary wedge pressure. J Am Coll Cardiol 1997;29:448-54.

13. Khouri SJ, Maly GT, Suh DD, et al. A practical approach to the echocardiographic evaluation of diastolic function. J Am Soc Echocardiogr 2004;17:290-7.

14. Gonzalez-Vilchez F, Ares M, et al. Combined use of pulsed and color M-mode Doppler echocardiography for the estimation of pulmonary capillary wedge pressure: an empirical approach based on an analytical relation. J Am Coll Cardiol 1999;34:515-23.

15. Westenberg JJ. CMR for Assessment of Diastolic Function. Curr Cardiovasc Imaging Rep 2011;4:149-58.

16. Kim RJ, Shah DJ, Judd RM. How we perform delayed enhancement imaging. J Cardiovasc Magn Reson 2003;5:505-14.

17. Westenberg JJ, Lamb HJ, van der Geest RJ, et al. Assessment of left ventricular dyssynchrony in patients with conduction delay and idiopathic dilated cardiomyopathy: head-to-head comparison between tissue doppler imaging and velocity-encoded magnetic resonance imaging. J Am Coll Cardiol 2006;47:2042-8.

18. Westenberg JJ, Roes SD, Ajmone MN, et al. Mitral valve and tricuspid valve blood flow: accurate quantification with 3D velocity-encoded MR imaging with retrospective valve tracking. Radiology 2008;249:792-800.

19. Marsan NA, Westenberg JJ, Tops LF, et al. Comparison between tissue Doppler imaging and velocity-encoded magnetic resonance imaging for measurement of myocardial velocities, assessment of left ventricular dyssynchrony, and estimation of left ventricular filling pressures in patients with ischemic cardiomyopathy. Am J Cardiol 2008;102:1366-72.

20. Marsan NA, Westenberg JJ, Ypenburg C, et al. Quantification of functional mitral regurgitation by real-time 3D echocardiography: comparison

3.4

with 3D velocity-encoded cardiac magnetic reso-nance. JACC Cardiovasc Imaging 2009;2:1245-52.

21. Roes SD, Hammer S, van der Geest RJ, et al. Flow assessment through four heart valves simultane-ously using 3-dimensional 3-directional velocity-encoded magnetic resonance imaging with retrospective valve tracking in healthy volunteers and patients with valvular regurgitation. Invest Radiol 2009;44:669-75.

22. Bland JM, Altman DG. Statistical methods for assessing agreement between two methods of clinical measurement. Lancet 1986;1:307-10.

23. Ludbrook J. Statistical techniques for comparing measurers and methods of measurement: a critical review. Clin Exp Pharmacol Physiol 2002;29:527-36.

24. Rivas-Gotz C, Manolios M, Thohan V, et al. Impact of left ventricular ejection fraction on estimation of left ventricular filling pressures using tissue Doppler and flow propagation velocity. Am J Cardiol 2003;91:780-4.

25. Westenberg JJ, de Roos A., Grotenhuis HB, et al. Improved aortic pulse wave velocity assessment from multislice two-directional in-plane velocity-encoded magnetic resonance imaging. J Magn Reson Imaging 2010;32:1086-94.

26. Grotenhuis HB, Westenberg JJ, Steendijk P, et al. Validation and reproducibility of aortic pulse wave velocity as assessed with velocity-encoded MRI. J Magn Reson Imaging 2009;30:521-6.

27. Markham LW, Michelfelder EC, Border WL, et al. Abnormalities of diastolic function precede di-lated cardiomyopathy associated with Duchenne muscular dystrophy. J Am Soc Echocardiogr 2006;19:865-71.

28. Calkoen EE, Roest AA, Kroft LJ, et al. Characteriza-tion and improved quantification of left ventricular inflow using streamline visualization with 4DFlow MRI in healthy controls and patients after atrio-ventricular septal defect correction. J Magn Reson Imaging. 2014 doi: 10.1002/jmri.24735

29. Taviani V, Patterson AJ, Graves MJ, et al. Accuracy and repeatability of fourier velocity encoded M-mode and two-dimensional cine phase contrast for pulse wave velocity measurement in the descending aorta. J Magn Reson Imaging 2010;31:1185-94.

Chapter 3.5

Altered left ventricular vortex ring formation by 4-dimensional flow magnetic resonance imaging after repair of atrioventricular septal defects

Emmeline E. Calkoen *, Mohammed S.M. Elbaz *, Jos J.M. Westenberg, Lucia J.M. Kroft,
Mark G. Hazekamp, Nico A. Blom, Albert de Roos,
Arno A.W. Roest and Rob J. van der Geest
*equal contribution

ABSTRACT

Objectives

During normal left ventricular (LV) filling, a vortex ring structure is formed distal to the left atrio-ventricular valve (LAVV). Vortex structures contribute to efficient flow organization. We aimed to investigate whether LAVV abnormality in patients with a corrected atrioventricular septal defect (AVSD) has impact on vortex ring formation.

Methods

Whole-heart 4DFlow MRI was performed in 32 patients (age 26±12 years) and 30 healthy controls (25±14 years). Vortex ring cores were detected at peak early (E-peak) and peak late filling (A-peak). When present, the three-dimensional (3D) position and orientation of the vortex ring was defined and the circularity index was calculated. Through-plane flow over the LAVV and the Vortex Formation Time (VFT) were quantified to analyze the relation of vortex flow with the inflow jet.

Results

Absence of a vortex ring during E-peak (controls 0% versus patients 19%, p=0.015) and A-peak (controls 10% versus patients 44%, p=0.008) was more frequent in patients. In 4 patients, this was accompanied by a high VFT (5.1-7.8 versus 2.4±0.6 in controls) and in another two patients with abnormal valve anatomy. In patients compared with controls, the vortex cores had a more anterior and apical position, closer to the ventricular wall, with a more elliptical shape and oblique orientation. The shape of the vortex core closely resembled the valve shape and its orientation was related to the LV inflow direction.

Conclusion

This study quantitatively shows the influence of abnormal LAVV and LV inflow on 3D vortex ring formation during LV inflow in corrected-AVSD patients compared with controls.

BACKGROUND

Patients with an atrioventricular septal defect (AVSD) require corrective surgery early in life to prevent pulmonary overflow and heart failure. As compared with the normal mitral valve, the mural (posterior) leaflet of the left atrioventricular valve (LAVV) is smaller and the anterolateral papillary muscle is positioned more lateral in AVSD hearts [1;2]. Furthermore, the presence of a single papillary muscle and double-orifice are described [3]. Moreover, surgical correction of an AVSD, including closure of the 'cleft', may result in restricted opening of the LAVV [4] and a more lateral inflow [5], which might affect efficiency of cardiac blood flow in the left ventricle (LV). Survival after surgical correction is excellent in current era, but re-operation rate due to valve regurgitation is high [6;7]. Long-term follow-up data on cardiac function or exercise capacity after AVSD correction is lacking. However, deterioration of cardiac function and NYHA-class is described during pregnancy, when cardiac flow increases [8].

Recently, the formation of a vortex within the LV during diastole was related to the inflow area through the mitral valve in healthy subjects [9]. The formation of vortex structures, (i.e. compact regions of swirling blood flow) in LV blood flow patterns during diastolic filling has recently emerged as a potential novel index for characterizing efficient LV blood flow and evaluating cardiac chamber (dys)function [10]. During LV filling, a vortex ring structure distal to the mitral valve leaflets and enclosing the inflow jet is observed. This vortical flow is considered an efficient mechanism for transporting a significant portion of LV filling volume towards the aorta [11], minimizing energy loss and helping mitral valve closure [12;13]. Recently, three-directional, three-dimensional (3D) and time-resolved velocity encoded MRI(4DFlow MRI) has been introduced to assess vortex ring formation during LV filling in vivo [9], because it has the advantage of a 3D evaluation of the vortex ring.

Given the relation between the vortex ring properties and the mitral valve morphology and LV inflow [9;14-17], we hypothesized that LAVV abnormalities and associated abnormal lateral inflow [5] after surgical AVSD correction may result in disturbed vortex flow during LV filling. Therefore, we used 4DFlow MRI to identify and quantitatively characterize the geometrical properties and anatomical location of vortex ring cores during early and late LV filling, allowing quantitative assessment of 3D vortex ring properties in AVSD-corrected patients and comparison to healthy controls.

METHODS

Study population

The study was approved by the ethical committee of the Leiden University Medical Center and written informed consent was obtained from all participants or their parents. Thirty-two patients with a history of corrected-AVSD were prospectively enrolled from a surgical database [18].

Thirty controls with a similar age without history of cardiac disease were included for comparison. Patients and controls in the current study were previously reported in studies with the aim to characterize and quantify diastolic trans-atrioventricular flow [5;19]. Twenty-four of the 30 healthy controls were reported in a study providing reference values for 3D vortex flow in the LV flow [9]. None of the previously published papers addresses vortex formation in corrected AVSD patients. For clarity we will use the term left atrioventricular valve (LAVV) in patients and controls, instead of referring to mitral valve in healthy subjects and LAVV in patients.

Magnetic Resonance Imaging acquisition and analysis

Whole-heart 4DFlow was obtained on a 3T MRI scanner (Ingenia, Philips Healthcare, Best, The Netherlands) with maximal gradient amplitude of 45mT/m for each axis and a slew rate of 200T/m/sec, using a combination of FlexCoverage Posterior coil in the table top with a dStream Torso coil, providing up to 32 coil elements for signal reception. Imaging details have been reported elsewhere [5]. In short, a 3D volume acquisition of the heart was performed with velocity encoding of 150cm/s in all three directions, spatial resolution of 2.3×2.3×3.0-4.2mm^3, 30 cardiac phases were retrospectively reconstructed to represent one average heartbeat, with a maximal true temporal resolution of 31ms. Furthermore, to quantify LV volumes and ejection fraction, a left 2-chamber and 4-chamber cine view and a short-axis cine stack of slices, was acquired with steady-state free-precession (SSFP) sequences as reported elsewhere [5].Spatial resolution was 1.0×1.0×8.0mm^3 and also for these acquisitions, 30 phases were retrospectively reconstructed. All acquisitions were performed with free breathing and no respiratory motion control. The cine SSFP acquisitions were all performed with 3 signal averages to suppress breathing artefacts. After manual segmentation of LV endocardial boundaries, the LV end-diastolic volume (LVEDV), end-systolic volume (ESV) and ejection fraction were calculated. Sphericity index of the LV was calculated as LVEDV/(π/6×long-axis at end-diastole^3).

A 3D vortex core analysis based on the Lambda2-method

Using the image analysis workflow as described previously [9], the cores of vortex structures within the LV blood flow during diastole as acquired from the 4DFlow MRI data were identified by a single observer using the Lambda2-method [20]. In short, the Lambda2-method is a fluid-dynamics-based method that uses the gradient properties of the velocity field to identify vortex cores in the flow. For each subject, the vortex cores were identified at the early (E-peak) and late (A-peak) filling, defined from the below described trans LAVV flow quantification, and visualized as isosurfaces.

   Qualitative visual inspection of the shape of detected vortex cores was performed to determine whether a 3D ring-shaped vortex core was present, defined as a vortex core with a donut-like (torus) shape (Figure 1). If a vortex ring core was detected during E-peak and/or A-peak, its 3D position (in normalized cylindrical coordinates), orientation and shape were quantitatively characterized as illustrated in Figure 1.

Figure 1. 3D-quantitative vortex core parameters.
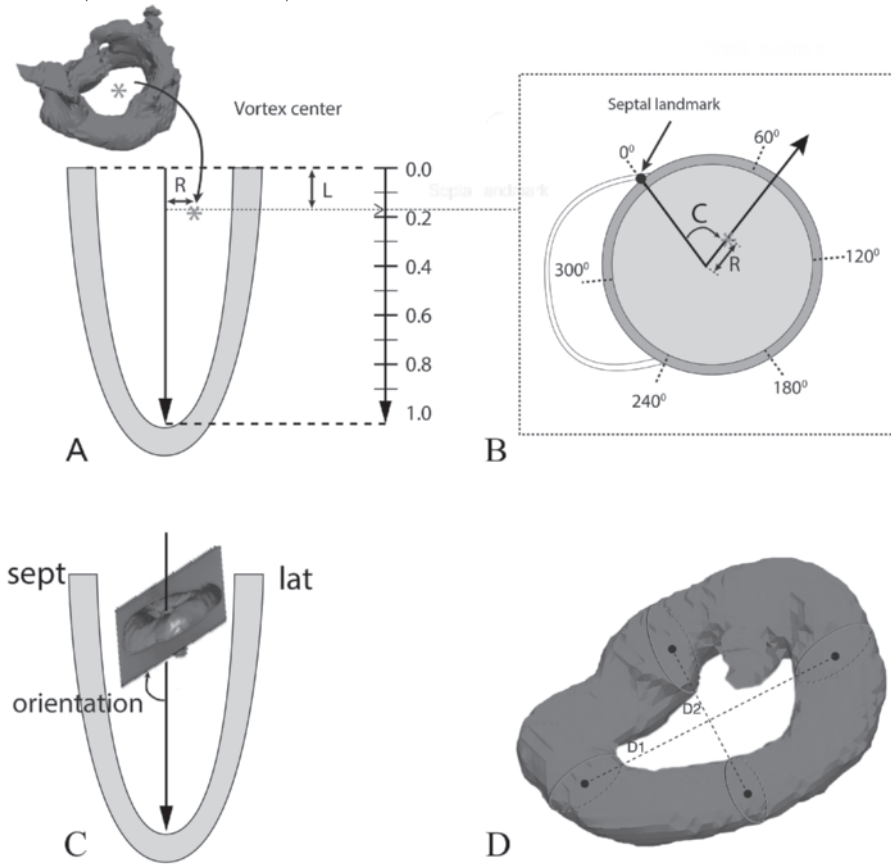
The cylindrical position of the vortex core center (asterisk in a) was defined using longitudinal (L), circumferential (C), and radial (R) coordinates relative to LV (A,B). L and R were normalized relative to the LV long-axis length and the radius of the LV endocardial cavity respectively. The orientation angle was defined relative to the long-axis (C)(sept = septal side, lat = lateral side). Circularity index (CI) was defined as the ratio between longest- (D1) and shortest diameter (D2) (D). (modified after Elbaz et al. JCMR (16))

Trans- left atrioventricular valve flow

Trans-LAVV flow was quantified using the 4DFlow MRI data and retrospective valve tracking [21]. From the through-plane LAVV velocity map, a flow-time curve of the LAVV flow was computed and E-peak and A-peak were defined. The early LV filling fraction was calculated as (E-wave inflow volume / total inflow volume) × 100%. To study the association with diastolic vortex formation, LAVV and inflow characteristics were evaluated. The inflow area and peak velocity during E-peak were quantified at the level of peak inflow velocity. The peak velocity inflow angle (i.e. angle between long-axis and inflow direction) at E-peak was measured using streamline visualization of the flow velocity field on the four-chamber view as previously described [5].

Vortex formation time index

The Vortex Formation Time (VFT), a dimensionless index previously proposed to quantify the process of vortex progression during early filling [23], was determined using the formula: VFT = ($V_{avg} \times E_{duration}$) / D, based on the average speed of the blood flow during the early filling period (V_{avg}), the duration of the E-filling ($E_{duration}$) and the maximum diameter (D). The D dominator was computed at E-peak from the area of the LAVV flow, measured on the velocity map after retrospective valve tracking at peak velocity level (i.e. tip of the valves). The diameters was calculated as $D = 2\sqrt{Area/\pi}$, assuming the inflow area to be circular.

Statistical analysis

Data analysis was performed using SPSS Statistics (version 20.0 IBM SPSS, Chicago, Illinois). Variables were tested for normal distribution using the Shapiro-Wilk test. Continuous variables are expressed as mean ± standard deviation (SD) and as median with inter-quartile range (IQR) where appropriate. Differences between presence of E-peak and A-peak vortex ring core were tested with a Pearson Chi-Square test. Differences between patients and controls and subjects with and without E-peak vortex ring core were performed with an unpaired T-test or Mann-Whitney-U-test. Correlation between inflow direction, LV volume and vortex position parameters were assessed with linear regression analysis (Pearson's r).

RESULTS

Patient characteristics

Characteristics of patients and healthy controls are presented in Table 1. Of 32 patients, 1 had a double-orifice LAVV [3], 1 had a single papillary muscle [3] and another patient was known with dextrocardia. In patients compared with controls, mean LV ejection fraction was lower, diastasis was shorter and LV sphericity index was higher.

Presence of 3D vortex cores during E-peak and A-peak

In all controls, during peak E-filling, a quasi-ring-shaped vortex core was identified distal to the mitral valve in the LV blood flow pattern (Figure 2). In 26 (81%, p=0.015) patients, such compact 3D vortex ring core distal to the LAVV was identified during peak E-filling. The shape of the detected 3D vortex ring cores in patients was more frequently deformed, albeit the vortex cores were still compact and recognizable (Figure 2).

Visually, the shape of vortex core tended to resemble the shape of the inflow area over the LAVV as observed on the through-plane velocity maps (Figure 2). In six patients (19 %) (Table 2), no E-peak vortex ring core was detected, instead only a complex irregular vortex shape was present. The six patients included the patient with a double-orifice LAVV (Figure 3) and the patient with a single papillary muscle. The other 4 patients without an E-peak vortex ring core had a

small LAVV area, higher peak velocity and VFT deviating more than 2SD (VFT = 5.1, 5.5, 7.4 and 7.8) (Table 2) from controls (2.6±0.6). The other patients with an E-peak vortex ring core had a mean VFT of 2.4±0.6, which was very similar to the controls. The LV shape parameters LVEDV and sphericity index, of the six patients without E-peak vortex, still fell within the ranges of the patients with an E-peak vortex ring core.

At peak A-filling, an asymmetrical compact vortex ring core formed at the basal LV level in 27 controls (90%) but only in 19 (59%, p=0.006) patients. Details of patients with and without A-peak vortex ring core are presented in Table 3. Patients and controls without an A-peak vortex ring core had shorter diastasis (14±17ms) as compared with patients and controls with an A-peak vortex ring (109±85ms, p<0.001).

## Quantitative 3D parameters of vortex ring cores and association with the LAVV and LV characteristics

The circumferential, longitudinal and radial position, orientation and circularity index were quantified for all detected vortex ring cores. During E-peak and A-peak the center of the vortex ring core was positioned more anterior (lower circumferential value), closer to the apex (higher

Table 1. Characteristics of healthy controls and patients. LVEDV = Left ventricular end-diastolic volume, BSA=body surface area, LAV=left atrial volume, LV=left ventricle, LAVV=left atrioventricular valve, VFT=vortex formation time, * excluding two cases without A-peak † indicates p<0.01, ‡indicates p<0.001.

	Controls	Corrected-AVSD patients
Age (years)	23 (13-38)	26 ± 12
Male (%)	14 (46)	9 (28)
Heart rate (bpm)	68 (60-78)	76 ± 13
Diastasis (ms)	116 ± 89	26 (0-67) * †
Type AVSD	-	21 (66%) partial 11 (33%) complete or intermediate
Time after surgical correction (years)		20 ± 9
Stroke volume LV (mL)	89 ± 23	85 ± 19
LVEDV (mL)	146 ± 42	155 ± 33
LVEDV / BSA (mL/m^2)	87 ± 13	91 ± 15
LV Sphericity index	0.37 ± 0.06	0.57 ± 0.14 ‡
Inflow area (cm^2)	9.2 ± 2.0	8.5 ± 2.5
Peak velocity (cm/s)	94 ± 15	93 (77-145)
VFT index	2.6 ± 0.6	2.4 (1.9-3.1)
Blood pressure systolic (mmHg)	112 ± 13	119 ± 20
Blood pressure diastolic (mmHg)	67 ± 9	67 ± 12
E/A ratio peak flow rate	2.5 ± 0.8	2.1 (1.7-2.6) *
Early filling fraction (%)	76 ± 5	73 ± 13
Ejection fraction (%)	61 ± 5	56 (52-58) ‡
LAVV regurgitation (%)	-	14 ± 8

3.5

Figure 2. Shape of vortex core corresponds with the inflow area.
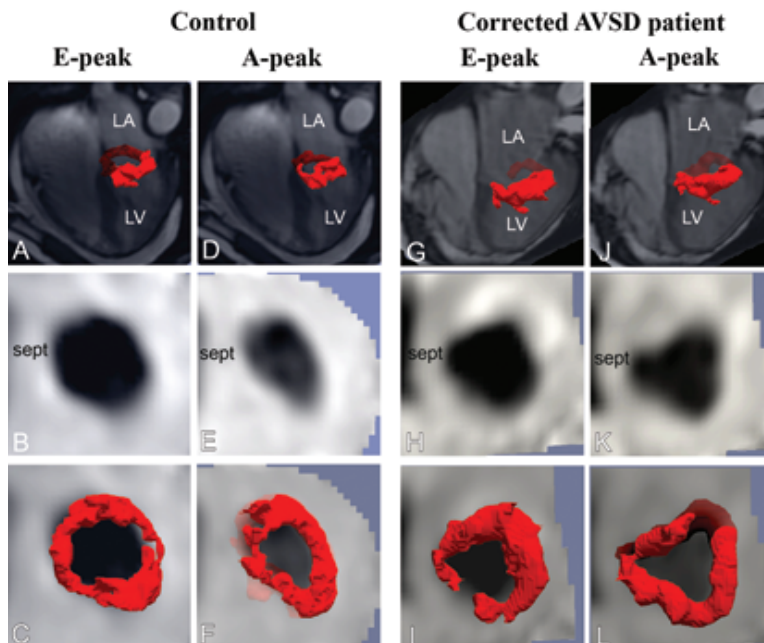
Vortex cores depicted on reformat planes of through-plane flow at peak inflow velocity (B, E, H, K) during early (E-peak) and late (A-peak) filling in a healthy control (A-F) and a patient (G-L). LA = Left atrium, LV = Left ventricle. Sept = septal side.

Figure 3. Patient with a double-orifice LAVV showing two separate inflow jets.
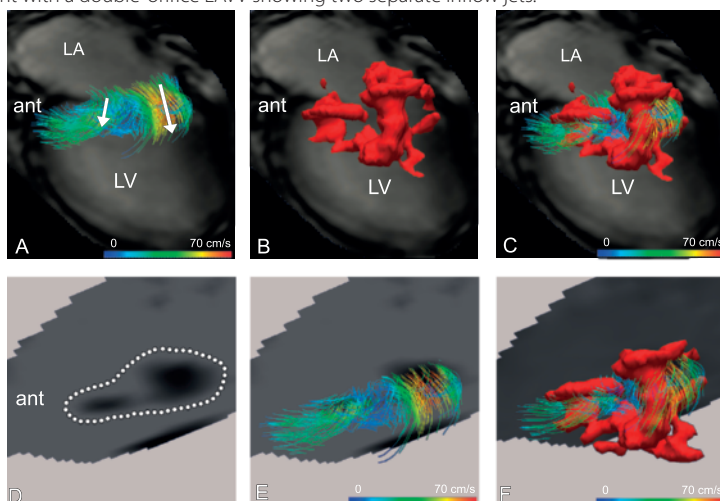
Streamlines (color coding representing velocity magnitude) show two inflow jets (white arrow A). The vortex core had a complex shape (B), but fitted with streamlines (C). Through-plane flow analysis showed two jets in the LAVV (dotted line in D). Positioning the streamlines (E) and vortex core (F) on top of the velocity map shows that a core is formed around both jets. LA = Left atrium, LV = Left ventricle. Ant = anterior.

Table 2. Characteristics of the 6 patients without a vortex ring core during E-peak or A-peak. Bpm = beats per minute, ms = milliseconds, LAVV = left atrioventricular valve, cm = centimeter, s = second, VFT = vortex formation time

	Pt 1	Pt 2	Pt 3	Pt 4	Pt 5	Pt 6
Age	10	23	20	36	12	32
Type AVSD	Partial double-orifices	Complete single papillary muscle	Partial	Complete	Complete	Complete dextro-cardia
Regurgitation %	10	23	20	36	12	32
Heart rate (bpm)	76	78	96	114	60	62
Diastasis (ms)	24	0	No A-peak	No A-peak	0	0
Early filling fraction (%)	61	80	100	100	81	88
Area LAVV (cm^2)	9.2	8.4	6.0	5.1	4.6	4.6
Peak velocity (cm/s)	58	110	144	158	146	155
VFT	1.6	2.5	5.1	5.5	7.8	7.4

Table 3. Characteristics of controls and patients with a vortex ring core present during E-peak. Bpm = beats per minute, ms = milliseconds, LAVV = left atrioventricular valve, cm = centimeter, s = second, VFT = vortex formation time.

|	Controls with E- and A-peak ring	Controls with only E-peak ring	Patients with E- and A-peak ring	Patients with only E-peak ring
N	27	3	19	7
Age	26 ± 13	11 ± 2	26 ± 14	28 ± 8
Type AVSD	-	-	14 partial 5 complete	5 partial 2 complete
Regurgitation %	-	-	12 ± 8	13 ± 6
Heart rate (bpm)	67 ± 10	95 ± 7	72 ± 12	80 ± 4
Diastasis (ms)	128 ± 86	7 ± 13	81 ± 79	22 ± 18
Passive filling fraction (%)	76 ± 5	79 ± 2	72 ± 11	68 ± 10
Area LAVV (cm^2)	9.5 ± 1.9	6.4 ± 0.8	8.8 ± 2.5	9.3 ± 2.3
Peak velocity (cm/s)	93 ± 16	105 ± 4	92 ± 15	94 ± 28
VFT	2.6 ± 0.6	2.6 ± 0.2	2.4 ± 0.6	2.4 ± 0.5

3.5

longitudinal value) and closer to the LV wall (higher radial value) in patients compared with controls (Table 4).

In healthy controls, the vortex orientation ranged from 55-88°, while in patients, the vortex orientation showed a wider range (14-134°). Three patients had a vortex orientation angle larger than 90° (i.e. 102°, 115° and 134°), indicating a reversed orientation of the ring (Figure 4) with the lateral side of the vortex being positioned towards the apex, in contrast to the controls where the septal side was positioned more apical. In patients with non-reversed vortex ring cores (orientation <90°), cores were in a more tilted position (50±20°) as compared with the controls (71±9°, p<0.001) (Figure 5). During A-peak, the vortex ring core orientation was in a non-reversed more

Table 4. Quantitative vortex core characteristics as presented in Figure 1 at E-peak and A-peak in controls and patients. * Including patients with a non-reversed orientation (N=23). Inclusion of all patients (N=26) gives a mean orientation of 58 ± 29, p=0.037.

		Controls (N=30)	Patients (N=26)	P value
E-peak	Circumferential	90 ± 26°	70 ± 21°	0.003
	Longitudinal	0.19 ± 0.04	0.23 ± 0.07	0.015
	Radial	0.26 ± 0.07	0.33 ± 0.08	0.001
	Orientation	71 ± 9°	50 ± 20° *	<0.001 *
	Circularity Index	0.80 ± 0.08	0.70 ± 0.13	0.002
		Controls (N=27)	Patients (N=19)	
A-peak	Circumferential	106 ± 27°	80 ± 28°	0.003
	Longitudinal	0.15 ± 0.05	0.19 ± 0.05	0.004
	Radial	0.20 ± 0.08	0.32 ± 0.14	0.002
	Orientation	72 ± 6°	54 ± 21°	0.001
	Circularity Index	0.63 (0.59-0.69)	0.60 ± 0.10	0.115

Figure 4. Reversed orientation of the vortex ring core in a corrected AVSD patient.
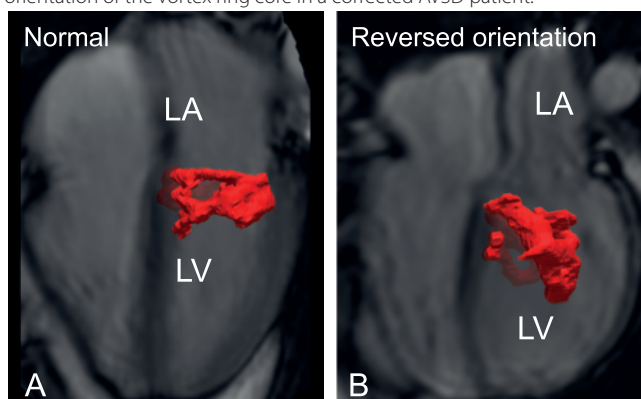
Healthy control (A) and patients (B). LA = Left atrium, LV = Left ventricle.

tilted position in all patients compared with controls (54±21° versus 72±6°, p=0.001). During both E-peak and A-peak, vortex ring cores were less circular in patients compared with controls (Figure 5) (Table 4).

In patients, vortex ring core orientation angle relative to the LV long-axis showed a significant correlation with the inflow angle (E-peak r=0.41, p=0.037 and A-peak r=0.62, p=0.005), inflow area during E-peak (r = 0.47, p=0.015) and LVEDV (E-peak r=0.61, p=0.001 and A-peak r=0.54 p=0.017). In controls no significant correlations were found between orientation angle and inflow angle, inflow area or LVEDV. In patients, sphericity index of the LV did not show a relation with vortex ring core characteristics. Ejection fraction did not correlate with vortex ring core
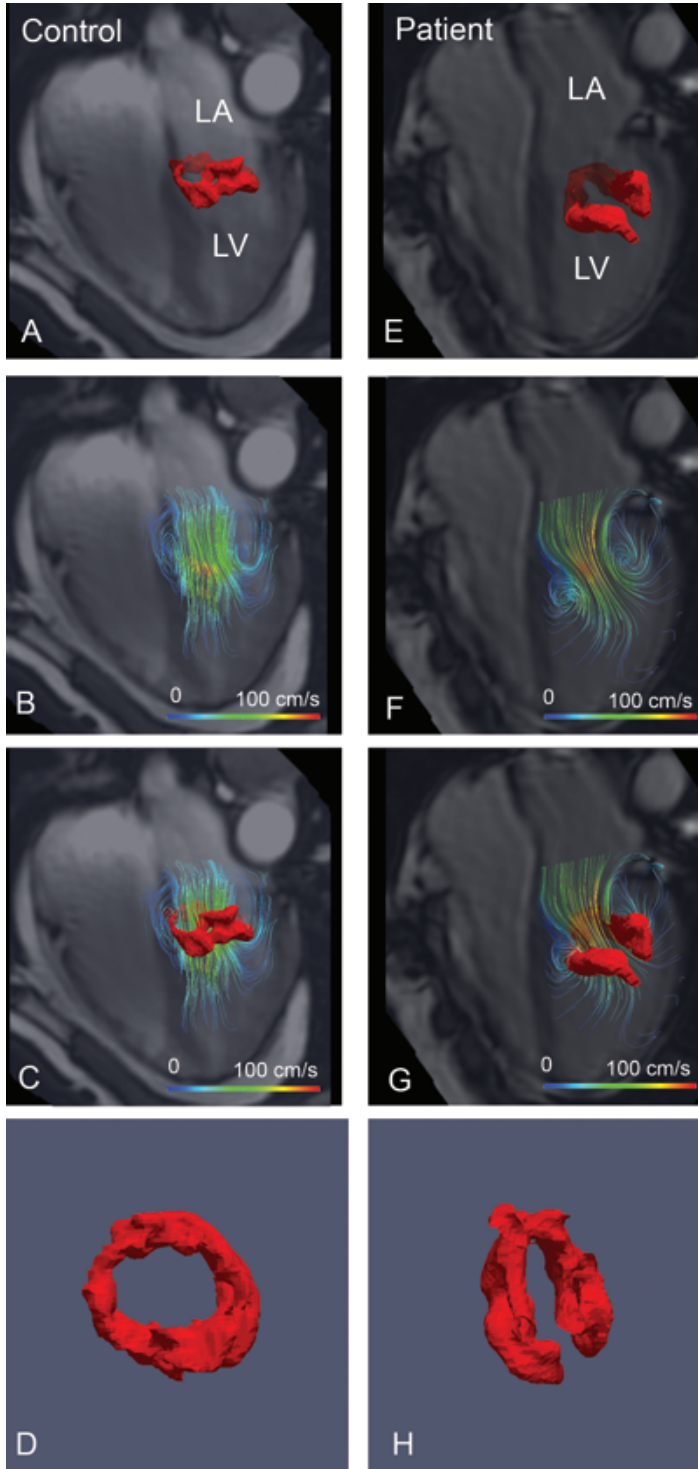
Figure 5. Example of a vortex core during E-peak in a patient and a control.

Streamline visualization (color coding represents velocity magnitude) shows a more lateral inflow direction in the patient (F) compared with the control (B). The vortex core has a more tilted orientation (G) and elliptical shape (H) in the patient as compared with the healthy control (C-D). LA = Left atrium, LV = Left ventricle.

3.5

presence or characteristics. In patients, no significant correlation (p=0.97) was found between regurgitation fraction and vortex orientation.

DISCUSSION

This study, for the first time, quantitatively describes the effect of LAVV abnormalities and abnormal LV inflow on 3D vortex ring formation in LV blood flow patterns during early and late filling, in patients with surgically corrected LAVV valves compared with healthy subjects. These findings highlight the close relationship between AVV morphology and LV filling characteristics, with LV vortex formation. Previous studies on vortex formation in the presence of LAVV abnormalities were performed in vitro, or were based on 2-dimensional analysis using echocardiography.

The current report provides an in vivo 3D analysis using 4D flow MRI. Key findings are as follows: (1) Absence ofvortex ring formation is more frequent in corrected-AVSD patients and is related to LAVVabnormalities (single papillary muscle and double-orifice) and a narrow LAVV diameter concomitant with high inflow velocities evidenced by a high VFT. (2) If a vortex ring core is present in corrected-AVSD patients, it has a different position, a more elliptical shape, and an oblique orientation compared with controls, and these differences correlate with LV inflow direction.

Absence of vortex ring core related to valve morphology and VFT

In the normal heart, adequate suction, correct shape of the valve leaflets and normal electrical conduction allow vortex ring formation during LV filling [23]. In our study, 6 patients did not develop a vortex ring. One of these patients had a double-orifice LAVV, resulting in two inflow jets as is also seen after edge-to-edge repair. Absence of a ring in this patient is in agreement with computational fluid dynamics (CFD) studies simulating edge-to-edge repair, resulting in abnormal vortex formation with increased energy loss and decreased LV filling efficiency [24]. Another patient without vortex ring formation had a single papillary muscle, stressing the contribution of the papillary muscles to the shape of the vortex ring [25].

Both cases underline the influence of morphological LAVV abnormalities on vortex formation. Next to two patients with abnormal anatomy, 4 other patients were observed without E-peak vortex ring formation. These four had a VFT more than 2 SDs higher, compared with the patients with an E-peak vortex ring core and controls. The VFT index, studied *in vitro* and *in vivo*, is known to have an optimal value range defining efficient vortex formation [22;26]. In patients with mitral stenosis, higher values of VFT have been related to absence of a well-formed vortex ring resulting in increased energy dissipation [27]. In the current MRI study, the VFT values in controls were lower than the reported range (3.5-5.5) measured with echocardiography [22]. This might be due to differences between modalities [28] and their definition of valve diameter measurement. However, the markedly higher VFT values in patients with an absent vortex ring confirms that

patients with a narrow LAVV diameter and higher peak velocity develop abnormal vortex flow [22,26]. In addition, VFT measurements were comparable and not significantly different between controls and patients when an E-vortex ring core was present. Absence of a separate A-peak vortex ring core was related to the shorter diastasis in patients similarly to what is reported in healthy controls [9].

Vortex ring formation related to LAVV and LV characteristics

In normal hearts, a vortex ring forms at the tip of the LAVV [29], with the septal side positioned towards the apex due to the unbalanced shape of the leaflets (i.e., longer anterior and shorter posterior leaflet) and interaction with LV wall [23,29]. The visual similarity between the 3D shape of the vortex ring core and the (abnormal) LAVV orifices (i.e. LAVV inflow area) in this study illustrates the impact of the abnormal LAVV on vortex ring formation. Moreover, the observed correlation between disturbed vortex characteristics and altered inflow area and direction, indicates an influence of abnormal valve and inflow on vortex ring formation. Our findings are in agreement with CFD experiments [16], 2D echocardiography analysis in human [17;30] and an MRI study in sheep [31] showing that LAVV repair and replacement are related to unnatural vortex formation. Aside from the impact of the valve abnormalities, the correlation between vortex ring orientation and LVEDV shows an impact of LV size on vortex formation. This finding is in agreement with the relation between LVEDV and vortex size observed in patients with dilated cardiomyopathy [32]. In current study, no relation was found between vortex ring core characteristics and sphericity index, as was described in a previous study using vortex filling fraction [11]. However, absence of such correlation might be due to the narrow range in sphericity index of patients in the current study. In addition no relation was found with the ejection fraction, which was close to normal in all patients. Consequently a possible impact of a restrictive LV, remains to be investigated.

Clinical implication

During AVSD correction, the common atrioventricular valve is separated and the cleft is closed. During surgical correction of an AVSD surgeons have to minimize valve regurgitation, without causing valve restriction. Even though the shape of the vortex will not be the main concern of the surgeon during correction of an AVSD, awareness of the effect of valve surgery on the formation of vortices in the LV blood flow is important, as changes in vortex formation might affect blood flow efficiency. Similar consideration accounts for LAVV surgery in other congenital and acquired heart disease.

    These results do not preclude the possibility that the aberrant vortex formation is a coping mechanism of the heart and has a favorable effect on cardiac function. However, CFD studies have shown increased energy dissipation in cases with a disturbed LAVV shape and abnormal vortex flow formation [14-16] and reduced efficiency of the heart pump in patients with a higher VFT index [33]. A reversed vortex resulted in an increased energy dissipation level compared with

3.5

a normally oriented vortex [15]. Whether the aberrant vortex formation also results in clinical relevant changes in flow efficiency in corrected AVSD patients remains to be investigated during long-term follow-up data of this patient group.

In the current study, global diastolic and systolic functions were within normal ranges, however vortex ring characteristics were significantly different in patients compared with controls. This finding may suggest that vortex formation provides a more sensitive indication of disturbed diastolic function than do conventional functional parameters, and confirms the suggested role of vortex analysis as early predictor of diastolic dysfunction [34]. In patients with unbalanced AVSD the inflow direction may play a role in LV growth as well [35]. Analysis of vortex formation in unbalanced AVSDs can potentially contribute to predicting LV growth and decision making for bi-ventricular repair.

The disturbed vortex formation observed at rest may become more pronounced during exercise or pregnancy when cardiac blood flow increases. Future studies are needed to analyze flow organization in situations with increased cardiac flow, such as during exercise. Furthermore, disturbed vortex ring formation might influence shear stress which serves as an epigenetic factor in cardiac remodeling [13]. Therefore, future long-term studies have to reveal if abnormal vortex formation affects energy loss or cardiac pumping efficiency, and/or may serve an early predictor for poor cardiac outcome [30].

Study Limitations

Absence or presence of a vortex ring was scored visually, however a previous study [9] showed that vortex detection can be done with low inter- and intra-observer variation. In the current study, the absence of vortex formation was further confirmed by the significant high VFT which is in line with previous work. 4DFlow MRI has the disadvantage of a relatively long scan duration (8-10 minutes), and is associated with relatively high costs compared with echocardiography.

Vortex core analysis was limited to the E-peak and A-peak, subsequently no data was available on the timing, forming and disappearance of the vortex cores. Parameters of diastolic and systolic function of patients were all close to normal reference values, which made correlation with clinical parameters difficult. LV inflow angle was measured on a 2D plane but was compared with a 3D-determined vortex orientation. If a vortex ring core was not elliptical, the circularity index was computed by approximating an ellipse around the deformed vortex shape. This approximation might not fully capture or characterize the deformed vortex ring shape.

CONCLUSION

Quantitative 3D vortex analysis of early- and late-filling vortex ring formation revealed a disturbed vortex ring formation in patients after correction of an AVSD. This disturbance is characterized by either absence of a formed vortex ring or alterations in the geometric properties and location

of the formed rings. These findings were associated with abnormal LV inflow and morphology of the LAVV in the studied patients. Using 3D analysis, the current *in vivo* study quantitatively confirms the relation between LAVV abnormalities and altered vortex ring formation in the LV. Our findings highlight the close relationship among AVV abnormalities. In addition, they create awareness of the influence of AVV abnormalities and AVV surgery on LV vortex formation. The exact implications of abnormal vortex formation and possible increased energy loss and cardiac remodeling, owing to aberrant vortex formation, needs further investigation.

3.5

REFERENCES

1. Penkoske PA, Neches WH, Anderson RH, et al. Further observations on the morphology of atrioventricular septal defects. J Thorac Cardiovasc Surg. 1985;90:611-22.

2. Takahashi K, Mackie AS, Thompson R, et al. Quantitative real-time three-dimensional echocardiography provides new insight into the mechanisms of mitral valve regurgitation post-repair of atrioventricular septal defect. J Am Soc Echocardiogr. 2012;25:1231-44.

3. Draulans-Noe HA, Wenink AC, Quaegebeur J. Single papillary muscle ("parachute valve") and double-orifice left ventricle in atrioventricular septal defect convergence of chordal attachment: surgical anatomy and results of surgery. Pediatr Cardiol. 1990;11:29-35.

4. Ando M, Takahashi Y. Variations of atrioventricular septal defects predisposing to regurgitation and stenosis. Ann Thorac Surg. 2010;90:614-21.

5. Calkoen EE, Roest AA, Kroft LJ, et al. Characterization and improved quantification of left ventricular inflow using streamline visualization with 4DFlow MRI in healthy controls and patients after atrioventricular septal defect correction. J Magn Reson Imaging. 2015;41:1512-20.

6. Ginde S, Lam J, Hill GD, et al. Long-term outcomes after surgical repair of complete atrioventricular septal defect. J Thorac Cardiovasc Surg. 2015;150:369-74.

7. St Louis JD, Jodhka U, Jacobs JP, et al. Contemporary outcomes of complete atrioventricular septal defect repair: analysis of the Society of Thoracic Surgeons Congenital Heart Surgery Database. J Thorac Cardiovasc Surg. 2014;148:2526-31.

8. Drenthen W, Pieper PG, van der Tuuk K, et al. Cardiac complications relating to pregnancy and recurrence of disease in the offspring of women with atrioventricular septal defects. Eur Heart J. 2005;26:2581-7.

9. Elbaz MS, Calkoen EE, Westenberg JJ, et al. Vortex flow during early and late left ventricular filling in normal subjects:quantitative characterization using retrospectively-gated 4D flow cardiovascular magnetic resonance and three-dimensional vortex core analysis. J Cardiovasc Magn Reson. 2014;16:78.

10. Hong GR, Pedrizzetti G, Tonti G, et al. Characterization and quantification of vortex flow in the human left ventricle by contrast echocardiography using vector particle image velocimetry. JACC Cardiovasc Imaging. 2008;1:705-17.

11. Martinez-Legazpi P, Bermejo J, Benito Y, et al. Contribution of the diastolic vortex ring to left ventricular filling. J Am Coll Cardiol. 2014;64:1711-21.

12. Bellhouse BJ. Fluid mechanics of a model mitral valve and left ventricle. Cardiovasc Res. 1972;6:199-210.

13. Pasipoularides A. Diastolic filling vortex forces and cardiac adaptations: probing the epigenetic nexus. Hellenic J Cardiol. 2012;53:458-69.

14. Hu Y, Shi L, Parameswaran S, Smirnov S, He Z. Left ventricular vortex under mitral valve edge-to-edge repair. Cardiovasc Eng Technol. 2010;1: 235-43.

15. Pedrizzetti G, Domenichini F, Tonti G. On the left ventricular vortex reversal after mitral valve replacement. Ann Biomed Eng. 2010;38:769-73.

16. Kheradvar A, Falahatpisheh A. The effects of dynamic saddle annulus and leaflet length on transmitral flow pattern and leaflet stress of a bileaflet bioprosthetic mitral valve. J Heart Valve Dis. 2012;21:225-33.

17. Faludi R, Szulik M, D'hooge J, et al. Left ventricular flow patterns in healthy subjects and patients with prosthetic mitral valves: an in vivo study using echocardiographic particle image velocimetry. J Thorac Cardiovasc Surg. 2010;139:1501-10.

18. Hoohenkerk GJ, Bruggemans EF, Rijlaarsdam M, et al. More than 30 years' experience with surgical correction of atrioventricular septal defects. Ann Thorac Surg. 2010;90:1554-61.

19. Calkoen EE, Westenberg JJ, Kroft LJ, et al. Characterization and quantification of dynamic eccentric regurgitation of the left atrioventricular valve after atrioventricular septal defect correction with 4D Flow cardiovascular magnetic resonance and retrospective valve tracking. J Cardiovasc Magn Reson. 2015;17:18.

20. Jeong J, Hussain F. On the identification of a vortex. J Fluid Mech. 1995;285: 69-94.

21. Westenberg JJ, Roes SD, Ajmone MN, et al. Mitral valve and tricuspid valve blood flow: accurate quantification with 3D velocity-encoded MR imaging with retrospective valve tracking. Radiology. 2008;249:792-800.

22. Gharib M, Rambod E, Kheradvar A, et al. Optimal vortex formation as an index of cardiac health. Proc Natl Acad Sci U S A. 2006;103:6305-8.

23. Kheradvar A, Assadi R, Falahatpisheh A, et al. Assessment of transmitral vortex formation in patients with diastolic dysfunction. J Am Soc Echocardiogr. 2012;25:220-7.

24. Du D, Jiang S,Wang Z, Hu Y, et al. Effects of suture position on left ventricular fluid mechanics under mitral valve edge-to-edge repair. Biomed Mater Eng. 2014;24:155-61.

25. Toger J, Kanski M, Carlsson M, et al. Vortex ring formation in the left ventricle of the heart: analysis by 4D flow MRI and Lagrangian coherent structures. Ann Biomed Eng. 2012;40: 2652-62.

26. Dabiri JO, Gharib M. The role of optimal vortex formation in biological fluid transport. Proc Biol Sci. 2005;272:1557-60.

27. Kheradvar A, Pedrizzetti G. Vortex formation in the heart. Vortex formation in the cardiovascular system. London: Springer; 2012. 70-2.

28. Paelinck BP, de Roos A, Bax JJ, et al. Feasibility of tissue magnetic resonance imaging: a pilot study in comparison with tissue Doppler imaging and invasive measurement. J Am Coll Cardiol. 2005;45:1109-16.

29. Kilner PJ, Yang GZ, Wilkes AJ, et al. Asymmetric redirection of flow through the heart. Nature. 2000;404: 759-61.

30. Sengupta PP, Narula J, Chandrashekhar Y. The dynamic vortex of a beating heart: wring out the old and ring in the new! J Am Coll Cardiol. 2014;64: 1722-4.

31. Machler H, Reiter G, Perthel M, et al. Influence of a tilting prosthetic mitral valve orientation on the left ventricular flow—an experimental in vivo magnetic resonance imaging study. Eur J Cardiothorac Surg. 2007;32:102-7.

32. Bermejo J, Benito Y, Alhama M, et al. Intraventricular vortex properties in nonischemic dilated cardiomyopathy. Am J Physiol Heart Circ Physiol. 2014;306:H718-29.

33. Jiamsripong P, Calleja AM, Alharthi MS, et al. Impact of acute moderate elevation in left ventricular afterload on diastolic transmitral flow efficiency: analysis by vortex formation time. J Am Soc Echocardiogr. 2009;22:427-31.

34. Pedrizzetti G, La CG, Alfieri O, Tonti G. The vortex—an early predictor of cardiovascular outcome? Nat Rev Cardiol. 2014;11:545-53.

35. Overman DM, Dummer KB, Moga FX, et al. Unbalanced atrioventricular septal defect: defining the limits of biventricular repair. Semin Thorac Cardiovasc Surg Pediatr Card Surg Annu. 2013;16:32-6.

3.5

Chapter 3.6

Characterization and quantification of dynamic eccentric regurgitation of the left atrioventricular valve after atrioventricular septal defect correction with 4DFlow cardiovascular magnetic resonance and retrospective valve tracking

Emmeline E. Calkoen, Jos J.M. Westenberg, Lucia J.M. Kroft, Nico A. Blom, Mark G. Hazekamp, Marry E. Rijlaarsdam, Monique R.M. Jongbloed, Albert de Roos and Arno A.W. Roest.

ABSTRACT

Background

To characterize and directly quantify regurgitant jets of left atrioventricular valve (LAVV) in patients with corrected atrioventricular septal defect (AVSD) by four-dimensional (4D)Flow Cardiovascular Magnetic Resonance (CMR), streamline visualization and retrospective valve tracking.

Methods

Medical ethical committee approval and informed consent from all patients or their parents were obtained. In 32 corrected AVSD patients (age 26±12 years), echocardiography and whole-heart 4DFlow MRI were performed. Using streamline visualization on 2- and 4-chamber views, the angle between regurgitation and annulus was followed throughout systole. On through-plane velocity-encoded images reformatted perpendicular to the regurgitation jet the cross-sectional jet circularity index was assessed and regurgitant volume and fraction were calculated. Correlation and agreement between different techniques was performed with Pearson's r and Spearman's rho correlation and Bland-Altman analysis.

Results

In 8 patients, multiple regurgitant jets over the LAVV were identified. Median variation in regurgitant jet angle within patients was 36°(IQR 18–64°) on the 2-chamber and 30°(IQR 20–40°) on the 4-chamber. Regurgitant jets had a circularity index of 0.61±0.16. Quantification of the regurgitation volume was feasible with 4DFlow CMR with excellent correlation between LAVV effective forward flow and aortic flow (r=0.97, p<0.001) for internal validation and moderate correlation with planimetry derived regurgitant volume (r=0.65, p<0.001) and echocardiographic grading (rho=0.51, p=0.003).

Conclusion

4DFlow CMR with streamline visualization revealed multiple, dynamic and eccentric regurgitant jets with non-circular cross-sectional shape in patients after AVSD correction. 4DFlow with retrospective valve tracking allows direct and accurate quantification of the regurgitation of these complex jets.

BACKGROUND

After correction of an atrioventricular septal defect (AVSD), regurgitation of the left atrioventricular valve (LAVV, i.e. the left part of the common atrioventricular valve after correction, connecting the left atrium with left ventricle) is common. Up to 11% of the patients with corrected AVSD require surgery of the LAVV during follow-up [1], and according to the grown-up congenital heart disease (GUCH) guidelines of the European Society Cardiology (ESC) surgical correction of LAVV regurgitation should be considered in asymptomatic patients with moderate to severe LAVV [2]. Therefore, reliable quantification of LAVV regurgitation is important for clinical decision-making.

Echocardiography is most commonly used to evaluate mitral valve or LAVV regurgitation, but echocardiographic quantification of the regurgitation is based on several assumption, such as a cross-sectional circular shape of the jet and a static occurrence and position of the jet throughout systole. In adult patients with mitral regurgitation of diverse origin, poor inter-observer agreement has been described for echocardiographic grading of mitral valve regurgitation using proximal isovelocity surface area (PISA) and vena contracta methods in cases of eccentric regurgitant jets, with non-circular cross-sectional shape or for non-pansystolic regurgitation [3, 4]. Also in patients with corrected AVSD, quantification of LAVV regurgitation with echocardiography has shown poor inter-observer agreement, possibly caused by the eccentric and multiple, non-circular characteristics of the jets [5]. Consequently, in patients after AVSD correction or patients with complex mitral valve regurgitation, no accurate reference method is available to assess LAVV/mitral valve regurgitant volume and fraction; for such cases, a combination of approaches is suggested [6, 7].

Four-dimensional (4D) Flow Cardiovascular Magnetic Resonance (CMR) allows visualization and reliable, validated and direct quantification of mitral valve flow using retrospective valve tracking perpendicular to inflow and regurgitant jet with the opportunity to perform internal validation [8, 9]. However, this approach has not been applied in patients after AVSD correction.

We hypothesize that the dynamics and shape of the regurgitant jets after AVSD correction are not in accordance with the assumptions on which the currently available direct quantification techniques are based. Furthermore, we hypothesize that 4DFlow CMR with retrospective valve tracking allows direct and accurate quantification of LAVV regurgitation by tracing the regurgitant jet(s) throughout systole with good internal validation of LAVV flow with aortic flow. Therefore, the purpose of the current study was to characterize and directly quantify regurgitant jets of the LAVV in patients with corrected AVSD by 4DFlow CMR, streamline visualization and retrospective valve tracking.

3.6

METHODS

Study population

The study protocol was approved by the medical ethical committee of the Leiden University Medical Center and informed consent was obtained from participants or their parents. Inclusion criteria were a history of AVSD correction and compatibility for MRI (age above 8 years, no-pacemaker dependency, non-Down syndrome). Thirty-four patients were prospectively enrolled between October 2012 and October 2013 from an available surgical database [1]. Twenty-five out of the thirty-four cases have been previously reported [10]. This prior article focussed on the optimal CMR quantification of diastolic left ventricular inflow, whereas in the current manuscript we report on regurgitation during systole. Two cases were excluded because of a history of LAVV replacement. To assess grading of LAVV regurgitation, patients underwent echocardiography and 4DFlow CMR. Transthoracic echocardiography images were acquired using a commercially available system equipped with a 3.5MHz transducer (Vivid 9, GE-Vingmed Ultrasound, Horton, Norway). A senior paediatric cardiologist (MR) with over 25 years of experience in echocardiography of congenital heart defects, visually classified/graded the regurgitation as none/trace, mild, moderate or severe, blinded for the 4DFlow results [5].

### Magnetic Resonance Imaging

A 3T CMR system (Ingenia, Philips Medical Systems, the Netherlands) with maximal amplitude of 45mT/m for each axis and a slew rate of 200T/m/sec, with a combination of FlexCoverage Posterior coil in the table top with a dStream Torso coil, providing up to 32 coil elements for signal reception was used. Whole-heart 4DFlow was performed with velocity-encoding of 150cm/s in all three directions, spatial resolution $2.3\times2.3\times3.0mm^3$, flip angle 10°, echo time (TE) 3.2ms, repetition time (TR) 7.7ms, true temporal resolution 31ms, SENSE factor 2 in anterior-posterior direction and Echo Planar Imaging with a factor 5. No segmented k-space acquisition was used. Mean acquisition time of the 4DFlow scan was 8 minutes (range 5-11 minutes). Commercially-available concomitant gradient correction and local phase correction filter were applied, from the software available on MRI system (Ingenia 3T MRI with Software Stream 4.1.3.0). Just prior to the 4DFlow acquisition, in the majority (26 out of 32) of patients Gadolinium contrast agent (0.015mmol/kilogram body weight, Dotarem®, Guerbet, Aulnay-sous-Bois, France) was administrated, for other clinical evaluations. Furthermore prior to contrast administration, cine 2D left 2-chamber, 4-chamber, coronal and sagittal aorta views and a cine muli-2D short-axis stack of slices were acquired, using steady-state free-precession sequences with TE/TR 1.5/3.0, 350mm field-of-view, 45° flip angle, acquisition resolution $1.0\times1.0\times8.0mm^3$. Retrospective gating was used with 30 phases reconstructed to represent one cardiac cycle. Free breathing was allowed without using motion suppression, three signal averages were taken to suppress effects of breathing motion.

**Magnetic Resonance Image analysis**

Image analysis was performed by one observer (EC) with two years of experience in CMR and verified by two observers (JW and LK) with over 15 years of experience in CMR. Image analysis was done using in-house developed Mass software (Leiden). Left ventricular end-diastolic volume (LVEDV) and end-systolic volume (LVESV) were calculated by planimetry: the endocardial border was manually traced at end-diastole and end-systole in short-axis slices, the enclosed areas were calculated, multiplied by slice thickness and summed over all slices. Ejection fraction (EF) was calculated as EF = (LVEDV-LVESV)/LVEDV. The maximum left atrial volume (LAV) was calculated according to the biplane area-length from the 2- and 4-chamber view using the formula (8/3π × Area(4-chamber) × Area(2-chamber))/(shortest atrial length). Atrial and ventricular volume were indexed for body surface area (BSA) according to Du Bois formula [11]. To assess the dynamics of the LAVV regurgitant jet, jet direction was visualized using streamlines [12], in two orthogonal stacks of parallel cine multiplanar reformatting planes (MPRs) in 2- and 4-chamber orientation, constructed from the magnitude gradient-echo images. At each phase during systole, the MPR with the largest regurgitant jet projection was used to measure the angle between the jet and the valve annulus (Figure 1). Prior to velocity mapping, the source velocity images were checked for aliasing artefacts. In case aliasing occurred in the region of interest, phase unwrapping was performed in the source images. Retrospective valve tracking was performed to assess trans-LAVV and aortic flow volumes as described previously [9]. In the presence of LAVV regurgitation, the reformatting plane was positioned perpendicular to the regurgitant jet, 1–2cm proximal to the valve throughout systole, to avoid sampling in an area with phase dispersion due to turbulent flow at the orifice of the regurgitation (Figure 2) [13]. In case of multiple regurgitant jets with different directions, a separate reformatting planes was constructed for each jet. The total regurgitant volume was determined by summing the regurgitant volume of each of the jets. To assess the shape of the regurgitant jet, the circularity index of the jet at the phase of maximum regurgitant flow was calculated as the shortest diameter/longest cross-sectional diameter (Figure 2). To determine diastolic inflow volume during diastole, the MPR plane was positioned perpendicular to the inflow direction (Figure 2) and tracking the valve. Transvalvular flow velocity was calculated by subtraction of myocardial velocity in through-plane direction from the mean velocity measured over the inflow area [14]. Transvalvular flow volume was subsequently calculated by integrating the transvalvular velocity over the inflow area (i.e., the flow rate) and then integrating over the cardiac cycle (Figure 2E). In case of aliasing, phase unwrapping of the original data set was performed in the source data using in-house developed software. The phase unwrapping algorithm uses the linear relation between image grey value and the velocity scale between -Venc and +Venc to recalculate velocity values exceeding this scale in wrapped areas [15]. Regurgitant fraction was calculated as the ratio between regurgitant volume and total flow volume over LAVV×100%. For internal validation, the effective forward flow over the LAVV was compared with the aortic flow volume. Aortic flow volume was assessed from a similar retrospective valve tracking procedure at the

3.6

aortic valve, obtained from the same 4DFlow acquisition. For comparison of 4DFlow derived regurgitation volume with a conventional CMR quantification technique, regurgitation volume was also quantified as the difference between planimetry-derived stroke volume (LVEDV-LVESV), based on short-axis images minus aortic flow, derived from the 4DFlow acquisition.

Figure 1. Multiple dynamic eccentric regurgitant jets.
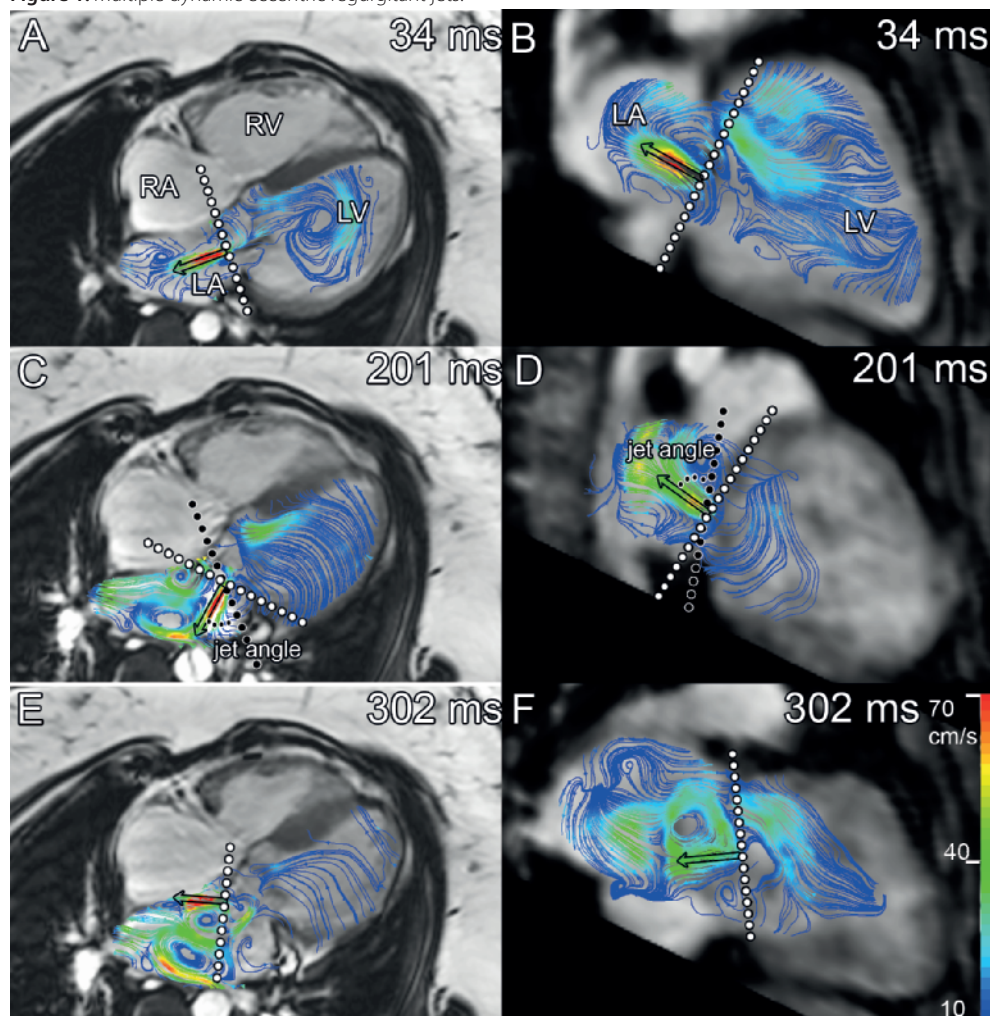
In one subjects in 4-chamber (A, C, E) and 2-chamber (B, D, F) view during early- (34 ms) (A,B), mid- (201 ms) (C,D) and late (302 ms) (E,F) systole (total RR 984ms). The jet starts nearly perpendicular to the annulus (A, B), but changes to a more lateral (C) and anterior direction (D). A second jet was observed in late systole (E). Black dots show the annulus plane and the white dots the plane perpendicular to the jet. In plane C and D, the angle measurements are illustrated between annulus and regurgitant jet.

Figure 2. Example of flow quantification.
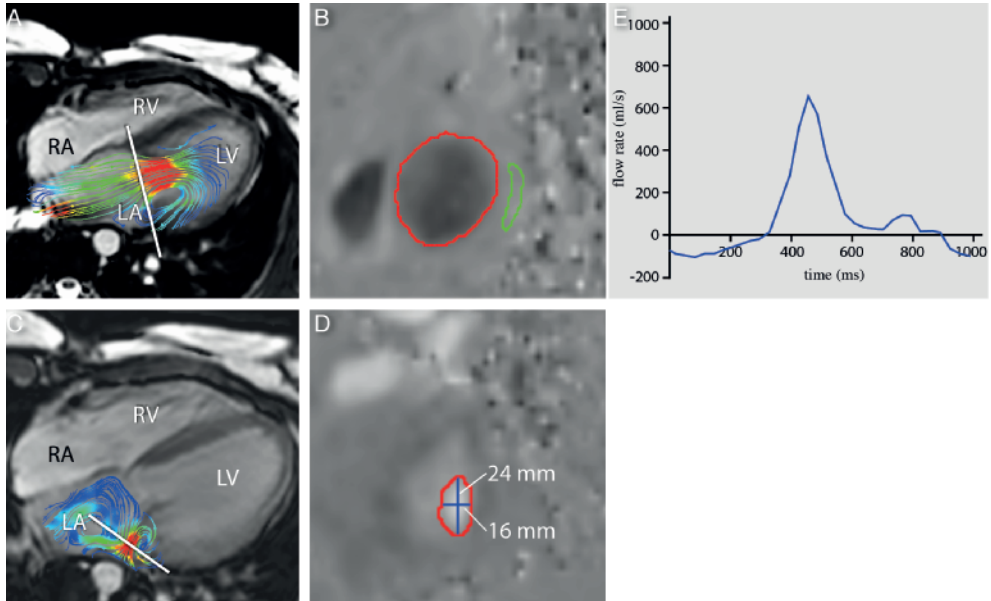
With retrospective valve tracking in a patient with the reformatting plane (white line) adjusted to the inflow during diastole (A) and perpendicular to the regurgitant jet during systole (C) with through-plane velocity of inflow (B red contour indicates LAVV flow, green contour traces a region within the free wall of the left ventricle for background correction) and the non-circular regurgitant jet (CI = 0.67) (D). In E the flow curve.

Statistical Analysis

Variables were tested for normal distribution using the Shapiro-Wilk test. Continuous variables are expressed as mean ± standard deviation (SD) and as median with inter-quartile range (IQR) where appropriate. Linear regression analysis and Bland-Altman analysis [16] were performed to assess agreement between LAVV effective forward flow and aortic flow. Correlation between left atrial and ventricular volume with regurgitation volume was assessed with linear regression analysis (Pearson's r). Spearman's regression analysis (rho) were used to assess correlation between regurgitant flow volume measured on 4DFlow CMR and visual grading of regurgitation. Data analysis was performed using SPSS Statistics (version 20.0 IBM SPSS, Chicago, Illinois).

RESULTS

Patient characteristics are presented in Table 1. Twenty-one (66%) patients underwent correction of a partial AVSD and 11 (34%) patients underwent correction of a complete AVSD at a median age of 52 (IQR 8–100) months. Patients were examined 20±9 years after correction. 4DFlow CMR data of all 32 patients were visually inspected to be of sufficient quality for image analysis and streamline visualization and trans-valvular flow quantification was possible. In one

Table 1. Patient characteristics. Data are presented as mean ± standard deviation or median with interquartile range where appropriate. *Indicates p<0.05. BSA = Body Surface Area, BMI = Body mass index, LVEDV = Left ventricular end diastolic volume, LAESV = Left atrial end systolic volume, EF = Ejection Fraction, LV = Left ventricle, NYHA class = New York Heart Association classification, AVSD = Atrioventricular septal defect.

	Patients
N	32
Male (N, %)	9 (28%)
Age (years)	26±12
BSA (m^2)	1.7±0.3
BMI	23 (IQR 19–29)
LVEDV / BSA (ml/m^2)	91±15
LAESV / BSA (ml/m^2)	45±11
EF LV (%)	55±5
NYHA class	30 (94%) class I, 2 (6%) class II
Type AVSD	21 (66%) partial, 11 (34%) complete
Age surgery (months)	52 (IQR 8–100)
Time after surgery (years)	20±9

patient aliasing occurred in the regurgitation jet and phase unwrapping was performed. Of 32 included patients, 2 patients underwent re-operation of the LAVV due to regurgitation. Mean left ventricular EF was 55±5% and 30 (94%) patients were categorized NYHA class I and two (6%) patients NYHA class II. Using echocardiography, LAVV regurgitation was classified based on visual grading as none to trace in 3 patients, mild in 15 patients and moderate in 14 patients.

Dynamics of LAVV regurgitation

In 26 patients, the LAVV regurgitant jet(s) were visualized with streamlines. The six patients (including the 3 patients with none to trace LAVV regurgitation) in whom the LAVV regurgitant could not be visualized with streamlines were quantified with a low regurgitation volume (1–4ml). In 8 (31%) patients, multiple LAVV regurgitant jets were observed (Figure 1). All regurgitant jets were dynamic with changes in the jet angle during systole. Minimal and maximal angle of the jet showed large variation between patients (Table 2 and Figure 3), with a lateral orientation of the jet on the 4-chamber view and various orientation on the 2-chamber view. The median difference between minimal and maximal LAVV regurgitant jet angle within patients was 36° (IQR 18–64°) on the 2-chamber and 30° (IQR 20–40°) on the 4-chamber. Cross-sectional jets areas were non-circular (Figure 2D), as evidenced by a circularity index of 0.61±0.16. No differences in jet dynamics were observed between the patients with partial AVSD and complete AVSD.

Quantification of LAVV regurgitation

Using 4DFlow CMR with retrospective plane tracking and streamline visualization, mean LAVV regurgitant volume was 11±6 ml and mean regurgitant fraction was 14±8%. Excellent correla-

Figure 3. Schematic representation of the regurgitant jet angle in 2- and 4-chamber view.
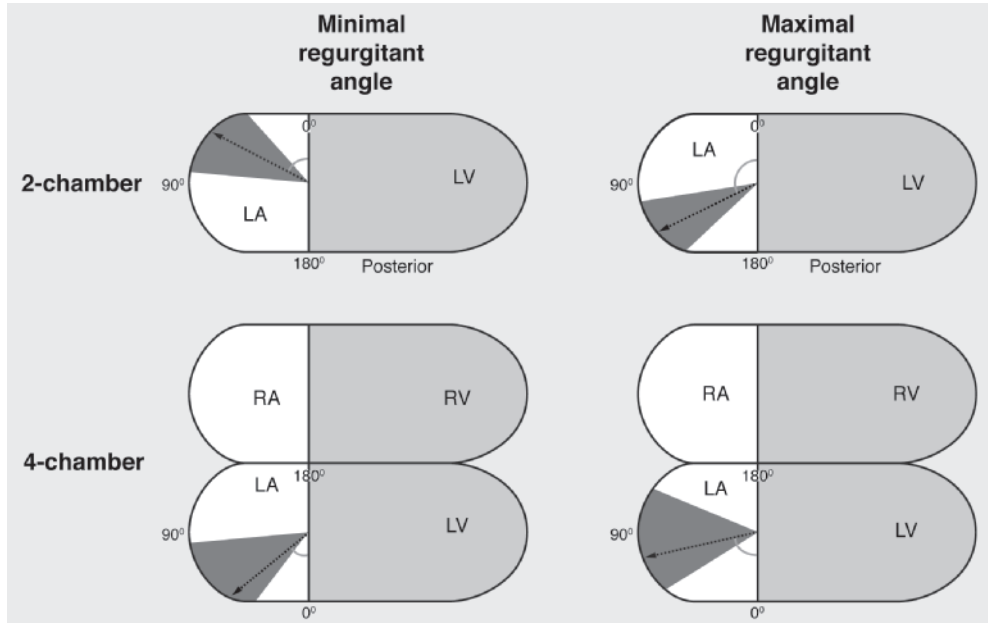

The median (black arrow) and interquartile range (dark grey) of the minimal and maximal regurgitant angles are presented. LA= left atrium, LV=left ventricle, RA=right atrium, RV=right ventricle.

tion (Pearson's r=0.97, p<0.001) and agreement (mean difference 0.3±4.0 ml, p=0.69, 95%-limit of agreement -8.0;8.6ml) was observed between aortic flow and LAVV effective forward flow (Figure 4). Correlation of the regurgitation volume derived from direct 4DFlow CMR with the combined method of planimetry - aortic flow method was Pearson's r=0.65 (p<0.001) (Figure 5). Correlation between planimetry (stroke volume) and aortic flow plus regurgitation fraction was Pearson's r=0.90. Regurgitant flow volume correlated with LAV relative to BSA (Pearson's r=0.53, p=0.002) and LVEDV relative to BSA (Pearson's r=0.44, p=0.016) in 30 patients with a corrected AVSD who did not underwent re-operation. Correlation between visual grading and 4DFlow CMR assessment of 4DFlow regurgitation volume was rho=0.51 (p=0.003) and of regurgitation fraction rho=0.63 (p <0.001) (Figure 6A,B).

3.6

Table 2. Regurgitant jet angle (degrees) on 2- and 4-chamber view. Data are presented as median with interquartile range

	Minimal angle	Maximal angle	Angle difference
4-chamber view	50° (IQR 37-85°)	77° (IQR 58-112°)	30° (IQR 20-40°)
2-chamber view	63° (IQR 42-90°)	116° (IQR 81-133°)	36° (IQR 18-64°)

Figure 4. Correlation and agreement between aortic flow and net LAVV flow.
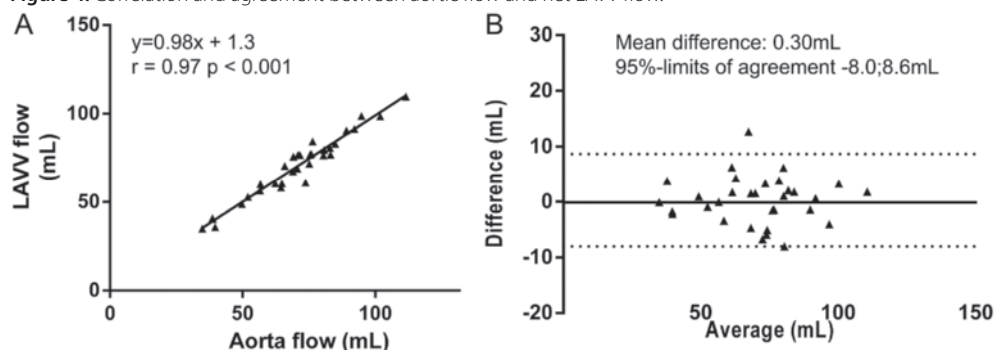
Correlation (A) and agreement (B).

Figure 5. Correlation and agreement between regurgitant volume based on planimetry minus aortic flow and regurgitant volume based on direct quantification from 4DFlow data.
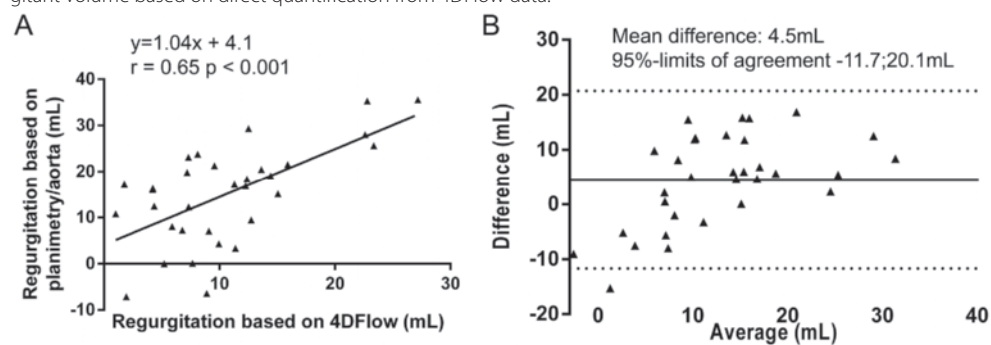
Correlation (A) and agreement (B).

Figure 6. Correlation between regurgitation classification based on visual echocardiography and CMR quantification.
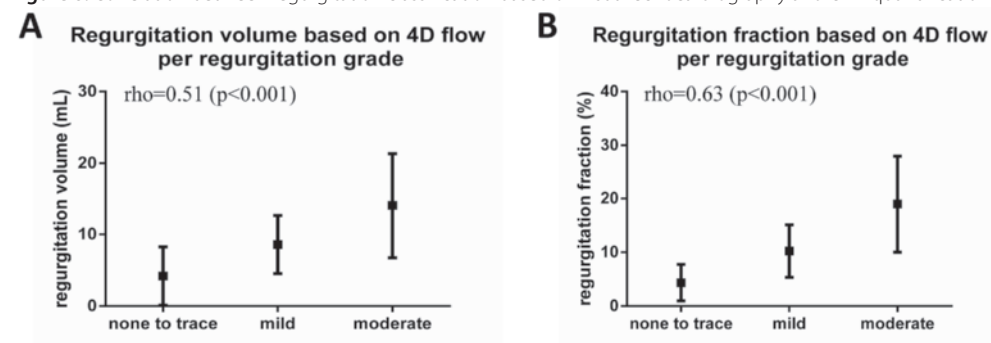
Mean and standard deviation of the quantitative measurements per visually scored regurgitation grade are given: A: regurgitation volume based on 4DFlow CMR and B: regurgitation fraction based on 4D flow CMR.

DISCUSSION

The key findings of current study were as follows: First, in patients with corrected AVSD, LAVV regurgitant jets are dynamic, eccentric and have a non-circular cross-sectional shape. Second, it is feasible to directly quantify LAVV regurgitation using 4DFlow CMR and retrospective valve tracking with excellent internal validation with aortic flow and this approach showed moderate correlation with the planimetry-based CMR approach.

In patients after AVSD correction, recurrent regurgitation of the LAVV is common and associated with leaflet prolapse, rest cleft, large annular area and a different position of the papillary muscle [1, 17]. Reoperation incidence due to LAVV regurgitation is as high as 11%. The ESC GUCH guidelines recommend surgical correction in case of moderate or severe LAVV regurgitation in symptomatic as well as in asymptomatic patients with signs of LV volume overload. Recommendations are however largely based on level C evidence (consensus of opinion of the experts and/or small studies, retrospective studies, registries). Clear indications for and timing of intervention remain debatable in this patient group, in part based on difficulties in the reliable assessment of the amount of LAVV regurgitation [18].

Little is known about the natural history or predictive value of chronic LAVV regurgitation in patients with corrected AVSD. Adult patients with asymptomatic chronic organic mitral valve regurgitation show a high likelihood to develop cardiac symptoms and high incidence of mortality [19, 20, 21, 22]. Chronic mitral valve regurgitation can remain asymptomatic for years, due to the increase in left atrial and ventricular volume [23], which was also found in our study. Due to this compensatory mechanism ejection fraction can remain normal despite myocardial dysfunction [24]. However, left atrial enlargement is a predictor of mortality and atrial fibrillation in patients with chronic mitral valve regurgitation due to flail leaflets or mitral valve prolapse and should be considered in clinical decision making for mitral valve correction [25, 26, 27]. Prolonged volume overload eventually results in cardiac hypertrophy and contractile dysfunction, with impaired output, increased end systolic volume and pulmonary congestion. Because of the poor prognosis of organic mitral valve regurgitation even in asymptomatic patients, early correction of organic mitral valve regurgitation should be considered according to adult guidelines [23].

Currently data on long-term outcome of patients with LAVV regurgitation after AVSD correction is lacking. This is complicated by the lack of a gold standard to quantify LAVV regurgitation in these patients. Furthermore, not all suggested quantification techniques have been evaluated in children with LAVV regurgitation after AVSD correction and no established cut-off values are available for LAVV/mitral valve regurgitation severity in children [18]. The observed eccentric, dynamic, multiple, non-circular jets in the current study can explain the reported low inter-observer agreement found in previous studies evaluating LAVV regurgitation after AVSD repair [5], because quantitative echocardiography techniques are based on several assumptions. Eccentric regurgitant jets, in contrast to central jets, are in close contact with the mitral leaflet

3.6

behind the regurgitant orifice and impinged to the medial or lateral wall of the left atrium [28]. The adherence and deviation of the jet to the valve leaflets and atrial wall, the so-called Coandă effect, causes up to 40% smaller color Doppler jet areas and leads to underestimation of eccentric jets with visual grading [29]. Vena contracta measurements are based on the assumption that the jet has a circular cross-sectional shape and measurements from multiple jets cannot be added [4]. Furthermore, the PISA-method is based on the assumption of hemispheric symmetry of the velocity distribution [4]. Due to these drawbacks, no gold standard is available to quantify the regurgitation of these complex jets with echocardiography and grading of regurgitation remains relatively subjective.

CMR offers non-invasive evaluation of atrial and ventricular dimensions and function with excellent reproducibly [30] within one comprehensive examination without geometric assumptions. Indirect quantification of LAVV regurgitation by subtracting the LAVV forward flow from the aortic flow has been shown feasible in patients with corrected AVSD [31]. Another approach to quantify LAVV regurgitation is the combination of planimetry-derived stroke volume with assessment of aortic flow volume [32]. However, both are indirect assessments of the regurgitant volume, and are not suitable in case of multiple valve lesions, such as aortic valve insufficiency or intra-cardiac shunts, such as a ventricular septal defect. Moreover, planimetry relies on accurate contour definitions, with concomitant intra- and interobserver variability, and separate acquisitions are needed with possible differences in heart rate, possibly explaining the moderate correlation and variation between 4DFlow and the combination of planimetry- and aortic flow. 4DFlow CMR can be used to directly quantify flow over the atrioventricular valves using retrospective valve tracking. This technique has been validated both in vitro and in vivo and proved to be accurate and reproducible [9]. 4DFlow CMR is independent of hemodynamic or geometric assumptions and it has the opportunity to retrospectively position the measurement plane according to flow direction during all phases of the cardiac cycle, and to use separate measurement planes for each jet in case of multiple jets, which is not possible with echocardiography. Furthermore, using 4DFlow CMR the measurement area perpendicular to the regurgitant jet can be adjusted in case of a non-circular cross-section regurgitant jet area, which is not possible using echocardiography. Furthermore, 4DFlow CMR has the advantage of internal validation of flow volume consistency as was shown to be excellent in our study as well as in a recent study in patients with a congenital heart disease [33]. Internal validation with aortic flow was excellent in the current study, including patients with complex jets. However, no gold standard is available that could be used to validate the 4DFlow CMR and therefore, in vivo validation is difficult. Nevertheless, this is the first approach that allows direct quantification of the regurgitant volume without the use of assumptions in this patient group, including children, with challenging LAVV regurgitation jets. The prognostic value of 4DFlow CMR regurgitation quantification has not been studied. Future, long-term follow-up studies are required to investigate cut-off values of quantification of regurgitation with 4DFlow CMR, which might differ from available echocardiography values and how these need to be used in patient management.

In this study, we have to acknowledge some limitations. Although 4DFlow CMR data was acquired, jet angles were measured in 2D planes based on streamline projections. Streamlines represent velocity direction at each location at one instant in time only. By measuring jet angles at different phases of systole, however, we provide useful information on jet direction at specific time points. Analysis of 4DFlow CMR, with manual positioning of the measurement plane, is time-consuming and might be affected by observer variation. However, compared with conventional 2D one-directional velocity-encoded CMR, additional analysis time consists only of time required for the valve tracking, which amounts to approximately 1–2 minutes per valve. Future technical advances may allow full automatic valve tracking and placement of the measurement plane perpendicular to the flow direction, which will reduce analysis time and also eliminate observer variation. Another limitation is that none of the studied patients were classified with severe regurgitation. Although we do not expect different results in these patients, future studies are needed to confirm regurgitant jet characteristics and the feasibility of quantification in patients with severe LAVV regurgitation after AVSD correction.

CONCLUSION

4DFlow CMR with streamline visualization revealed multiple, dynamic, non-circular, eccentric regurgitant jets of the LAVV in corrected AVSD patients and enables direct quantification of the regurgitation of these challenging jets**.** The observed complex jets explicate the limitations of qualitative and quantitative assessment of LAVV in these patients with echocardiography [5, 18]. Quantification of LAVV regurgitation with 4DFlow CMR with retrospective valve tracking showed good internal validation and has the potential to be used as an adjunct to echocardiography for more comprehensive evaluation of LAVV regurgitation. Future studies in patient groups with congenital and acquired heart disease are needed to investigate the potential use of 4DFlow in evaluation of mitral valve/LAVV regurgitation and its effect on cardiac function during follow-up.

3.6

REFERENCES

1. Hoohenkerk GJ, Bruggemans EF, Rijlaarsdam M, et al.: More than 30 years' experience with surgical correction of atrioventricular septal defects. Ann. Thorac.Surg. 2010;90:1554-1561.

2. Baumgartner H, Bonhoeffer P, De Groot NM, et al.: ESC Guidelines for the management of grown-up congenital heart disease. Eur.Heart J. 2010;31:2915-2957.

3. Biner S, Rafique A, Rafii F, et al.: Reproducibility of proximal isovelocity surface area, vena contracta, and regurgitant jet area for assessment of mitral regurgitation severity. JACC.Cardiovasc.Imaging 2010;3:235-243.

4. Lancellotti P, Moura L, Pierard LA, et al.: European Association of Echocardiography recommendations for the assessment of valvular regurgitation. Part 2: mitral and tricuspid regurgitation (native valve disease). Eur.J.Echocardiogr. 2010;11:307-332.

5. Prakash A, Lacro RV, Sleeper LA, et al.: Challenges in Echocardiographic Assessment of Mitral Regurgitation in Children After Repair of Atrioventricular Septal Defect. Pediatr.Cardiol. 2011;33:205-214.

6. Zoghbi WA, Chambers JB, Dumesnil JG, et al.: Recommendations for evaluation of prosthetic valves with echocardiography and doppler ultrasound. J.Am.Soc.Echocardiogr. 2009;22:975-1014.

7. Thavendiranathan P, Phelan D, Thomas JD, et al.: Quantitative assessment of mitral regurgitation: validation of new methods. J.Am.Coll.Cardiol. 2012;60:1470-1483.

8. Roes SD, Hammer S, van der Geest RJ, et al.: Flow assessment through four heart valves simultaneously using 3-dimensional 3-directional velocity-encoded magnetic resonance imaging with retrospective valve tracking in healthy volunteers and patients with valvular regurgitation. Invest Radiol. 2009;44:669-675.

9. Westenberg JJ, Roes SD, Ajmone MN, et al.: Mitral valve and tricuspid valve blood flow: accurate quantification with 3D velocity-encoded MR imaging with retrospective valve tracking. Radiology 2008;249:792-800.

10. Calkoen EE, Roest AA, Kroft LJ, et al.: Characterization and improved quantification of left ventricular inflow using streamline visualization with 4DFlow MRI in healthy controls and patients after atrioventricular septal defect correction. J.Magn Reson. Imaging 2015;41:1512-20.

11. Du Bois D, Du Bois EF: A formula to estimate the approximate surface area if height and weight be known. 1916. Nutrition 1989;5:303-311.

12. Napel S, Lee DH, Frayne R, et al. Visualizing three-dimensional flow with simulated streamlines and three-dimensional phase-contrast MR imaging. J.Magn Reson.Imaging 1992;2:143-153.

13. Wolf RL, Ehman RL, Riederer SJ, et al.: Analysis of systematic and random error in MR volumetric flow measurements. Magn Reson.Med. 1993;30:82-91.

14. Kayser HW, Soel BC, van der Wall EE, et al.: MR velocity mapping of tricuspid flow: correction for through-plane motion. J.Magn Reson.Imaging 1997;7:669-673.

15. Lotz J, Meier C, Leppert A, et al.: Cardiovascular flow measurement with phase-contrast MR imaging: basic facts and implementation. Radiographics 2002;22:651-671.

16. Bland JM, Altman DG: Statistical methods for assessing agreement between two methods of clinical measurement. Lancet 1986;1:307-310.

17. Takahashi K, Mackie AS, Thompson R, et al.: Quantitative Real-Time Three-Dimensional Echocardiography Provides New Insight into the Mechanisms of Mitral Valve Regurgitation Post-Repair of Atrioventricular Septal Defect. J.Am.Soc. Echocardiogr. 2012;25:1231-1244.

18. Li JS, Colan SD, Sleeper LA, et al.: Lessons learned from a pediatric clinical trial: the Pediatric Heart Network angiotensin-converting enzyme inhibition in mitral regurgitation study. Am.Heart J. 2011;161:233-240.

19. Ling LH, Enriquez-Sarano M, Seward JB, et al.: Clinical outcome of mitral regurgitation due to flail leaflet. N.Engl.J.Med. 1996;335:1417-1423.

20. Enriquez-Sarano M, Avierinos JF, Messika-Zeitoun D, et al.: Quantitative determinants of the

outcome of asymptomatic mitral regurgitation. N.Engl.J.Med. 2005;352:875-883.

21. Delahaye JP, Gare JP, Viguier E, et al.: Natural history of severe mitral regurgitation. Eur.Heart J. 1991;12 Suppl B:5-9.

22. Avierinos JF, Gersh BJ, Melton LJ, et al.: Natural history of asymptomatic mitral valve prolapse in the community. Circulation 2002;106:1355-1361.

23. Bonow RO, Carabello BA, Chatterjee K, et al.: 2008 focused update incorporated into the ACC/AHA 2006 guidelines for the management of patients with valvular heart disease: a report of the American College of Cardiology/American Heart Association Task Force on Practice Guidelines. J.Am.Coll.Cardiol. 2008;52:e1-142.

24. Carabello BA, Nolan SP, McGuire LB: Assessment of preoperative left ventricular function in patients with mitral regurgitation: value of the end-systolic wall stress-end-systolic volume ratio. Circulation 1981;64:1212-1217.

25. Rusinaru D, Tribouilloy C, Grigioni F, et al.: Left atrial size is a potent predictor of mortality in mitral regurgitation due to flail leaflets: results from a large international multicenter study. Circ.Cardiovasc. Imaging 2011;4:473-481.

26. Grigioni F, Avierinos JF, Ling LH, et al.: Atrial fibrillation complicating the course of degenerative mitral regurgitation: determinants and long-term outcome. J.Am.Coll.Cardiol. 2002;40:84-92.

27. Bonow RO: Left atrial function in mitral regurgitation: guilt by association. JACC.Cardiovasc.Imaging 2014;7:233-235.

28. Hall SA, Brickner ME, Willett DL, et al.: Assessment of mitral regurgitation severity by Doppler color flow mapping of the vena contracta. Circulation 1997;95:636-642.

29. Ginghina C: The Coanda effect in cardiology. J.Cardiovasc.Med. 2007;8:411-413.

30. Grothues F, Smith GC, Moon JC, et al.: Comparison of interstudy reproducibility of cardiovascular magnetic resonance with two-dimensional echocardiography in normal subjects and in patients with heart failure or left ventricular hypertrophy. Am.J.Cardiol. 2002;90:29-34.

31. Fujita N, Chazouilleres AF, Hartiala JJ, et al.: Quantification of mitral regurgitation by velocity-encoded cine nuclear magnetic resonance imaging. J.Am. Coll.Cardiol. 1994;23:951-958.

32. Kizilbash AM, Hundley WG, Willett DL, et al.: Comparison of quantitative Doppler with magnetic resonance imaging for assessment of the severity of mitral regurgitation. Am.J.Cardiol. 1998;81:792-795.

33. Hsiao A, Tariq U, Alley MT, et al.: Inlet and outlet valve flow and regurgitant volume may be directly and reliably quantified with accelerated, volumetric phase-contrast MRI. J.Magn Reson.Imaging 2015;41:376-85.

3.6

Chapter 3.7

Abnormal left atrial flow patterns in patients after atrioventricular septal defect correction and regurgitation: evaluation with 4DFlow MRI and particle tracing

Emmeline E. Calkoen, Mohammed S.M. Elbaz, Patrick J.H. de Koning, Monique R.M. Jongbloed, Lucia J.M. Kroft, Rob J. van der Geest, Nico A. Blom, Albert de Roos, Arno A.W. Roest and Jos J.M. Westenberg

ABSTRACT:

Background

During ventricular systole, a compact recirculating flow pattern forms in the left atrial (LA) blood flow. We aimed to evaluate LA recirculating flow structures in healthy volunteers and patients with corrected atrioventricular septum defect (AVSD) with both none to mild and moderate left atrioventricular valve (LAVV) regurgitation with the use of 4DFlow MRI.

Methods and Results

Data was obtained in eighteen controls (age 24±14 years) and eighteen corrected AVSD patients: nine (24±12 years) with none to mild regurgitation (<9%) and nine (21±13 years) with moderate regurgitation (>17%). In healthy controls, a single recirculating flow structure was visualized in the LA by streamlines (size 4.3±2.9mL) with a similar volume as the lambda2-extracted vortex core (3.9mL, IQR 3.0- 6.8 mL, p=0.27). In patients with regurgitation of the LAVV, two recirculating flow structures were observed in the LA, with opposing circulation direction. Recirculating blood flow contribution originated less frequently from the left pulmonary veins (LPVs) in patients with none to mild regurgitation (27±25%, p=0.023) and moderate regurgitation (6%, IQR 0-23%, p=0.002) compared with controls (49±21%).

Conclusion

Quantitative 3D analysis showed disturbed recirculating LA flow patterns in corrected AVSD patients with decreased contribution to the vortex cores from the LPVs. Furthermore, LAVV regurgitation caused multiple recirculating flow structures and disturbed flow from the LPVs.

INTRODUCTION

The left atrium (LA) has a reservoir function during ventricular systole when blood enters from the right pulmonary veins (RPVs) and left pulmonary veins (LPVs). During diastole, after opening of the left atrioventricular valve (LAVV), the LA serves as a conduit when blood flows from the RPVs and LPVs through the LA into the left ventricle. Efficient filling of the LA, contraction and draining into the ventricle contribute to adequate cardiac function [1].

Recirculating flow patterns and vortex formation are well described in the left ventricle and are known to contribute to efficient blood flow [2]. Recirculating flow in the LA has been described in healthy hearts during systole and mid-diastole based on streamline and pathline analysis from intra-cardiac blood flow velocity data. This phenomenon is suggested to play a role in preventing thrombus formation, preservation of LA flow momentum during ventricular systole and efficient diastolic left ventricular (LV) filling [1;3-5]. Previous studies suggest that the recirculating flow during ventricular systole mainly consist of blood originating from the LPVs. Blood flow from the RPVs was proposed to be directed along the inter-atrial septum towards the ventricle [1].

Regurgitation of the left atrioventricular valve (LAVV) has been a predictor for a poor clinical outcome even in asymptomatic patients [6]. An increase in turbulent kinetic energy in the LA has been described around LAVV regurgitation jets [7]. Patients after atrioventricular septal defect (AVSD) correction often present with LAVV regurgitation [8] and the re-operation rate is as high as 28% [9]. Moreover, the regurgitation direction in corrected AVSD patients is lateral towards the ostia of the LPVs, though the direction varies dynamically during systole [10]. We hypothesize that the dynamic and eccentric regurgitant jet in these patients disturbs formation of normal LA recirculating blood flow patterns.

Novel 4DFlow MRI techniques allow 3D quantification of intra-cardiac flow patterns and vortex analysis [11;12]. Therefore, the aim of this explorative study was to evaluate flow patterns in the LA in healthy subjects and patients after AVSD correction with the use of 4DFlow MRI-based visualization methods. In this study, normal flow behavior in the LA will be evaluated in healthy controls and in patients after correction of an AVSD correction. Furthermore, the effect of LAVV regurgitation on LA flow patterns will be studied by comparing left atrial flow patterns in patients with none-to-mild versus moderate LAVV regurgitation.

3.7

METHODS

Twenty healthy controls and twenty patients with a corrected AVSD were included. Patients were selected from a total group of 34 patients who underwent cardiac MRI. Selection was based on regurgitation grade: ten patients were selected with none to mild regurgitation (regurgitation fraction below 9%) and ten patients with moderate regurgitation (regurgitation fraction above

17%). Subjects with aliasing in LA velocity data were excluded. Informed consent was obtained from all patients and controls and/or their parents. Subjects and controls in the current study were also included in previous studies using 4DFlow MRI [10;12;13], but in none of these studies atrial flow patterns were evaluated.

Magnetic Resonance Imaging

All subjects underwent whole-heart 4DFlow MRI on a 3T system (Ingenia, Philips Medical Systems, The Netherlands) with maximal amplitude of 45mT/m for each axis and a slew rate of 200T/m/sec. A combination of FlexCoverage Posterior coil in the table top with a dStream Torso coil, providing up to 32 coil elements for signal reception was used, with the following acquisition settings: velocity-encoding of 150cm/s in all three directions, spatial resolution 2.3×2.3×3.0-4.2mm^3, flip angle 10°, echo time (TE) 3.2ms, repetition time (TR) 7.7ms, true temporal resolution (4×TR) 31ms, SENSE factor 2 in anterior-posterior direction and Echo Planar Imaging with a factor 5. Retrospective VCG-gating was used with 30 phases reconstructed to represent one average heart cycle and free breathing without motion compensation was allowed. Commercially-available concomitant gradient correction and local phase correction filter were applied from the software available on MRI system (Ingenia 3 T with Software Stream 4.1.3.0). Acquisition time of the 4DFlow scan with a heart beat 60-80bpm was typically 8-10 minutes. Cine 2D left 2-chamber and 4-chamber views were acquired to quantify maximal left atrial volume according to the biplane area-length method (8/3π × Area(4-chamber) × Area(2-chamber))/(shortest atrial length).

Streamline evaluation of compact recirculating flow

As regurgitation occurs during ventricular systole, flow patterns were evaluated during the reservoir function phases of the LA. Streamline display of the velocity field at any instant of time allows visualization of flow structures at a specific time point [14]. Streamline visualization using Mass software (LUMC, Leiden, The Netherlands) was used to assess and quantify compact recirculating flow structures in the LA. A stack of reformatted planes parallel to the 4-chamber view was analyzed with streamlines to visualize the flow pattern in the LA. The number of compact recirculating flow structures (i.e. where streamlines are circular and connected) was visually scored and the rotational direction with respect to the feet-head axis (clockwise or counter-clockwise) was determined (Figure 1A). A previous study showed that the vortex inside the atrium reached its largest volume just before the end of systole [1]. Therefore, the volume of the compact recirculating flow structure was measured two phases before end-systole. The compact recirculating flow structure was manually outlined in each axial slice and the areas were summed and multiplied by the slice thickness to compute the volume of the recirculating flow structure.
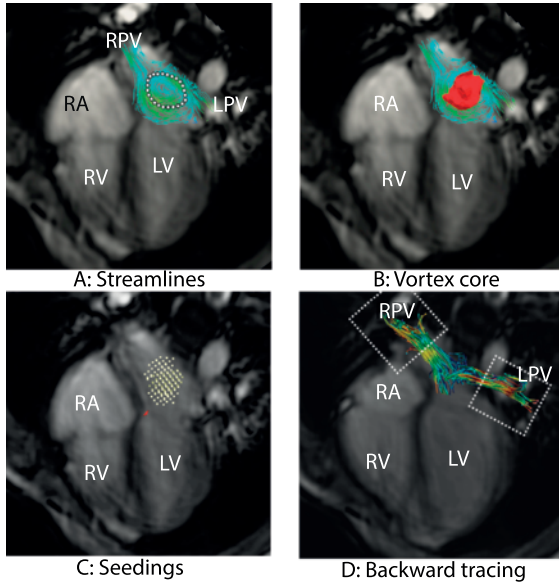
Figure 1. Explanation of used methodology.

Streamline visualization shows recirculating flow (dotted line in A) in clockwise direction with respect to the feet-head axis. The lambda2-method is used to extract the vortex core (red in B). Vortex cores are filled with seeds (dots in C). Backwards particle tracing allows the distinction between flow from the right pulmonary veins (RPV) and left pulmonary veins (LPV). RA = right atrium, RV = right atrium, LV = left ventricle.

Figure 2. Differences in left atrial flow between healthy control and patient.
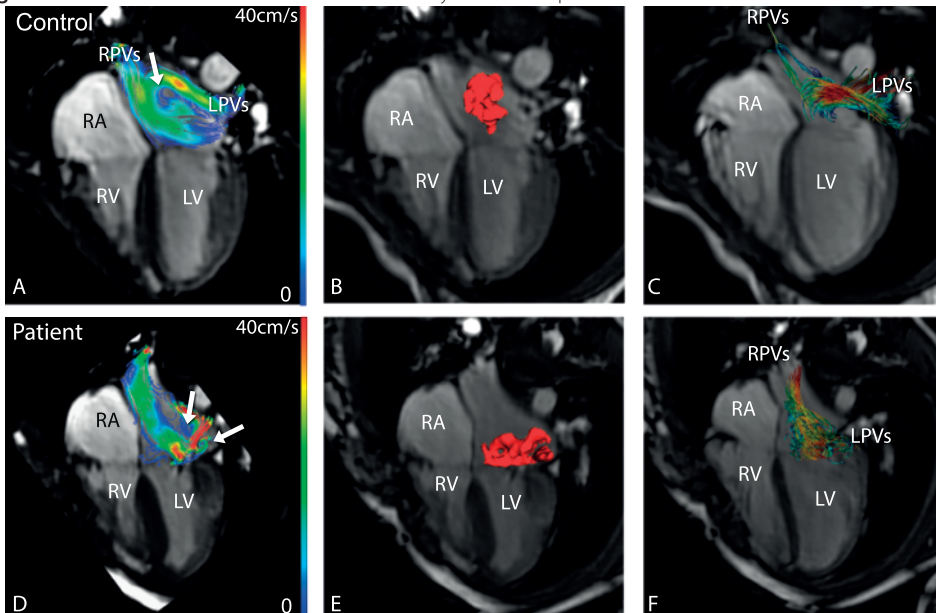
Healthy control (A-C) and a patient with 36% left atrioventricular valve regurgitation (D-F). Streamline visualization shows a single counter-clockwise (with respect to the feet-head axis) recirculating flow structure in the control (arrow in A) compared with multiple recirculating flow structures in the patient (arrows in D). The vortex core in the patient is less compact and nearer to the atrioventricular valve (E). Backward tracing in the healthy control shows predominant contribution of the left pulmonary veins (LPVs) to the vortex core, whereas in the patient only contribution from the right pulmonary veins (RPVs) is observed (F). RA = right atrium, RV = right atrium, LV = left ventricle.

3.7

Vortex detection in the left atrium and particle tracing

Three-dimensional (3D) vortex cores can be identified using the gradient properties of the 4DFlow MRI data [12]. Vortex core detection was used to provide a more objective definition of the compact region of recirculating flow in the LA. Backwards particle tracing [15] was then used to distinguish respective contribution of the LPVs and RPVs to the detected vortex core. First, the LA was manually segmented on magnitude images of the 4DFlow scans. Subsequently the lambda2-method [12] was used to detect the vortex core from the velocity field two phases before end-systole. The 3D velocity data of the whole-heart 4DFlow acquisition was used for particle tracing algorithm, using 4th order Runge-Kutta numerical integration to create pathlines. To identify the origin of the recirculating flow, each voxel in the vortex core was designated as a seed point and backward particle tracing was performed until the start of systole. At the first phase of systole the particles were scored as 1) originating from LPVs; 2) originating from RPVs; 3) originating from LV (i.e., regurgitation); 4) particles already present in LA at start of systole (Figure 1). Particles entering the LA from outside the heart and not part of the pulmonary venous flow or LV regurgitation were excluded and considered as tracing errors (i.e., particles crossing the myocardial wall due to the discrete time step or spatial discretization used in the integration algorithm or due to other sources of error such as imaging artifacts). Additionally, to calculate the contribution of particles originating from LPVs and RPVs to the whole LA volume, at the same phase (two phases before systole) the whole atrium was seeded with particles and backwards tracing was performed to the start of systole.

Retrospective flow quantification

Using the same 4DFlow data set, retrospective valve tracking and through-plane flow mapping over the aorta and LAVV was performed. From aortic and LAVV flow-time curves the start and end of systole were determined as well as the regurgitation fraction [16]. Furthermore, the combined flow through the superior and inferior LPVs and the combined flow through the superior and inferior RPVs was quantified by retrospectively placing measurement planes at the ostium of each pulmonary vein, perpendicular to the inflow direction into the LA as visualized with streamlines. A resultant flow-time curve was formed for the summed LPVs and RPVs and peak systolic (S) and peak diastolic (D) flow from the pulmonary veins was defined. Furthermore, the time to peak systolic flow was determined.

Statistical analysis

Data are described as mean ± standard deviation or median (interquartile range) where appropriate. Differences between patients and controls are calculated with an independent t-test or Mann-Whitney U test where appropriate. The within-subject difference were tested with a paired t-test or Wilcoxon signed-rank test where appropriate between 1) volume of the compact recirculating flow structure (defined by streamlines) and vortex core volume (defined using the lambda2-method) 2) the left atrial inflow volume defined with particle tracing and the total

trans-pulmonary vein inflow. Correlation between different flow volumes were evaluated with Pearson's test.

RESULTS

Visual grading of the 4DFlow scans revealed aliasing in the area of the LA in 2 controls and 2 patients (1 with none to mild regurgitation and 1 with moderate regurgitation), who were excluded from further analysis. Characteristics of included subjects are described in Table 1.

Table 1. subject characteristics. * p <0.05 as compared with controls. mL = milliliter, BSA = body surface area, LV = left ventricle.

	Controls	Patients with none-mild LAVV regurgitation	Patients with moderate LAVV regurgitation
Number	18	9	9
Age (years)	24 ± 14	24 ± 12	21 ± 13
Male (%)	50	66	6
Type of AVSD		6 partial, 3 complete/intermediate	5 partial, 4 complete/intermediate
Age of surgery (months)		58 ± 55	69 ± 110
Time after surgery (years)	-	19 ± 9	16 ± 8
Regurgitation fraction (%)	-	5 ± 2	24 ± 6
Atrial volume (mL)	60 ± 31	74 ± 21	72 ± 24
Atrial volume / BSA (mL/m^2)	34 ± 13	41 ± 8	48 ± 8 *
LV Ejection fraction (%)	62 ± 4	57 ± 4 *	55 ± 8 *

Controls

In the remaining 18 controls, a single counter-clockwise (with respect to the feet-head axis) compact recirculating flow pattern could be detected with streamline visualization during ventricular systole (Figure 2A). The manually segmented compact recirculating flow structure had a median volume of 4.3 ± 2.9mL when measured just before end-systole. These measured volumes showed modest correlation with total LA volume (r = 0.60, p = 0.009), but not with age (p = 0.73). In all controls, a vortex core could be detected with the lambda2-method in the LA. The median volume (3.9mL, IQR 3.0 – 6.8mL) was not different from the volume detected with streamlines (mean difference 0.51mL, p = 0.267 with 95%CI -0.7 – 1.7mL) and correlation between both volumes was r = 0.61 (p = 0.007).

Backward tracing of the vortex core volume revealed a mean of 49 ± 21% of the total vortex volume originating from the LPVs, a median of 7% IQR 3 – 14% originating from the RPVs with a remaining mean of 40 ± 15% of the total vortex volume originating from blood particles already present within the atrium at the start of ventricular systole.

3.7

The flow from the four pulmonary veins could be separately detected and quantified in 15 of 18 controls. In the remaining three controls, streamline visualization was not adequate to depict LA inflow at the ostium of all four veins respectively, and to perform retrospective flow mapping. For the remaining 15 controls, the combined flow from the four veins (38 ± 15mL) was comparable to the combined particle volumes of the LPVs and RPVs after seeding the whole atrium and backward tracing (36 ± 15mL) (mean difference -1.8 mL, p = 0.60, 95%CI -9.3 – 6.0 mL). Pulmonary venous flow during ventricular systole in controls showed a right-left volume ratio of 1.2 ± 0.4. Peak velocity was significantly higher in the LPVs (54 ± 14cm/s) as compared with the RPVs (36 ± 11cm/s, p<0.001). Peak systolic flow rate was reached in the LPVs 195 ± 49ms and in the RPV 107ms IQR 87 – 175ms (difference p = 0.003) after the start of ventricular systole.

Patients

All patients were in sinus rhythm, one patient previously underwent a cardioversion because of atrial fibrillation. In patients, the normal LA flow pattern was disturbed. Differences between both patient groups (none to mild regurgitation and moderate regurgitation) and the controls are presented in Table 2.

Of the patients with none to mild regurgitation streamline visualization revealed a single recirculating flow pattern in the LA as seen in controls in 8 (89%) patients and two separate compact recirculating flow structures in 1 (11%) patient, with a regurgitation fraction of 9%. Total volume of compact recirculating flow patterns combined was 3.2 ± 2.0mL in the none to mild regurgitation group, which was not significantly different from the vortex core volume in controls (mean difference patients with none to mild regurgitation to controls 1.0 mL, p = 0.34, 95%CI -1.2 – 3.3 mL). In patients with none to mild regurgitation, particles seeded from inside the vortex core originated less frequently from the LPVs compared with controls (27 ± 25%, p = 0.023). Moreover, an increased contribution to the vortex core of blood already present in the LA at the start of ventricular systole was observed in patients with none to mild regurgitation compared with controls (57 ± 23%, p = 0.03). Using retrospective mapping, detection of flow from four separate pulmonary veins was possible in all patients with none to mild regurgitation and revealed a non-significantly different right-left volume ratio as described in controls (1.1 IQR 0.9 – 1.6, p = 0.61). Peak flow velocity was similar in patient and controls in LPVs and RPVs (Table 2). In patients with none to mild regurgitation, peak flow rate was reached later in the RPVs as compared with controls (mean difference -69ms, 95%CI -121 – -18ms, p = 0.01).

In contrast to the controls, in patients with moderate regurgitation, streamline visualization revealed two or three separate compact recirculating flow structures in the LA in 8 (89%) patients (difference between patient groups p = 0.002) (Figure 2C). In patients with multiple recirculating flow structures, two structures could be detected around the regurgitant jet; one circulating in counter-clockwise direction and one in clockwise direction with respect to the feet-head axis. In 3 out of 9 patients with recirculating flow around the regurgitant jet, another (third) counter-clockwise recirculating flow pattern was seen more cranially in the atrium. Total volume of com-

pact recirculating flow patterns combined was 4.7 ± 3.4mL in the moderate regurgitation group, which was not significantly different from the vortex core volume in controls (mean difference patients with moderate regurgitation -0.4mL, p = 0.74, 95%CI -3.0 – 2.1 mL). In patients with moderate regurgitation, particles seeded from inside the vortex core originated less frequently from the LPVs compared with controls (6% IQR 0 – 23%, p = 0.002). A trend towards an increased contribution to the vortex core of blood already present in the LA at the start of ventricular systole was observed in patients with moderate regurgitation (62 ± 27%, p = 0.05) compared with controls. Pulmonary venous flow quantification, possible in five patients with moderate regurgitation, revealed a non-significantly different right-left volume ratio as described in controls (1.3 ± 0.4, p = 0.90). Peak flow velocity was similar in patients and controls in the LPVs and RPVs

Table 2. Differences between controls and the two patients groups. * indicate p < 0.05 as compared with controls. ^ pulmonary vein right-left ratio only computed in cases with four pulmonary veins detected. Rotational direction is described with respect to the feet-head axis.

		Controls	Patients with none-mild LAVV regurgitation	Patients with moderate LAVV regurgitation
N		18	9	9
Streamlines	**Volume compact recirculating flow (mL)**	4.3 ± 2.9	3.2 ± 2.0	4.7 ± 3.4
	Rotational direction	100% single, counter-clockwise	89% single counter-clockwise, 11% one counter-clock wise and one clockwise	11% single counter-clockwise, 11% two counter-clockwise structures and 78% one counter-clockwise and one clockwise
Vortex core	**Volume vortex (mL)**	3.9 (IQR 3.0 - 6.8)	4.0 (IQR 3.3 - 6.8)	4.2 (IQR 2.3 - 6.7)
	Contribution LPVs (%)	49 ± 21	27 ± 25 *	6 (IQR 0 – 23) *
	Contribution RPVs (%)	7 (IQR 3 – 14)	16 ± 15	17 (IQR 4 – 31)
	Residual in atrium (%)	40 ± 15	57 ± 23 *	62 ± 27 *
Pulmonary venous flow	**Right-left ratio systolic volume ^**	1.3 ± 0.3	1.1 (IQR 0.9 - 1.6)	1.3 ± 0.4
	Peak velocity LPVs (cm/s)	54 ± 14	46 ± 12	49 ± 17
	Peak velocity RPVs (cm/s)	36 ± 11	33 ± 12	36 ± 12
	Time to peak LPVs (ms)	195 ± 49	207 ± 53	242 ± 28 *
	Time to peak RPVs (ms)	107 (IQR 87 - 175)	201 ± 74 *	223 ± 61 *

3.7

(Table 2). Systolic peak flow rate was reached later in the cardiac cycle in patients with moderate regurgitation compared with controls in both the LPVs (mean difference -48ms, 95%CI -84 – -12ms, p = 0.012) and the RPVs (mean difference -92ms, 95%CI -139 – -44ms, p = 0.001). Time to systolic peak flow rate in the LPVs was moderately correlated with the regurgitation fraction (r = 0.49, p = 0.04) whereas timing of peak flow rate in RPVs was not significantly correlated.

DISCUSSION

This explorative study provides new insights in blood flow characteristics in the LA in healthy controls and patients after AVSD correction with recurrent LAVV regurgitation, with the combined use of streamline visualization, semi-automated vortex core detection and particle tracing of pulmonary venous flow of 4DFlow MRI data. Key findings of the study are 1) in controls, on average 49% of volume of the single compact recirculating flow structure in the LA originates from the LPVs, but also on average 7% contribution to the volume originating from the RPVs was observed; 2) in corrected AVSD patients with none to mild regurgitation and with moderate regurgitation, the LPVs contribute less to the vortex core and systolic peak flow was reached later in the RPV; 3) additional differences in corrected AVSD patients with moderate LAVV regurgitation are multiple compact recirculating flow patterns and delayed systolic peak flow in the LPV that was related to regurgitation fraction.

Vortex formation in the LA in healthy controls

During ventricular systole the LA is filled and serves as an expanding reservoir. Previous studies observed recirculating blood in the LA [1;3-5], which in some studies is addressed as vortex flow. The recirculating flow conceivably avoids stasis and thrombosis and minimizes static pressure on the atrial wall [17]. Recirculating flow also contributes to the preservation of momentum in blood flow during ventricular systole, when the atrium is filled. Preserved momentum may aid efficient LV filling during early diastole.

Previous MRI studies used vector graphs, streamline analysis and pathline analysis [1;4;18] to visualize recirculating flow in 3D, however quantification of duration and size (area) of recirculating flow was limited to a 2D plane. Park et al. used echocardiography [5], with the advantage of a high frame rate and real-time imaging, but the limitation of analyzing 3D structures on 2D images. Complementing the quantification based on streamlines, the current study used the lambda2-method [12], to allow quantification of atrial vortex flow in 3D. Volumes of streamline-based recirculating flow were comparable to lambda2-detected atrial vortex cores, however, the shape of vortex cores appeared more irregular than the usually compact structures as segmented on streamline representation.

Postulations that flow from the LPVs mainly contributes to the LA recirculating flow formation and that flow from the RPVs is mostly directed along the LA wall with only little contribution to

the vortex, were thus far based on qualitative evaluations only [1]. The current study quantitatively showed that flow from LPVs in healthy controls has a substantially higher contribution to the vortex core than flow from RPVs (on average 49% versus 7%). The higher peak velocities in the flow from the LPVs compared with the RPVs might be a factor in this difference in contribution. However, even in healthy volunteers a large variation in venous contribution was observed, which is possibly caused by diversity in pulmonary vein anatomy [19], which was not assessed in this study.

Left atrial flow in patients after AVSD correction

A recent 4DFlow streamline-based study showed frequent absence of a vortex core in the LA in patients with a variety of organic heart disease, which was related to pulmonary venous peak velocity, but not pulmonary vein insertion angle [18]. In studies using computer fluid dynamics [20], echocardiography [5] and 4DFlow MRI [3], abnormal LA flow was also described in patients with atrial fibrillation and a relation with thrombus formation was suggested in these patients [21].

Decreased contribution of blood flow from the LPVs to the vortex core was observed in corrected AVSD patients with moderate as well as none to mild regurgitation. Therefore, the laterally directed regurgitation (i.e., towards the LPVs) can only partly explain the decreased contribution of flow from the LPVs to the atrial vortex core in corrected AVSD. Contributing effects may include the different pulmonary vein and LA anatomy after AVSD correction, possibly caused by remodeling after surgery. The delayed peak flow rate in the LPVs was predominately present in patients with moderate LAVV regurgitation and correlated to the regurgitation fraction and might therefore be a direct result of regurgitation or caused by increased atrial pressure secondary to regurgitation.

In the current study, patients after AVSD correction showed a disturbed recirculating flow pattern. Patients after AVSD correction often develop eccentric and dynamic regurgitation of LAVV. In patients with regurgitation, two recirculating structures were detected around the regurgitation jet(s). In an in vitro study, regurgitation jets with a high velocity in the presence of a prosthetic mechanical heart valve were related to aberrant LA vortex formation and an increase of shear stress in the blood flow near the wall, which directly activates platelets and has the ability to damage endothelial cells [22]. If endothelial cells fail to produce enough platelet inhibitors, this can lead to thrombus formation. The vortex formation observed around the regurgitant jet(s) in our study may similarly affect the atrial wall. Subsequently, it may contribute to the LA enlargement, diastolic dysfunction and atrial fibrillation observed in patients with chronic regurgitation of the LAVV [6]. On the other hand, others have suggested a protective property of LAVV regurgitation for thrombus formation, due to the increased velocity which may prevent stasis [23].

The clinical relevance of our preliminary findings comprises the role of disturbed LA flow patterns on outcome in patients with and without regurgitation. Early correction of moderate-

3.7

severe regurgitation is debated even in asymptomatic patients [6] as regurgitation may result in LA dilatation, diastolic dysfunction and atrial fibrillation. Our study showed that LA blood flow in patients after AVSD correction is disturbed, and specifically LAVV regurgitation disturbs normal recirculating flow structures during ventricular systole. The parameters described in this study can be used in future studies to investigate if regurgitation in patients with other congenital or acquired heart disease similarly disturbs LA flow patterns. Further insights in LA flow patterns will help to better understand the effect of regurgitation on the LA and will eventually allow better prediction of the effect of regurgitation, which may be of benefit to optimization of timing of interventions.

Study limitations

Current study is a pilot study with small numbers of patients and no patients with severe LAVV regurgitation were available. Compact recirculating flow patterns were manually segmented based on streamline visualization. Streamlines only present the velocity field at an instant in time and therefore cannot represent the true trajectory of recirculating flow. To overcome the limitations of streamlines and the manual segmentation, we have in addition used a semi-automatic method to detect vortex cores, which resulted in similar volumes. Particle tracing resembles the true pathlines of blood flow over time, however changes in velocity magnitude and direction faster than the temporal and spatial resolution allow to detect, cannot be represented in the tracing algorithm. The border between atrium and pulmonary veins was manually segmented, which might have introduced inaccuracies in quantification.

CONCLUSION

Using 4DFlow MRI, quantitative 3D analysis of recirculating flow structures and vortex cores in the LA blood flow during ventricular systole showed a higher contribution of blood flow from the LPVs versus RPVs in healthy controls. Furthermore, patients after AVSD correction with and without regurgitation presented a decreased contribution of flow from the LPVs to the vortex cores. Finally, LAVV regurgitation in patients with a corrected AVSD resulted in disturbed LA flow patterns with two recirculating flow structures around the regurgitation jet with an opposed circulation direction. Follow-up studies in patients with disturbed LA flow are needed to further explore the long-term consequences of this disturbed atrial flow on cardiac function.

REFERENCES

1. Fyrenius A, Wigstrom L, Ebbers T, et al. Three dimensional flow in the human left atrium. Heart 2001;86:448-55.

2. Pedrizzetti G, La CG, Alfieri O, et al. The vortex--an early predictor of cardiovascular outcome? Nat Rev Cardiol 2014;11:545-53.

3. Fluckiger JU, Goldberger JJ, Lee DC, et al. Left atrial flow velocity distribution and flow coherence using four-dimensional FLOW MRI: A pilot study investigating the impact of age and Pre- and Postintervention atrial fibrillation on atrial hemodynamics. J Magn Reson Imaging 2013;38:580-7.

4. Foll D, Taeger S, Bode C, et al. Age, gender, blood pressure, and ventricular geometry influence normal 3D blood flow characteristics in the left heart. Eur Heart J Cardiovasc Imaging 2013;14:366-73.

5. Park KH, Son JW, Park WJ, et al. Characterization of the left atrial vortex flow by two-dimensional transesophageal contrast echocardiography using particle image velocimetry. Ultrasound Med Biol 2013;39:62-71.

6. Enriquez-Sarano M, Avierinos JF, Messika-Zeitoun D, et al. Quantitative determinants of the outcome of asymptomatic mitral regurgitation. N Engl J Med 2005;352:875-83.

7. Dyverfeldt P, Kvitting JP, Carlhall CJ, et al. Hemodynamic aspects of mitral regurgitation assessed by generalized phase-contrast MRI. J Magn Reson Imaging 2011;33:582-8.

8. Hoohenkerk GJ, Bruggemans EF, Rijlaarsdam M, et al. More than 30 years' experience with surgical correction of atrioventricular septal defects. Ann Thorac Surg 2010;90:1554-61.

9. Lange R, Guenther T, Busch R, et al. The presence of Down syndrome is not a risk factor in complete atrioventricular septal defect repair. J Thorac Cardiovasc Surg 2007;134:304-10.

10. Calkoen EE, Westenberg JJ, Kroft LJ, et al. Characterization and quantification of dynamic eccentric regurgitation of the left atrioventricular valve after atrioventricular septal defect correction with 4D Flow cardiovascular magnetic resonance and retrospective valve tracking. J Cardiovasc Magn Reson 2015;17:18.

11. Calkoen EE, Roest AA, van der Geest RJ, et al. Cardiovascular function and flow by 4-dimensional magnetic resonance imaging techniques: new applications. J Thorac Imaging 2014;29:185-96.

12. Elbaz MS, Calkoen EE, Westenberg JJ, et al. Vortex flow during early and late left ventricular filling in normal subjects: quantitative characterization using retrospectively-gated 4D flow cardiovascular magnetic resonance and three-dimensional vortex core analysis. J Cardiovasc Magn Reson 2014;16:78.

13. Calkoen EE, Roest AA, Kroft LJ, et al. Characterization and improved quantification of left ventricular inflow using streamline visualization with 4DFlow MRI in healthy controls and patients after atrioventricular septal defect correction. J Magn Reson Imaging 2015;41:1512-20.

14. Napel S, Lee DH, Frayne R, et al. Visualizing three-dimensional flow with simulated streamlines and three-dimensional phase-contrast MR imaging. J Magn Reson Imaging 1992;2:143-53.

15. Buonocore MH. Visualizing blood flow patterns using streamlines, arrows, and particle paths. Magn Reson Med 1998;40:210-26.

16. Westenberg JJ, Roes SD, Ajmone MN, et al. Mitral valve and tricuspid valve blood flow: accurate quantification with 3D velocity-encoded MR imaging with retrospective valve tracking. Radiology 2008;249:792-800.

17. Sengupta PP, Narula J.A LA mode atrioventricular mechanical coupling. JACC Cardiovasc Imaging 2014;7:109-11.

18. Suwa K, Saitoh T, Takehara Y, et al. Characteristics of Intra-Left Atrial Flow Dynamics and Factors Affecting Formation of the Vortex Flow. Circ J. 2015;79:144-52.

19. Porres DV, Morenza OP, Pallisa E, et al. Learning from the pulmonary veins. Radiographics 2013;33:999-1022.

20. Mouret F, Garitey V, Bertrand E, et al. In vitro atrial flow dynamics: normal conditions versus atrial fibrillation. J Biomech 2004;37:1749-55.

3.7

21.   Markl M, Lee DC, Ng J, Carr M, et al. Left Atrial 4-Dimensional Flow Magnetic Resonance Imaging: Stasis and Velocity Mapping in Patients With Atrial Fibrillation. Invest Radiol. 2015: in press.

22.   Milo S, Rambod E, Gutfinger C, et al. Mitral mechanical heart valves: in vitro studies of their closure, vortex and microbubble formation with possible medical implications. Eur J Cardiothorac Surg 2003;24:364-70.

23.   Fukuda N, Hirai T, Ohara K, et al. Relation of the severity of mitral regurgitation to thromboembolic risk in patients with atrial fibrillation. Int J Cardiol 2011;146:197-201.
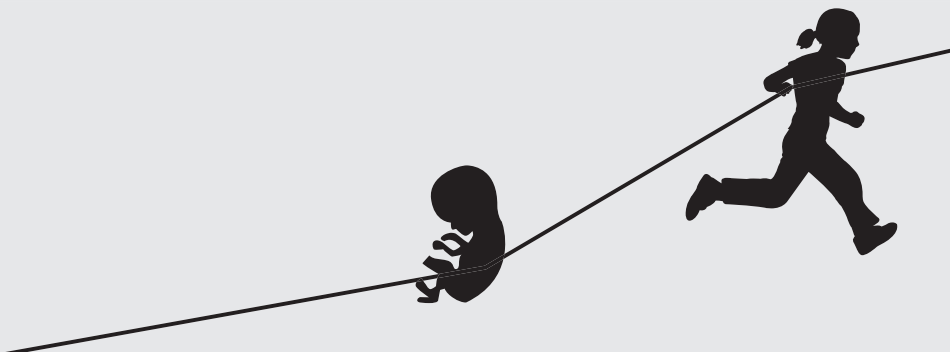
Part 4

Summary and future perspectives
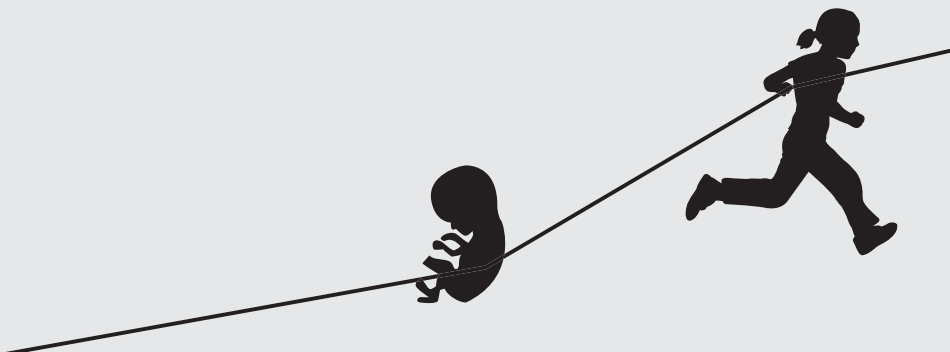
Chapter 4.1

Summary and future perspectives

The aim of this thesis is to review the current knowledge on atrioventricular septal defect (AVSD) development, early diagnosis and long-term follow-up (**Part 1**), to study the pathogenesis of AVSD (**Part 2**) and finally to analyze cardiac outcome long-term after AVSD correction (**Part 3**) with special emphasis on intra-cardiac flow patterns. Studies are performed with novel imaging techniques as fetal echocardiography and 4-dimensional velocity-encoded cardiac magnetic resonance imaging (4DFlow MRI).

Chapter 1.2 of this thesis contains a bench to bedside overview of AVSD. The spectrum of AVSD, comprises a variability in the extent of the defects in the septal tissue in proximity of the atrioventricular valves and of abnormalities of the atrioventricular valves themselves. As controversy exists in literature regarding terminology of AVSD, nomenclature and classification are addressed. The discovered developmental aspects (i.e. looping, mesenchymal cap, endocardial cushions and dorsal mesenchymal protrusion) and novel insights in genetic and maternal risk factors for AVSD are discussed. Additionally, an overview of innovations and challenges of diagnosis, which can already be made during the first trimester, is provided. The review displays that data on long-term follow-up of cardiac function after AVSD correction is limited and that literature mainly discourses the increasing survival rate and high incidence of surgical re-intervention because of left atrioventricular valve (LAVV) regurgitation. Finally, the review highlights differences between non-syndromic patients and patients with Down syndrome in the incidence of AVSD and in the associated cardiac anomalies. Early studies report poor outcome in AVSD patients with Down syndrome, whereas more recent studies report equal survival and even lower incidence of surgical re-intervention of valve regurgitation in patients with Down Syndrome as compared with non-syndromic patients. Recognition of anatomical factors related to outcome may aid identification of riskfactors and predictors of outcome during follow-up of patients with AVSD.

PATHOGENESIS OF AVSD

Contributing developmental factors

In the first 10 weeks of gestation looping, remodeling and septation of the initially linear heart tube results in a heart with two atria, two atrioventricular valves, two ventricles and a septated outflow tract with a seperated pulmonary valve and aortic valve. In **Chapter 1.2** it is shown that development of an AVSD can be a result of incomplete development of different congenital structures (i.e. endocardial cushions, mesenchymal cap, dorsal mesenchymal protrusion). The detected genes associated with AVSD affect one or more of these structures. The combination of an inflow- and an outflow-tract defect, as seen in patients with AVSD with Tetralogy of Fallot, stresses the assumption that a defect in genes expressed in the progenitor cells dorsal of the heart, also referred to as the second heart field (e.g. genes like vascular endothelial growth factor described in Chapter 2.4), can be the culprit of both inflow- and outflow-tract defects. On

4.1

the other hand, the variety of involved genetic and epigenetic factor can explain the range in subtypes of AVSD.

Within AVSD, variation exists in the location and extent of the defect of the (atrioventricular) membranous septum and atrioventricular valves. Around a quarter of patients with Down syndrome develop an AVSD. There are, however, signs that patients with Down syndrome without AVSD also develop abnormalities, evidenced by the observation of prenatal tricuspid regurgitation and mitralvalve prolapse. In **Chapter 2.1** abnormalities of the membranous septum and atrioventricular valves are observed even in patients with Down syndrome without AVSD. Microscopy of fetal hearts shows differences, especially a larger membranous septum and dysplastic atrioventricular valves in fetuses with Down syndrome without AVSD as compared with normal hearts. Echocardiography reveals a shorter muscular ventricular septum in Down syndrome patients both with and without AVSD as compared with normal hearts. These findings confirm the hypothesis that the spectrum of AVSD forms a sliding scale. Therefore, an AVSD *without* shunting, i.e. an AVSD-valve morphology (common valve with linear insertion), where the common valve is attached to both the atrial and the ventricular septum, might also exist. We speculate that the extensiveness of AVSD is influenced by the degree of maldevelopment of the different structures involved in atrioventricular septation and may relate to differences in affected gene(s) involved.

Fetal echocardiography: the impact of flow

The primitive heart tube starts to beat in the 5th week of pregnancy (22 days after conception). Eventhough organs are not depending on active fetal circulation yet, blood flow is crucial for haematopoesis and cardiogenesis. Studying blood flow during heart development might consequently give valuable information on normal and abnormal heart development. Current ultrasound techniques in human allow detection of an AVSD in the first trimester, between 10 and 14 weeks of gestation, by skilled staff with high-end ultrasound equipment, as is reviewed in **Chapter 2.2**. Visualization of the heart and cardiac blood flow is not (yet) possible during the stages of early cardiac development in human, due to limited ultrasound frequency. In mouse, high-frequency ultrasound as early as embryonic day 10.5 (6 weeks after gestation in human), allows analysis of cardiac function before complete septation. In **Chapter 2.3** reference values are provided of functional parameters measured at three subsequent stages of development (embryonic day 12.5, 14.5 and 17.5) in wild type mouse embryos. Reliable assessment of left and right ventricular function is possible and diastolic and systolic function improves during normal heart development. Additionally, application of high frequency ultrasound in genetically mutated mouse models will potentially give further insight in hemodynamic during abnormal heart development. Vascular endothelial growth factor (*VEGF*) is in human related to development of AVSD and Tetralogy of Fallot. Murine *Vegf*$^{120/1120}$ embryos, that overexpress the *Vegf*^{120} isoform, are known to develop a Tetralogy of Fallot phenotype. In **Chapter 2.4**, also abnormalities of the atrioventricular valves and an AVSD are described in *Vegf*$^{120/1120}$ mouse embryos. Moreover, high

frequency ultrasound reveals a reduced heart rate in *Vegf*[120/120] embryos at three developmental stages, which is confirmed by *ex-vivo* optical mapping. Subsequently, different possible causes of the reduced heart rate are analyzed. Immunohistochemistry analyses reveals a smaller and less compact sinoatrial node (SAN), with hyper-vascularization, which might contribute to the sinus bradycardia. Furthermore, the observed increased expression of the high conductance gap junction *Connexin43* in the SAN, which is normally expressed in the working myocardium, potentially increases loading time of SAN cells and reduces essential isolation of the SAN from the surrounding atrial myocardium, which may contribute to the observed bradycardia.

LONG-TERM FOLLOW-UP AFTER AVSD CORRECTION

During the surgical correction of AVSD, one or two patches are placed to close shunt(s) between the left and right heart. Most often the remaining 'cleft' in the LAVV is surgically closed to pre-vent regurgitation. Due to the different papillary muscle position, leaflet size and the surgical correction, the shape of the LAVV in corrected AVSD is different from the normal mitral valve. Survival after AVSD correction is as high as 100% in the current era. However, incidence of surgi-cal re-intervention is reported between 2 and 29%, mainly because of regurgitation of the LAVV. Data on cardiac function long-term after AVSD correction is limited. Cardiac magnetic resonance imaging is the gold standard in the evaluation of cardiac function long-term after correction of a congenital heart defect. Furthermore, the recent introduction of 4DFlow allows comprehensive assessment of cardiac function and cardiovascular blood flow phenomena.

In **Chapter 3.1** the use of 4DFlow MRI to assess cardiac function and the rapid development of applications to visualize and quantify cardiovascular blood flow are described. New visualization tools have enriched knowledge on blood flow hemodynamics and efficiency in the cardiovas-cular system. Most reports focus on normal and abnormal flow in the aorta, whereas data of intra-cardiac flow is limited. One of the available visualization tools is streamline visualization. Streamlines are lines instantaneously tangent to the local velocity vector in each position at a specific time point and connected to all points along the direction of this line. Therefore, streamlines can be used to visualize the flow direction only at a given time point. This limitation can be overcome with particle tracing. With particle tracing virtual particles are positioned at a predefined position and time and subsequently released inside the three dimensional (3D) velocity field and then followed backwards or forwards in time. The trajectory of the particles is calculated in 3D by either forward or backward tracing, by using the local velocity at each position and time point and calculating the next or previous position of this particle.

Disturbed left ventricular inflow

In **Chapter 3.2** streamlines are used to analyze inflow direction in patients after AVSD correc-tion. In these patients a dynamic and more lateral inflow direction is observed as compared

4.1

with healthy controls. In addition, more accurate measurement of the trans LAVV flow can be achieved by adjusting the measurement plane perpendicular to the peak velocities as visualized by streamlines. In **Chapter 3.3** the inflow is further investigated in 3D and in time with the use of particle tracing. In this study intra-cardiac particles are labelled as components of flow discriminating 1) *direct flow* entering and exiting the LV within the analyzed diastole and systole, 2) *retained inflow* entering during diastole but remaining in the LV during the following systole, 3) *delayed ejection flow* already present in LV prior to diastole but exiting the LV during the following systole and 4) *residual volume* present and remaining in the LV during the analyzed diastole and systole cardiac cycle and 5) *regurgitant flow*. Subsequently, quantification of flow is done with the use of the American Heart Association standardized 16-segment left ventricular cavity model. In patients after AVSD correction direct flow components are decreased and the delayed ejection components and residual volume components are increased. Inflow into the (infero- and antero-) lateral segments confirms the lateral inflow direction observed using streamline visualization in chapter 3.2. In addition, an increase of flow into the apical segments is found. Interestingly, the flow in the (inferior) lateral and apical segments is predominantely retained flow, suggesting flow in these directions to be less efficient.

An additional consequence of the more lateral inflow direction is that this may interfere with the assessment of diastolic function parameters with echocardiography as echocardiography relies on accurate alignment of the Doppler beam. One of these diastolic function parameters is velocity propagation. In **Chapter 3.4** a novel velocity encoded MRI method to assess velocity propagation is introduced and a comparison is made with the traditionally used Color M-mode echocardiography approach. In healthy subjects and patients with ischemic heart failure, the new method demonstrates good agreement with echocardiography to identify LV impaired relaxation. In contrast to echocardiography, this novel approach allows retrospective placement of the measurement line parallel to the inflow direction. This might be beneficial in patients with abnormal inflow direction, such as AVSD patients or patients with a poor echo window, such as patients with Duchenne muscular dystrophy.

Disturbed vortex formation in the left ventricle

As the inflow direction is disturbed in corrected AVSD patients, the subsequent study aims to investigate whether vortex formation in the left ventricle is also affected. When blood enters the left ventricle through the LAVV during diastole, shear layers separate and a vortex ring forms. A vortex ring is a compact region of swirling blood flow and is purposed to aid transport of blood flow, minimize kinetic energy loss, help LAVV closure and prevent thrombus formation. In a previous study (Elbaz et al. JCMR 2014) we have shown that a separate ring forms during early and late diastole, with the late filling having a position closer to the atrioventricular valve and closer to the ventricular long axis. The shape of the late filling vortex ring is less circular compared with the early filling ring and this circularity is related to the circularity of the inflow jet. In **chapter 3.5** the vortex formation in corrected AVSD patients is compared with the vortex

formation in healthy controls. In contrast to controls, who all display a vortex ring during early filling, in 18% of patients after AVSD correction the vortex ring in the left ventricle is found to be absent. Absence of vortex ring formation is related to a high vortex formation time (due to high inflow velocity) and abnormalities of the LAVV (i.e. single papillary muscle and double orifices LAVV). Moreover, when a vortex ring is present, the center of the vortex core is positioned more towards the lateral wall, closer towards the apex and more anterior. Furthermore the vortex ring is more tilted with its septal side down and with a less circular shape. The abnormal orientation is related to the inflow direction on streamlines. Because patients included in the study are relatively asymptomatic, correlation between vortex formation and conventional function parameters is difficult. However, the results from this study prove the impact of the valve shape on vortex formation *in vivo* and in 3D, which was previously suggested in in vitro studies or in 2D analysis.

Regurgitation of the left atrioventricular valve and atrial flow patterns

Regurgitation of the LAVV is common after AVSD correction and surgical re-intervention incidence to correct LAVV regurgitation is high. Echocardiography is the technique most commonly used to evaluate regurgitation of the LAVV. However, poor inter-observer agreement is described for echocardiographic grading of regurgitation in corrected AVSD patients. In **chapter 3.6** the regurgitation in corrected AVSD patients is characterized with streamlines. Multiple regurgitant jets are observed, with a dynamic behavior during systole, a non-circular shape and an overall eccentric (lateral) regurgitation direction. These findings explain why quantification of regurgitation with echocardiography is difficult in these patients, because Doppler quantification techniques (i.e. PISA and Vena Contracta measurements) are based on the assumption that the regurgitation jet is single and circular. Furthermore, echocardiography is known to underestimate eccentric regurgitation. Streamline visualization allows retrospective positioning of the measurement plane perpendicular to the jet during systole, which results in quantification of the amount of regurgitation with excellent internal flow validation. Correlation between grading of regurgitation with echocardiography and 4DFlow valve tracking is modest. The eccentric and dynamic regurgitation of the LAVV in corrected AVSD patients disturbs the normal left atrial flow pattern as is shown in **Chapter 3.7**. With the combined use of streamlines, vortex core extraction and particle tracing, a single recirculating flow pattern is displayed in the left atrium of healthy volunteers. The recirculating flow was predominantly formed from blood coming from the left pulmonary veins. In corrected AVSD patients with regurgitation, multiple recirculating flow patterns are seen around the regurgitant jet(s) and contribution of left pulmonary vein blood to the recirculating flow is diminished. Furthermore, the peak flow rate in the left pulmonary veins is delayed. The disturbed recirculating flow patterns in the left atrium may contribute to the poor clinical outcome of even asymptomatic patients with regurgitation of the LAVV.

4.1

CONCLUSIONS AND FUTURE PERSPECTIVES

AVSD development

This thesis shows diversity in subtypes of AVSD and highlights different developmental/genetic cascades that can result in an AVSD. The increasing amount of studies on genetic and epigenetic factors of heart development will step by step unravel the multiple factors involved in development of AVSD. Studies in other genetically mutated mouse models of Down syndrome related genes (e.g DSCAM, CRELD1) or genes that are currently not related to Down syndrome (e.g. Pdgfr- α, Nkx2.5, Tbx5) will provide insight in the differences in AVSD between patients with Down syndrome and non-syndromic patients. Studies in mouse models will also provide better understanding of the effect that specific genes have on the different structures involved in AVSD pathogenesis and in which subtype of AVSD they result.

Furthermore, it is made plausible that AVSD is a sliding scale and that patients with Down syndrome without AVSD also have abnormalities of the membranous septum and atrioventricular valves. Future studies in these patients and in family members of AVSD patients are needed to further evaluate these cardiac abnormalities and determine if clinical outcome is also affected.

In the current thesis, high frequency ultrasound in mouse embryos shows to be a promising technique to study cardiovascular flow in early stages of heart development. In humans with congenital heart disease sick sinus syndrome is observed. Disturbed *VEGF* signaling has been associated with congenital heart defects (AVSD and Tetralogy of Fallot) in human and in mouse models. Whether disturbed *VEGF* signaling, that in the current thesis is shown to disturb SAN formation in mouse embryos, also plays a part in abnormal SAN development in humans with congenital heart disease remains to be investigated. Also, the relevance of *VEGF* signaling in other components of the cardiac conduction system or its innervation remains to be determined. In zebrafish, a reduced heart rate showed to disturb valve development via shear stress related genes as *Klf2*. From our studies it is impossible to distinguish whether the abnormal atrioventricular valves in *Vegf$^{120/120}$* embryos are solely an effect of the *Vegf* mutation or if a reduced heart rate also plays a part. Studies with pharmacological influenced heart rate combined with high frequency ultrasound in mouse embryos may gather more insight in the effect of heart rate on atrioventricular valve development and atrioventricular septation.

Intra-cardiac flow in patients with congenital heart disease

In part 3 of this thesis, 4DFlow MRI data reveals that patients with an abnormal LAVV after AVSD correction have aberrant intra-cardiac flow patterns. During diastole the inflow into the left ventricle is directed more towards the lateral wall, more towards the apex and vortex formation is abnormal. The disturbed inflow is most likely due to the congenitally different morphology and position of the LAVV, as well as the cleft closure during correction of an AVSD. This stresses the impact of valve surgery on intra-cardiac flow. Next to the aberrant inflow, during systole the dynamic and eccentric regurgitation of the LAVV disturbs the normal recirculating flow patterns

in the left atrium. We cannot preclude that the aberrant flow in the atrium and ventricle is a coping mechanism of the heart and has a favorable effect on the cardiac function. However, *in vitro* studies have shown that a lateral inflow direction and disturbed vortex flow, as found in our studies, cause an increase in energy dissipation. Furthermore, the disturbed flow in the left atrium and left ventricle may affect myocardial remodeling through changes in wall shear stress and in that way cause regional hypertrophy and stiffening. Newly available applications to quantify different forms of energy from 4DFlow MRI data, will potentially be able to tell whether the disturbed intra-cardiac flow is indeed related to more energy loss and less efficient flow. Future long-term follow-up studies have to show whether the observed changes in blood flow in corrected AVSD patients eventually result in poor clinical outcome.

In addition, in part 3 of this thesis it is shown that patients after AVSD correction have complex, multiple, dynamic and eccentric regurgitation jets. In patients after AVSD correction, streamline visualization from 4DFlow MRI can advance quantification of LAVV inflow and regurgitation. Retrospective valve tracking with the use of streamline visualization has the potency to be similarly beneficial in other patient groups with congenital and acquired heart disease. The adjustment of the measurement plane perpendicular to the flow during the cardiac cycle will especially be beneficial in patients with a disturbed inflow direction and eccentric and dynamic regurgitant jets, that are challenging to quantify with echocardiography. Development of computerized valve tracking will enable shorter post-processing time and potentially reduce observer variation.

Intra-cardiac flow analyses with 4DFlow MRI provided interesting new data in patients with a congenital heart disease, however the limitations of the different imaging techniques have to be kept in mind. In addition, validation of techniques with phantoms and echocardiography remain important. Evaluation of intra-cardiac flow in patients with a congenital heart diseas is a relatively new field. The offered 4DFlow visualization techniques in the current thesis have the potency to provide valuable information of patients with other congenital heart defects (i.e. after single ventricular repair or in Tetralogy of Fallot). Additionally, knowledge on intra-cardiac flow may allow better understanding of diastolic (dys)function. Furthermore, quantification of flow component distribution and vortex cores in the left ventricle could potentially serve as an early predictor of cardiac dysfunction.

4.1

Continuing efforts to incorporate results of basic science studies into clinically oriented studies, will allow optimal comprehension of the mechanisms behind the phenomena observed in congenital heart disease patients, which will ultimately benefit clinical practice.
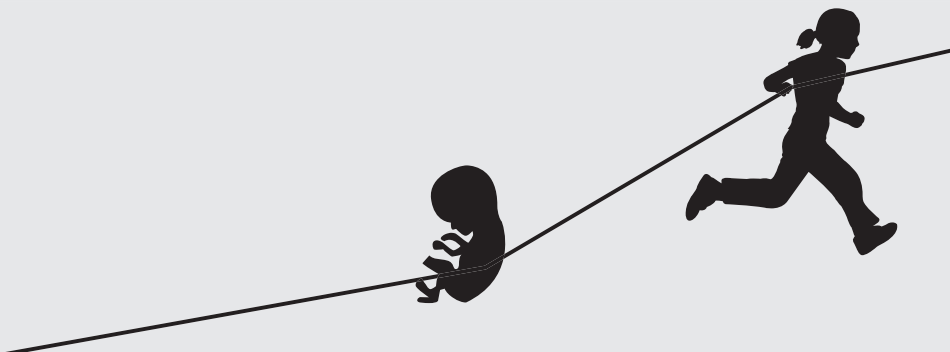
Part 5

Appendices
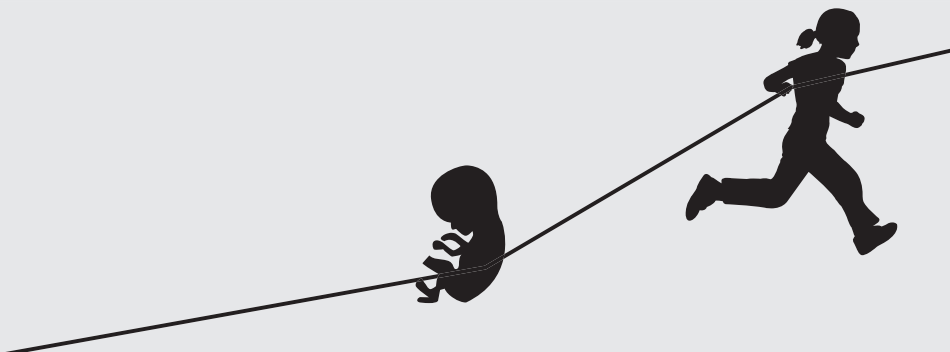
Chapter 5.1

Nederlandse samenvatting

ATRIOVENTRICULAIR SEPTUM DEFECT: GEAVANCEERDE BEELDVORMING VAN VROEGE ONTWIKKELING TOT LANGE TERMIJN FOLLOW-UP

Dit proefschrift gaat over de aangeboren hartafwijking atrioventriculair septum defect (AVSD). Een hart met een AVSD heeft, in tegenstelling tot een 'normaal' hart met vier gescheiden hart kamers (Figuur 1A), een opening tussen de linker en rechter hart helft ter plaatse van de overgang van de boezems naar de kamers (Figuur 1B). In deel 1 van dit proefschrift wordt een literatuur overzicht gegeven van het ontstaan, de diagnose, de therapie en de lange termijn gevolgen van een AVSD. Vervolgens wordt in deel 2 het ontstaan van een AVSD verder onderzocht en worden in deel 3 de lange termijn gevolgen van een AVSD meer gedetailleerd bestudeerd. In deel 2 en 3 is speciale aandacht voor de (veranderde) bloedstroom in het hart onderzocht met echocardiografie en magnetische resonantie imaging (MRI) technieken.

DEEL 1: LITERATUUR OVERZICHT

Hoofdstuk 1.2 geeft een literatuur overzicht van het AVSD vanaf de vroege ontwikkeling tot de lange termijn follow-up. De verschillende types AVSD en de gebruikte nomenclatuur worden beschreven. Daarnaast wordt ingegaan op de recent ontdekte genetische en epigenetische factoren betrokken bij AVSD ontwikkeling. Uit het review blijkt dat studies naar de lange termijn uitkomsten na AVSD correctie beperkt zijn tot gegevens van overleving en incidentie van een tweede operatie. Over de functie van het hart na een AVSD operatie is weinig bekend. Ongeveer de helft van de patiënten met een AVSD heeft het syndroom van Down. Uit het review komen verschillen naar voren in de anatomie en de lange termijn gevolgen van een AVSD tussen patiënten met en zonder het syndroom van Down.

DEEL 2: HET ONTSTAAN VAN EEN AVSD

In de eerste 10 weken na de bevruchting ontstaat vanuit het primaire hartbuisje, na buigen ('loopen'), modellering en septatie, een hart met twee boezems, twee kamers, twee grote uitstroom vaten en vier hartkleppen. Door abnormale ontwikkeling van drie verschillende structuren (de endocard kussens, de mesenchymal cap en de dorsal mesenchymal protrusion) kan een AVSD ontstaan. Bij patiënten met het syndroom van Down komt een AVSD veel voor. Er zijn echter ook aanwijzingen dat harten van patiënten met het syndroom van Down zonder septum defect verschillen van 'normale' harten. In **hoofdstuk 2.1** wordt beschreven dat patiënten met het syndroom van Down zonder septum defect een groter bindweefsel (membraneus) septum, afwijkende kleppen tussen de boezems en de kamers (atrioventriculair kleppen) en een korter tussenschot van spierweefsel tussen het linker en rechter ventrikel (ventrikel septum) hebben.

5.1

Dit suggereert een glijdende schaal van een AVSD hart zonder shunt tot een compleet AVSD hart met een verbinding op boezem en kamer niveau.

Het primitieve hartbuisje klopt al vanaf de 22ste dag na de bevruchting. Verschillende studies hebben aangetoond dat de bloedstroom door het ontwikkelende hart bijdraagt aan septatie en het ontwikkelen van hartkleppen. Studies naar bloedstroom in het hart kunnen daarom mogelijk een bijdrage leveren aan het begrijpen van normale en abnormale hartontwikkeling. In **hoofdstuk 2.2** wordt beschreven dat het met de huidige echo-technieken, uitgevoerd door ervaren onderzoekers, mogelijk is een AVSD te diagnosticeren tijdens het eerste trimester (tussen 10 en 14 weken na de bevruchting). Echter het bestuderen van de bloedstroom tijdens de hartontwikkeling is nog niet mogelijk in mensen. Bij de muis is dit wel mogelijk. In **hoofdstuk 2.3** wordt getoond dat betrouwbare metingen kunnen worden verricht met hoog frequente echo tijdens verschillende stadia van ontwikkeling van het hart van normale muizen embryo's. In dit hoofdstuk worden ook referentie waarden gegeven. Het gebruik van deze hoog frequente echo techniek in studies met genetisch gemodificeerde muismodellen kan in de toekomst veel kennis opleveren over abnormale hartontwikkeling. Het gen Vasculair Endothelial Growth Factor (VEGF) is bij de mens geassocieerd met een AVSD en een andere hartafwijking: Tetralogy van Fallot. In **hoofdstuk 2.4** worden afwijkingen van de atrioventriculair kleppen in het muismodel VEGF[120/120] beschreven. Bovendien wordt met hoog frequente echo getoond dat deze muizen een tragere hartslag hebben tijdens de hartontwikkeling. De trage hartslag wordt bevestigd met optical mapping. In dit hoofdstuk wordt vervolgens onderzocht waarom de hartslag van deze muizen embryo's traag is. De sinusknoop van de VEGF[120/120] muizen embryo's is kleiner en minder compact, met veranderde vaat innervatie. Bovendien is er een verhoogde expressie van het snel geleidende transport kanaal Connexin43. Of de sinusknoop ook afwijkend is in mensen met afwijkingen in het VEGF gen moet verder onderzocht worden. Op basis van deze studie kan geen onderscheid gemaakt worden tussen het effect van de genafwijking en het effect van de trage hartslag op de klepontwikkeling. Studies die de hartfrequentie versnellen of vertragen met medicatie kunnen mogelijk meer inzicht geven in de rol van hartfrequentie op klepontwikkeling.


DEEL 3: VERSTOORDE BLOEDSTROOM NA AVSD CORRECTIE

Een AVSD moet bij de meeste kinderen in het eerste levensjaar worden gecorrigeerd, om te veel bloedstroom naar de longen, met als gevolg verhoogde longvaatdrukken, te voorkomen. Tijdens de operatie worden één of twee stukjes kunststof gebruikt om de verbinding tussen de linker en rechter harthelft dicht te maken (Figuur 1C). Hierdoor wordt de klep tussen de boezem en de kamers (de atrioventriculair klep) gesplitst in een linker (in het normale hart de mitralisklep) en een rechter (in het normale hart de tricuspidalisklep) deel. Naast het dichtmaken van de verbinding worden vaak hechtingen in de linker atrioventriculair klep gezet om lekkage te voorkomen. Het oorspronkelijke verschil in anatomie en de chirurgische correctie zorgen ervoor

dat de vorm van de linker atrioventriculair klep afwijkt van de normale mitralisklep (Figuur 2A en E). Overleving na AVSD correctie is in de huidige tijd heel goed (tot 100%), maar de incidentie van een tweede operatie is hoog (tussen 2-29%), met name door kleplekkage. Over de hartfunctie na AVSD correctie is weinig bekend. Met cardiovasculaire MRI kan goed gekeken worden naar de hartfunctie en nieuwe technieken maken visualisatie van de bloedstroom in het hart mogelijk.

Met zogenaamde '4DFlow MRI' kan de bloedstroom in het hart in drie richtingen en in de tijd worden opgenomen. In **hoofdstuk 3.1** wordt het gebruik van 4DFlow voor het bestuderen van de hartfunctie beschreven. Daarnaast worden nieuwe toepassingen om de bloedstroom te visualiseren en kwantificeren beschreven. Een van de toepassingen is 'streamline visualisatie' waarbij verbindingslijnen tussen snelheidsvectoren op een bepaald tijdsmoment worden weergegeven. Om de beweging van het bloed beter in de tijd weer te geven worden 'pathlines' gebruikt, waarbij op basis van de stroomrichting en snelheid een virtueel deeltje gevolgd wordt in de tijd.

In **hoofdstuk 3.2** wordt met streamlines laten zien dat de bloedstroom in gecorrigeerde AVSD patiënten een meer laterale instroom hoek heeft. Bovendien laat de studie zien dat de bloedstroom betrouwbaarder te kwantificeren is als gemeten wordt in een vlak loodrecht op deze streamlines. De analyse in deze studie is op één tijdsmoment en 2-dimensionaal. In **hoofdstuk 3.3** wordt de instroom richting door de linker atrioventriculair klep verder bestudeerd met behulp van pathlines. Hieruit blijkt dat in gecorrigeerde AVSD patiënten een kleiner deel van de bloedstroom dat het hart binnenkomt in de zelfde hartslag weer wordt uitgepompt in vergelijking met de controle groep. Daarnaast wordt, 3-dimensionaal, de laterale instroom richting bevestigd en is er een groter aantal deeltjes dat via het apicale deel van het hart stroomt. In

Figuur 1. Het AVSD.
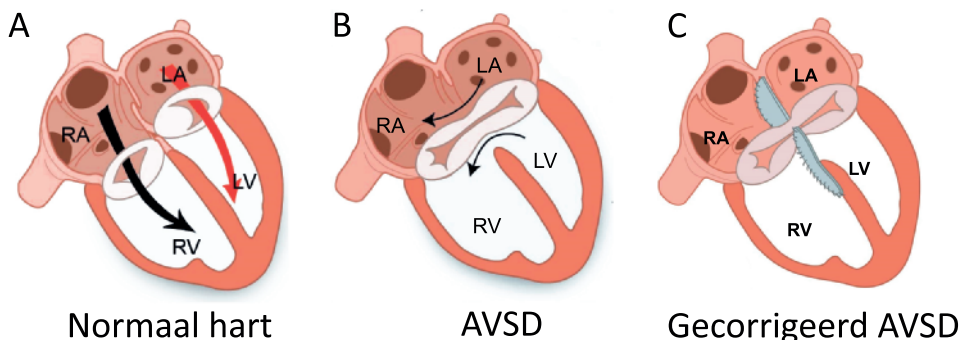
Het normale hart met 2 gescheiden kleppen tussen de boezems en de kamers (A). Een compleet AVSD met verbinding tussen de boezems en de kamers (pijlen in B). En een gecorrigeerd AVSD hart met in lichtblauw de met kunststof dichtgemaakte verbindingen (C). RA = rechter atrium/boezem, LA = linker atrium/boezem, RV = rechter ventrikel/kamer, LV = linker ventrikel/kamer.

hoofdstuk 3.4 wordt een techniek beschreven om de golf voortplanting (propagatie) snelheid (velocity) te meten met behulp van MRI. Snelheid propagatie is een maat voor de diastolische functie van het hart.

Tijdens het vullen van de hartkamers, vormt zich in de bloedstroom een vortex ring op de top van de atrioventriculair kleppen. Een vortex ring is een compact gebied van om zijn as draaiende (bloed)stroom. Een vortex ring minimaliseert verlies van kinetische energie, helpt bij het sluiten van de kleppen en voorkomt de vorming van bloedstolsels. In **hoofdstuk 3.5** wordt de invloed van de veranderde instroom van bloed in het hart, die werd gevonden in de hoofdstukken 3.2 en 3.3, op vortex ring vorming bestudeerd. In dit hoofdstuk blijkt dat de vortex ring in gecorrigeerde AVSD patiënten vaker afwezig is. Als hij wel vormt heeft de vortex ring een veranderde vorm en positie (Figuur 2). Deze veranderde vorm komt overeen met de abnormale vorm van de linker atrioventriculair klep.

Kleplekkage na AVSD correctie komt vaak voor. Kleplekkage lijdt op langere termijn tot hartfalen. Het kwantificeren van deze lekkage is belangrijk voor de indicatie stelling van een her-operatie. Met echocardiografie is de lekkage niet betrouwbaar te meten. In **hoofdstuk 3.6** wordt de richting van de lekkage in de linker boezem bestudeerd met behulp van streamlines. Uit deze studie blijkt dat de lekkage excentrisch is en tijdens de systole van richting verandert. Dit verklaart waarom de lekkage moeilijk te meten is met echocardiografie. Met 4DFlow MRI kan het meetvlak gedurende de systole loodrecht op de van richting veranderende lekkage worden geplaatst. Met deze methode blijkt de lekkage wel betrouwbaar te meten. De 4DFlow

Figuur 2. Bloedstroom in het hart.
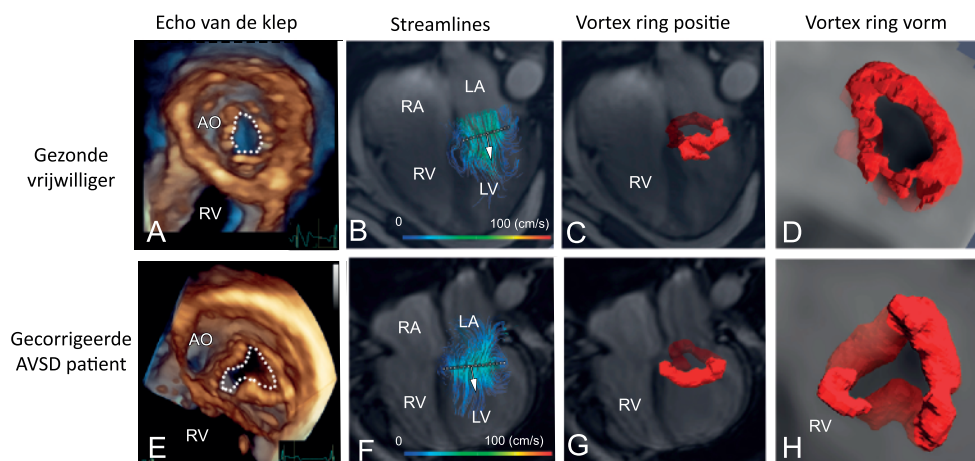
In figuur a en e is het verschil te zien tussen de vorm van de linker atrioventriculair klep van een gezonde vrijwilliger (stippellijnen in a) en gecorrigeerde AVSD patient (stippellijnen in e). De streamlines laten de bloedstroom richting zien (b en f). De rode vortex ring van de patient heeft een andere positie (g) en vorm (h) in vergelijking met de vrijwilliger (c en d). AO = aorta. RA = rechter atrium/boezem, LA = linker atrium/boezem, RV = rechter ventrikel/kamer, LV = linker ventrikel/kamer.
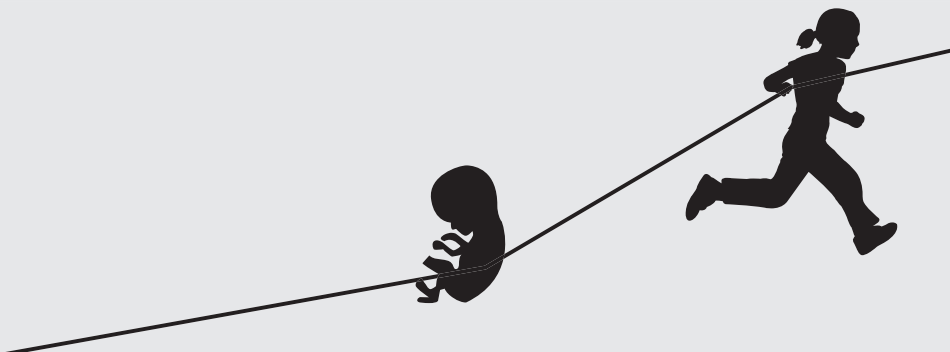
methode is daarom waardevol voor patiënten met (aangeboren) klepafwijkingen of lekkage. In **hoofdstuk 3.7** wordt vervolgens getoond dat de lekkage door de atrioventriculaire klep de circulerende bloedstroom in de linker boezem verstoort.

De veranderde bloedstroom in het hart van gecorrigeerde AVSD patiënten benadrukt de invloed van congenitale chirurgie op de normale bloedstroom in het hart. Studies met computer modellen hebben laten zien dat een laterale instroom richting en abnormale vortex ring vorming gepaard gaan met energie verlies. De veranderde bloedstroom in gecorrigeerde AVSD patiënten lijdt mogelijk ook tot meer energie verlies. Dit moet onderzocht worden in vervolg studies. Daarnaast moet verder onderzocht worden of de veranderde bloedstroom ook invloed heeft op de hartspier. De studies in deel 3 van dit proefschrift laten zien dat 4DFlow MRI waardevolle nieuwe inzichten geeft in de hemodynamiek in het normale hart en in de (verminderde) cardiale functie van patiënten met aangeboren hartafwijkingen.

Het blijft belangrijk om basale studies met klinische studies te combineren om steeds meer te kunnen begrijpen van aangeboren afwijkingen en zo de patiëntenzorg verder te verbeteren.
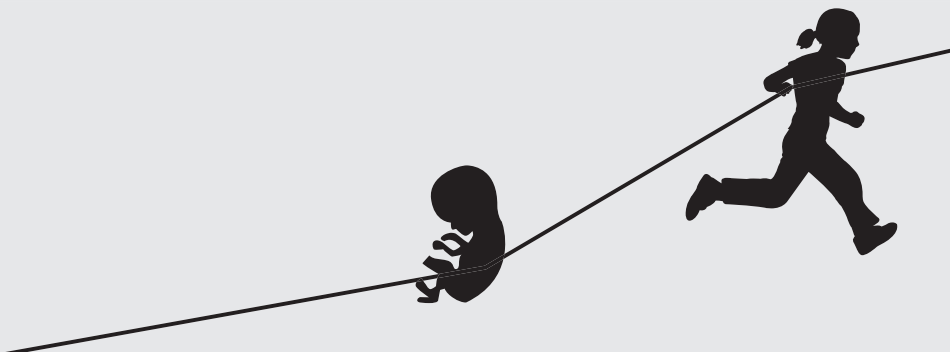
5.1

Chapter 5.2

Publications

1. Elbaz MS, Roest AA, **Calkoen EE**, de koning P, Lelieveldt BP, van der Geest RJ and Westenberg JJ. Assessment of viscous energy loss and the association with 3D vortex ring formation in left ventricular inflow: in vivo evaluation using 4DFlow MRI. MRM 2016 epub

2. **Calkoen EE**, Hazekamp MG, Blom NA, Elders BB, Gittenberger-de Groot AC, Haak MC, Bartelings MM, Roest AA, Jongbloed MR. Atrioventricular septal defect: From embryonic development to long-term follow-up. Int J Cardiol. 2016;202:784-795

3. **Calkoen EE**, Elbaz MS, Westenberg JJ, Kroft LJ, Hazekamp MG, Roest AA, van der Geest RJ. Altered left ventricular vortex ring formation by 4-dimensional flow magnetic resonance imaging after repair of atrioventricular septal defects. J Thorac Cardiovasc Surg. 2015;150:1233-1240

4. **Calkoen EE,** de Koning PJ, Blom NA, Kroft LJ, de Roos A, Wolterbeek R, Roest AA, Westenberg JJ . Disturbed Intracardiac Flow Organization After Atrioventricular Septal Defect Correction as Assessed With 4D Flow Magnetic Resonance Imaging and Quantitative Particle Tracing. Invest Radiol. 2015;50:850-7

5. **Calkoen EE,** Adriaanse B, Haak M, Bartelings M, Kolesnik A, Niszczota C, van Vugt J, Roest A, Blom N, Gittenberger-de Groot A, Jongbloed M. How Normal Is a 'Normal' Heart in Fetuses and Infants with Down Syndrome? Fetal Diagn Ther. 2015 Jun 20

6. **Calkoen EE**, Marsan NA, Bax JJ, van den Boogaard PJ, Roest AA, de Roos A, Westenberg JJ. High-temporal velocity-encoded MRI for the assessment of left ventricular inflow propagation velocity: Comparison with color M-mode echocardiography. J Magn Reson Imaging. 2015;42:1297-304

7. **Calkoen EE**, Westenberg JJ, Kroft LJ, Blom NA, Hazekamp MG, Rijlaarsdam ME, Jongbloed MR, de Roos A, Roest AA. Characterization and quantification of dynamic eccentric regurgitation of the left atrioventricular valve after atrioventricular septal defect correction with 4D Flow cardiovascular magnetic resonance and retrospective valve tracking. J Cardiovasc Magn Reson. 2015;17:18

8. **Calkoen EE**, Vicente-Steijn R, Hahurij ND, van Munsteren CJ, Roest AA, DeRuiter MC, Steendijk P, Schalij MJ, Gittenberger-de Groot AC, Blom NA, Jongbloed MR. Abnormal sinoatrial node development resulting from disturbed vascular endothelial growth factor signaling. Int J Cardiol. 2015;183:249-57

9. **Calkoen EE**, Roest AAW, Kroft LJM, Geest van der RJ, Jongbloed MRM, Boogaard vd PJ, Blom NA, Hazekamp MG, Roos de A, Westenberg JJM Characterization and improved quantification of left ventricular inflow using streamline visualization with 4DFlow MRI in healthy controls and patients after atrioventricular septal defect correction. J Magn Res Img 2015;41:1512-20

10. **Calkoen EE**, Elbaz MS, Westenberg JJ, Lelieveldt BP, Roest AA, van der Geest RJ. Vortex flow during early and late left ventricular filling in normal subjects: quantitative characterization using retrospectively-gated 4D flow cardiovascular magnetic resonance and three-dimensional vortex core analysis. J Cardiovasc Magn Reson. 2014;16:78

11. Gittenberger-de Groot AC, **Calkoen EE**, Poelmann RE, Bartelings MM, Jongbloed MRM. Morphogenesis and molecular considerations on congenital cardiac septal defects Ann Med 2014;46:640-52

12. **Calkoen EE**, Jansen FAR , Jongbloed MRM, Bartelings MM, Haak MC Imaging the first-trimester heart: ultrasound correlation with morphology. Cardiology in the young 2014;24 Suppl 2:3-12

13. **Calkoen EE**, Roest AAW, Geest van der RJ, Roos de A, Westenberg JJM Cardiovascular function and flow by 4D MRI techniques: new applications. J Thorac Imaging. 2014;29:185-96

14. **Calkoen EE,** Hahurij ND, Jongbloed MRM, Roest AAW, Gittenberger-de Groot AC, Poelmann RE, Ruiter de MC, Munsteren van CJ, Steendijk P, Blom NA. Echocardiographic assessment of embryonic and fetal mouse heart development: A Focus on Haemodynamics and Morphology. The Scientific World Journal 2014 23;:531324

15. **Calkoen EE**, Gabra HOS, Roebuck DJ, Kiely E, Elliott MJ. Aortopexy as treatment for tracheobronchomalacia in children: an 18 year single-centre experience. Pediatric Critical Care Medicine 2011 Sep;12:545-51

16. Fraga JC, **Calkoen EE**, Gabra HO, McLaren CA, Roebuck DJ, Elliott MJ. Aortopexy for persistent tracheal obstruction after double aortic arch repair J Pediatr Surg. 2009;44:1454-7

17. Fraga JC, Gabra HO, **Calkoen EE**, McLaren CA, Roebuck DJ, Elliott MJ. Long segment congenital tracheal stenosis in twins successfully treated by slide tracheoplasty. J Pediatr Surg. 2009;44:640-3.

5.2

Chapter 5.3

Dankwoord

Van muis tot mens en van microscopie tot 4DFlow MRI: dit proefschrift is het resultaat van samenwerking van de afdelingen kindercardiologie, anatomie&embryologie, radiologie, cardiologie en klinische&experimentele beeldverwerking (LKEB). Het was een voorrecht om met zoveel mensen samen te werken. Een speciaal woord van dank gaat uit naar:

Patiënten, vrijwilligers en hun ouders - voor deelname aan het onderzoek.

Professor dr. Nico Blom - voor de mogelijkheden te promoveren en samen te werken met verschillende afdelingen.

dr. Arno Roest - voor enthousiasme, positiviteit, betrokkenheid en danspassen.

dr. Monique Jongbloed - voor enthousiasme, gedrevenheid, precisie en oplossingsgerichtheid.

dr. Jos Westenberg – voor enthousiasme, behulpzaamheid en overdracht van kennis van 4DFlow.

Prof. dr. T. Ebels and dr. L. Grosse-Wortmann for taking part in the thesis committee and traveling all the way to Leiden.

Professor de Roos, dr. Kroft, Pieter van den Boogaard, Professor de Ruiter,
Professor Gittenberger-de Groot, dr. Bartelings, Professor Poelmann, dr. Hahurij, dr. Van der Geest,
dr. Rijlaarsdam, Professor Hazekamp, dr. Haak, Professor Schalij, Professor Bax, dr. Delgado, dr. Marsan,
Kwestan Hamasur - voor samenwerking, begeleiding en bijdrage aan artikelen.

Patrick de Koning - voor het toepasbaar maken van *particle tracing* voor een arts.

Mohammed Elbaz – for combining technical with clinical knowledge.

Gerrit Kracht en Ron Slagter - voor prachtige illustraties.

Sabine, Tjitske, Ilona, Corjan, Danny en Denise - voor het warme welkom op de afdeling kindergeneeskunde.

All collegues of the anatomy department and Sjoerd - for a great time in building 2.

Bauke - voor vele donderdagen achter de microscoop en op de fiets.

Conny - voor de tijd samen op de 9de verdieping en je hulp en geduld met de qPCR.

Bert en Jan - voor jullie hulp bij kleuringen en alle grappen.

Rebecca - voor hulp in de magische wereld van immuunkleuringen, qPCR en optical mapping, en voor de gezellige gesprekken tijdens lunch, koffie of borrel.

Tim en Annelot - voor een grap, een muziek tip, schaatsen, fietsen, lachen of een drankje.
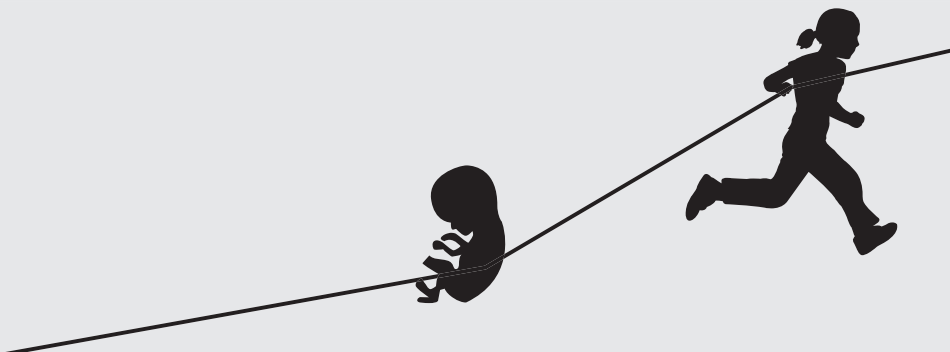
Vrienden en familie - voor interesse in mijn promotie en de mogelijkheid te relativeren met veel gezelligheid.

Willem en Jolande - voor een goed voorbeeld in doorzetten en eindeloos vertrouwen.

Andries en Tom - voor samen zijn.

5.3

Chapter 5.4

Curriculum Vitae

Emmeline Calkoen was born on June 5th 1985 in Rotterdam. She completed secondary school in Breda in 2003. After a year in England and India she started studying medicine at the University of Amsterdam. For a research internship, she spent 6 months in Great Ormond Street Hospital, in London to study clinical outcome of aortopexy under supervison of Professor Martin Elliot. She spend three months of her clinical rotations in Tanzania. She obtained her medical degree in 2011. After graduation she worked 5 months as a house officer in the Emma Children's Hospital in Amsterdam. Thereafter, under supervision of prof. dr. Blom (department of pediatric cardiology, Leiden University Medical Centre), dr. Roest (department of pediatric cardiology, Leiden University Medical Centre) and dr. Jongbloed (department of clinical anatomy and cardiology, Leiden University Medical Centre), she started as a PhD candidate focusing on development and long-term follow-up of an atrioventricular septal defect. In March 2015 she finished her PhD project and started training to become a general practitioner at the VU University, Amsterdam.

5.4